NUCLEAR MAGNETIC RESONANCE STUDIES OF COMPLEX MATERIALS SYSTEMS: FROM AMPLIFICATION TO ANISOTROPY

BY

ARIANE MAY VARTANIAN

DISSERTATION

Submitted in partial fulfillment of the requirements
for the degree of Doctor of Philosophy in Chemistry
in the Graduate College of the
University of Illinois at Urbana-Champaign, 2016

Urbana, Illinois

Doctoral Committee:

Professor Catherine J. Murphy, Co-Chair, Co-Director of Research
Professor Steven C. Zimmerman, Co-Chair, Co-Director of Research
Professor Paul V. Braun, Co-Director of Research
Assistant Professor Qian Chen

Abstract

This dissertation explores complex materials systems, with a special focus on developing nuclear resonance spectroscopy (NMR) techniques to decipher chemical environments at the molecular level. **Chapter 1** describes the design and synthesis of a two-state materials system based on an autocatalytic, positive feedback loop that amplifies a rare input into a massive output. **Chapters 2 – 4** probe nanoparticle systems with shape or functional anisotropy. **Chapter 2** details new approaches to add functionality to shape-anisotropic particles. **Chapter 3** establishes NMR spectroscopy as a powerful tool for interpreting the ligand shell morphology, spatial arrangement, dynamics, and distinct chemical environments that are trademarks of shape- and functionally-anisotropic particles. **Chapter 4** exploits the heterogeneous reactivity of shape-anisotropic particles to fabricate sophisticated, supramolecular building blocks that can form dynamic assemblies controlled by their association constants. **Chapter 5** builds on the robust NMR techniques in the preceding chapters to analyze complex nano-bio interactions that are otherwise difficult to probe.

Acknowledgments

I cannot thank my advisers enough. To all three, I have enormous gratitude for the patience, freedom, and trust they've extended over the years. Being in three research groups turned my academic wanderlust into something marketable: broad scientific fluency. Thanks for putting up with me while I figured it all out. Each of you has been a fantastic mentor in your own way. In alphabetical order: Paul Braun, you won me over from day one with your ingenuity and big, exciting ideas. The way you connect discordant concepts into unifying theories inspires me to always search for those hidden connections. Cathy Murphy, you never discouraged my curiosity, but instead let me take hold of a research idea and run with it, even if it didn't quite fit whatever grant was demanding results from you. For that reason I've learned more about thinking independently and critically than I thought I was capable of. Steve Zimmerman, I still remember what you told me when I visited as a prospective student: you admitted that you identify more as an artist than as a scientist. You've been as much of a kindred spirit as an adviser can be, and I admire that you pause to appreciate the beauty in chemical systems, because aestheticizing the molecular world is what got me into chemistry in the first place.

I'm grateful to the other two members of my committee, current and former. Qian Chen, thank you for filling in on such short notice. I attended your group meeting presentation when I was a first-year, and I think it's pretty great that the star grad student I respected then is now a faculty member on my committee. Alison Fout, thanks for your easygoing support and encouragement of my career during the past few years.

Each one of my groups has become a mini family, and I'm fortunate to have been surrounded by so many sharp, supportive colleagues. I owe thanks to all of my group mates, but there are a handful to whom I'd like to give an extra nod. In the Braun group, Corissa Lee and Austin Pickett deserve thanks for taking me under their wing as (Grass)Hopper. While writing this thesis and reading through my old lab notebook, I remembered how you guys pointed out my truly egregious mistakes, taught me how to nap clandestinely, and made those tough early days fun. Although I "lived" in the Zimmerman group for only a short time, all of you welcomed me as though I was a permanent fixture, going out of your way to invite me to group potlucks, find me chemicals, or offer tips in synthetic chemistry. Thanks in particular to Dawn Ernenwein for being such a good postdoc mentor and collaborator. I have many to thank in the Murphy

group, where I spent most of my time. You all have given countless suggestions in group meetings and practice talks, challenged my ideas, and offered gracious help when I was overwhelmed. I am most grateful to my current officemates, Wayne Lin, Elissa Grzincic, and Nardine Abadeer, for being the friendly faces I've seen day after day.

Talking to my medley of outside collaborators, from engineers to physical chemists to biologists, has considerably broadened my scientific scope. Thanks to all those in the Autonomous Materials Systems group at Illinois, and to those in the Center for Sustainable Nanotechnology all over the country.

Because of its staff, the NMR lab has secured its title as the friendliest user facility on campus. I think I gravitated toward NMR studies because I wanted to spend more time there. Lingyang Zhu, you have been such a phenomenal resource. Every time I left a meeting with you, I felt rejuvenated and hungry to do more NMR experiments. I wish you were one of those page-a-day calendars so that I could wake up every morning and absorb another bit of your knowledge. Dean Olson, you're a beam of light in a dingy hall. Thanks for cheering me up every time I walked into the NMR lab, and for addressing every email to me with a clever nickname I can't soon forget (H*ari*cots Verts). I'm so glad we have such an awesome NMR lab.

Five special women have ensured I've never lacked TLC in grad school – the IMP "moms" and staff: Connie Knight, Beth Myler, Theresa Struss, Karen Watson, and Stacy Dudzinski. In addition to all the departmental know-how and wonderful help, thank you so much for the extra things you've done that make me truly happy to be in this department – bringing your dogs to the office for us to cuddle, the themed treats you bake for Halloween, all the personal words of encouragement over the years.

I owe so much to my amazing friends here. You all made the good days great and the bad days go by faster. I have many fond memories with my roommates at the Ohio Street House (affectionately, Delta Tau Phi)—Sarah White, Elissa Grzincic, Josh Kaitz, Jeremy Smith, Stephen Ammann, and Tracey Codding—including fighting off giant sewer rats and grilling on the front lawn on lazy summer evenings. Those memorable times would've been incomplete without my other friends: Windy Santa Cruz, Maria LaGasse, Maria Bautista, Angela Kouris, Olbelina Ulloa, Tony Grillo, Bethany Grillo, Jon Durney, Hannah Haley, and Ben Brandsen. There have been many others. Thank you all for almost six years of incredible friendship and fun.

To my hockey team: I would not have made it through grad school without you girls. This team has meant more to me than most things I'll ever experience. I'm not ashamed to say that on many occasions it was my hunger to take home a league championship, not a diploma, that kept me in school. Well, we still haven't won a championship, but I can't stay any longer. I expect to see the banner when I visit next.

Ryan Musa, thanks for being a nice face to look at when I couldn't sleep because this thesis gave me insomnia. There are few as kind-hearted as you, and I am glad you exist.

Special thanks to my beloved 1995 Honda Civic, Calien. I've spent more time with him in the past eleven years than with any single human outside my family. He's taken me on road trips through the desert, across the plains, and over mountains; driven me back and forth from lab at weird hours; and been witness to everything in my life. He turns 21 this year, and very sadly, I have to toast him goodbye.

Finally, I'm grateful to my family – obviously, words can't express the degree to which I thank them. My grandparents, cousins, aunts and uncle have been an unbelievable support network. My dad gave me his sense of humor and the academic curiosity that I've always admired and aimed to imitate. I'm following in his path. The biggest thanks goes to my mom, who has been by my side through it all. Thank you for putting up with my horrible pranks over the years, for drawing little cartoons of my life, for setting aside your own interests for mine, and for all the other big and little things you've done over the years. You continue to teach me through your actions that being a good person (and family member and friend) is the most important thing to strive for.

Table of Contents

Chapter 1 Chemical Amplification in Materials Systems 1

1.1 Introduction 1

1.2 Selection and synthesis of acid amplifiers 4

1.3 Characterization of conversion 7

1.4 Acid amplification in polymers 15

1.5 Experimental 22

Chapter 2 Adding Functionality to Shape-Anisotropic Particles 32

2.1 Introduction 32

2.2 Click chemistry 39

2.3 Hyperbranched polyglycerols 41

2.4 Polystyrene 45

2.5 Polymersomes 46

2.6 Experimental 50

Chapter 3 NMR Studies of Particles with Shape and Functional Anisotropy 57

3.1 Introduction 57

3.2 High-yield gold rods: Obtaining necessary concentrations for NMR 67

3.3 Particles with shape anisotropy: Bilayer versus monolayer 69

3.4 Markers of shape anisotropy 78

3.5 Particles with shape and functional anisotropy 94

3.6 Experimental 99

Chapter 4 Supramolecular Anisotropic Building Blocks 101

4.1 Introduction . . . 101
4.2 Quadruple hydrogen-bonding modules . . . 108
4.3 Cucurbituril complexes . . . 113
4.4 Experimental . . . 115

Chapter 5 NMR Studies of Complex Nanoparticle-Biology Interactions . . . 129
5.1 Introduction . . . 129
5.2 Lipid corona formation: DMPC:DMPG and PAH gold particles . . . 132
5.3 No interaction: DOPC:DOTAP and gold particles . . . 137
5.4 Other vesicles . . . 140
5.5 Effects of cholesterol in vesicles . . . 141
5.6 Experimental . . . 143

Chapter 6 References . . . 147

Chapter 1

Chemical Amplification in Materials Systems

1.1 Introduction

Autonomic materials that respond productively to external stimuli are desirable, but often fail to exhibit a productive change in properties because the triggering event is either too weak or rare to cause wide scale chemical changes. Necessary is a chemistry that amplifies a rare trigger into a substantial signal, yet does not spontaneously actuate in the absence of a trigger. Examples of triggered bistable systems exist in nature; these include the neuronal firing pathway and cellular processes such as apoptosis, differentiation, and signaling.[1] These systems exist in either an initial or activated state, separated by an activation barrier high enough to minimize thermal activation. They are stable in the presence of sub-threshold stimuli, but once a specific stimulus exceeds a threshold value, the population is largely driven to the activated state and cannot reset to the original state. Although such systems would find utility in fields as diverse as self-healing and drug delivery,[2] they have not been realized in the synthetic world, in part because the criteria are challenging to fulfill synthetically.[3] The ensemble of molecules must respond to a small activation event, driven to completion by a positive feedback loop that links the output response back to the input. As a thought experiment, imagine a jar filled with Prince Rupert's Drops, tadpole-shaped glass droplets under large internal stresses.[4] The head of the drop can withstand immense force, but as soon as the threadlike tail snaps, the released potential energy causes fractures to propagate rapidly throughout the drop, which then explodes. In a jar filled with Prince Rupert's Drops, the explosion of one shattered drop would snap other fragile tails and pulverize the entire jar. We describe here the synthetic equivalent of a jar of Prince Rupert's Drops: a two-state material with a built-in positive feedback loop, such that a rare above-threshold stimulus fuels a vigorous reaction throughout the material, with the added element that the product of the reaction performs productive polymer chemistry. This material is based on an acidolytic molecule that autocatalytically generates protons, embedded within a polymer matrix that undergoes cationic crosslinking.

Autocatalysis provides a positive feedback loop and the potential for strong signal amplification. Because acid is central to many crosslinking mechanisms, we selected autocatalytic acid amplifiers as a model system.[5] Each molecule

liberates at least one equivalent of strong acid after catalytic acid "snaps" its acidolytic "Achilles heel." Both the initial catalytic proton and the newly released protons are capable of catalyzing additional acid amplifiers, generating a strong positive feedback loop that continues until the acid amplifier population is exhausted or if the acid is quenched faster than it is produced. Acid amplification has been demonstrated in photolithography, where it is used as a tool to enhance the response of a photoresist to a small number of photons. Acid amplifiers embedded in a compatible polymer matrix provide the opportunity for triggered autocatalytic acid generation followed by productive chemistry (e.g., cationic crosslinking). This two-state polymer system is separated by a threshold, because only acid strength exceeding the acidolytic activation barrier can drive a global transformation from fluid polymer (initial state) to a crosslinked solid (activated state). This bistability is irreversible.

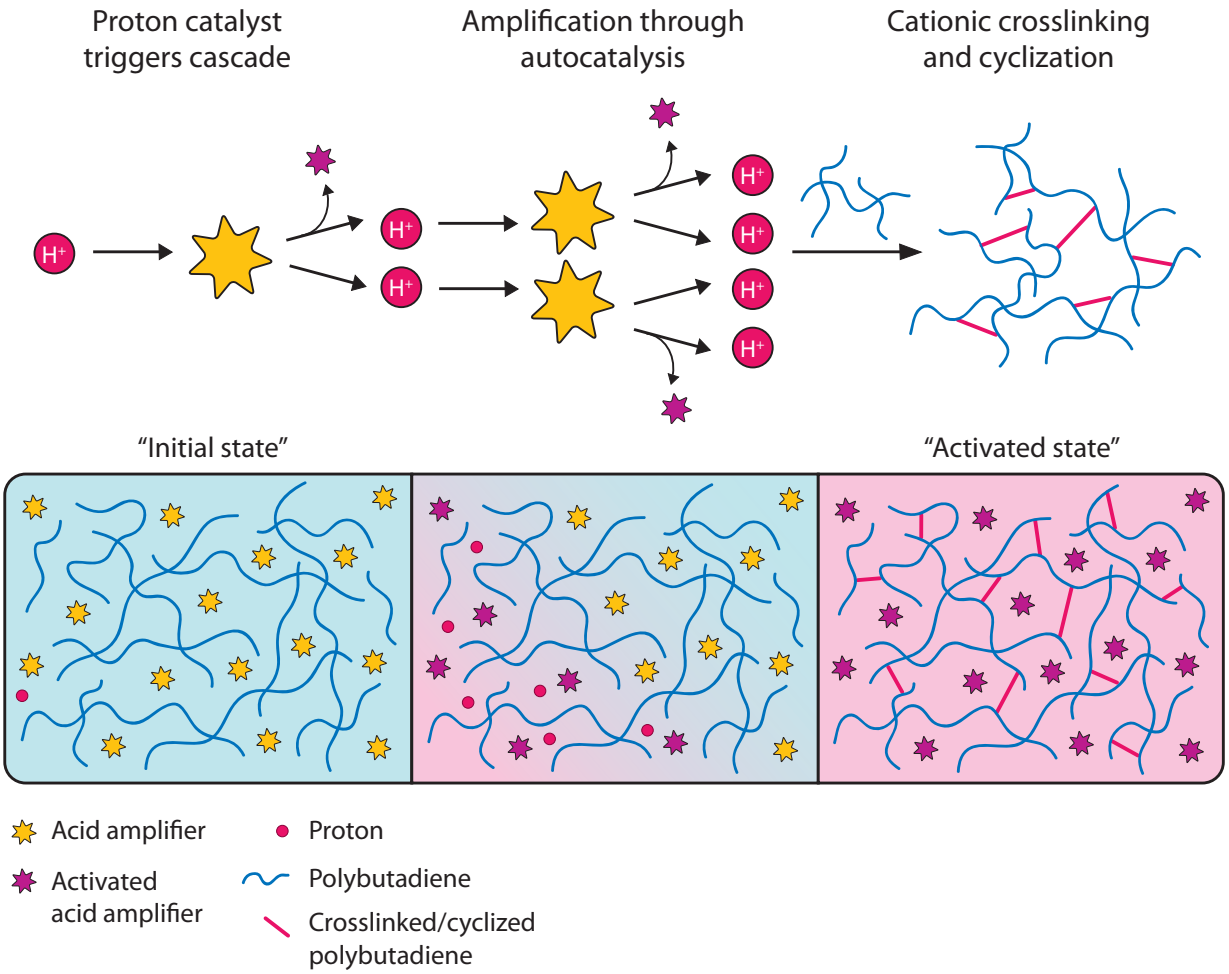

Figure 1.1 In our chemically-amplified system, a small proton input initiates a positive feedback mechanism to produce a large output of protons. The proliferated acid goes on to crosslink a polymer, driving it from a liquid "initial" state to a solid "activated" state.

The motivation for specifically targeting an acid trigger is our collaborating group's previous work on polymer-

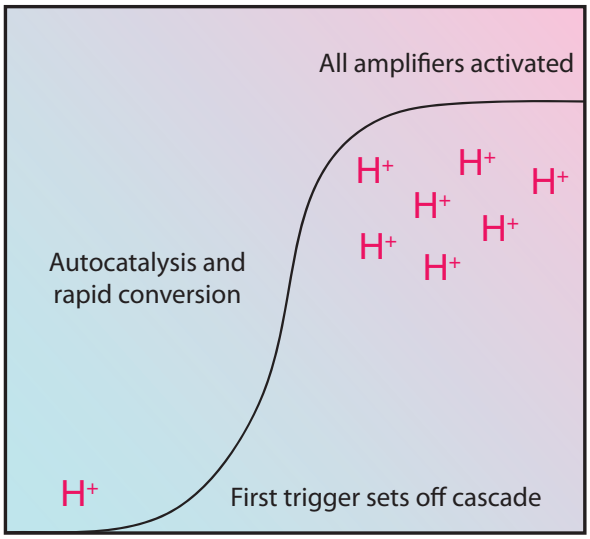

Figure 1.2 Acid amplification follows sigmoidal conversion kinetics, a marker of autocatalytic systems.

bound mechanophores that generate hydrochloric acid under mechanical force.[6] Mechanophores are responsive chemical species that are actuated by mechanical energy. They possess a labile element that purposely and predictably rearranges under force, driving a productive reaction that is distinct from mechanical failure. For example, functional mechanophores have been designed to change colors or form reactive or catalytic species. The acid-producing mechanophore contains a *gem*-dichlorocyclopropane component, which is known to rearrange under force to a 2,3-dihaloalkene or eliminate acid under other conditions.[7,8] To drive the reaction toward the latter elimination pathway, the mechanophore was based on an indene framework, such that the 5-membered ring is favorably aromatized as HCl is eliminated. Because force is typically transferred to the mechanophore by tethering polymer chains to both ends of the labile bond, the mechanophore was incorporated into poly(methyl acrylate) as a crosslinker. However, stress on the polymer chains activates only a small percentage of the mechanophores, enough to effect a slight pH drop, but insufficient to induce macroscopic matrix changes. Under the proper conditions, coupling of this rare mechanochemical event to our acid-amplifying pathway may lead to a robust material that crosslinks under force (Figure 1.4).

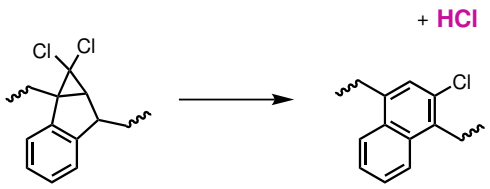

Figure 1.3 The acid-generation mechanophore eliminates one equivalent of hydrochloric acid per force-induced molecular rearrangement.

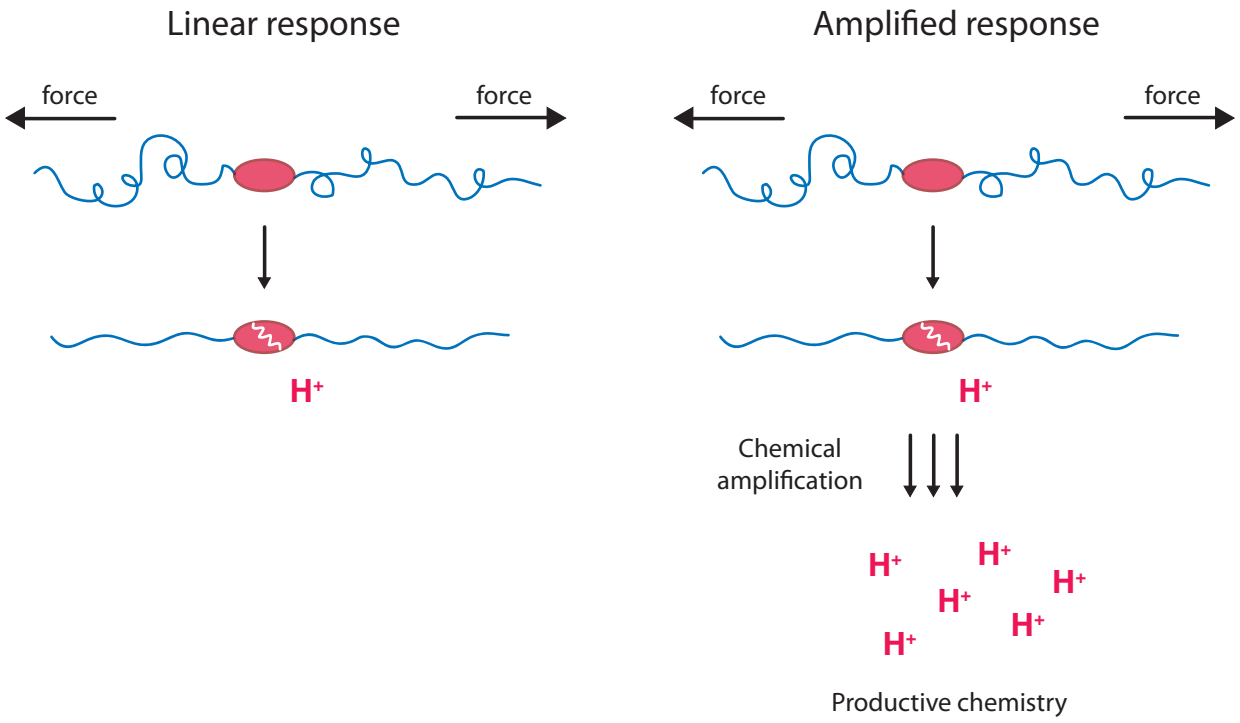

Figure 1.4 In a linear response, one molecular event produces one proton. A nonlinear response via a chemical amplification pathway is necessary to generate enough protons to perform subsequent productive chemistry.

1.2 Selection and synthesis of acid amplifiers

Previous work using acid amplifiers has focused almost exclusively on photolithography, using them as a tool to enhance the sensitivity and rate of photoacid-induced acidolytic reactions in thin film resists.[9] For development of a responsive material, an acid amplifier should fulfill a number of criteria. The acid amplifier should activate autocatalytically, the trigger should be selective to acid and stable under ambient conditions, and the product acid should be strong and mobile enough in a bulk matrix to perform the desired reaction. Various families of acid amplifiers are known, including benzyl sulfonates,[10] acetoacetates,[11] β-ketals,[12,13] 1,2-diol monosulfonates,[14] and trioxanes.[15] Some of these acid amplifiers can release two or three equivalents of acid per molecule, greatly enhancing the rate of acid proliferation.[15] Although all acid amplifiers use an acid catalyst to create more acid, not all decompose autocatalytically; the product acid must be strong enough to act as the catalyst in subsequent cycles. Many of the acid precursor motifs found in the literature are sulfonate esters, because they make excellent leaving groups and the resulting sulfonic acid can catalyze a variety of organic reactions. From a synthetic perspective, sulfonates are simple to incorporate into a molecule by alcohol esterification, and the acidity, stability, and reactivity of sulfonates and sulfonic acids are easily tuned.

Once an acid amplifier is chosen, it can be built into the architecture of a responsive material (Figure 1.5). The matrix

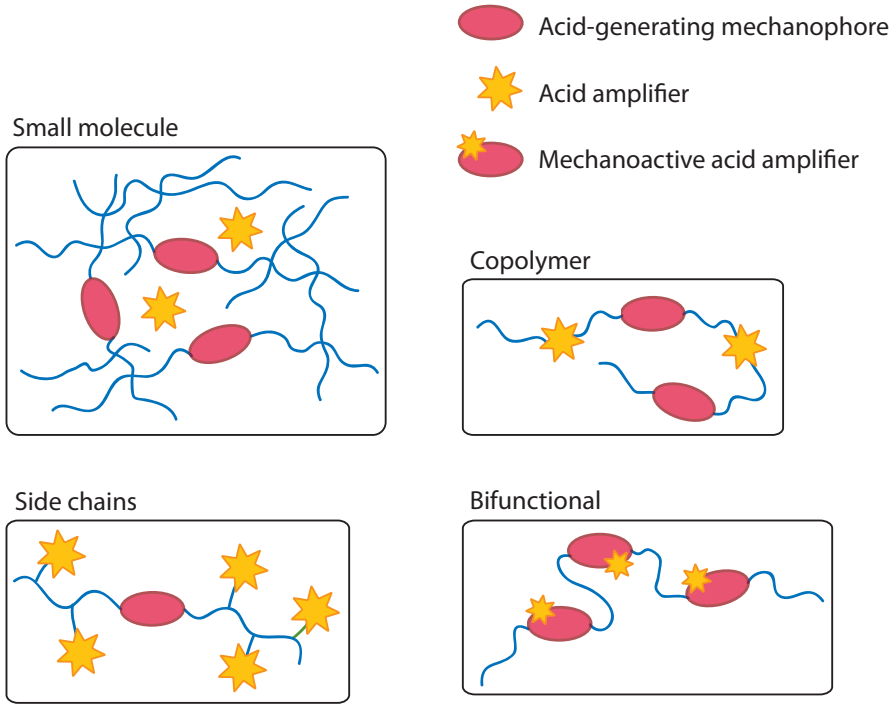

Figure 1.5 Acid amplifiers can be incorporated into a variety of polymer frameworks.

itself should contain acid-reactive sites so that it undergoes a macroscopic transformation upon acid proliferation. The initial acid catalyst can be internal, if an acid-generating mechanophore is tethered to the matrix, or external. In the most straightforward design, neat acid amplifier is loaded into the responsive matrix as a small molecule additive. The acid product is freely mobile to catalyze further reactions. The acid amplifier can also be crafted into a monomer to be copolymerized with the mechanophore, with the amplifier appended as side chains or integrated into the polymer body itself. Depending on the design of the monomer, activation would leave the polymer with dangling acid groups, eject free acid groups, or elicit autocatalytic fragmentation of the entire polymer chain. Finally, the most ambitious—and challenging—goal is the design of a mechanoactive acid amplifier, in which a trigger(s) is cleavable by both force and acid, so initial application of force sets off the autocatalytic cascade.

The first molecules studied were intended as frameworks to design a mechanoactive acid amplifier, which must have its force-sensitive bonds fastened between polymer chains. Benzyl tosylates, substituted at the *para* position with an acidolytic *tert*-butoxycarbonyloxy (*t*-BOC)-protected alcohol group, were prepared.[10] *p*-substituents dramatically affect both the thermal stability and reactivity of benzyl sulfonates, so cleavage (either acidolytically or mechanically) at that position might be easiest to tune. After acidic cleavage of *t*-BOC and subsequent formation of isobutylene and carbon dioxide, the deprotected electron-donating alcohol group stabilizes the benzyl cation, promoting decomposition of the sulfonate into sulfonic acid. We envisioned that we could attach initiator groups to the benzyl species

and protecting group, embedding the structure within a polymer chain. Mechanical force could "rip off" the *para* protecting group, triggering autocatalytic production of sulfonic acid. However, thermal stability was poor of both 4-(*tert*-butoxycarbonyloxy)benzyltoluenesulfonate and an analog with a *meta* nitro group intended to improve stability, with degradation occurring at room temperature in the course of days, and in elevated temperatures spontaneously. Moreover, we realized the synthetic barriers to an actual mechanically-active acid amplifier were high, so the benzyl tosylate framework was set aside.

For practical purposes, the next candidates had straightforward, gram-scale syntheses and decent thermal stability. Brainard and colleagues reported comprehensive studies on the design and kinetics of a family of methylbutylsulfonate acid amplifiers, lending insight into their modes of catalysis.[16,17] They found that their acid amplifiers with tertiary triggers decomposed autocatalytically, whereas secondary triggers were not sufficiently acidolytic and required additional superacid to decompose. In addition, methoxy triggers led to much faster rates of decomposition than did hydroxyl triggers. The authors identified a correlation between the least negative values of entropy of activation $\Delta S^{\ddagger}$ and the fastest rates (and $\Delta G^{\ddagger}$ values). Based on these results, we selected 3-methoxy-3-methylbutyl-4-toluenesulfonate, the fastest-decomposing molecule that produces tosylic acid. Acid-catalyzed decomposition of this molecule is energetically favorable: a protonated methoxy trigger cleaves to yield an allylic sulfonate ester, which decomposes into strong tosylic acid and benign isoprene as a byproduct. We were also able to build this acid amplifier into a styrenesulfonate monomer, such that catalysis leads to polystyrene (or copolymer) laden with sulfonic acid species. However, although we were able to demonstrate autocatalytic amplification in certain matrices (more below), neither the tosylic acid appeared to be strong enough nor the autocatalytic rate fast enough for our purposes. To fix these issues, we replaced the toluenesulfonate ester with a pentafluorobenzenesulfonate ester. The highly-electronegative fluorine atoms greatly stabilize the sulfonate ester, improving its leaving group ability and conjugate acid's strength. In regard to its lower thermal stability, our tests indicated that the molecule did not catalyze thermally at our reaction temperatures. The primary downside is that the fluorinated acid might diffuse slightly more slowly through a matrix than tosylic acid, but the difference is probably negligible. Whereas the authors lamented the poor lithographic performance of the perfluorinated acid amplifier, the very characteristics that make it unsuitable for photolithography make it an excellent candidate for a responsive material.

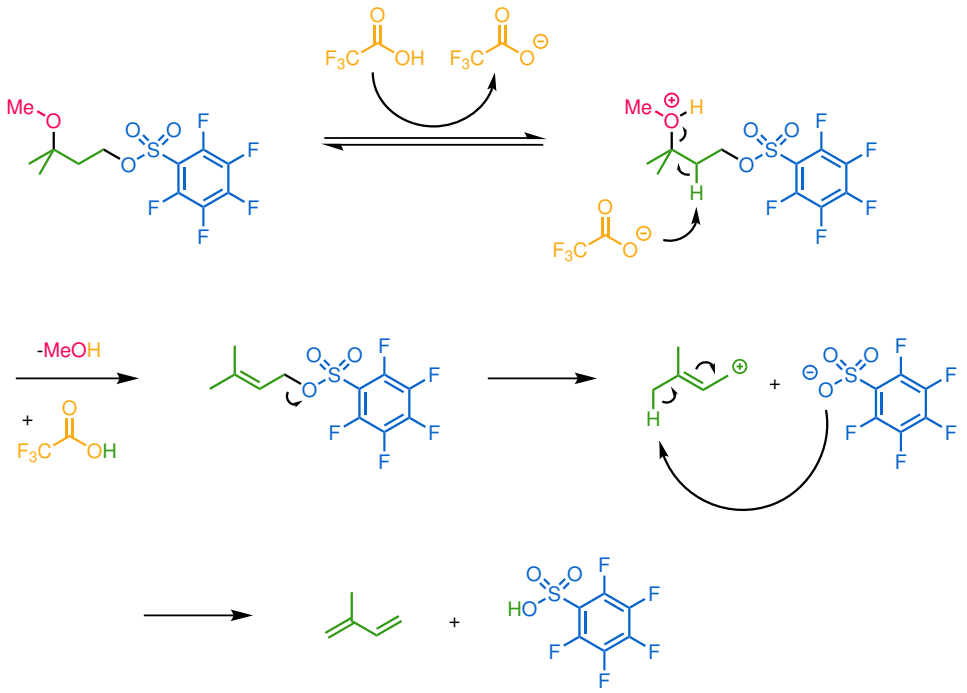

Figure 1.6 The autocatalytic amplification mechanism for 3-methoxy-3-methylbutyl-pentafluorobenzenesulfonate involves protonation of a methoxy trigger, regeneration of the acid catalyst, and formation of a very strong perfluorinated sulfonic acid.

In the perfluorinated amplifier's proposed autocatalytic mechanism, an acid catalyst protonates the methoxy trigger, priming it to be a stable leaving group as methanol (Figure 1.6). The catalyst is regenerated when it abstracts the β proton, driving the elimination reaction that "breaks" the trigger and pushes off methanol. The allyl sulfonate ester then leaves, forming an allylic carbocation and the sulfonate. The sulfonate becomes protonated in another β-elimination reaction to stabilize the carbocation, and the final products are isoprene (the rearranged body) and sulfonic acid. This cycle starts over, with both the product acid and the original catalyst available for the initial protonation step.

1.3 Characterization of conversion

1.3.1 Identification of byproducts

When 3-methoxy-3-methylbutyl-4-toluenesulfonate is activated by an acid catalyst and unravels to release the sulfonic acid precursor, isoprene is left as the rearranged species. Thus, identifying isoprene in the reaction solution should confirm both acid amplifier activation and its proposed mechanism. The dry polymeric resin Amberlyst 15, hydrogen form, was chosen as a solid-state acid catalyst to not convolute the reaction mixture with additional solubilized

species. The resin features sulfonic acid groups on crosslinked styrene-divinylbenzene copolymer beads. A solution of 3-methoxy-3-methylbutyl-4-toluenesulfonate and Amberlyst 15 resin in acetonitrile was stirred for 15 minutes to catalyze the reaction. An equal volume of cyclohexane was added to extract any organic species, including isoprene if present, and the organic layer was removed and saved for analysis.

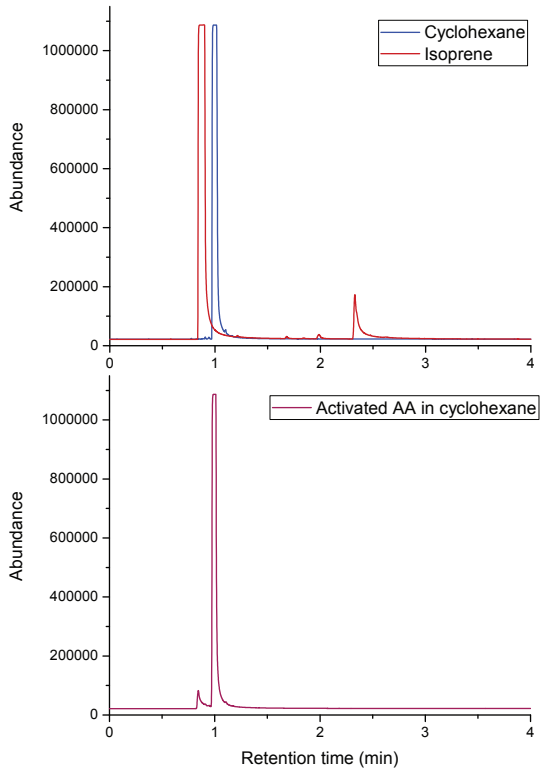

Figure 1.7 Gas chromatography demonstrates that isoprene is formed when the acid amplifier is introduced to an acid catalyst, supporting the proposed mechanism and successful activation.

Gas chromatography was run for a cyclohexane standard, an isoprene standard, and the activated acid amplifier organic layer. Retention time for cyclohexane was 1.01 min and for isoprene was 0.84 min and 2.33 min (the second longer time may be due to dimer impurities in the standard). The activated acid amplifier organic layer contained two species with retention times at 0.84 and 1.01 min, confirming that only isoprene and cyclohexane are present (Figure 1.7).

1.3.2 UV-Vis studies

Methyl orange was chosen as a pH indicator because of its observable color change at mid-range acidities. Methyl orange is red in highly acidic solutions, and yellow in more alkaline ones. In acetonitrile, it is pink at pH values lower

than 3.1, orange at pH values between 3.1 and 4.4, and yellow at pH values above 4.4. The acidic, red species absorbs at approximately 540 nm, and the basic, yellow species absorbs at approximately 420 nm.

The UV-Vis spectrum of 3-methoxy-3-methylbutyl-4-toluenesulfonate in acetonitrile confirmed that the acid amplifier alone does not absorb in the measured wavelengths. For the pH indicator experiments, the acid-amplified sample was prepared with methyl orange and neat 3-methoxy-3-methylbutyl-4-toluenesulfonate dissolved in acetonitrile, whereas the control contained only methyl orange in acetonitrile. Amberlyst 15 resin was added as acid catalyst to both samples, and UV-Vis spectra were taken immediately (t = 0 minutes) and at various time points up to t = 30 minutes (Figure 1.8).

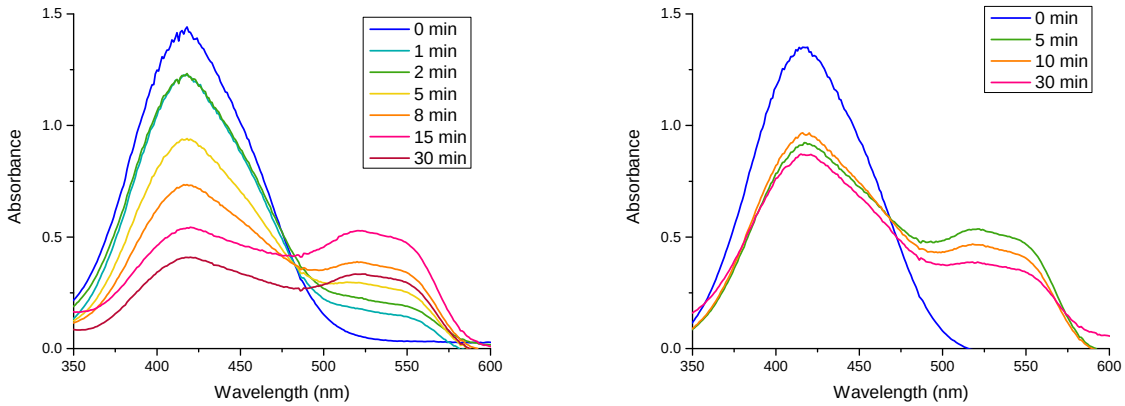

Figure 1.8 UV-vis spectra of methyl orange and an acid catalyst in acetonitrile. The acid-amplified solution becomes more acidic over time (left), whereas the control solution does not (right).

In the acid amplifier sample, at t = 0 minutes, only the methyl orange basic form is observable at λmax = 420 nm. As time progresses, the basic form decreases in absorbance along with the appearance and increase of the acidic form at λmax = 540 nm. For the control sample, the decrease in basic form and increase in acidic form levels out after about 5 minutes. Interestingly, neither sample has a clear isosbestic point. By visual observation of the sample, the solution also begins to lose color intensity over time, eventually becoming colorless. We reasoned that the resin beads gradually pull the methyl orange dye out of solution; the aromatic body of methyl orange is likely to have an affinity for the styrene-divinylbenzene resin matrix.

1.3.3 NMR studies

Matrix dependence

To determine what type of solid-state matrix would best promote the amplification mechanism, NMR studies were performed in several deuterated solvents: toluene-d_8, benzene-d_6, cyclohexane-d_{12}, THF-d_8, and chloroform-d. The acid amplifier 3-methoxy-3-methylbutyl-2,3,4,5,6-pentafluorobenzenesulfonate (21.3 mg, or 87 mM) was dissolved in 0.7 mL of solvent in an NMR tube, and excess trifluoroacetic acid (TFA; 11.4 μL, or 210 mM) was added and the tube capped immediately. The mixture was allowed to rest for 18 hours at room temperature, after which a ^{1}H NMR spectrum was taken of each.

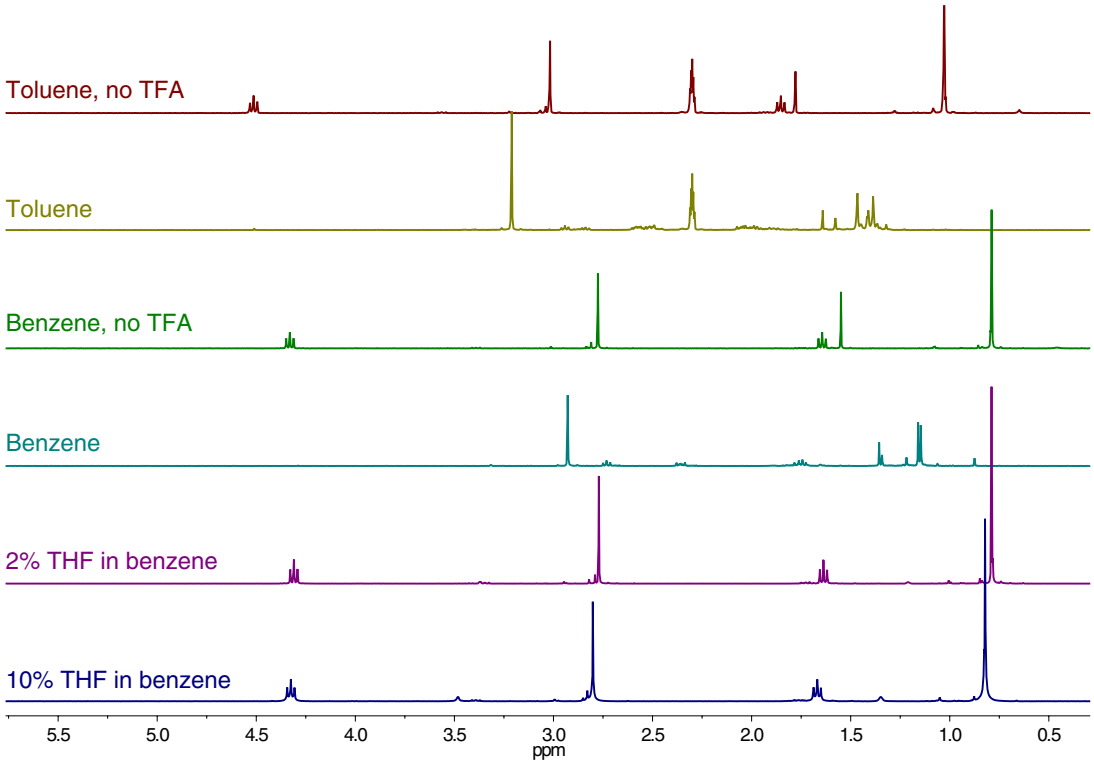

Figure 1.9 ^{1}H NMR spectra of the acid amplifier and acid catalyst in a variety of deuterated solvents. Acid amplification proceeds best in aromatic hydrocarbons, whereas nucleophilic or basic solvents appear to quench the reaction.

The extent of acid amplifier activation was judged qualitatively by observing the disappearance of the acid amplifier's four resonances (chemical shift, δ, dependent on solvent): triplet in the 4.3 – 4.5 ppm range (– O – CH_2), singlet in the 2.8 – 3.2 ppm range (– O – CH_3), triplet in the 1.6 – 2.1 ppm range (– C – CH_2), and singlet in the 0.8 – 1.3 ppm range (– C – CH_3). Only in toluene and benzene did the acid amplifier activate completely, as supported by the disappearance

of all four resonances and appearance of several new, messy peaks. In cyclohexane and chloroform, some new peaks were observed, but the original four peaks were still present; this result suggests that activation is possible but very slow in those solvents. In THF, the acid amplifier appeared to be stable against activation. To verify THF's role in preventing activation, the same NMR experiment was repeated in 2% (volume %) THF in benzene and 10% THF in benzene. In neither solvent mixture did the acid amplifier activate: both post-18 hour spectra in THF/benzene looked nearly identical to the pre-18 hour (i.e., no TFA added) spectrum of acid amplifier in benzene, and were distinctly different from the post-18 hour spectrum in benzene (Figure 1.9).

Taken together, these data suggest that the mechanism of acid amplification is most efficient in nonpolar, hydrocarbon matrices with aromatic or vinylic character. Because polar solvents favor proton ionization by stabilizing the charges created, this result is surprising but can be explained by a number of factors.[18] The mechanism of amplification first requires that TFA donates its proton to the methoxy trigger, leaving the trifluoroacetate anion, which is poorly stabilized by the nonpolar environment. This lack of stability may drive the next step, abstraction of a proton by the anion in a β-elimination reaction. Similarly, a later mechanistic step describes the formation of a sulfonate anion, which then picks off another proton to stabilize both the anion and the allylic cation. The proton abstraction steps should be highly favored in a nonpolar solvent. The preference for aromatic solvents over cyclohexane may be explained by the aromatics' stabilization of the isoprene formed during the reaction, through interaction of π-bonds. In addition, the reaction-quenching effect of just 2% THF in benzene supports the theory that nucleophilic or basic sites compete for protons with the methoxy trigger, and that this competing pathway dramatically slows down or inhibits the amplification mechanism. Finally, nonpolar solvents widen the pK_a gap between acids as compared to polar solvents, because the anionic conjugate base of the acid is so poorly solvated that the electronic properties that determine acidity (or, put another way, the electronics that dictate how stable the conjugate base is) are emphasized.[19] Therefore, there is a greater pK_a difference between the acid catalyst (TFA) and the stronger product acid (pentafluorobenzenesulfonic acid). As the sulfonic acid is produced, the equilibrium shifts such that TFA is effectively less acidic in the mixture. The sulfonic acid and TFA both compete to donate a proton to the methoxy trigger, but as the stronger acid, the sulfonic acid is more likely to be the donor. This shifting equilibrium drives the formation of more sulfonic acid, pushing the reaction forward. The accentuated pK_a difference between TFA and pentafluorobenzenesulfonic acid in nonpolar solvents may intensify this driving force.

Acid-catalyzed activation vs. heat degradation

(For the purposes of this discussion, "activation" refers to the acid-catalyzed, autocatalytic process in which the acid amplifier proliferates protons, and "degradation" refers to any process not triggered by a catalyst proton.) Acid amplifiers

are notorious for their poor thermal stability, and in many cases degrade within days at room temperature and very quickly at elevated temperatures. For some acid amplifiers with overly-labile triggers, this degradation process may follow the same mechanism as its acid-catalyzed activation, snapping the trigger and proliferating acid. In other words, these acid amplifiers are actuated by either acid or heat (or ambient conditions in extreme cases). For this work, we desired a selective acid amplifier that undergoes autocatalysis only by an acid catalyst, a true molecular Prince Rupert's Drop whose trigger can withstand challenging conditions—but unravels in the presence of a mere proton.

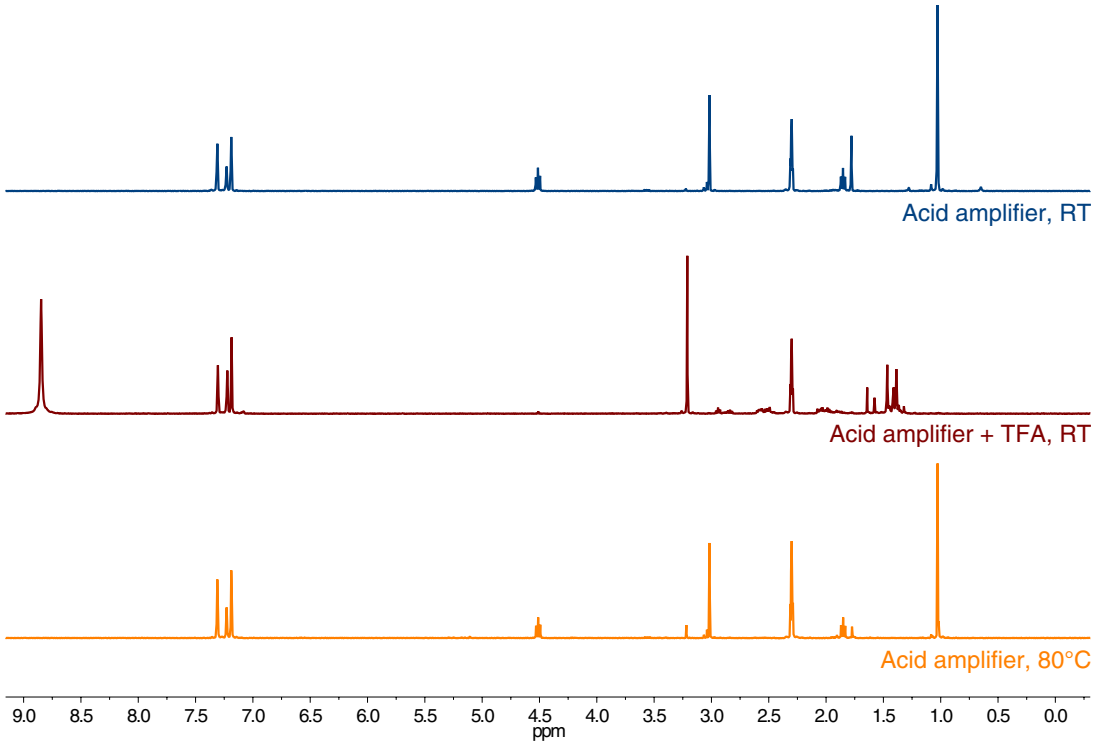

Figure 1.10 ^{1}H NMR of acid amplifier with an acid or heat trigger. The trigger is selective: the acid amplifier remains stable at 80°C, whereas it activates at RT with an acid trigger.

The acid- or heat-catalyzed products of 3-methoxy-3-methylbutyl-2,3,4,5,6-pentafluorobenzenesulfonate were analyzed by ^{1}H NMR spectroscopy to determine whether the processes follow the same mechanism. The acid amplifier was dissolved in toluene-d_8 and divided into aliquots. The acid-catalyzed sample was treated with TFA and the sample kept at room temperature for 18 hours. The heat-catalyzed sample was kept at 80°C for 18 hours in the absence of an acid catalyst. A control sample was simply kept at room temperature for 18 hours.

When compared to the control, the acid-catalyzed sample produced a completely different spectrum (also described above in the solvent dependence study) (Figure 1.10). None of the original four acid amplifier resonances were present and several new peaks appeared, presumably byproducts of the autocatalytic mechanism. However, the spectrum of the

heat-catalyzed sample was nearly indistinguishable from that of the control: all four acid amplifier peaks were present, with no new peaks. This result suggests that not only is this acid amplifier remarkably stable at high temperatures, any potential thermal degradation does not follow the same autocatalytic pathway as acid-catalyzed actuation. The methoxy trigger appears to be stable at a minimum of 80°C; heat does not cause the CH_3O^- anion to leave on its own.

Kinetics and conversion

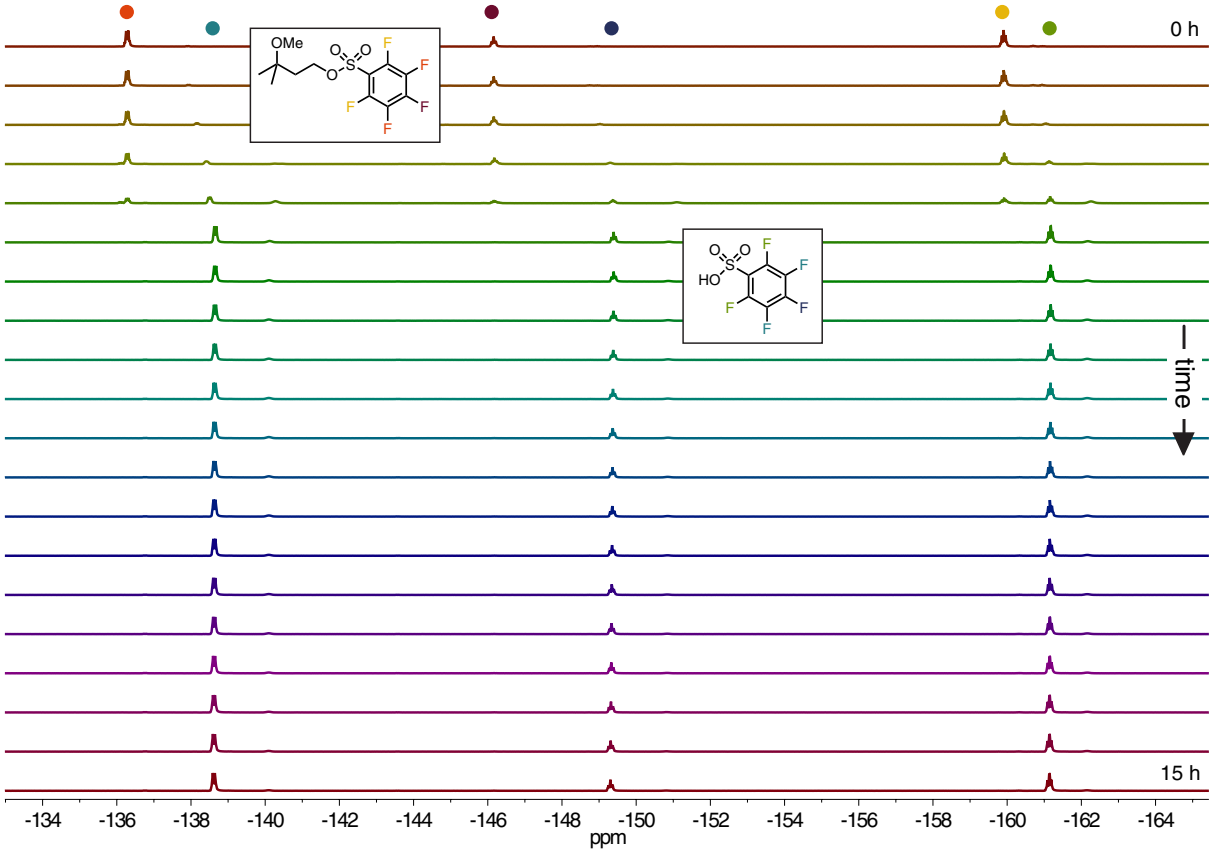

Figure 1.11 ^{19}F NMR of the acid amplifier and TFA in benzene-d_6 at 60°C. The three fluorine peaks of the acid amplifier convert completely to three new peaks corresponding to the fluorinated acid product.

Reaction monitoring via ^1H and ^{19}F NMR in benzene-d_6 confirmed the complete degradation of acid amplifier over 18 hours at 25°C and 4 hours at 60°C when exposed to trifluoroacetic acid (TFA)(Figure 1.11). At t = 0, three ^{19}F resonances assigned to 3-methoxy-3-methylbutyl pentafluorobenzenesulfonate are observed: a doublet of triplets at -136.28 ppm (*meta*-fluoro), a triplet at -146.16 ppm (*para*-fluoro), and a triplet at -159.90 (*ortho*-fluoro). Over time, those three resonances reduce in intensity, along with the appearance of three new resonances. These new resonances can be assigned to the forming pentafluorobenzenesulfonic acid: a doublet of triplets at -138.62 ppm (*meta*-fluoro), a

triplet at -149.31 ppm (*para*-fluoro), and a triplet at -161.13 ppm (*ortho*-fluoro). Interestingly, the trifluoroacetic acid resonance also experiences a change in chemical shift over 4 hours, from -76.55 to -75.97 ppm. The normalized integral values of the acid amplifier (starting material) and sulfonic acid (product) were plotted against time.1.12

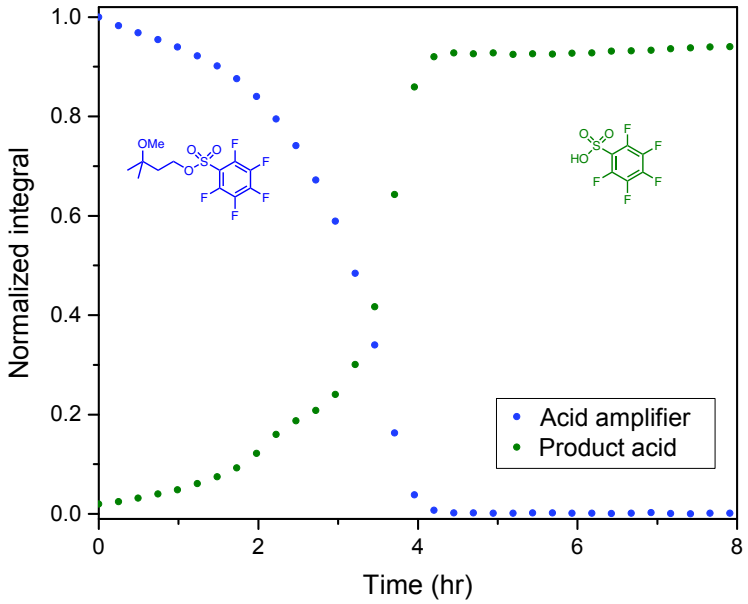

Figure 1.12 Integration values from ^{19}F NMR reaction monitoring. Conversion of acid amplifier to product acid follows a roughly sigmoidal trend, as expected for autocatalysis. Complete conversion is observed after 4 h.

The kinetic curve of conversion for autocatalysis is sigmoidal, and our data follows a similar trend, as shown by the relative integrals of fluorine peaks in the starting material versus product (Figure 1.12). Initial conversion begins gradually as the first few acid amplifiers are catalyzed, then due to autocatalysis, acid production escalates and finally tapers off as the acid amplifier population is exhausted.

Proton NMR serves as a remarkable probe for the acidity of the solution. The chemical shift of the TFA proton moved sharply upfield—9.18 to 8.62 ppm—as the reaction progressed at 25°C, then drifted gradually back downfield to 8.70 ppm (Figures 1.131.14). Since more acidic protons appear downfield by virtue of their increased dissociation, long length of the O-H bond, and decreased shielding from electron density, a possible explanation is that the stronger pentafluorosulfonic acid product (predicted pKa more negative than -3) "competes" with TFA (pKa = 0.5) as its concentration in solution increases.[20,21] Thus, the TFA proton is effectively less acidic, and less easily abstracted. The pk_a gap between the two acids is accentuated in a nonpolar solvent such as benzene.[19] The observed trend agrees with the rapid proliferation of a strong acid, then a tapering off in concentration as the acid amplifiers are consumed. Additionally,

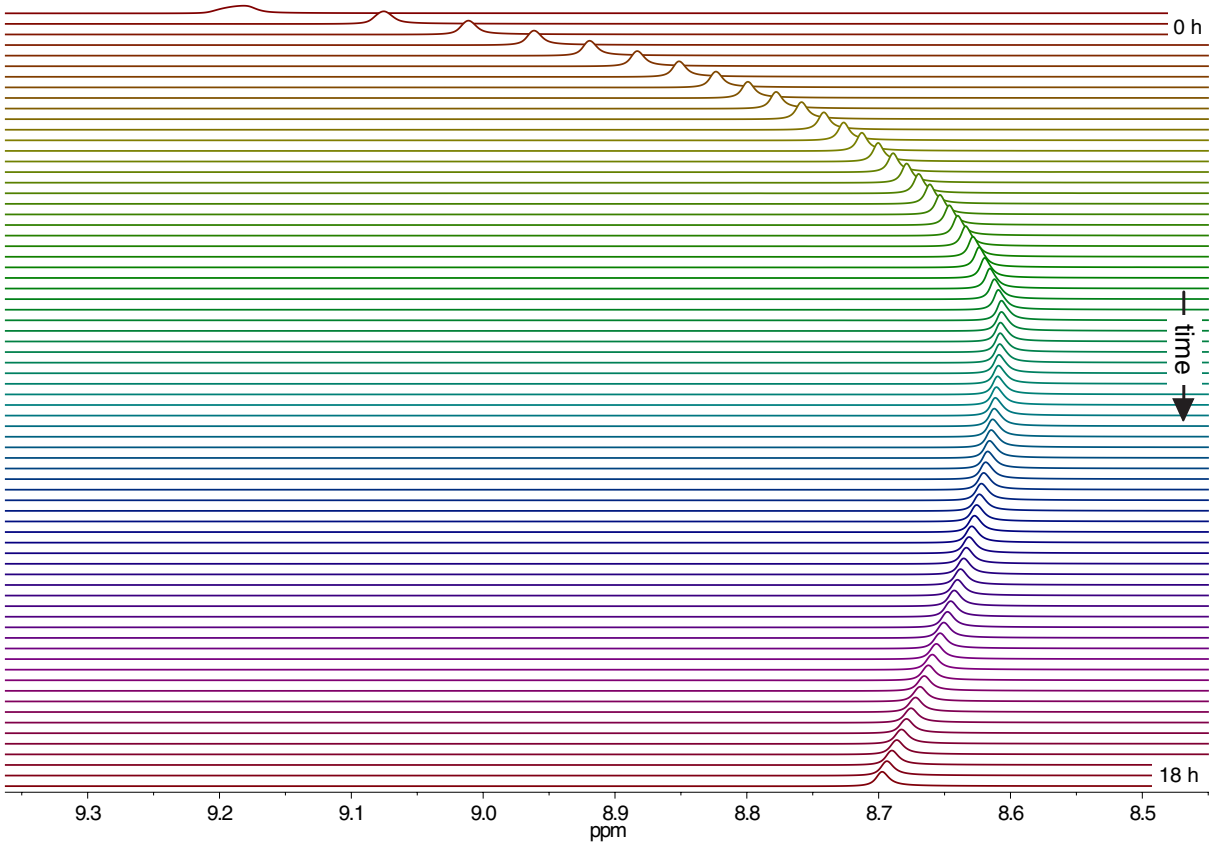

Figure 1.13 ^{1}H NMR of acid amplifier and TFA in benzene-d_6 at 25°C. The resonance frequency of the TFA proton peak serves as a visual indicator of the acidity of the solution.

as the time progresses, the linewidth of the acidic proton narrows; this is consistent with decreased hydrogen bonding or chemical exchange. The reversal of chemical shift and slight downward drift after about 8 hours may be an effect of solvent polarity or pH changes.

1.4 Acid amplification in polymers

1.4.1 Epoxy crosslinking

Because acid amplifiers coupled with photoacid generators (PAGs) are widely used in photolithography, the epoxy negative photoresist SU-8 was first chosen as a matrix. SU-8 contains Bisphenol A Novolac epoxy oligomers, with an average of 8 epoxy units per oligomer, and mixed triarylsulfonium hexafluoroantimonate salts as the PAG. Upon exposure to UV light at 365 nm, the formed hexafluoroantimonic acid protonates the epoxide groups, leaving them

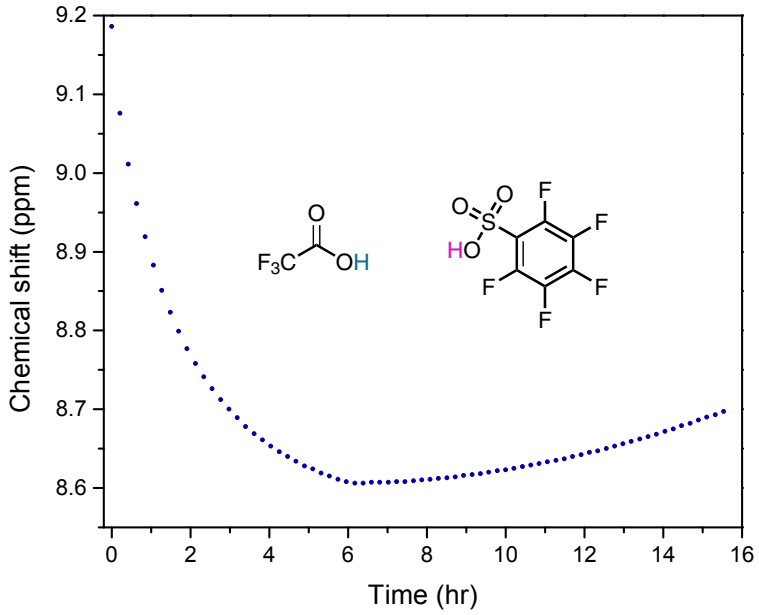

Figure 1.14 The chemical shift of the TFA proton changes frequency, suggesting that TFA becomes less "effectively acidic" as the newly-produced, stronger sulfonic acid competes for protonation sites.

ready for crosslinking. However, crosslinking is significantly stalled until the resin is heated in the post-bake process. Once crosslinked, SU-8 becomes insoluble; areas that are not crosslinked can be washed away with solvent. The aim here was to replace UV light for an acid catalyst, and compare the efficiency of crosslinking between SU-8 loaded with acid amplifier and SU-8 without, so a formulation of SU-8 that does not contain PAG was chosen.

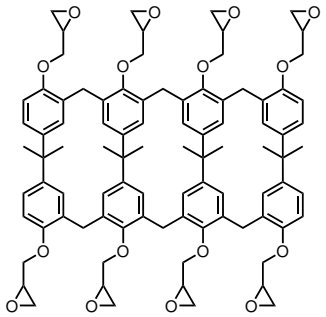

Figure 1.15 The structure of SU-8 epoxy.

Two issues were immediately apparent. Firstly, the glass transition temperature (T_g) of SU-8 is 64°C, meaning molecules inside the matrix have low mobility at room temperature, suppressing molecular and proton diffusion. To increase mobility, we opted to leave SU-8 in its commercial solvent, cyclopentanone. Secondly, because polymerization of SU-8 usually requires heat, we wondered if the reaction could occur at room temperature if the oligomers were

solvated.

By Fick's laws of diffusion, the rate of diffusion of a proton in SU-8 could be roughly estimated.

$$x = \sqrt{Dt} \tag{1.1}$$

x: distance traveled in cm

D: diffusion coefficient in cm^2/s

t: time in s

The diffusion coefficient, D, of a proton in water is 10^{-5} cm^2/s. Assume for a proton in solvated SU-8, $D = 10^{-7}$ cm^2/s. Therefore, it would take approximately 10 seconds for a proton to travel 10 μm in SU-8, an experimentally-reasonable amount of time.

To test whether solvated oligomers could crosslink at room temperature, SU-8 with PAG was first used. In the typical procedure for spincoating SU-8, a glass slide was cleaned with acetone and isopropanol. An adhesion layer was first spincoated with SU-8 2000.5, which makes a 500 nm film. Nitrogen was blown over the glass slide and a blunt-tip cut glass pipette to remove dust. The glass slide was placed in the spincoater, and the pipette was used to cover the entire substrate with SU-8. The spincoater was set at 2000 rpm for 40 seconds. The slide was then transferred to a hot plate and covered with aluminum foil, where it was heated at 65°C for 5 min and 95°C for 25 min for the prebake, which drives off solvent. The slide was then cooled for 2 min and exposed to UV light at 365 nm for 15 minutes. In the postbake, the substrate was heated under the same conditions as the prebake in order to heat the SU-8 above T_g. Finally, the sample was developed by soaking in propylene glycol methyl ether acetate (PGMEA) overnight, then rinsed with isopropanol. For the thick layer, SU-8 2010 was chosen to make a 5 μm film. The same procedure as for the adhesion layer was followed through the spincoating step. However, the thick layer did not undergo the prebake step, in order to keep the oligomers solvated, or the postbake step, to test polymerization efficiency at room temperature. Instead, the slide was exposed to 365 nm UV light for 15 minutes immediately after spincoating, then left for 2 hours before developing. The SU-8 with PAG was insoluble after the developing step, confirming that the crosslinking can occur at room temperature when solvated. To make sure the acid amplifier 3-methoxy-3-methylbutyl-4-toluenesulfonate would not inhibit crosslinking, SU-8 with PAG was loaded with the acid amplifier (10% by volume), exposed to UV and postbaked; crosslinking was observed.

Next, we moved onto SU-8 without PAG (SU-8 R 2010) as the thick layer to eliminate the use of UV irradiation. This SU-8 was loaded with the acid amplifier (5, 10, or 20% by volume), whereas SU-8 R without acid amplifier served as the

control. Glass slides were prepared with adhesion layers, followed by spincoating with either thick layer as described above, except with a few modifications. There was no UV exposure step (along with no pre- or postbake steps), the spincoating rotation speed was reduced to 1000 rpm to thicken the layer, and some of the slide was left uncoated to create an edge to help visualize crosslinking.

For the catalysis step, we needed a way to expose the SU-8 to the acid catalyst for a controlled amount of time, so we selected a gaseous acid that could be flowed over the sample and then the sample removed. Hydrochloric acid (HCl) was the first acid catalyst tried. A gas flow apparatus was set up as such: nitrogen was flowed through a bubbler filled with an aqueous solution of HCl, and the acidic vapors were carried into a vacuum-greased and sealed chamber that held the SU-8 substrate. Excess acidic gas flow was bubbled into water. HCl was flowed through the chamber for various durations, from 30 seconds to 5 minutes. However, HCl solution up to 10 M was not sufficient to crosslink either the acid amplifier-loaded SU-8 (at any concentration) or the control (indicated by dissolution in PGMEA).

Trifluoroacetic acid (TFA) was then chosen as the candidate catalyst. As an organic acid, TFA is compatible with anhydrous conditions, which may be important for both the amplification and crosslinking chemistry. It is also a strong acid, with a pKa of 0.5 in water. Finally, it has a high vapor pressure (boiling point = 72°C), so the sample can be easily treated with TFA vapors and then removed. SU-8 samples, prepared as described earlier, were placed in a special glass slide holder suspended over a thin layer of TFA in a sealed 8-dram vial. When 100% TFA was added to the vial, both acid amplified and control samples crosslinked within 15 minutes, turning brown and peeling off the glass substrate; the vapors crosslinked the top layer of SU-8, causing it to shrivel up before crosslinking the rest. The acid activity (or "effective concentration" of TFA) was then manipulated by dissolving TFA in a high boiling point solvent, tetraethylene glycol dimethyl ether (tetraglyme, boiling point = 275°C). The samples were exposed to the TFA/tetraglyme mixtures for up to 36 h. At 2% TFA in tetraglyme (by volume), no crosslinking occurred for either the acid amplified or control sample. At 5, 10, and 20% TFA, crosslinking appeared to occur on the surface, but not through the entire matrix.

These data suggest two points: that the amplification process does not proceed efficiently in this matrix, which is supported by the NMR solvent dependence study; and that the acid amplifier 3-methoxy-3-methylbutyl-4-toluene-sulfonate is not labile enough, or the tosylic acid product not sufficiently strong, to carry out the epoxy crosslinking reaction in the timeframe measured.

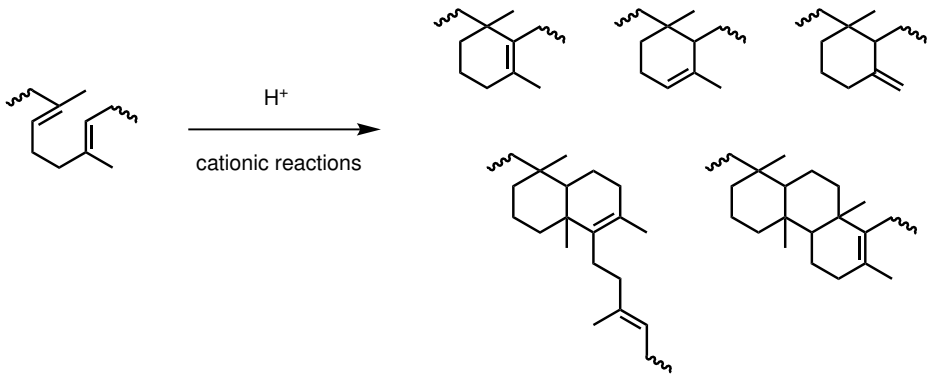

Figure 1.16 In the presence of acid, polybutadienes undergo a variety of intra- and intermolecular cationic reactions, including crosslinking and cyclization.

Figure 1.17 The structures of vinyl-1,2-polybutadiene (left) and cis-1,4-polybutadiene (right).

1.4.2 Polybutadiene crosslinking and cyclization

To test the amplification chemistry in a model polymer system, we sought to find an appropriate organic matrix. The acid amplifier 3-methoxy-3-methylbutyl-4-toluenesulfonate was also replaced for 3-methoxy-3-methylbutyl-pentafluorobenzenesulfonate, which was expected to be a more effective amplifier. As described earlier, amplification proceeds best in a nonpolar medium with no competing basic or nucleophilic sites, which significantly suppress autocatalysis. Thus, we ruled out polymers such as epoxies and selected small molecular weight polybutadienes as model nonpolar, low glass transition temperature (T_g) polymers for our autocatalytic chemistry. The low T_g means that these polybutadienes are a viscous liquid at room temperature, allowing proton and acid amplifier mobility, and an additional solvent is not necessary because the acid amplifier and TFA catalyst are both soluble in the polymer. The alkene-rich chains of the polybutadiene undergo cationic crosslinking and cyclization reactions initiated by acids (Figure 1.16).[22,23] Unlike similar polymers whose crosslinking processes require mineral or Lewis acids and catalysts, polybutadiene can crosslink with organic acids, critical for our required water-free chemistry.[24,25] Both crosslinking and cyclization processes are thought to proceed through the formation of a carbenium ion by an available proton, and occur in parallel, transforming oligomeric polybutadiene from a viscous fluid to an elastomeric gel or glassy solid.[26] Such macroscopic phase changes would be easily observable if the autocatalytic chemistry is successful. Of course, polybutadiene and its copolymers, such as styrene-butadiene rubber (SBR) and acrylonitrile butadiene styrene (ABS), are versatile and industrially important materials, so this system may also have some practical implications.

For this work, we chose two small molecular weight butadienes, a primarily vinyl-1,2-polybutadiene (M_w = 2,000 g/mol) and a primarily cis-1,4-polybutadiene (M_w = 3,000 g/mol) (Figure 1.17). The pendent alkene groups of the vinyl form should favor crosslinking, while the cis form may be more likely to cyclize intramolecularly. It was expected that the fluorinated sulfonic acid produced by our acid amplifier would be strong enough to induce cationic processes, and that the polymer matrices would thus experience significant mechanical property changes.

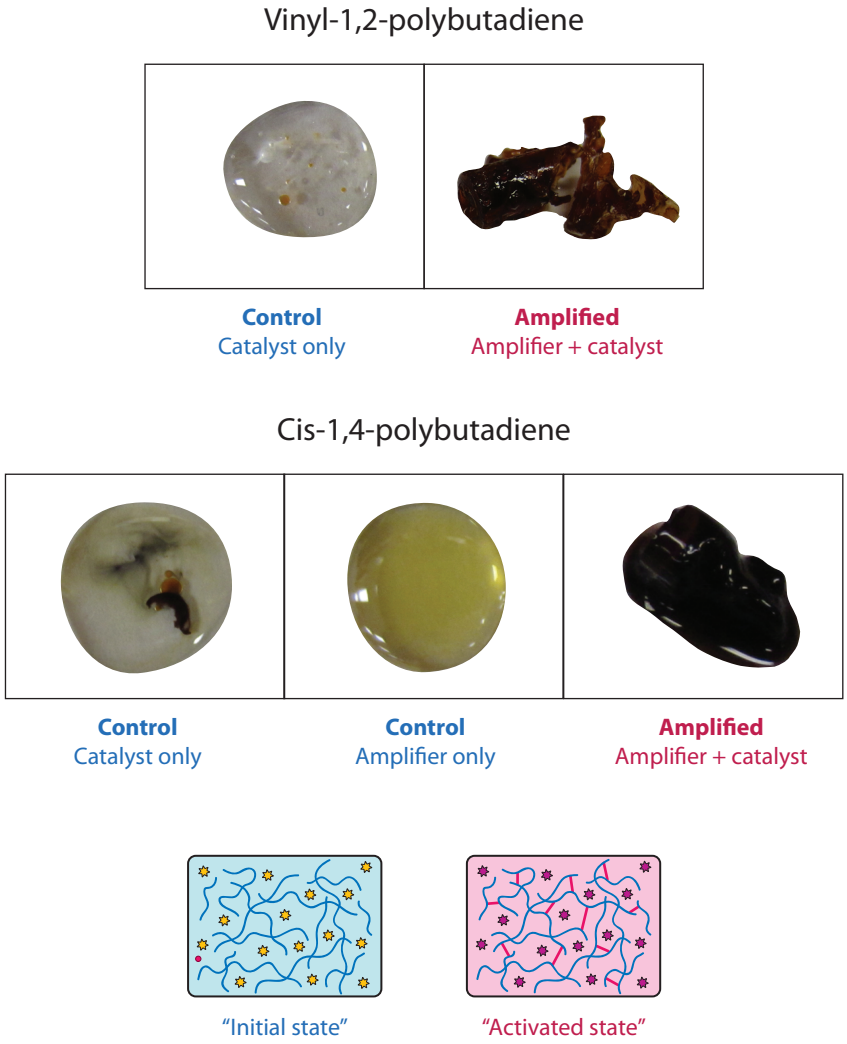

Figure 1.18 Vinyl- and cis-polybutadienes were loaded with acid amplifier and triggered with catalytic TFA at 70°C. Macroscopic changes were observed in both polymers, transforming from a viscous solution (initial state) to a rubbery or glassy solid (activated state). Control samples, containing only catalyst or only amplifier, remained a viscous solution, without a global phase change. A schematic of the proposed molecular composition of "initial" and "activated" states is shown at bottom.

Vacuum-purged polybutadiene was mixed with neat acid amplifier (2.5% by volume) and TFA catalyst (1% by volume), and the homogenous solution was loaded into a sealed inert polyethylene-polypropylene syringe. (The ex-

periment was also performed to the same effect in glass vials to determine that the plastic syringes do not affect the chemistry. The syringes permitted removal of headspace and easy extraction of the polymers for characterization.) The solutions were heated to 70°C in an oven. Whereas the acid amplifier can undergo autocatalysis slowly at room temperature, mild heating appears to improve the rate of polybutadiene crosslinking and cyclization.[27] After 30 minutes, both the vinyl and cis polymers loaded with both TFA and acid amplifier had undergone a dramatic phase change, to a glassy solid and rubbery gel, respectively. Both materials were insoluble in a range of organic solvents, indicating that they were crosslinked. To mimic a "rare" acid-trigger event and verify the autocatalytic nature of the acid-generating chemistry, varying molar ratios of TFA to acid amplifier (1:1 and 1:10) were tested. These samples all crosslinked, although the 1:10 TFA:AA ratio took a longer time to achieve complete crosslinking. In addition, we tested hydrochloric acid as a catalyst to extend the concept to a larger range of practical materials, including the HCl-producing mechanophore. Concentrated HCl successfully crosslinked the polymer at a slower rate than did TFA, probably because of dampening effects of water on the autocatalytic mechanism.

As controls, samples of polybutadiene were prepared in the absence of either acid amplifier or acid catalyst and subject to the same conditions (Figure 1.18). Polybutadiene without acid amplifier, catalyzed with either TFA or HCl, showed no global macroscopic changes even after 24 hours of heating. In the cis-polybutadiene matrix, the acid catalyst crosslinked only the small section of polymer that it was in contact with, observed as a colorless fluid with a tiny amount of brown gel. The vinyl-polybutadiene experienced very little to negligible crosslinking with only the catalyst. In both cases, the rare or weak catalyst was not itself sufficient to induce global crosslinking. The polymers loaded with only acid amplifier, and no catalyst, also did not experience a phase change. Cis-polybutadiene became yellow after heating but remained a fluid, suggesting that the acid amplifier degrades or interacts with this matrix at 70°C in a way that does not produce acid. Along with the previous NMR results confirming that the acid amplifier does not proceed down the autocatalytic pathway at 80°C in the absence of acid catalyst, we can exclude the possibility that heat alone induces crosslinking. With these results, we have demonstrated that our amplification chemistry is robust enough to crosslink a bulk polymer matrix, and selective enough to be actuated by only an acid catalyst.

Preliminary characterization used gel rheology to determine the moduli and mechanical properties of these cross-linked materials, and pH measurements of the gels to confirm the higher acid concentration in the amplified system. To complete this work, we will perform a series of NMR experiments to determine the threshold of acid catalyst required to activate autocatalysis, and mechanical testing on the oligomeric and cross-linked polymers. Finally, to tie these results back to mechanochemistry, we are working with collaborators in the Moore group to embed their acid-generating mechanophore into our amplified matrix to create the first force-triggered crosslinking polymer.

1.5 Experimental

1.5.1 General

All materials were used as received, unless otherwise indicated. Reported reaction temperatures refer to the temperature of the heating medium. Nuclear magnetic resonance (NMR) spectra were acquired using a Varian Unity 400 MHz, Varian Unity Inova 400 MHz, or Varian Unity 500 MHz spectrometer. Spectra were processed with MNova or VnmrJ. Chemical shifts are reported in parts per million (ppm) and were referenced to the residual proton solvent peak. Splitting patterns are designated as s (singlet), d (doublet), t (triplet), q (quadruplet), dd (doublet of doublets), m (multiplet), and br (broad).

1.5.2 Synthesis of acid amplifiers

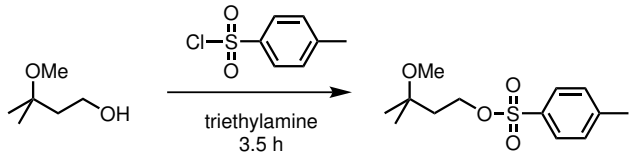

3-methoxy-3-methylbutyl-4-toluenesulfonate

To a solution of 3-methoxy-3-methyl-1-butanol (3.8 mL, 30.0 mmol) and triethylamine (30 mL, 215 mmol) was added *para*-toluenesulfonyl chloride (4.7 g, 24.5 mmol), and the cloudy white mixture was stirred for 3.5 h. The cream-white mixture was diluted in ethyl acetate (100 mL), then washed with 1 M HCl (6 x 50 mL), saturated aqueous $NaHCO_3$ (50 mL), and brine (50 mL). The organic layer was dried over sodium sulfate, gravity filtered, and concentrated *in vacuo* to yield a pale yellow oil (5.60 g, 84%). ^{1}H NMR (400 MHz; $CDCl_3$): δ 7.78 (d, 2H), 7.34 (d, 2H), 4.12 (t, 2H), 3.09 (s, 3H), 2.44 (s, 3H), 1.86 (t, 2H), 1.12 (s, 6H) ppm (Figure 1.19).

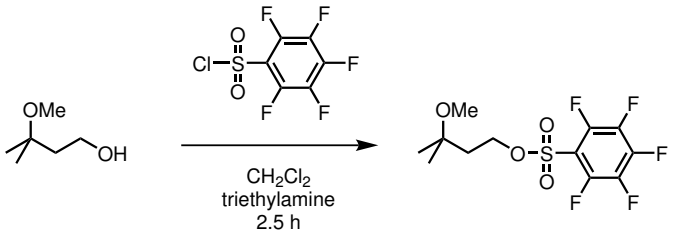

3-methoxy-3-methylbutyl-2,3,4,5,6-pentafluorobenzenesulfonate

Pentafluorobenzenesulfonyl chloride (1.1 mL, 7.5 mmol) was added to a solution of 3-methoxy-3-methyl-1-butanol (1.16 mL, 9 mmol) and triethylamine (0.84 mL, 6 mmol) in dichloromethane (12 mL). The yellow solution was stirred under nitrogen for 2 h, after which saturated aqueous $NaHCO_3$ was added and the mixture stirred for an additional 30 min. The organics were extracted with dichloromethane (100 mL) and washed with 0.5 M HCl (3 x 50 mL), saturated aqueous $NaHCO_3$ (50 mL), and brine (50 mL). The organic layer was dried over sodium sulfate and concentrated *in vacuo* to give the crude product as a yellow oil. The crude oil was purified using silica gel column chromatography with 2:3 (v:v) ethyl acetate:hexanes to yield a colorless liquid (1.23 g, 47%). ^{1}H NMR (400 MHz; $CDCl_3$): δ 4.44 (t, 2H), 3.15 (s, 3H), 1.99 (t, 2H), 1.19 (s, 6H) ppm (Figure 1.20).

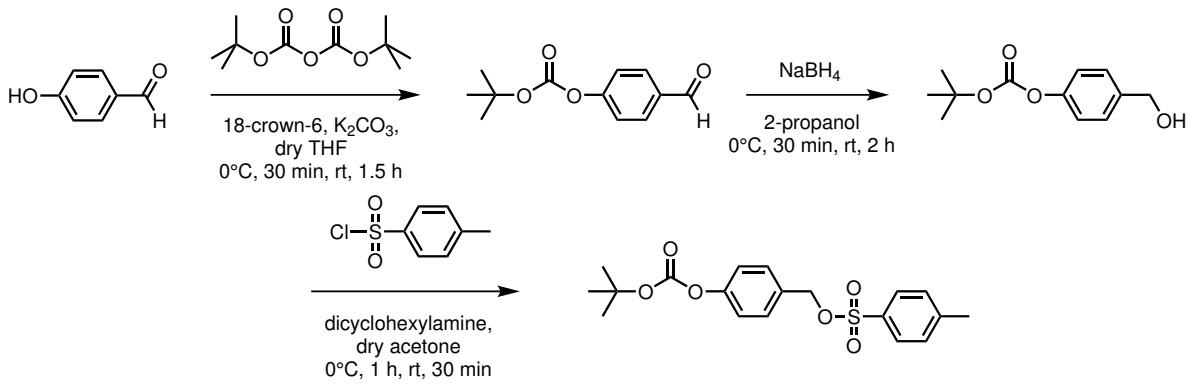

4-(*tert*-butoxycarbonyloxy)benzaldehyde

A solution of di-*tert*-butyl dicarbonate (3.0 g, 14 mmol) and 18-crown-6 (0.05 g, 0.19 mmol) in dry THF (7.5 mL) was added dropwise to a solution of 4-hydroxybenzaldehyde (1.6 g, 13 mmol) in dry THF (7.5 mL) in the presence of K_2CO_3 (2.5 g, 18 mmol) at 0°C. The golden-yellow mixture was stirred for 30 min at 0°C and then for 1 h at RT. The mixture was gravity filtered and concentrated *in vacuo* to a solvent volume of 3 mL, after which dichloromethane (15 mL) was added. The organic layer was washed with brine (2 x 15 mL), dried over magnesium sulfate, and gravity filtered. The solvent was removed under reduced pressure to yield a yellow solid (1.69 g, 59%). ^{1}H NMR (400 MHz; $CDCl_3$): δ 9.99 (s, 1H), 7.92 (d, 2H), 7.36 (d, 2H), 1.57 (s, 9H) ppm (Figure 1.21).

4-(*tert*-butoxycarbonyloxy)benzyl alcohol

To a solution of 4-(*tert*-butoxycarbonyloxy)benzaldehyde (1.33 g, 5.9 mmol) in 2-propanol (35 mL) was added $NaBH_4$ (0.16 g, 4.3 mmol) at 0°C. The yellow solution was stirred at 0°C for 30 min and for 2 h at RT. Chloroform (100 mL) was added, and the organics were washed with brine (2 x 125 mL) and dried over magnesium sulfate. The solution was dried over magnesium sulfate and concentrated *in vacuo* to yield a yellow liquid (1.52 g, 158%, excess yield from 2-propanol). ^{1}H NMR (400 MHz; $CDCl_3$): δ 7.36 (d, 2H), 7.15 (d, 2H), 4.66 (s, 2H), 1.93 (broad s, 1H), 1.55 (s, 9H) ppm (Figure 1.25). Extra peaks from residual 2-propanol.

4-(*tert*-butoxycarbonyloxy)benzyltoluenesulfonate

A solution of dicyclohexylamine (1.3 g, 7.2 mmol) in dry acetone (2 mL) was added dropwise over the course of 30 min to a stirring solution of 4-(*tert*-butoxycarbonyloxy)benzyl alcohol (1.5 g, 6.7 mmol) and *para*-toluenesulfonyl chloride (1.4 g, 7.2 mmol) in dry acetone (17 mL) at 0°C. The cloudy white mixture was stirred for an additional 30 min at 0°C and for 30 min at RT. Water (6 mL) was added and the mixture stirred for 15 minutes. The acetone was removed under reduced pressure, and the white suspension was dissolved in dichloromethane (30 mL). The organic layer was washed with water (3 x 30 mL), 0.2 M HCl (30 mL), 0.1 M Na_2CO_2 (30 mL), and water (30 mL). The organics were dried over magnesium sulfate, gravity filtered, and concentrated *in vacuo* to yield a white solid, which was determined to be partly pure by NMR (Figure 1.23).

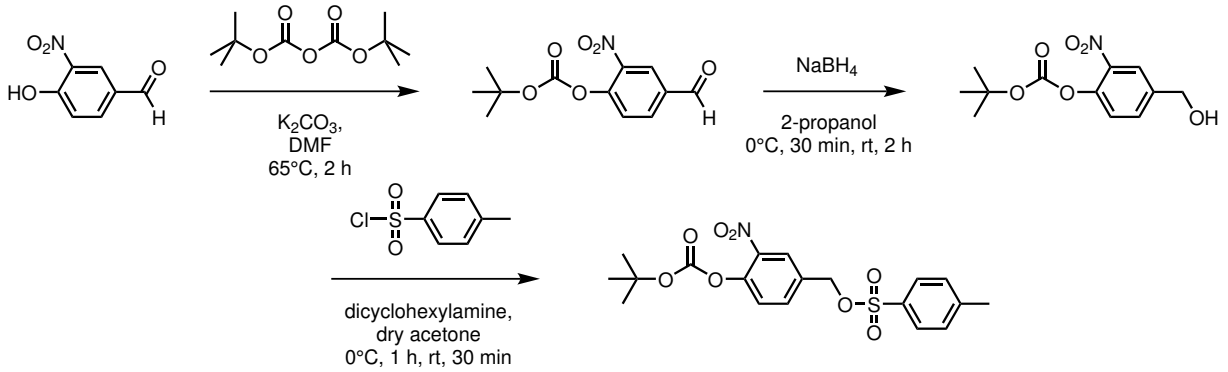

3-nitro-4-(*tert*-butoxycarbonyloxy)benzaldehyde

A stirring solution of 3-nitro-4-hydroxybenzaldehyde (4.0 g, 24.0 mmol) and di-*tert*-butyl dicarbonate (5.5 g, 25 mmol) in DMF (30 mL) was heated to 65°C for 2 h in the presence of K_2CO_3 (4.0 g, 29 mmol). The rust-red mixture was gravity

filtered and suspended in chloroform (100 mL). The organic solution was washed with brine (7 x 100 mL), dried over magnesium sulfate, and gravity filtered. The solvent was removed under reduced pressure, leaving the crude product as a yellow oil. The crude solid was purified by silica gel column chromatography with 2:3 (v:v) ethyl acetate:hexanes to yield the product as a light yellow powder (2.90 g, 45%). ^{1}H NMR (500 MHz; $CDCl_3$): δ 10.06 (s, 1H), 8.60 (d, 1H), 8.18 (dd, 1H), 7.51 (d, 1H), 1.58 (s, 9H) ppm (Figure 1.24).

3-nitro-4-(*tert*-butoxycarbonyloxy)benzyl alcohol

$NaBH_4$ (0.07 g, 1.8 mmol) was added to a solution of 3-nitro-4-(*tert*-butoxycarbonyloxy)benzaldehyde (0.56 g, 2.5 mmol) in 2-propanol (15 mL). The yellow solution was stirred at 0°C for 30 min and at RT for 2 h. Chloroform (40 mL) was added to the orange reaction mixture, and the organics were washed with brine (2 x 50 mL), dried over magnesium sulfate, and gravity filtered. The solvent was removed under reduced pressure to leave the crude product as a thick yellow oil. The oil was purified by silica gel column chromatography with benzene, followed by ethyl acetate, to yield the product as a bright yellow oil (0.29 g, 60%). ^{1}H NMR (400 MHz; $CDCl_3$): δ 8.11 (s, 1H), 7.65 (dd, 1H), 7.29 (d, 1H), 4.77 (s, 2H), 2.04 (s, 1H), 1.57 (s, 9H) ppm (Figure 1.25).

3-nitro-4-(*tert*-butoxycarbonyloxy)benzyltoluenesulfonate

A solution of dicyclohexylamine (0.22 g, 1.2 mmol) in dry acetone (1 mL) was added dropwise over the course of 30 min to a stirring solution of 3-nitro-4-(*tert*-butoxycarbonyloxy)benzyl alcohol (0.29 g, 1.1 mmol) and *para*-toluenesulfonyl chloride (0.23 g, 1.2 mmol) in dry acetone (3 mL) at 0°C. The cloudy yellow solution was stirred at 0°C for an additional 30 min, then at RT for 30 min. Water (1 mL) was added, and the mixture was stirred for 15 min. The acetone was removed under reduced pressure, and dichloromethane (4.5 mL) was added to the suspension. The organic layer was washed with water (3 x 5 mL), 0.2 M HCl (5 mL), 0.1 M Na_2CO_3, and water before being dried over magnesium sulfate and gravity filtered. The solvent was removed under reduced pressure to yield the crude product as a yellow oil. Silica gel column chromatography was used to purify the crude oil with benzene, and then toluene, to yield the product as a pale yellow oil. The product was determined to be partly pure by NMR (Figure 1.26).

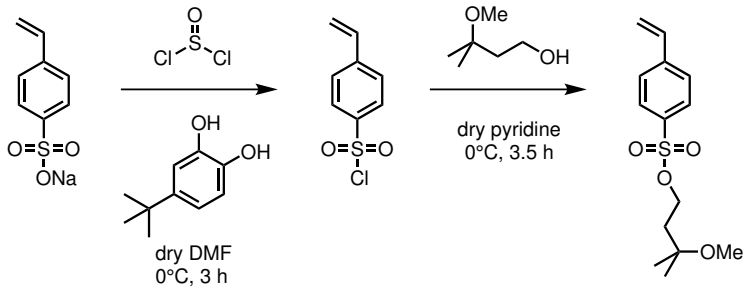

4-styrenesulfonyl chloride

In a flame-dried flask under nitrogen at 0°C was stirred thionyl chloride (28 mL, 390 mmol) and 4-*tert*-butylcatechol (0.3 g, 1.8 mmol) in dry DMF (30 mL). Sodium 4-styrenesulfonate (10.0 g, 48.5 mmol) was added in small amounts, and the mixture was stirred for 3 h at 0°C and then left to stand for 24 h in a refrigerator. Ice water (200 mL) was added, and the organics were extracted with toluene (3 x 100 mL) and washed with water (2 x 100 mL) and brine (100 mL). The organic layer was dried over magnesium sulfate, gravity filtered, and concentrated *in vacuo* to yield the product as a yellow-gold liquid (8.7 g, 89%). ^{1}H NMR (400 MHz; $CDCl_3$): δ 7.99 (d, 2H), 7.61 (d, 2H), 6.78 (dd, 1H), 5.97 (d, 1H), 5.54 (d, 1H) ppm (Figure 1.27).

3-methoxy-3-methylbutyl-4-styrenesulfonate

A stirring solution of 4-styrenesulfonyl chloride (4.6 g, 22.7 mmol) in dry pyridine (25 mL) was cooled to 0°C. 3-methoxy-3-methyl-1-butanol was added, and the reaction mixture was stirred at 0°C for 3.5 h. Ethyl acetate (150 mL) was added to the yellow solution with white precipitate. The organics were washed with 1 M HCl (3 x 150 mL), saturated aqueous $NaHCO_3$ (150 mL), and brine (150 mL), then dried over magnesium sulfate and gravity filtered. The solvent was evaporated under reduced pressure to yield the crude product, which was purified by silica gel column chromatography with 9:1 (v:v) dichloromethane:methanol. The product (1.23 g, 19%) was determined to be mostly pure by NMR with 3-methoxy-3-methyl-1-butanol as the impurity. ^{1}H NMR (500 MHz; $CDCl_3$): δ 7.85 (d, 2H), 7.55 (d, 2H), 6.75 (dd, 1H), 5.90 (d, 1H), 5.45 (d, 1H), 4.14 (t, 2H), 3.09 (s, 3H), 1.87 (t, 2H), 1.12 (s, 6H) ppm. δ 3.78 (t, 2H), 3.21 (s, 3H), 1.74 (t, 2H), 1.22 (s, 6H) ppm from 3-methoxy-3-methyl-1-butanol (Figure 1.28).

1.5.3 Supplementary information

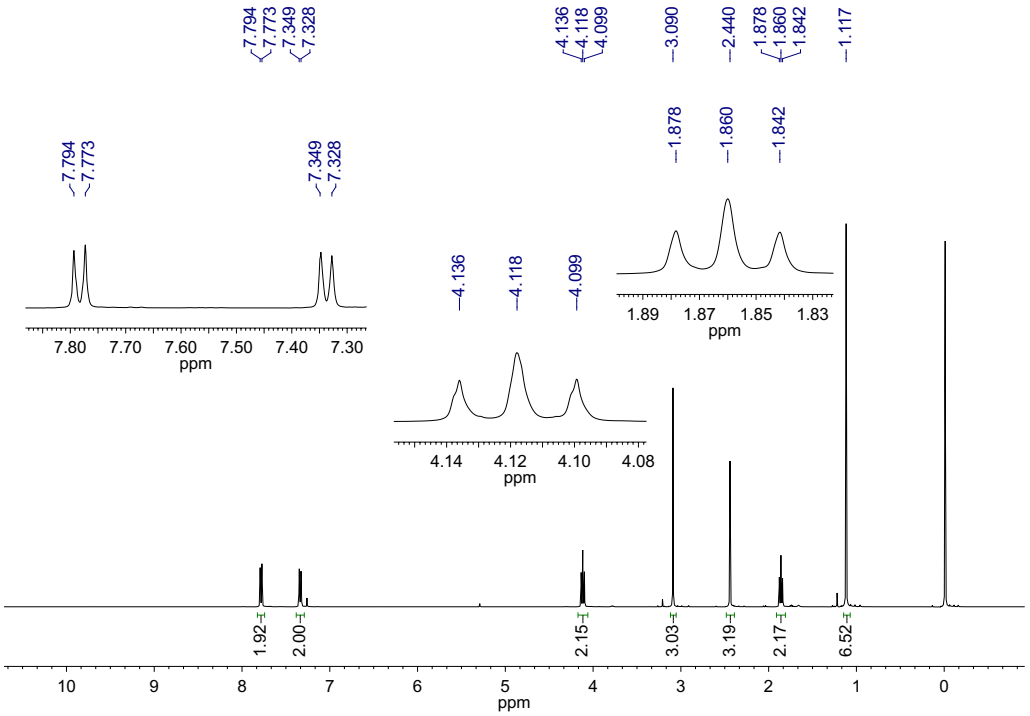

Figure 1.19 [1]H NMR: 3-methoxy-3-methylbutyl-4-toluenesulfonate.

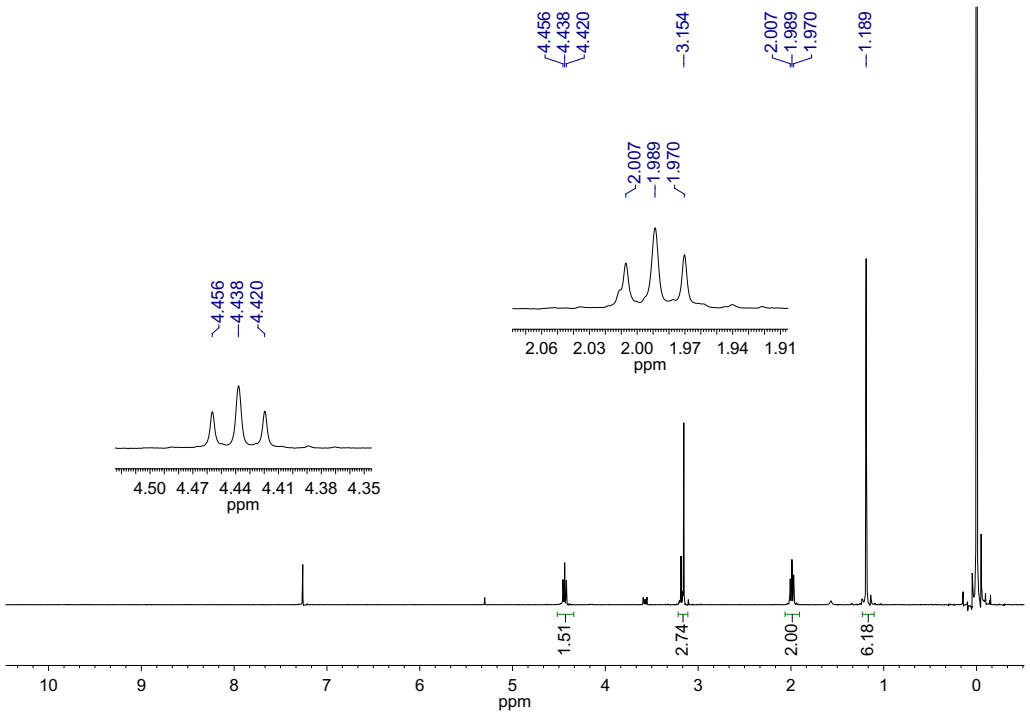

Figure 1.20 [1]H NMR: 3-methoxy-3-methylbutyl-2,3,4,5,6-pentafluorobenzenesulfonate.

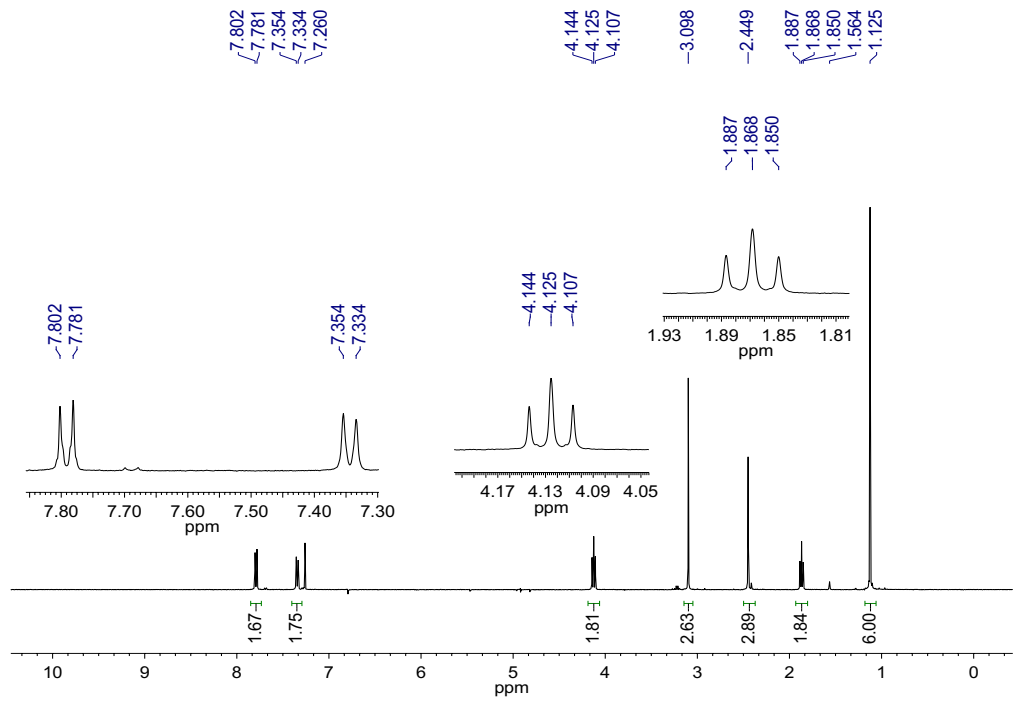

Figure 1.21 [1]H NMR: 4-(*tert*-butoxycarbonyloxy)benzaldehyde.

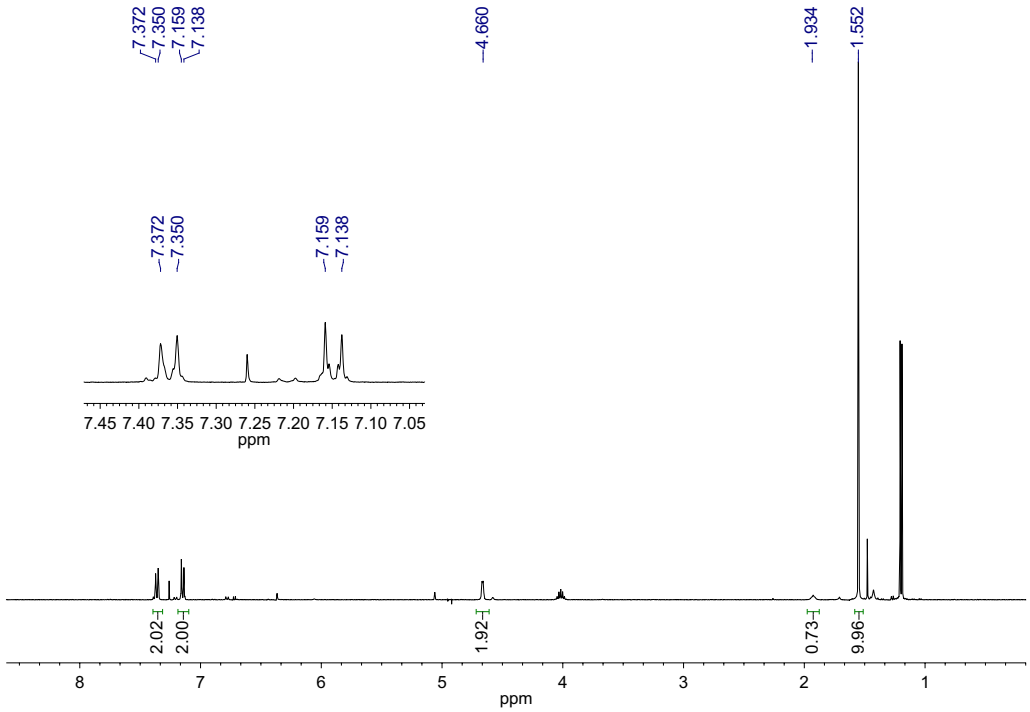

Figure 1.22 [1]H NMR: 4-(*tert*-butoxycarbonyloxy)benzyl alcohol.

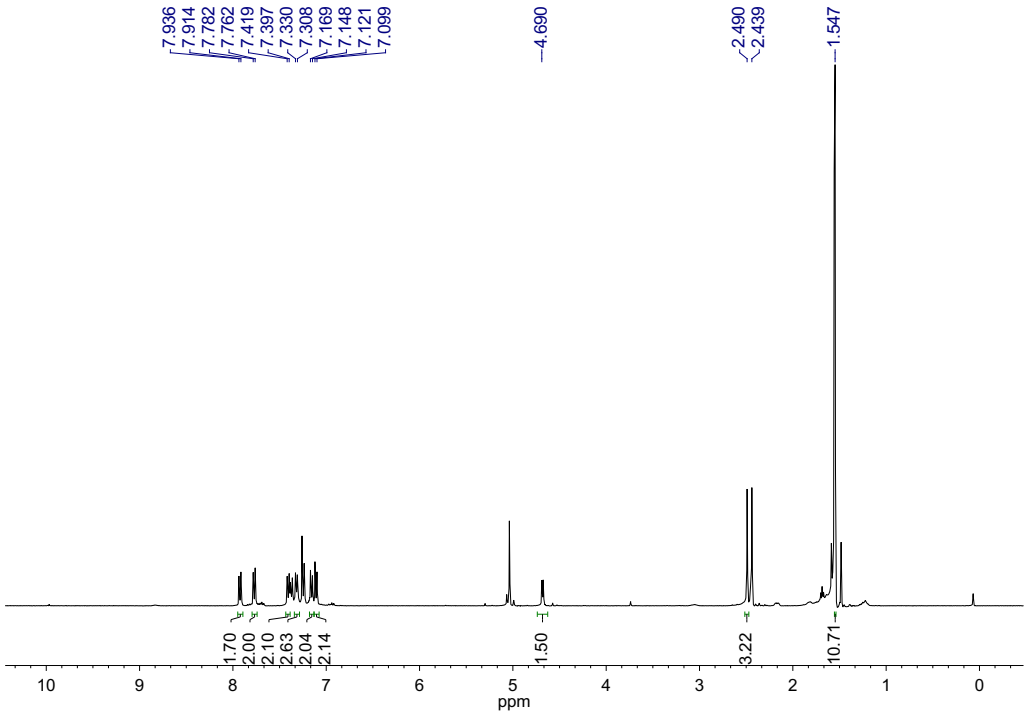

Figure 1.23 [1]H NMR: 4-(*tert*-butoxycarbonyloxy)benzyltoluenesulfonate.

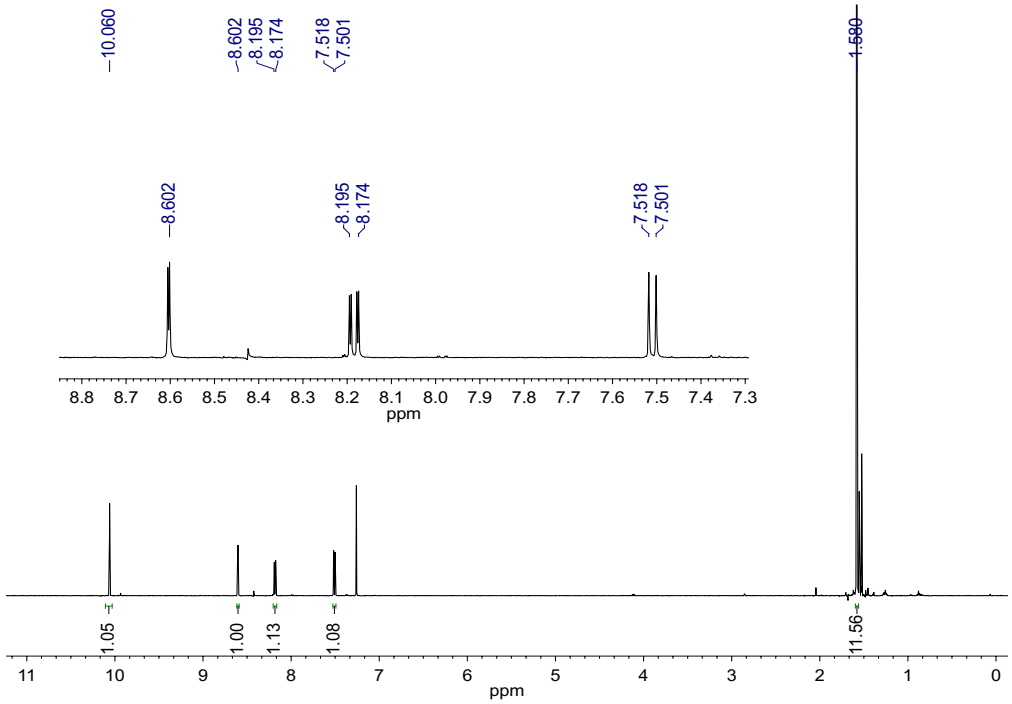

Figure 1.24 [1]H NMR: 3-nitro-4-(*tert*-butoxycarbonyloxy)benzaldehyde.

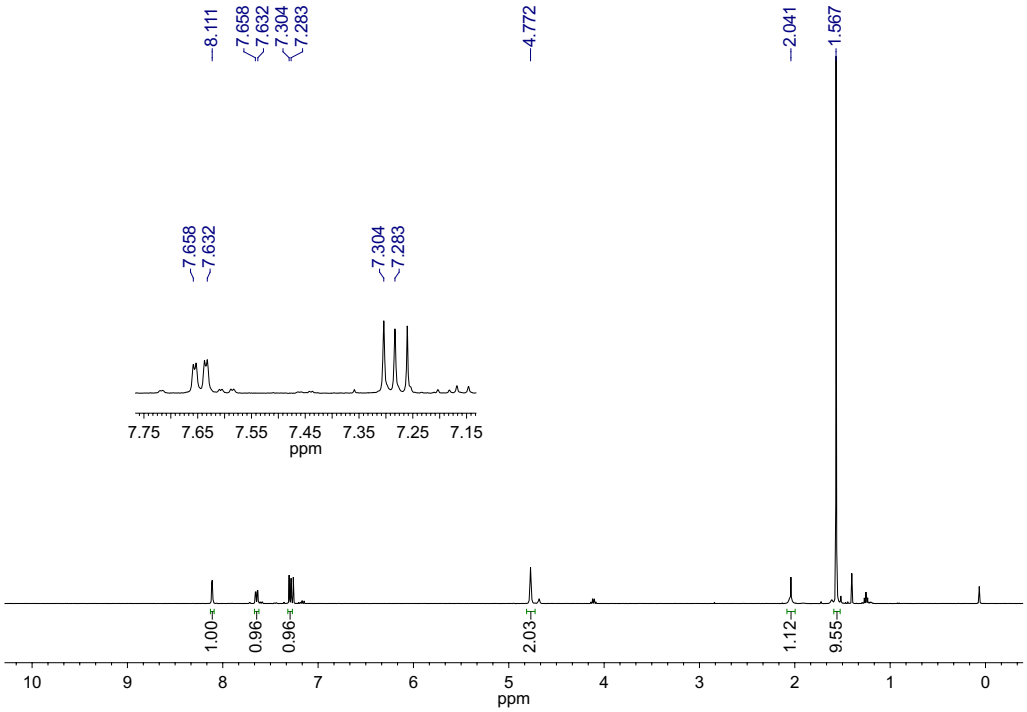

Figure 1.25 [1]H NMR: 3-nitro-4-(*tert*-butoxycarbonyloxy)benzyl alcohol.

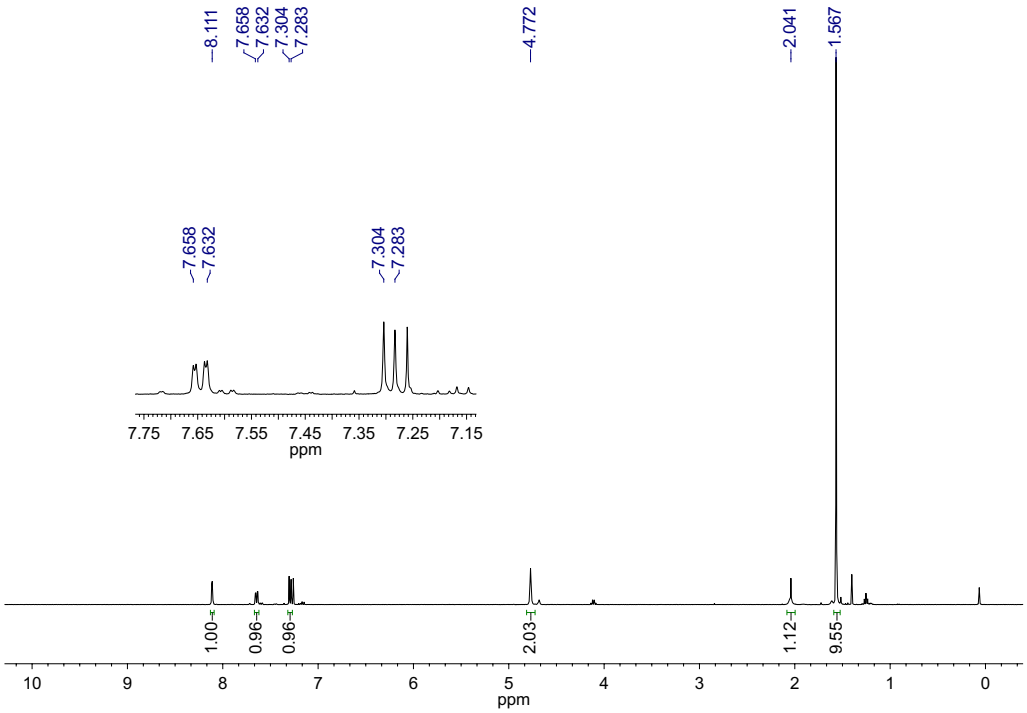

Figure 1.26 [1]H NMR: 3-nitro-4-(*tert*-butoxycarbonyloxy)benzyltoluenesulfonate.

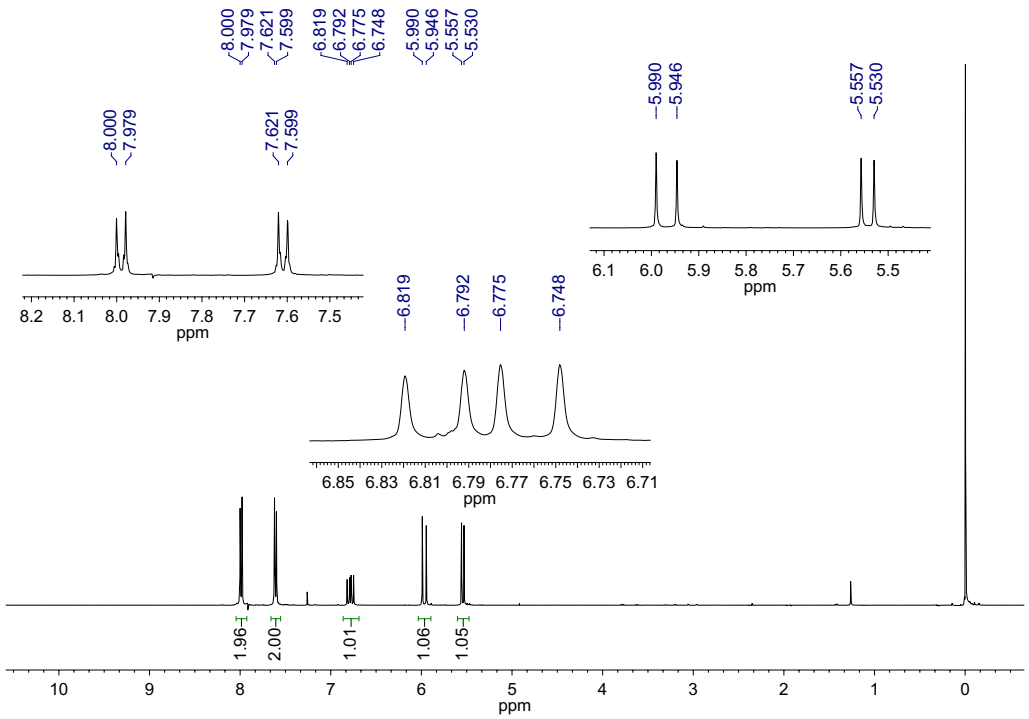

Figure 1.27 [1]H NMR: 4-styrenesulfonyl chloride.

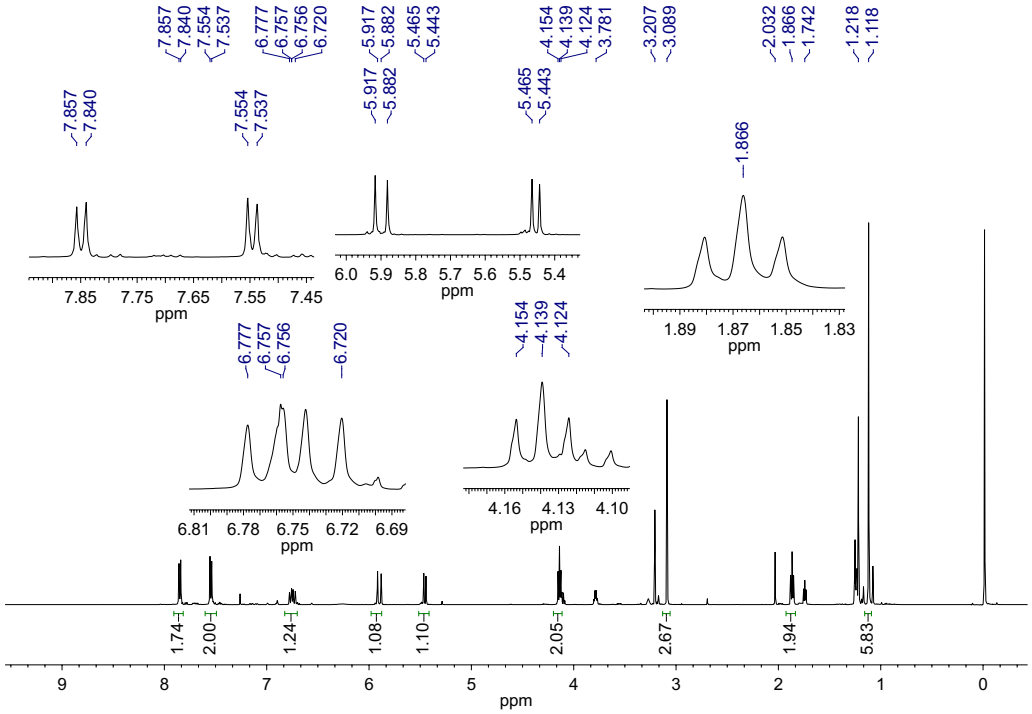

Figure 1.28 [1]H NMR: 3-methoxy-3-methylbutyl-4-styrenesulfonate.

Chapter 2

Adding Functionality to Shape-Anisotropic Particles

2.1 Introduction

Chemists have long prided themselves on their ability to create what is desired—to intelligently design and synthesize molecules that realize a fundamental goal. The advent of nanotechnology has driven the design need to the nanoscale. As individual nanoparticles assemble into collections of particles, new properties emerge that are useful both for various applications and for understanding the unifying principles behind the organization of matter. Discovery of these emergent properties has fueled the desire to control particle assembly into defined architectures.

Particles must feature anisotropy, arising from shape or functionality, to bond directionally to other particles. In contrast, spherical, isotropic particles lack programmability; they assemble according to basic packing considerations. Anisotropic particles have long fascinated scientists, and their properties and assembly behavior have been the subjects of many theoretical studies over the years. However, only recently has experiment caught up with theory, as we have begun to witness the synthesis of a tremendous diversity of particles with shape anisotropy.[28] These synthetic advances have galvanized the field. Although shape anisotropy creates directional entropic forces to drive assembly, shape alone does not provide enough control to direct a variety of interactions between particles, such as might be needed to assemble sophisticated architectures. Anisotropic functionality must be added to program different directional bonds into a collection of particles—but how?

Using individual nanoparticles as an analogy for molecules, one can design predictable two- and three-dimensional supramolecular structures. The selective organic functionalization of certain facets or regions of these particles leads to "patchy particles" whose directional interactions offer a new paradigm in design control of bottom-up materials synthesis.[29,30] Taking cues from biological systems, such as virus capsids that self-assemble from specific directional interactions, provides a framework for designing precise and reliable structures. Anisotropy in our synthetic models may arise from particle shape, surface patterns, or organic or biological constituents. "Valency" may also be imparted to the building blocks by functionalizing select facets.[31,32] Capping two opposite faces of a hydrophilic cube with hy-

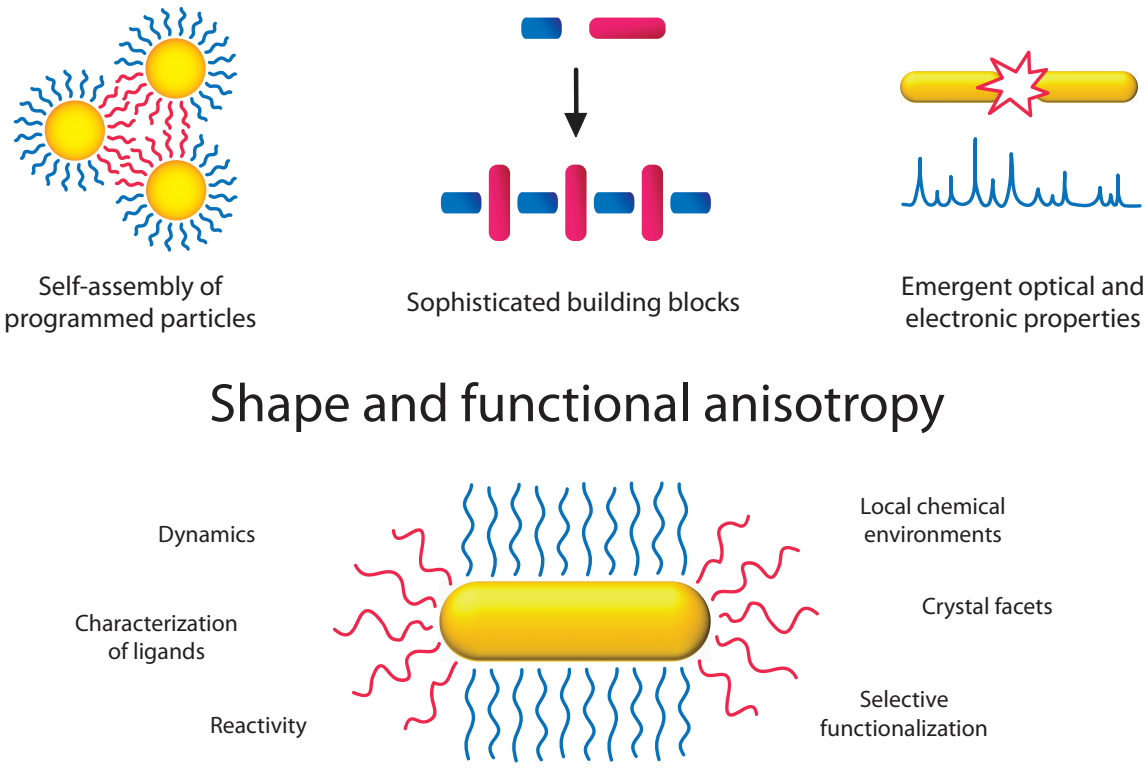

Figure 2.1 Particles featuring shape and/or functional anisotropy are much more complex, interesting, and challenging systems to study than are isotropic particles.

drophobic moieties leads to an "atom" that bonds with square planar geometry, whereas designing a tetrahedron with reactive faces creates an sp^3-bonding "carbon." We envision that these nanoscale building blocks can become the new "atoms" and "molecules" of smart supramolecular assemblies with widespread applications.

2.1.1 A model for shape and functional anisotropy: Gold nanorods

Nanoparticles with shape anisotropy can be further customized with functional anisotropy. A factor of their geometry, shape-anisotropic particles inherently have variations in radii of curvature, crystal facets, and ligand coverage along their surface, and this is the root of their nonuniform reactivity. Many anisotropic growth mechanisms leave exposed crystal facets on a single nanoparticle, which become reactive hotspots. For example, metallic gold deposits onto CdSe semiconductor rods with a clear preference for the tips rather than the sides,[33] and PbSe grows selectively on the ends of CdS and CdSe nanorods.[34] In both of these cases, the crystal facets of the rods' ends are more reactive than the side facets. Although deposition of metallic salts provides an inorganic route to functional anisotropy, it is also possible to

direct organic functionality to certain locations of a shape-anisotropic particle. A gold nanorod (AuNR), in particular, is an exemplar model of how reactive heterogeneity can be exploited to achieve this. Gold nanorods stabilized with the surfactant cetyltrimethylammonium bromide (CTAB) have a sterically driven advantage in anisotropic functionalization. The CTAB molecules are tightly packed at the rods' longitudinal facets, where they can form a contiguous bilayer. However, the high radius of curvature at the nanorods' ends precludes dense arrangement of surfactant molecules there, so the ligand coverage is presumed to be more fluxional (Figure 2.2). The paucity of CTAB at the end faces makes them more chemically accessible, and indeed the rods' ends are more reactive to cyanide dissolution than the sides are.[35] Interestingly, rods passivated by phospholipids seem to have a fairly uniform, well-arranged bilayer, even at the curved ends.[36] CTAB appears to be unique in its poor bilayer uniformity, but this appears to be a fortuitous blessing because it provides a direct pathway to functional anisotropy.

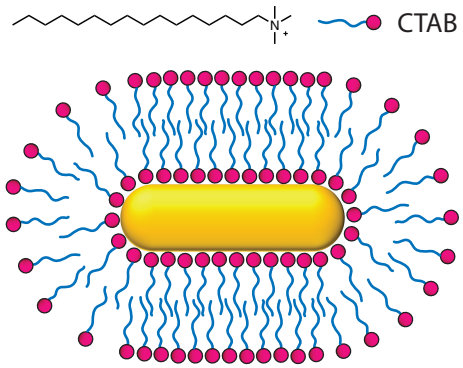

Figure 2.2 CTAB is thought to form a bilayer on the surface of a gold rod.

Self-assembly behavior, usually visualized by transmission electron microscopy (TEM) and ultraviolet–visible (UV–vis) absorption spectral changes, is often the primary evidence for functional anisotropy. One early example placed disulfide-biotin analogs on the ends of gold rods, then incubated the rods with streptavidin.[37] Statistical analysis of resulting TEM images showed that the end-to-end arrangement was significantly favored. In a similar fashion using biomolecules, the tips of gold rods were functionalized with a thrombin-binding aptamer, and addition of thrombin assembled the rods end-to-end.[38] There are many such examples of "end-activated" rods, where the ends are imbued with a moiety that can further perform chemistry. However, it is much more challenging to exclusively "activate" the sides of the rods, which are coated with the functionally less-interesting CTAB. A clever workaround solved this issue by "deactivating" the ends with nonreactive ligands, a chain-stopper of sorts. The authors first treated the CTAB rods with small amounts of a thiolated non-target DNA strand, which saturated the ends and blocked them from further reaction. Thus, when active DNA thiols were added, they were forced to adsorb to the sides. After incubating the rods with gold spheres capped with complementary DNA strands, TEM imaging showed that the spheres attached almost exclusively

to the rods' sides.[39] This study illuminates the importance of the molar ratio of thiol to nanorods in controlling thiol placement; at low concentrations of thiol, the ligand bound primarily to the ends, but high concentrations overloaded the surface and replaced almost all of the CTAB, precluding anisotropic functionalization. Metals such as platinum and palladium can also be selectively deposited onto either the long or transverse axis of gold rods. One approach grew silica as a nonreactive cloak on either on the side or the ends, which was realized by directing the adsorption of the precursor tetraethyl orthosilicate (TEOS). Then, simply reducing metal salt onto the rod drove metal overgrowth on the silica-free exposed surfaces.[40]

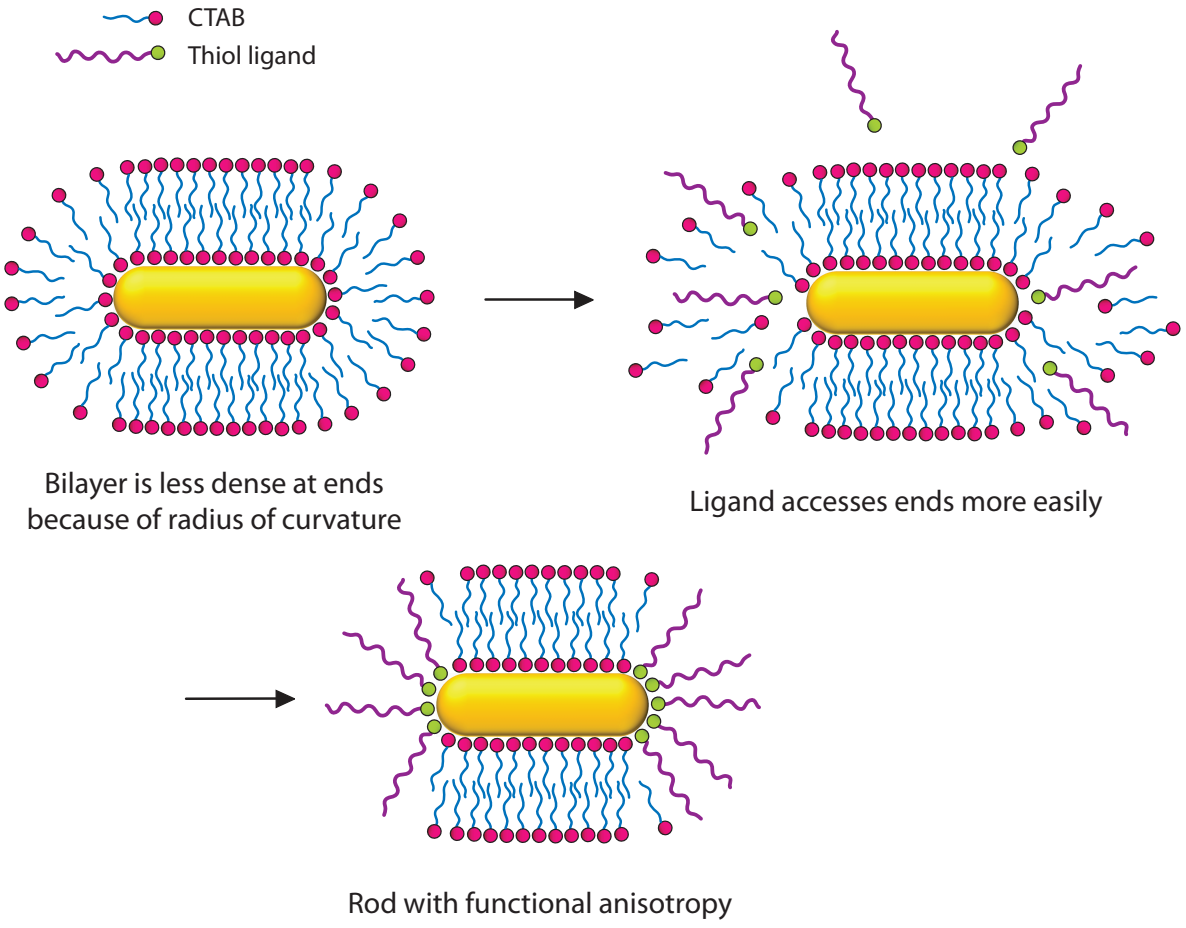

Figure 2.3 The CTAB bilayer is widely accepted to be looser and more fluxional at the highly-curved rod ends, leaving the ends more exposed to competing ligands. This surface heterogeneity provides a convenient pathway to functional anisotropy.

In their prolific work, Kumacheva and colleagues have affixed even bulky, hydrophobic polymers preferentially to gold rod ends. Thiol-terminated polystyrene targeted the tips, creating "triblock" nanorods as the plasmonic analogue of amphiphilic block polymers.[41] Just like block copolymers that phase separate and assemble in striking forms, the amphiphilic rods displayed curious self-assembly properties and in various solvent mixtures formed chains, rings,

bundles, or spheres. Tuning the molecular weight of the polystyrene altered the final morphology of the giant assemblies. Subsequent studies treated the amphiphilic rods as monomers that could be "polymerized" in a step-growth-like mechanism into supramolecular plasmonic chains.[42,43] The bond angles and lengths between monomers, and the rates and degrees of polymerization, were controlled and characterized in an elegant extension of the analogy. To stop chain growth at a certain length, patchy particles served as colloidal corks: a "reactive" polystyrene domain attached to the growing chain, and an exposed polyethylene glycol domain halted further hydrophobics-driven "polymerization."[44]

2.1.2 The surface chemistry of gold nanorods

The shape anisotropy of gold nanorods contributes striking optical properties and nonuniform chemical reactivity. Gold nanoparticles interact strongly with light, producing a plasmon band that arises from the coherent oscillation of conduction band electrons.[45] For rods, this plasmon bifurcates, each band corresponding to oscillation along either the transverse or longitudinal axis.[46] The transverse band absorbs around 520 nm, whereas the absorption wavelength of the longitudinal band depends directly on the rod's aspect ratio, a measure of its length versus width. The longitudinal band can be tailored to absorb throughout the near-IR and visible regions. Gold nanorods are capable of absorbing a large amount of light and dispelling the energy as heat into their surroundings—the photothermal effect[47]—which has been exploited in cancer therapeutics and light-triggered drug delivery.[48]

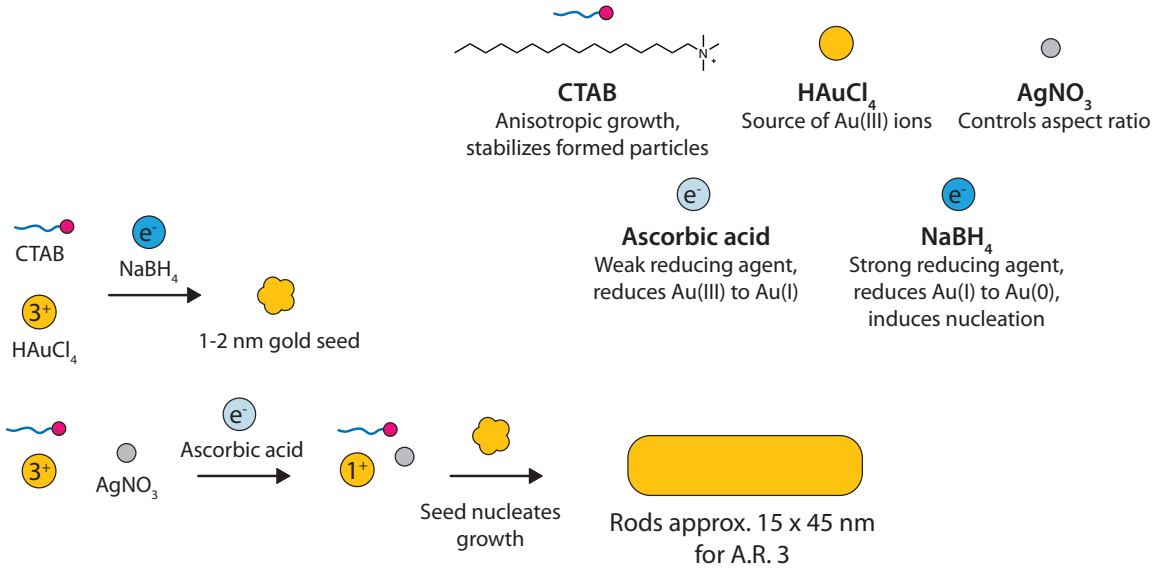

Figure 2.4 Schematic of the standard seed- and silver-mediated gold nanorod synthesis.

Gold nanorods of controlled aspect ratio are synthesized in high yield via a surfactant-stabilized, seed-mediated

growth method.[49] In this method, chloroauric acid ($HAuCl_4$) is reduced with sodium borohydride ($NaBH_4$) in the presence of the surfactant cetyltrimethylammonium bromide (CTAB) to yield about 2 nm spherical seed particles. These seeds are added to a CTAB-saturated aqueous growth solution containing additional gold salt, ascorbic acid as a weak reducing agent, and silver nitrate to control the aspect ratio. CTAB forms a densely-packed bilayer on the surface, with its positively-charged ammonium head groups facing either the gold surface or the aqueous environment; this charged bilayer stabilizes the particles against aggregation. By thermogravimetric analysis (TGA), weight loss at two separate temperatures supports release of a loose outer layer and a strongly-bound inner layer.[50] Fourier transform infrared spectroscopy (FTIR) also provides evidence for a headgroup species by the gold surface.[50]

Although the mechanism is not precisely understood, there are prevailing theories for what causes the break in symmetry to direct anisotropic growth. Rather than acting as a soft micellar template as once thought, CTAB likely binds preferentially to the long axis due to sterics, leaving only the end tips open for metallic growth. Silver nitrate appears to be the key to control over the aspect ratio of the rods. One theory is that a $Ag[BrCTA]^2$ complex forms a capping monolayer along the longitudinal axis, blocking gold deposition there and promoting one-dimensional growth.[51] Increasing the silver ion concentration yields rods with aspect ratios up to four; the longitudinal plasmon bands absorb in the range between 520 and 850 nm. Higher aspect ratio rods may be accessed through different protocols.

Unfortunately, the surfactant bilayer that directs anisotropic growth also stymies functionalization of the rods. The surface chemistry of gold monolayers and spherical gold nanoparticles is well-studied,[52] and indeed it is quite simple to functionalize these forms of gold, but the methods cannot always be translated to nanorods.[53] The CTAB bilayer stabilizes the rods such that disruption of the bilayer, without a comparable replacement, often results in irreversible aggregation. The bilayer is apparently dense and thick along the longitudinal axis (each CTAB molecule is about 2.2 nm long, so a bilayer with minimal interdigitation would be about 3-4 nm thick), so it is challenging for many common ligands to permeate it to access the gold surface. It is energetically unfavorable to perturb the bilayer organization and for a hydrophilic ligand to enter the hydrophobic core at all; this is a considerable problem, considering that most ligands used for functionalizing aqueous preparations of rods are hydrophilic. On the other hand, small hydrophobic ligands are likely to bury themselves within the bilayer core instead of displacing CTAB.[54] Additionally, CTAB rods are stable only in water and aggregate instantly in the organic solvents that solubilize many desirable ligands. Inconveniently, direct addition of miscible organic ligand solutions to aqueous solutions of rods usually results in aggregation; not only does the organic solvent destabilize the rods, the penetrating molecules also disrupt the CTAB bilayer before they fully bind to the surface themselves, thus opening up regions of unpassivated metal. This frustrating property of rods makes them difficult to functionalize with many organic molecules. If CTAB is successfully replaced with hydrophobic ligands, the rods need to be transferred to an organic phase. Centrifugation and redispersion of the aqueous pellet in

organic solvent can be adequate if the solvent is miscible with water, but often this is not the case; lyophilization of rods works only if they are stable to the process. There have been a few reported successes with phase transfer methods.[55,56] Because of all the associated challenges, there has yet to exist a standard approach to functionalizing gold nanorods. Most reported methods are specific to the ligand solubility, size, and functional groups; functionalization conditions; and intended application.

Functionalization approaches fall into two general categories: ligand exchange and *in situ* reactions on particles. As explained above, traditional ligand exchange with small molecule thiols, the paradigm for gold monolayers and spheres, is challenging with nanorods. These problems can be circumvented by first exchanging CTAB for poly(ethylene glycol) methyl ether thiol (mPEG-thiol) in an aqueous solution, centrifuging, and then dispersing the PEG rod pellet in a miscible organic solvent for the small molecule exchange.[57] PEG chains are large enough to protect the gold surface as CTAB is being desorbed, and are compatible with a variety of organic solvents. Adding concentrated thiol solutions in ethanol or THF directly to CTAB rods also works in some cases, if the substituting ligand can penetrate the bilayer and can fill in spaces where CTAB is removed. Interestingly, it has been suggested that bulky thiol ligands preferentially bind to the transverse axis of CTAB rods where the CTAB bilayer is less dense, a phenomenon that provides a pathway to functional anisotropy (this property will be explored further in **Chapter 3**).

Whereas ligand exchange is generally limited to molecules with functional groups with affinity for gold (e.g., thiols, disulfides, amines and carbonyls), *in situ* covalent reactions on particles accommodate organic ligands with diverse structures. Robust dithiocarbamate bonds form on gold surfaces in the presence of a secondary amine and carbon disulfide, a convenient and orthogonal route to fastening sensitive ligands on gold particles.[58] Wrapping positively-charged CTAB rods with alternating layers of charged polyelectrolytes yields rods that are stable in water and certain organic solvents (DMSO, acetonitrile, DMF, methanol, ethanol, acetone, 1-propanol, 1,4-dioxane, and diethyleneglycol, among solvents tested), making available a network of functional groups at the surface for further transformations.[59,60] For example, poly(acrylic acid) (PAA), poly(allylamine hydrochloride) (PAH), and poly(styrenesulfonic acid) (PSS) are commonly used to provide carboxylic acid, amine, or sulfonic acid groups, respectively. The polyelectrolyte method has the added advantage of encasing the CTAB bilayer (each polymer layer is about 1.5 nm thick), preventing CTAB molecules from desorbing naturally from the surface.[48] Because CTAB is toxic to living systems, polyelectrolyte wrapping is often used in biological applications.[61,62]

2.2 Click chemistry

Click chemistry provides a reliable, straightforward route to joining modular units in high yield and specificity.[63] The reaction conditions are typically benign and can be done in aqueous media, a necessity for most of the gold nanoparticle chemistry performed in the group. Click chemistry is widely exploited in materials chemistry, which by nature is interdisciplinary, since it easily bridges the vast diversity within the field.[64,65] To develop novel functional materials using gold nanorods, the surface chemistry must be modified reproducibly and efficiently. Often, this surface chemistry involves organic ligands, polymers, proteins, and other species with solubility and processing quirks far different from gold. Whereas most surface modification techniques such as electrostatic adsorption, organic covalent bond formation, or gold-thiol monolayer assembly involve specific sets of reagents, solvents, and harsh reaction conditions, which may be incompatible with either the gold or the surface species, the relaxed specifications of click chemistry prove ideal for these hybrid materials. In the exemplary copper-catalyzed azide-alkyne cycloaddition (CuAAC) reaction, a triazole is formed between an azide group on one species and an alkyne on the other. This reaction can be performed in water or solvent mixtures, making it particularly applicable to gold nanoparticle modification with water-soluble ligands.

An earlier report describes the preparation of azide-functionalized short rods, which were subsequently clicked to acetylene-functionalized trypsin.[66] We found that this procedure often led to unstable particles, so modifications were made to improve the yield. Short rods were first electrostatically wrapped with poly(styrenesulfonic acid-*co*-maleic acid) sodium salt (PSS-MA) in a mole ratio of 3:1 PSS:MA; the original report used a mole ratio of 1:1 PSS:MA. This particular polyelectrolyte was chosen for its carboxylate groups, which would be later transformed to neutral azides, and its sulfonate groups, which would remain unmodified and thus maintain the particle's negative surface charge, preventing aggregation. Increasing the relative amount of PSS increases the surface charge density after azide functionalization, improving particle-particle repulsion and stability. Indeed, particles appeared significantly more stable with the new polyelectrolyte. Successful polyelectrolyte wrapping was confirmed by ζ-potential values, which flipped from strongly positive for the CTAB rods (+18 mV) to strongly negative for the PSS-MA rods (-42 mV); this charge flip is evidence that the anionic electrolytes adsorbed onto the quaternary ammonium groups of the CTAB bilayer. UV-vis spectroscopy indicated a slight red shift of 4 nm after wrapping, which is consistent with literature-reported shifts after polyelectrolyte coating. Finally, dynamic light scattering (DLS) showed that the effective diameter of the rods increased approximately 1 nm, from 23.6 ± 0.2 nm to 24.7 ± 0.3 nm.

Transformation of the carboxylate to azide groups was accomplished using carbodiimide-mediated coupling to an amine-PEG-azide linker. The original report used 1-ethyl-3-(3-dimethylaminopropyl) carbodiimide (EDC) as the coupling agent, but in our studies addition of the neat powder to the rod suspension led in most cases to irreversible

aggregation. Adding EDC as an aqueous solution seemed to improve the stability slightly, but not enough. This instability might be explained by the mechanism of EDC coupling: the addition of EDC to a carboxylate group results in a reactive "activated" ester, but one that is unstable and prone to hydrolysis. N-hydroxysuccinimide (NHS) is often used with EDC to stabilize the activated ester so that it has a half-life of 4-5 hours at neutral pH. With this in mind, N-hydroxysulfosuccinimide (sulfo-NHS, the water-soluble analog) was added to the protocol.

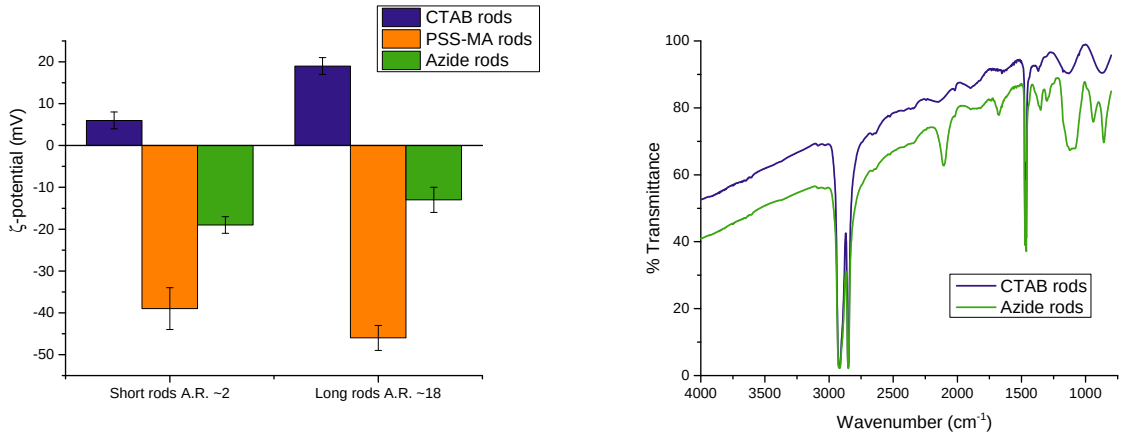

Figure 2.5 Characterization of azide rods by zeta potential analysis (left) and FTIR spectroscopy (right).

Formation of the activated NHS ester is most efficient at a pH between 4.7 and 6, while the coupling reaction between the activated NHS ester and an amine is most efficient at a pH between 7 and 8. The PSS-MA rods were suspended in 2-(N-morpholino)ethanesulfonic acid (MES) buffer at pH 5.5, to which EDC and an excess of sulfo-NHS were added. The solution was vortexed gently for 2 minutes to allow the reagents to access the carboxylate groups. The activated ester was allowed to form undisturbed for 15 minutes, and then the solution was purified via centrifugation to quench the reaction. The pellet of activated ester nanorods was resuspended in sodium phosphate buffer at pH 7.2, and an aqueous solution of 11-azido-3,6,9-trioxaundecan-1-amine (N_3-PEG-NH_2) was added. The reaction mixture was vortexed gently for 2 minutes, and the coupling reaction was allowed to proceed for 22 hours. After centrifugation, the azide-functionalized rods were resuspended in nanopure water and characterized. The ζ-potential of the rods decreased to -19 mV, consistent with the conversion of maleic acid groups to azide species and sulfonate groups unchanged (Figure 2.5). For Fourier transmission infrared spectroscopy (FTIR), rod solutions were drop-cast on a polyethylene film. The appearance of an azide stretch around 2100 cm^{-1}, not present in CTAB rods or PSS-MA rods, confirmed the functionalization of azide rods (Figure 2.5).

2.3 Hyperbranched polyglycerols

Hyperbranched polyglycerols (HPGs) have a highly-branched structure similar to dendrimers, but can be synthesized on the kilogram scale in a single step by the anionic polymerization of glycidol.[67] By adjusting the equivalents of glycidol in the reaction, the controlled polymerization can produce molecular weights from 1,000 to 1,000,000 g/mol.[68] HPGs are synthetically versatile: use of a functional initiator affords a functional core, and the polyol periphery is easily modified. Indeed, HPGs have been produced with biomolecular recognition units, H-bonding units, and host-guest modules, or with crosslinkable moieties that create a more rigid structure.[69] They can host small molecules within their dense polyether-polyol branches, suggesting their use in encapsulation and triggered release.[70,71] Furthermore, HPGs are biocompatible, showing protein absorption resistance and cell toxicity profiles superior to polyethylene glycol (PEG).[72,73] This feature makes HPGs attractive building blocks or particle coatings for bio-related applications.[74]

One objective of this work was to reduce the toxicity of gold nanorods by replacing or covering the CTAB bilayer with HPGs. As mentioned earlier, gold rods have potential for utility in biomedicine, but their practical use is precluded by the toxicity of CTAB to living systems; many reports have reduced this toxicity through polyelectrolyte wrapping or ligand exchange. HPGs were grafted onto gold rods in two approaches: 1) CuAAC click chemistry between alkyne-cored HPG and azide rods, and 2) ligand exchange of thiol-cored HPG for CTAB.

Alkyne-cored HPG was synthesized by performing the one-pot polymerization of glycidol on a functional alkyne initiator.[75] Pent-4-yn-1-ol was 10% deprotonated with sodium hydride, and glycidol was added dropwise to the initiator and thickening mixture. After glycidol addition was complete, the mixture was dissolved, treated with ion exchange resin, and filtered. The viscous product was purified via fractional precipitation with cold ether to yield a final polymer with a molecular weight around 11,000 g/mol, determined by gel permeation chromatography (GPC). Because the molecular weight is controlled primarily by equivalents of glycidol to initiator, 337 equivalents of doubly distilled glycidol were added to 1 equivalent of alkyne for a theoretical molecular weight of 25,000 g/mol. The low molecular weight obtained is typical of neat polymerization; dioxane or other solvents can be added to improve the degree of polymerization. ^{1}H NMR spectroscopy confirmed the inclusion of the alkyne initiator.

To attach the alkyne HPG to azide rods, a standard protocol was followed for CuAAC click chemistry. Separate aqueous solutions of azide rods and alkyne HPG were first degassed by bubbling nitrogen into each solution. The rods and HPG solution were vortexed together for 2 minutes to ensure that the reaction mixture was homogenous, and ascorbic acid and copper sulfate were added. The mixture was further vortexed and stored at 1°C for 22 hours for the click reaction to complete. The purified rods were stable and did not aggregate after centrifugation. However, characterization was challenging because the scale of the reaction was quite small, and the concentration of rods too

low, to yield a meaningful FTIR signal. The multi-step synthesis, from preparation of azide rods to the click reaction, led to aggregation and instability in larger scale. This was not surprising, since it is often difficult to scale up syntheses on the nanoscale, especially when there are several intermediate products that each require purification and encounter yield loss. A more elegant solution was explored through ligand exchange, eliminating the intermediates altogether.

Preparation of a thiol-cored HPG followed a similar synthesis to that of alkyne HPG, using 66 equivalents of glycidol to 1 equivalent of a disulfide initiator, for a theoretical molecular weight of 2,500 g/mol.[76] (The equivalents of glycidol correspond to a theoretical molecular weight of 5,000 g/mol for the disulfide, which is later cleaved in half.) The initiator, 2-hydroxyethyl disulfide, was deprotonated, glycidol added dropwise, and the workup completed as described for the alkyne HPG, to yield disulfide HPG. To reduce the disulfide core to a thiol group, the viscous yellow polymer was dried under vacuum to remove excess solvent, then dissolved in ethanol. An excess of the reducing agent dithioerythritol (DTE) was added and the pH of the solution adjusted to 10 – 11 with ammonium hydroxide. The reduced polymer was fractionally precipitated from acetone to yield thiol HPG. The molecular weight of the disulfide was determined by GPC to be about 5,000 g/mol with a PDI of 1.09, and disulfide core incorporation was confirmed via ^{1}H NMR spectroscopy by identifying the triplet at 2.89 ppm corresponding to the $-S-CH_2$ protons. GPC could not determine the molecular weight of the thiol because the disulfide reformed in the column (Figure 2.6), but reduction was verified with an Ellman's reagent (5,5'-dithiobis-(2-nitrobenzoic acid)) (DTNB) assay, which produced a yellow dianion (λ_{max} = 412 nm) for the thiol (Figure 2.6). The molecular weight of the thiol HPG is estimated to be about 2,500 g/mol. The final polymer was dried under vacuum and stored at 4°C.

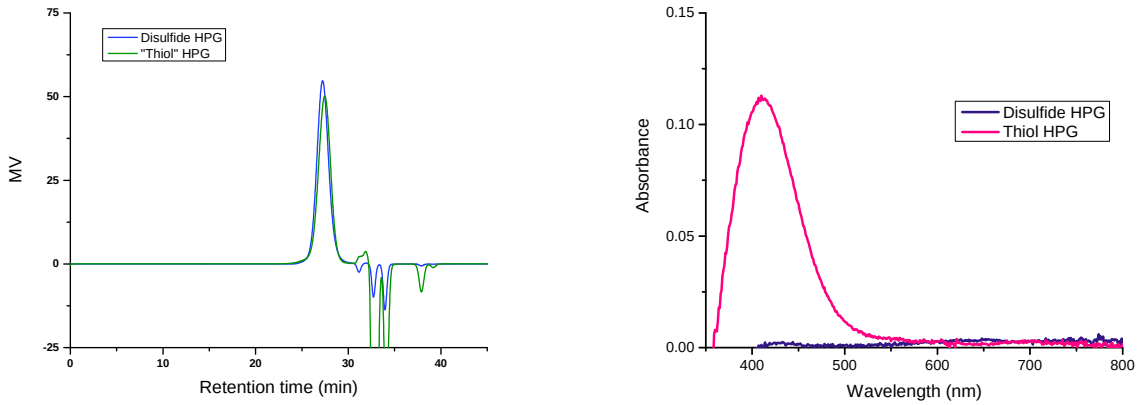

Figure 2.6 Characterization of disulfide and thiol HPG by GPC (left) showed that the molecular weight of the disulfide was approximately 5,000 g/mol. A DTNB assay (right) verified the presence of thiol in the reduced polymer.

Ligand exchange of the thiol HPG was performed on not only CTAB rods but also citrate-capped spheres. Citrate, as a fairly labile ligand, should be easier to displace than the CTAB bilayer, so the spheres can serve as a reference point

for troubleshooting reaction conditions. For functionalization of the citrate spheres, an excess of aqueous thiol HPG solution was added to spheres suspended in DMF, and the mixture was allowed to react for 2 days. The HPG spheres were purified by dialysis and centrifugation. To functionalize the rods, an aqueous solution of excess thiol HPG and rods were sonicated for 30 minutes to help the bulky thiol penetrate the bilayer and left to react for 2 days. The reaction mixture was then loaded into 1,000 MWCO dialysis tubing and dialyzed for 3 days before centrifugation. Dialysis was performed as a gentle way to encourage desorption of CTAB from the gold surface and remove most of the displaced surfactant before the single round of centrifugation. Two rounds of centrifugation often results in product loss.

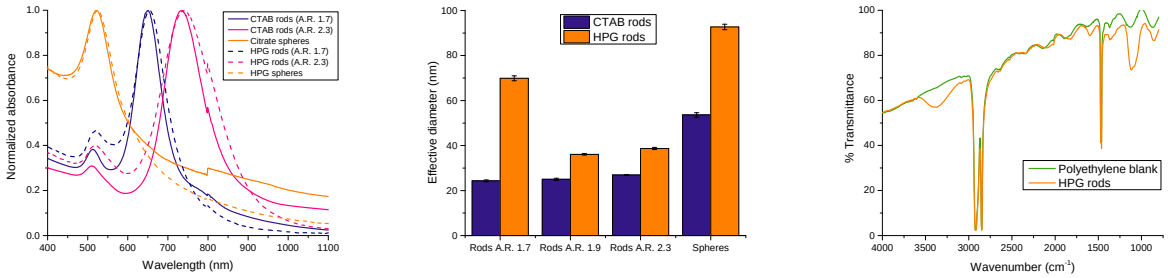

Figure 2.7 Characterization of HPG rods by UV-vis spectroscopy (left), DLS (middle), and FTIR spectroscopy (right) suggested that rods were successfully functionalized.

Characterization of the HPG rods conformed largely to expectations. Transmission electron microscopy (TEM) images showed a polymer layer around the HPG rods that was not present in CTAB rods. The λ_{max} values red-shifted very slightly (2-3 nm), consistent with a small change in the dielectric medium, and the narrow width of the bands suggested that the rods were not aggregated (Figure 2.7). Dynamic light scattering estimated that the rods increased in size by about 10 nm (Figure 2.7). Although the size of a free globule of 2,500 g/mol HPG is only about 1-2 nm, totaling an expected diameter increase of 2-4 nm, the hydrophilic HPG branches probably acquire a layer of hydration that increases the particle's effective diameter in solution. Additionally, because DLS does not provide accurate measurements for nonspherical particles, the effective diameter is more an indication of some increase in size than an absolute measurement. FTIR spectroscopy of dehydrated samples on polyethylene films was used to confirm the presence of alcohol or ether groups, as stretches were observed at 3400 and 1150 cm^{-1}, respectively (Figure 2.7). However, ζ-potential measurements were surprising, consistently flipping from positive (CTAB rods) to highly negative values (HPG rods) in both water and buffer at pH 7 (Figure 2.8). Citrate spheres whose surface had been replaced with HPG became more highly negative. A hydroxylated rod should be neutral at the surface, unless all of the alcohol groups are deprotonated or some surface impurity is attached to the HPG branches. Addition of dilute HCl did bring the ζ-potential values closer to zero, suggesting that basic species are present. While it is highly unlikely that the alcohols are deprotonated in water, a possible explanation is that the thiol-HPGs do not form a "perfect" monolayer on the gold surface, since the branched structure may prevent the buried thiols from accessing the gold. The polyether-polyol arms

may self-associate or hydrogen bond into a bilayer with thiol groups facing the aqueous environment, which may then oxidize in the presence of residual oxygen in the water.

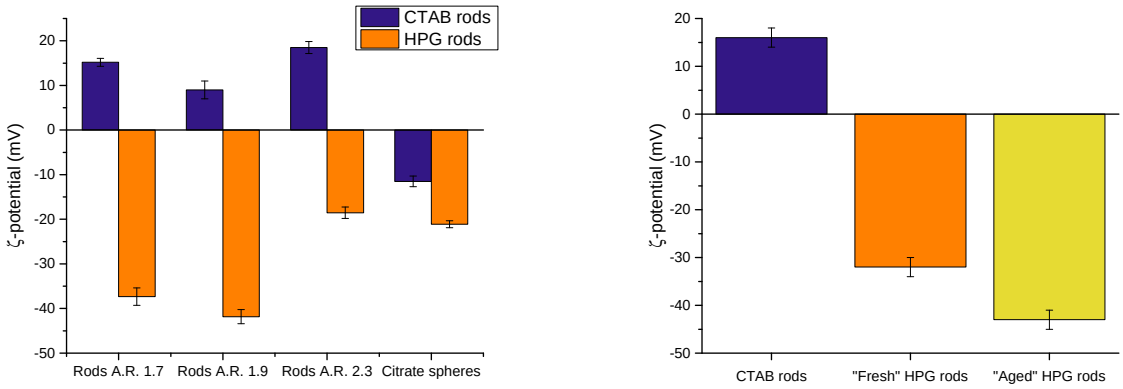

Figure 2.8 ζ-potential values of HPG rods were consistently negative.

Because it has been shown that the transverse axis of rods are more reactive to thiols, we studied whether gently reacting rods with thiol HPG (adding low equivalents of the thiol and allowing to sit for 24 hours) would lead to rods with CTAB bound to the longitudinal axis and HPG bound to the tips only. Successful end-capping provides a route to discretely-spaced end-to-end rods, which have applications in surface-enhanced Raman spectroscopy and photonics. TEM images comparing CTAB rods to presumable HPG-end-capped rods were promising. Analysis of those rods that had self-assembled end-to-end—just a subset of all the rods on the grid—revealed that the average interparticle distance of CTAB rods was just 1.6 ± 0.7 nm, while the average distance between HPG-end-capped rods was 4.7 ± 2.1 nm. This increase in interparticle distance corresponds to the estimated size of two HPG units, about 3-4 nm together, so it is possible that HPG is bound to the tips only or the entire surface. The sample size of 15 interparticle measurements is admittedly small but was limited by the number of rods that had assembled end-to-end.

To demonstrate the versatility of functionalizing rods with HPG variants, CTAB rods were also electrostatically wrapped with sulfated HPG. The peripheral alcohol groups were transformed to sulfate groups, leaving many negatively charged $-O-SO_3^-$ groups on each polymer. A polyelectrolyte wrapping procedure was carried out similarly to that described for PSS-MA. ζ-potentials flipped from positive (CTAB rods) to highly negative (sulfate HPG rods, at -27.7 ± 3 and -36.8 ± 2 mV for 3,000 and 8,000 g/mol HPG, respectively). The simplicity of this method may prove useful for applications where surface passivation by HPG is necessary. For example, CTAB rods are often wrapped with several layers of polyelectrolytes to limit the toxic effects of CTAB. Wrapping with electrolytic HPG may be even more protective, because HPGs have a more branched structure and cushioning water layer than most polyelectrolytes do. Polyelectrolyte HPGs are not limited to sulfate groups; the alcohol groups offer plenty of functionalization pathways.

2.4 Polystyrene

To make hydrophobic rods that could be dispersed in nonpolar organic solvents or self-assemble in co-solvent mixtures, polystyrene was chosen as the surface agent because of its commercial availability and familiarity in the literature. Two approaches to replace CTAB with polystyrene were performed. In the first method, styrene monomer was added to an aqueous solution of CTAB rods and vortexed for 5 minutes, encouraging the styrene to partition within the aliphatic CTAB bilayer, as has been shown for small hydrophobic species. Ammonium persulfate was then added as a radical initiator to polymerize the styrene monomers inside the bilayer, and the polymerization was allowed to take place for 15 hours.[77] However, the rods aggregated after centrifugation, suggesting that the surface was now completely hydrophobic and the rods were not stable in water; phase transfer may be a required step before or during centrifugation. In a more successful approach, a concentrated aqueous solution of CTAB rods was added very slowly dropwise to a solution of thiolated polystyrene (13,100 g/mol) in THF. The solution was gently agitated every 5 minutes to disperse the aqueous and THF layers. After addition, the mixture sat undisturbed for 42 hours to promote ligand exchange. The rods were purified via centrifugation without aggregation. The resulting rods were soluble in THF, DMF, and benzene, and insoluble in water, strong evidence for polystyrene surface coverage. The centrifuged pellets were redispersed in DMF for UV-vis characterization, which showed significant red-shifting (about 50 nm) of polystyrene rods as compared to CTAB rods (Figure 2.9). DLS measurements showed that there was no large change in size, so the red-shifting cannot be explained by aggregation. Thus, the red-shifting is most likely caused by a significant change in the dielectric medium near the surface of the rods, consistent with expectations for a hydrophobic polystyrene rod.

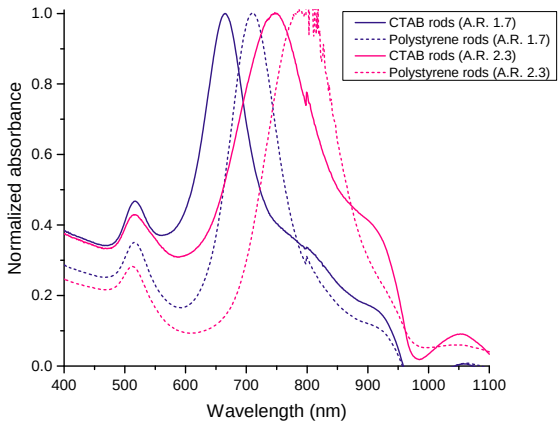

Figure 2.9 Polystyrene rods in DMF undergo a dramatic red-shift by UV-vis spectroscopy, indicating a change in the local dialectic medium.

To examine the self-assembly behavior of these polystyrene rods, a study was performed in water and organic co-

solvent mixtures. For each mixture, the appropriate volume of water was added dropwise to polystyrene rods suspended in either DMF or THF. Co-solvent mixtures studied for water:DMF were (v:v) 1:10, 1:5, 1:3, 1:2, and 1:1. Mixtures studied for water:THF were 1:10, 1:5, and 1:3. The solution was gently agitated after each drop was added, and no precipitation was observed. After addition, the mixture sat for 2 hours to allow stabilization of any self-assembled structures, then was dialyzed against 1 L water in a 3,500 MWCO cassette to remove DMF but not excess polystyrene (13,100 g/mol).

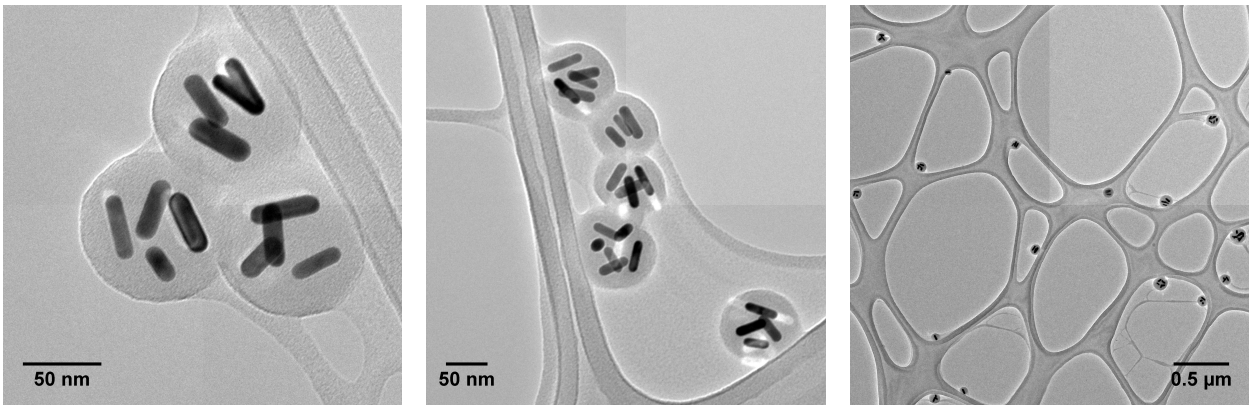

Figure 2.10 TEM images of polystyrene rod assemblies in 1:5 v:v H_2O:DMF.

A drop of the solution was placed onto a TEM grid and allowed to sit for 10 minutes before excess water was wicked away to limit evaporation effects on observed assembly. TEM images showed that discrete morphologies formed most strikingly for the water:DMF 1:5 co-solvent mixture: a few rods (3-4) surrounded by a low-contrast, thick spherical shell of about 70 nm (Figure 2.10). Based on the contrast and the dialysis MWCO, this shell is likely excess polystyrene. A theory for this behavior is that the solubilized polystyrene rods and excess polystyrene in DMF are encouraged to form stable, small aggregates as water is added, to minimize the surface area of interaction between polystyrene and water. Rather than precipitating, the polystyrene chains stabilize small bundles of polystyrene nanorods, or the rods themselves template the formation of the polystyrene spheres. The plasmon band of these assemblies shows a remarkable red-shift of over 100 nm without observable broadening, suggesting that plasmonic coupling occurs in each discrete aggregate, and the effective diameters of around 60 nm appeared to be quite monodisperse (Figure 2.11).

2.5 Polymersomes

Our collaborator has designed novel polymersomes—hollow vesicles self-assembled from amphiphilic block copolymers [78,79]—with HPGs as the hydrophilic component. [80] The synthetic equivalent of liposomes, polymersomes boast improved mechanical strength and synthetic tunability as compared to their biomolecular counterparts. The hydrophobic

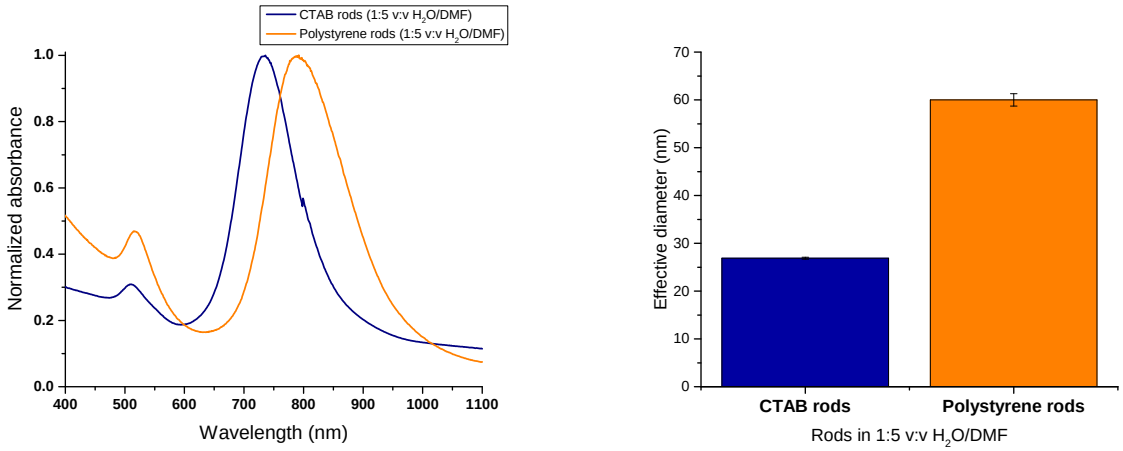

Figure 2.11 Characterization of polystyrene rod assemblies in 1:5 v:v H_2O:DMF by UV-vis spectroscopy (left) and DLS (right).

blocks collapse and associate in water to form a bilayer membrane that can be loaded with hydrophobic species, while the hydrophilic polymer chains line the aqueous inner and outer interfaces.[81,82] Our "HPG-somes" may be versatile encapsulants for diverse applications, and they have potential as the foundation of photothermal polymersomes.[80,83] Gold nanorods and small molecules can be directed to select regions of the polymersome—the spacious aqueous core, the hydrophobic membrane, or the outer boundary—as a function of surface chemistry and noncovalent interactions.[84,85] In response to irradiation at their plasmon λ_{max}, the rods should heat their local environment, rupturing the polymersome either through heat-cleavable linkages or equilibrium disruption.[47,61] Because the aspect ratio (and longitudinal λ_{max}) of rods is easily tuned, we envisioned orthogonal light-driven release chemistries, in which changing the irradiation wavelength leads to release of selective cargo from vesicles with built-in rods. One could also attempt to use the photothermal effect to reconfigure the geometry of an assembled nanorod "supermolecule," i.e., functional group cleavage leading a polyhedron to lose its vertices or a vesicle to change solubility and rearrange *in situ*.

Polymersomes of a polystyrene-HPG diblock copolymer were assembled as described in our published work.[80] Briefly, water was added very slowly dropwise to a vigorously stirring solution of polystyrene-*block*-HPG in DMF. The turbid solution stirred for 1 day and water added to kinetically trap and stabilize the assembled structures. The solution was then dialyzed in 1,000 MWCO tubing (to remove DMF) or a larger MWCO tubing (to remove unassembled copolymer) against 1 L water for up to two weeks. The relative size of the blocks determines the morphology of the assembled product: there is a "magic ratio" of hydrophilic to total copolymer mass that yields polymersomes, dependent on the glass transition temperature of the hydrophobic block, the water to organic solvent ratio, and conformations of the blocks, but is usually cited to be around 25-45% for linear polymers. It is plausible that hyperbranched polymers do not follow the same trend. Polystyrene$_{10K}$-HPG$_{8K}$ and polystyrene$_{10K}$-HPG$_{3K}$ (notation indicates the molecular weight

of each polymer block) are on the outskirts of these ranges, and both form translucent blue-white solutions after assembly, a typical indication of vesicle formation. Because polystyrene$_{10K}$-HPG$_{8K}$ forms approximately 500 nm spherical structures (compared to the approximately 150 nm structures of polystyrene$_{10K}$-HPG$_{3K}$), it might be more likely to accommodate nanorods with dimensions of 30 x 10 nm.

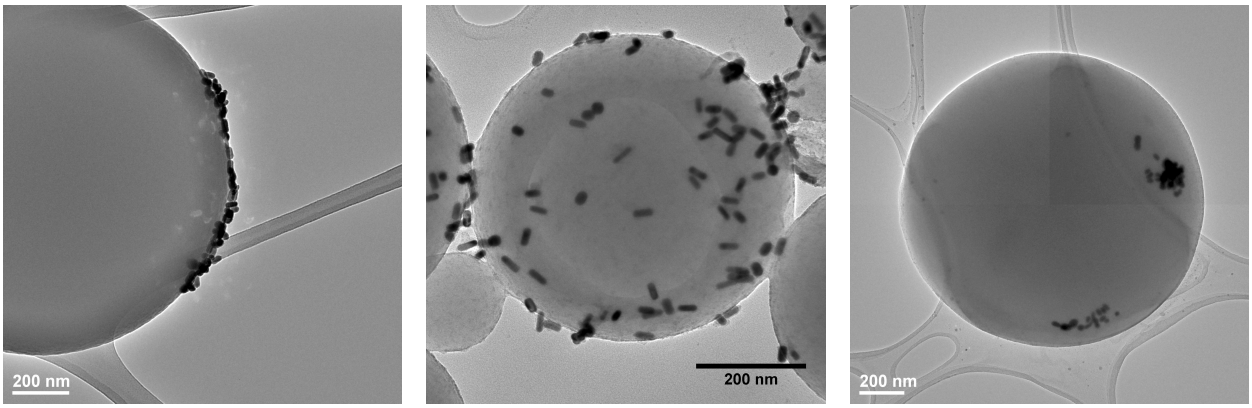

Figure 2.12 TEM images of polystyrene$_{10K}$-HPG$_{3K}$ polymersomes assembled with CTAB rods (left), HPG rods (middle), and polystyrene rods (right).

To explore the range of accessible plasmonic supermolecules, the self-assembly behavior of gold nanorods with polystyrene$_{10K}$-HPG$_{3K}$ was studied. The surface character of the nanorods directs their location in the vesicle. HPG-coated rods should attach to the vesicle exterior or bury themselves in the core, by virtue of hydrogen bonding and van der Waals interactions between polyols. Positively-charged CTAB rods might not interact with the vesicles in any preferential manner. On the other hand, polystyrene-coated rods should embed themselves within the hydrophobic bilayer.

Self-assembly of the block copolymers with hydrophilic rods was achieved as described earlier for polymersomes, but by adding an aqueous solution of nanorods dropwise to the polymer in DMF. Rods should partition to their preferred phase during the course of polymersome formation. The turbid solutions were dialyzed to remove DMF and excess polymer, and drop-cast onto a TEM grid for analysis. TEM images indicated, surprisingly, that both CTAB rods and HPG rods decorated the outer boundary of the vesicles (Figure 2.12). However, it is difficult to rule out the effect of evaporation on assembly.

Polystyrene rods were expected to intercalate inside the vesicle membrane, if indeed polymersomes form. TEM characterization does not definitively identify the assemblies as polymersomes, and not micelles: TEM images show spheres without an evident bilayer; cryo-TEM or different solvent mixtures may be necessary to visualize the bilayer. Thus, the polystyrene rods may serve as "TEM probes," as their location in the spheres should provide insight as to where the hydrophobic regions are. To prepare the hybrid vesicles, a homogenous solution of polystyrene$_{10K}$-HPG$_{8K}$

and concentrated polystyrene rods in DMF was stirred vigorously while water was added dropwise. The turbid solution was stirred and dialyzed as described earlier, then drop-cast onto TEM grids and excess water wicked away to reduce evaporation effects. TEM images showed that the rods tended to align within the vesicles, close to the surface, consistent with where the hydrophobic membrane should be, but it is unclear whether the rods are inside the vesicles or simply on the surface (Figure 2.12). Dynamic light scattering of the hybrid rod and polymer vesicles confirmed that they are comparable in size to vesicles formed from the copolymer alone, suggesting that the nanorods did not significantly disturb or augment vesicle formation. It will be interesting to study whether rods can mediate the formation of different size—or even shape—vesicles, as a function of the rods' aspect ratio and surface chemistry.

Because an eventual goal is to exploit the photothermal properties of gold nanorods to disrupt the equilibrium of the polymersomes, the vesicles' heat stability was studied.[47,61,71,86] Ideally, for practical photothermal applications the polymersomes should withstand slight heating but disassemble by around 40°C, since tremendous laser power is required for large temperature changes. Aqueous solutions of the polystyrene$_{10K}$-HPG$_{3K}$ vesicles were equilibrated at 25, 50, and 70°C for 1 hour, and the vesicle sizes were measured with DLS. There was no visual change in the solutions after heating, and there was no major change in size as compared to room temperature for any of the samples (effective diameters for 25, 50, and 70°C, respectively: 143.1 ± 0.9 nm, 188.7 ± 2.7 nm, and 158.7 ± 1.4 nm). Because one would expect to see a decrease in size if the vesicle ruptures or a dramatic increase if vesicles fuse or aggregate, these results demonstrate that the vesicles have remarkable thermal stability. It is interesting that the vesicles appeared to increase in size at 50°C but return to close to original size by 70°C. This behavior could be due to heat-swelling of HPG at higher temperatures, or water sequestration in HPG branches. The glass transition temperature of polystyrene is above 100°C, so it is likely that only heating above the T_g will induce morphological changes. However, the thermal stability precludes "easy" photothermal triggering, since heating by the gold nanorods of > 75°C can only be achieved by pulsed lasers and high loading. Heat-cleavable linkers may need to be incorporated for more practical photothermal vesicles.

There are several potential directions for this research. The functionalization of certain facets or axes of nanoparticles leads to "patchy particles" whose directional interactions offer precise control in rational particle assembly. Rods are well-suited for selective functionalization because of the anisotropic reactivity of the axes. It would be interesting to explore the tethering of HPG "pom-poms" to the tips of polystyrene rods to make hydrophilic-hydrophobic-hydrophilic triblock rods, which may assume the role in polymersomes that cholesterol plays in phospholipid bilayers, intercalating between the hydrophobic chains of the membrane and providing mechanical rigidity, resistance to permeability, and perhaps even guidance in initial assembly. Additionally, HPGs have protein adsorption resistance and cytotoxicity profiles that are in most studies better than PEG. This biocompatibility is a function of several features: their branches afford dynamic flexibility and thus experience a greater loss in conformational entropy upon protein adsorption, discourag-

ing surface binding, and their well-hydrated chains provide a protective water cushion around the particle. Sustainable nanomaterials are an urgent area of interest, so these HPG-based nanostructures may enjoy surface passivation effects and favorable toxicity profiles.

2.6 Experimental

2.6.1 General

All materials were used as received, unless otherwise indicated. Nanoparticle reactions were performed in new polyethylene centrifuge tubes, new glass vials, or glassware cleaned with aqua regia. Reported reaction temperatures refer to the temperature of the heating medium. Ultrapure deionized water was collected from a Barnstead NANOPURE water filtration system. Dynamic light scattering (DLS) and ζ-potential data were taken on a Brookhaven ZetaPALs analyzer. UV-vis spectra were obtained on a Varian Cary Scan 500 spectrometer. Transmission electron microscopy (TEM) samples were prepared on Lacey Formvar/Carbon, 200 mesh, 97 μm grids (Ted Pella), and TEM images were taken on a JEOL 2100 instrument and processed with Gatan DigitalMicrograph and ImageJ.

Nuclear magnetic resonance (NMR) spectra were acquired using a Varian Unity Inova narrow-bore 500 MHz spectrometer. Spectra were processed with MNova or VnmrJ. Chemical shifts are reported in parts per million (ppm) and were referenced to the residual proton solvent peak. Splitting patterns are designated as s (singlet), d (doublet), t (triplet), q (quadruplet), dd (doublet of doublets), m (multiplet), and br (broad).

2.6.2 Synthesis of hyperbranched polyglycerols (HPGs)

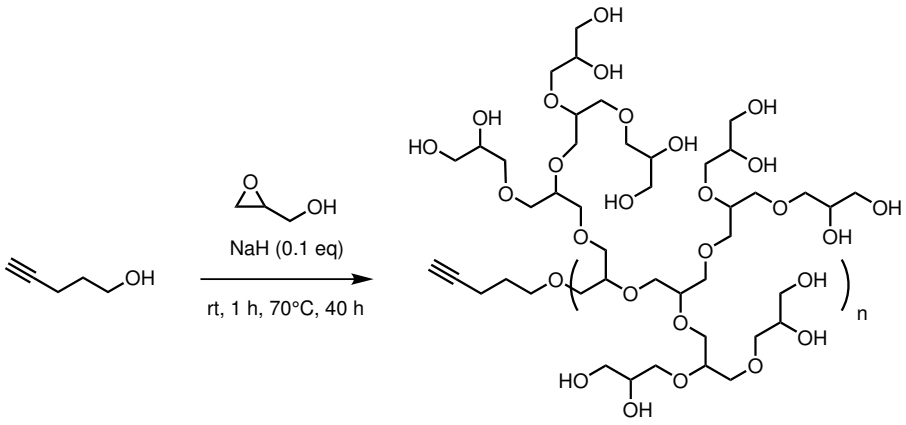

Alkyne-cored HPG

Pent-4-yn-1-ol initiator (2.11 mmol, 0.2 mL) was 10% deprotonated with sodium hydride (0.211 mmol, 0.008 g) in a thrice-flame-dried flask, and doubly distilled glycidol (712 mmol, 45 mL) was added dropwise (1.2 mL/hr) with a syringe pump under nitrogen. The mixture was heated to 70°C an hour into the addition. After glycidol addition was complete, the viscous mixture was stirred for three hours with a mechanical stirrer. The heat was reduced to 50°C, and methanol was added to dissolve the polymer. Ion exchange resin (Amberlite IR 1200 hydrogen form, prewashed) was added and the mixture stirred for one hour, and then filtered and washed with 50 mL methanol. The product was purified via fractional precipitation in cold ether three times to yield a final polymer of M_w of 11,000 g/mol, determined by gel permeation chromatography (GPC). Between each precipitation, the polymer was centrifuged at 4,500 rpm for 15 minutes at 4°C. Successful alkyne core incorporation was confirmed via ^{1}H NMR in methanol-d_4 on a 500 MHz narrow-bore instrument.

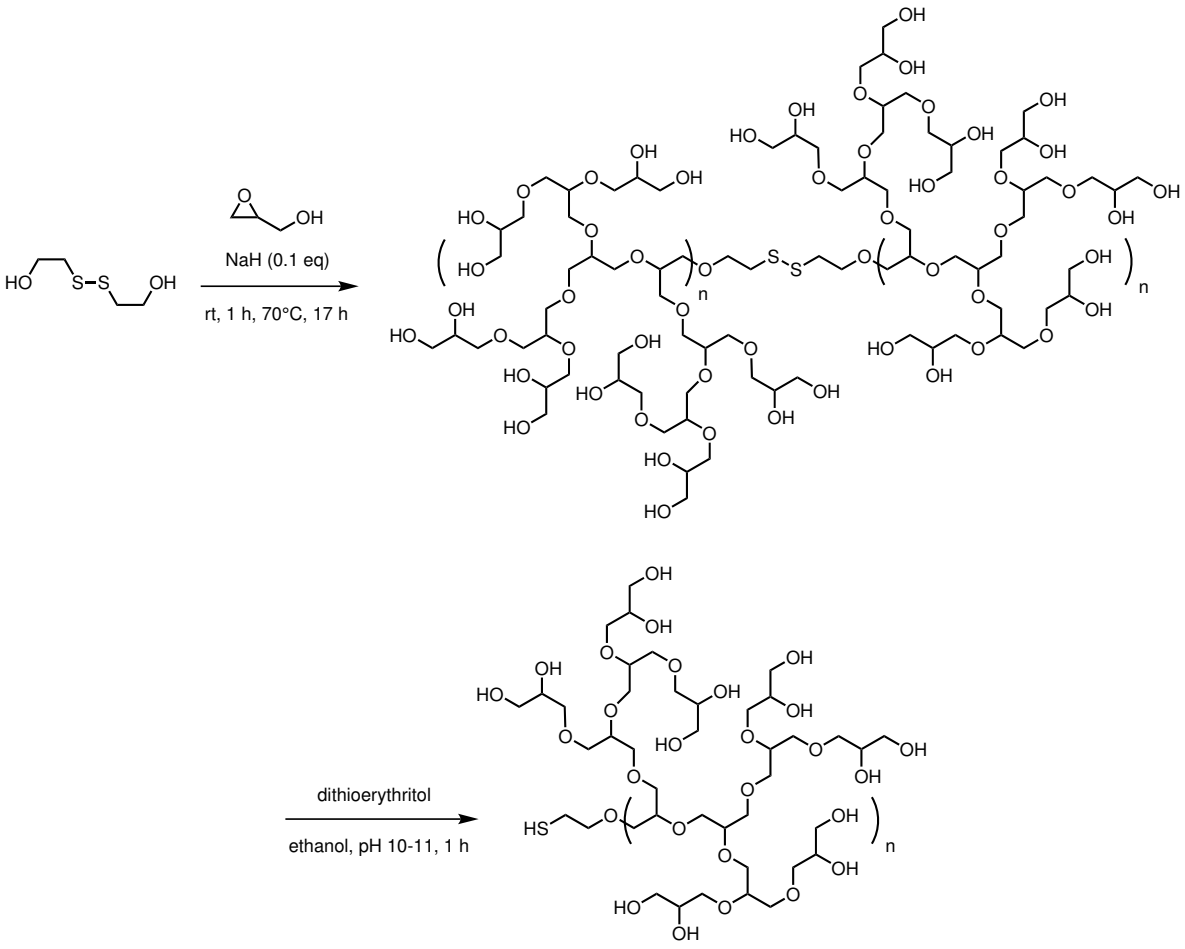

Thiol-cored HPG

2-hydroxyethyl disulfide (4.09 mmol, 0.5 mL) was 10% deprotonated with sodium hydride (0.409 mmol, 0.016 g) in a thrice-flame-dried flask, and doubly distilled glycidol (268 mmol, 18 mL) was added dropwise (1.2 mL/hr) with a syringe pump under nitrogen. The mixture was heated to 70°C after an hour, and the workup was completed as described for the alkyne-cored HPG, to yield disulfide HPG. Dried disulfide HPG (384 mg) was dissolved in 25 mL ethanol and an excess of dithioerythritol (1 mmol, 160 mg) was added. The pH of the solution was adjusted to 10 – 11 with ammonium hydroxide, and the mixture was stirred for one hour. The reduced polymer was fractionally precipitated from acetone three times to yield thiol-cored HPG. The molecular weight of the disulfide was determined by GPC to be about 5,000 g/mol with a PDI of 1.09, and disulfide core incorporation was confirmed via ^{1}H NMR in DMSO-d_6 by identifying the triplet at 2.89 ppm corresponding to the $-S-CH_2$ protons. GPC could not determine the molecular weight of the thiol because the disulfide reformed in the column, but reduction was verified with an Ellman's reagent (5,5'-dithiobis-(2-nitrobenzoic acid)) (DTNB) assay, which produced a yellow dianion (λ_{max} = 412 nm) for the thiol. The molecular weight of the thiol should be approximately 2,500 g/mol based on the molecular weight of the disulfide. The final polymer was dried under vacuum and stored at 4°C.

2.6.3 Synthesis of particles

CTAB rods

Gold nanorods of controlled aspect ratio were synthesized in high yield via a surfactant-stabilized, seed-mediated growth method. To make 1-2 nm spherical seeds, fresh, cold sodium borohydride ($NaBH_4$) (0.6 mL, 0.01 M) was added to a solution of chloroauric acid ($HAuCl_4$) (250 µL, 0.01 M) in cetyltrimethylammonium bromide (CTAB) (9.75 mL, 0.1 M). The seed solution was stirred rapidly for 10 minutes, and then allowed to "age" for at least 1 hour to quench excess $NaBH_4$. To synthesize rods of varying aspect ratio, a certain volume (0.01 to 0.1 mL) of 0.01 M silver nitrate ($AgNO_3$), chloroauric acid (0.5 mL, 0.01 M), and ascorbic acid (55 µL, 0.1 M) were added to CTAB (9.5 mL). After the solution was inverted several times until it became colorless, seed (12 µL) was added and the mixture inverted again. The rods were allowed to form overnight (14-16 hours), centrifuged twice at 11,000 rcf for 15 m to remove excess CTAB, and redispersed in water. The aspect ratio was controlled by the amount of silver nitrate added. To make a large batch of rods, a typical procedure was as follows: In a 1 L Erlenmeyer flask was added 760 mL 0.1 M CTAB, 0.48 mL 0.1 M $AgNO_3$, 40.0 mL $HAuCl_4$, 4.4 mL 0.1 ascorbic acid, and 960 µL gold seed. The mixture was swirled vigorously and allowed to sit 22 h, after which it was centrifuged twice at 11,000 rcf for 20 minutes.

High aspect ratio CTAB rods

High aspect ratio gold nanorods (aspect ratio about 18) were synthesized in low yield but high purity in the absence of silver ions. 250 μL 0.01 M $HAuCl_4$ was added to each of two 15 mL centrifuge tubes, and 2.5 mL 0.01 M $HAuCl_4$ was added to a 200 mL flask. CTAB was added to the 15 mL tubes up to 9 mL total volume, and 90 mL added to the 200 mL flask. 50 μL 0.1 M ascorbic acid was added to each 15 mL tube and 0.5 mL was added to the 200 mL flask, and all three containers were gently shaken or inverted to yield a colorless solution. 1 mL seed solution was added to one of the centrifuge tubes and inverted, and after 15 seconds 1 mL of that solution was added to the second centrifuge tube and inverted. After 30 seconds, all the contents of the second tube were added to the flask, which was gently shaken and stored, sealed with Parafilm, for 14 hours. Then, the entire growth solution was emptied, leaving a thin rust-colored film on the bottom of the flask. This film was agitated in a few mL of water, yielding a green-brown solution of long rods. The rods were centrifuged once at 7,000 rcf for 6 minutes.

Citrate gold spheres

Spherical gold nanoparticles with a diameter of 18 nm were synthesized via citrate reduction. In a 200 mL conical flask, 2.5 mL 0.01 M $HAuCl_4$ and 100 mL water were heated to a rolling boil. 10 mL 1% sodium citrate solution was added, the mixture was boiled for 10 minutes, and the red particle solution was cooled and purified once via centrifugation at 11,000 rcf for 15 minutes. Longer boiling times correlated with larger particles.

2.6.4 Functionalization of particles

PSS-MA rods

Purified CTAB rods were dispersed in 1 mL nanopure water, and 100 μL 0.1 M NaCl solution and 200 μL 10 mg/mL PSS-MA solution were added at once. The solution was vortexed for one minute and allowed to sit undisturbed for 2.5 hours. The rods were purified by centrifugation at 7,000 rcf for 6 minutes.

Azide rods

To 5 mL 5x-diluted nanorods in 2-(N-morpholino)ethanesulfonic acid (MES) buffer at pH 5.5, 1.5 mg 1-ethyl-3-(3-dimethylaminopropyl) carbodiimide (EDC) and 4.0 mg N-hydroxysulfosuccinimide (sulfo-NHS) were added. The

solution was vortexed gently for 2 minutes. The activated ester was allowed to form for 15 minutes, and then the solution was purified via centrifugation at 7,000 rpm for 15 minutes. The pellet of activated ester nanorods was resuspended in 1 mL sodium phosphate buffer at pH 7.2, and 100 μL 0.1 M 11-azido-3,6,9-trioxaundecan-1-amine (N_3-PEG-NH_2) was added. The reaction mixture was vortexed gently for 2 minutes, and the coupling reaction proceeded for 22 hours. After centrifugation at 8,000 rcf for 10 minutes, the azide-functionalized rods were resuspended in nanopure water.

HPG rods, click chemistry

Azide rods and an aqueous solution of 12 mg/mL alkyne HPG were first degassed by bubbling nitrogen through the solution. 1 mL rods and 10 μL of alkyne HPG solution were vortexed together for 2 minutes, and 10 μL 0.2 M ascorbic acid and 10 μL 0.1 M copper sulfate were added. The mixture was vortexed for 2 minutes, and then stored at 1°C for 22 hours. The clicked rods were centrifuged at 14,000 rcf for 10 minutes to purify and redispersed in water. The rods were stable and did not aggregate after centrifugation.

HPG spheres, ligand exchange

For the citrate NPs, 200 μL 42 mg/mL thiol HPG was added to 1 mL as-prepared citrate NPs in DMF, agitated, and allowed to react for 47 hours. The solution was dialyzed in a 10,000 MWCO cassette, centrifuged, and redispersed in nanopure water for characterization.

HPG rods, ligand exchange

For the rods, two techniques were tried: 1 mL of 1 nM CTAB rods and 150 μL 42 mg/mL thiol HPG were sonicated for 30 minutes and left to react for 46 hours; or 1 mL 1.4 nM CTAB rods and 0.5 mL 20 mg/mL thiol HPG were sonicated for 10 seconds, loaded into 1,000 MWCO dialysis tubing, and dialyzed against nanopure water for 3 days. The centrifuged pellets were redispersed in water.

Polystyrene rods

5 μL styrene was added to 10 mL diluted CTAB rods and vortexed for 5 minutes, encouraging the styrene to partition within the aliphatic CTAB bilayer. 4 μL 0.1 M ammonium persulfate was added as a radical initiator to "zip" the styrene monomers, and the polymerization was allowed to take place for 15 hours. However, after centrifugation at 8,000 rcf for

20 min, the rods had aggregated, indicating either instability or complete hydrophobic surface modification. A different procedure was more successful: to a 2 mg/mL solution of thiol-polystyrene (13,100 g/mol) in THF was added dropwise (5 μL/min) 0.3 mL of concentrated CTAB rods. The solution was gently agitated every 5 minutes to homogenize the aqueous and organic layers. After addition, the mixture sat undisturbed for 42 hours to promote ligand exchange. The rods were purified via centrifugation at 11,000 rcf for 15 minutes.

2.6.5 DTNB (Ellman's reagent) assay

To make 990 μL of 5,5'-dithiobis-(2-nitrobenzoic acid) (DTNB) working reagent, 50 μL DTNB stock solution (2 mM DTNB, 50 mM sodium acetate), 100 μL Tris stock solution (1 M, pH 8), and 840 μL water were combined. A UV-vis background was taken of the working reagent. 10 μL of the thiol solution was added to the working reagent, and the solution was mixed thoroughly and allowed to rest at RT for 5 min. A UV-vis spectrum was recorded of the mixture, and observance of the yellow dianion at λ_{max} = 412 nm indicated presence of a thiol group.

2.6.6 Self-assembly studies

Polystyrene rods in co-solvent mixtures

Water (at indicated v/v%) was added dropwise (5 μL/min) to 0.5 mL polystyrene rods in DMF. The solution was gently agitated after each drop was added, and no precipitation was observed. After addition, the mixture sat for 2 hours to allow stabilization of any self-assembled structures, then was dialyzed against 1 L water in a 3,500 MWCO cassette to remove DMF. For TEM imaging, a drop of the solution was placed onto a TEM grid and excess water was wicked away after 10 minutes.

Polymersome formation

In a typical procedure, 1 mL water was added dropwise (1 mL/hr) to a vigorously stirring solution of 1 mL of 10 mg/mL polystyrene-*co*-HPG in DMF. After addition, the turbid solution stirred for 24 hours, and 3 mL water was added. The solution was then dialyzed in 1,000 MWCO tubing (to remove DMF) or a larger MWCO tubing (to remove unassembled copolymer) against 1 L water.

Polymersome and rod assembly

Self-assembly of the block copolymers with hydrophilic rods was conducted as described earlier for polymersomes, but by adding 1 mL aqueous solution of nanorods dropwise to the polymer in DMF. The turbid solutions were dialyzed in a 10,000 MWCO cassette to remove DMF and drop-cast onto a TEM grid and allowed to evaporate.

To self-assemble the copolymers with the hydrophobic rods, a homogenous solution of 5 mg polystyrene$_{10K}$-HPG$_{8K}$ and concentrated polystyrene rods in 2.5 mL DMF was stirred vigorously while 1 mL water was added dropwise (1 mL/hr). The turbid solution was stirred for 24 hours and dialyzed against 1 L water in a 10,000 MWCO cassette to remove DMF. The solution was then drop-cast onto TEM grids and excess water wicked away.

Chapter 3

NMR Studies of Particles with Shape and Functional Anisotropy

3.1 Introduction

It is not trivial to determine the ligand shell composition and morphology of inorganic nanoparticles. This challenge is magnified in anisotropic particles, particularly those with heterogeneous or "patchy" domains. The controversial work of Stellaci and colleagues on striped particles indicates as much: the authors allege that scanning tunneling microscopy (STM) confirms the presence of stripe-like domains on small gold nanoparticles,[87] but this conclusion has been notoriously contested by those who believe the domains are simply an artifact of the STM image.[88] Although this ongoing dispute has reached almost farcical proportions, inciting critiques, commentaries, and even symposia more than a decade after the publication of the original study,[89] it underscores just how difficult it is to conclusively characterize surfaces on the nanoscale. Indeed, this uncertainty remains one of the most frustrating aspects of nanochemistry and limits its power as a branch of synthetic chemistry. Nanochemistry today finds a parallel in the days of organic chemistry before NMR spectroscopy, when mass spectrometry, elemental analysis, or boiling point analysis could hint at the identity of a molecule without elucidating its connectivity. Given that the surface of a nanoparticle influences much of its behavior, and functional particles are being increasingly engineered, it is now urgent to develop methodologies to understand their surface character.

Solution NMR spectroscopy is the gold standard for structure elucidation in organic chemistry, but it is not widely used in nanoparticle characterization. Compared to other available techniques, NMR spectroscopy suffers from low sensitivity due to the small interaction energy of the magnetic field with the nuclei, requiring concentrations of at least 10^{-5} M or 10^{16}-10^{18} sensitive nuclei.[90] These concentrations are often not realistic for nanoparticles. Even when the requisite concentrations are reached and the bound ligands are observable by NMR, the spectra do not provide the same clarity as for small, free organic molecules. The linewidths of bound molecules are significantly broadened, often smearing splitting patterns beyond recognition and distorting integration values. Therefore, it can be difficult to assign resonances, and near-impossible to quantify nuclei.

Though the limitations have narrowed the use of NMR for nanochemistry, NMR actually delivers key information that is unattainable by other analytical techniques. We argue that NMR solely occupies a niche in understanding physical and chemical properties of nanoparticles, and that its utility is far greater than its popularity would suggest.

3.1.1 What NMR can tell us about particles

The magnetic field experienced by a nucleus determines the energy gap between its spin states and thus the frequency at which it resonates, also called the chemical shift (δ). The local field at the nucleus is very sensitive to its electronic environment, which includes the atoms it is connected to through bonds as well as through space. When a nucleus is surrounded by high electron density, it is said to be shielded to the effect of the applied magnetic field, and its chemical shift frequency is low. On the other hand, if the nucleus neighbors an electronegative atom that pulls electron density away, it more strongly experiences the field, so deshielded nuclei have higher chemical shifts. Nuclei with even the slightest difference in their electronic environments resonate at distinctly separated chemical shifts, wherein lies much of the power of NMR for structure elucidation. Related to this concept is the Knight shift, a dramatic change in the resonant frequency observed in nuclei in metallic environments.[91,92] The conduction electrons in the metal couple to the nuclei, which feel an added effective field. In metal nanoparticles, conduction electrons at the particle surface can exert this effect on bound ligands. Indeed, organic ligands on gold particles almost always experience a significant change in chemical shift. Although it is not clear whether this is attributable to the Knight shift or another phenomenon, this chemical shift change is a marker of bound ligands.[93] In the gold spheres and rods studied in this work, ligand resonances either shift upfield or downfield when they are attached to the surface, highlighting variations in the gold-ligand bond and in the degrees of shielding.

Line broadening is also diagnostic of attached ligands. An organic molecule anchored to a heavy particle tumbles at a much slower rate in solution, affecting relaxation processes (Figure 3.1).[90] The NMR signal arises from the over-population of nuclei in the excited state after the magnetic pulse is applied. As the population distribution of nuclei returns to equilibrium (i.e., excited to ground state), the signal decays over time. Two relaxation processes affect the rate of decay: spin-lattice relaxation (time constant T_1), and spin-spin relaxation (time constant T_2). Spin-lattice relaxation describes the redistribution of spin populations to thermal equilibrium, as spins dissipate the energy from the magnetic pulse to the surrounding lattice. The spin-lattice relaxation time (T_1) is measured by rate of return to magnetization in the z-direction after a 90° pulse. T_1 influences the loss of signal intensity. Spin-spin relaxation, on the other hand, arises from the interaction of spins with each other. After the pulse, the nuclei precess in phase, but eventually the ensemble of nuclei lose phase coherence, resetting magnetization in the xy-direction to zero. T_2, the spin-spin relaxation time, is

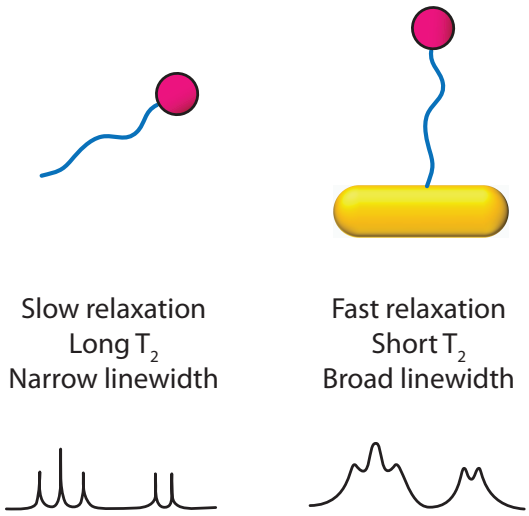

Figure 3.1 Rapidly-tumbling nuclei tend to have slow relaxation times and narrow linewidths, whereas slowly-tumbling nuclei have faster relaxation times and broader linewidths.

inversely proportional to linewidth. Molecules that tumble slowly have fast T_2 values, and thus broad linewidths, for a few reasons. Neighboring spins induce magnetic moments in each other (dipole-dipole coupling), so molecular motion causes tiny, fluctuating local magnetic fields that disrupt the precession frequency of each spin. Slow molecular tumbling enhances the field variation between nuclei, and phase decoherence happens more quickly. In addition, the electronic environment around a nucleus is heterogeneous, so the chemical shift is affected by the nucleus's orientation to the external magnetic field (chemical shift anisotropy).[92] Fast molecular tumbling typically averages out all the possible orientations, but a slowly-tumbling molecule may be oriented in several directions with respect to the field. All of these chemical shifts are observed together as a broadened line. Studying relaxation processes is a particular advantage of NMR spectroscopy because very fast atomic motions that occur on the pico- and nanosecond time scales reveal themselves as comparably slow relaxation times on the millisecond to second time scale, elucidating atomic dynamics that otherwise would be near-impossible to probe.[94]

Although line broadening from "troublesome" rapid relaxation is often cited as a pitfall of particle NMR, there is no reason to fear relaxation effects and broadening. Together with chemical shifts, linewidths and relaxation values provide a surprising amount of insight into the mobility and dynamics, local viscosity, and conformation of ligands, as well as the physical properties of the particle itself. By tracking changes in chemical shift or broadening in a reaction, one can extract information on kinetics and binding constants. Particle samples are prone to inhomogeneity, with features such as high polydispersity, varied ligand conformations, surface defects or reactive hotspots, and shape and functional anisotropy. As ensemble measurements, NMR resonances reflect the heterogeneity of the sample. Because tumbling

rate is proportional to the size of the particle, ligands attached to larger particles will generally have broader linewidths. This can be a useful tool in identifying capping agents in mixtures of heterogeneous particle sizes. Likewise, mobile nuclei tumble more quickly, so T_2 values and linewidths can determine ligand attachment points and conformations.[95] Due to particle curvature, a ligand's nuclei become increasingly more mobile with increasing distance from the particle surface; nuclei close to the surface are effectively immobilized, whereas those close to the solvent interface are dynamic. Nuclei closer to the surface also often experience a larger change in chemical shift, although this is not always the case, because the electronic environment can evolve anywhere along the ligand.

The majority of reported NMR studies have been limited to isotropic spherical nanoparticles with homogenous monolayers; very little NMR research has tapped into functional or shape anisotropy in particles.[96] There are several reasons for the paucity in work on anisotropy. Most NMR analyses of nanoparticles target thiolate monolayer-protected spheres with very small core diameters (< 5 nm), which do not suffer as severely from fast relaxation times and broadening.[93] Such small spheres can often be made in yields and concentrations high enough for adequate NMR detection.

In contrast, gold nanorods—the prevailing model for shape anisotropy due to their well-controlled synthesis—have dimensions about an order of magnitude larger (typically around 15 x 45 nm, for a rod with an aspect ratio of 3) and are challenging to make in high yield. Such heavy particles are expected to tumble so slowly as to produce NMR spectra with extremely low signal-to-noise ratios. The yield of the standard synthesis, measured by mass conversion of gold salt to particles, is only about 15%. Scaled-up syntheses can be done but may suffer from high polydispersity. In addition, the synthesis of gold rods relies on the surfactant cetyltrimethylammonium bromide (CTAB); much evidence exists that CTAB forms a dense, charged bilayer on the gold surface that prevents aggregation by electrostatic repulsion. The CTAB bilayer is complex and is thought to contain multiple distinct ligand environments: the inner and outer leaflet of the bilayer, perhaps with variations in molecular interdigitation; the longitudinal axis, which appears locally "flat" in the long dimension and curved along the circumference of the rod's width; the transverse axis, which has a sharp radius of curvature; crystallographic facets with different chemical reactivities; and regions of fluctuating disorder. It is no wonder that NMR analysis of the surface of a gold rod is stymied by its convoluted character. Therefore, it is enticing to develop NMR methods robust enough to reveal information about the rod's enigmatic surface.

3.1.2 NMR markers for particle anisotropy

Mysterious peaks have been observed in particle NMR studies, with no definitive explanation for their persistent appearance. Bimodal peak separation was discovered in both proton and carbon NMR spectra of small gold particles capped with tiopronin; individual ligand nuclei gave rise to two resonant frequencies. This unxpected result suggested

that the ligands were associated with two types of gold clusters with different binding modes and chemical environments, hinting that the local environment of a ligand influences its NMR signal, often to a surprising degree.[93]

In another noteworthy study, a sharp aromatic peak was observed in the proton NMR spectra of "striped" gold particles with a mixed monolayer of diphenyl thiol (DPT) and dodecanethiol (DDT).[97] Although the peak overlaps with the broad peak of bound DPT, the authors provided convincing evidence that it does not arise from free DPT, as would be immediately speculated. This peak did not decrease in intensity or disappear with increasing cycles of purification, including trials of dialysis, filtration, and centrifugation, and it also did not overlap with the resonances of free DPT when additional free ligand was added to the particle solution. Furthermore, diffusion-ordered NMR determined that the diffusion coefficients of the broad, bound DPT peak and the sharp peak are the same, and that adding free DPT to the particles increases the average diffusion rate. That the sharp peak diffuses at the same rate as the bound ligand suggests that it arises from a species attached to a particle—an intriguing result given its chemical shift and narrow linewidth. What could account for a bound ligand with such a distinct NMR signature? The authors propose that ligands located at different binding sites, and thus chemical environments, can give rise to unique NMR signals. In other words, NMR signals can pinpoint the ligand's spatial location on the surface of a particle. This is a powerful theory, because there are currently few ways to identify surface composition and morphology.

This theory relies, of course, on the particle having distinctive regions. In the case of the DPT-DDT striped particles, diametrically opposed polar defect regions have already been predicted and observed. These regions are at least two orders of magnitude more reactive than the rest of the surface, presumably because the ligands are packed loosely and the energetic barrier to accessing the gold is much lower there. If the ligands are packed loosely, they are less ordered and more conformationally mobile—closer in likeness to a free ligand. It stands to reason that ligands at these reactive sites would generate NMR signals with narrower linewidths, and slightly different resonance frequencies, than their bound counterparts. To test whether the signals do indeed locate those reactive sites, the competing ligand aminoanthracene was added to the particles, with the expectation that it would preferentially exchange with the DPT at the reactive sites. The original sharp signal disappeared and was replaced by sharp peaks at a different frequency from free aminoanthracene; the new sharp peaks were seemingly from aminoanthracene now bound to the reactive polar regions.

Very recently was reported a fascinating, rigorous analysis of the dynamics and conformation of the ligand shell of a gold nanoparticle.[98] The structure of the particle was determined with atomic precision to have exactly 102 gold atoms and 44 passivating *para*-mercaptobenzoic acid ligands. Previously, single-crystal X-ray diffraction elucidated the C_2 symmetry of the particles, identifying 22 symmetry-unique ligand environments in the shell;[99] NMR studies later revealed the ligand layer to be as complex in local environments and dynamics as a protein[100]—quite remarkable for what

appears by common measures (e.g., TEM) to be a "simple" nanoparticle. Two thiolate-gold bond types were found: a short RS – Au – SR form and a long RS – Au – (SR) – Au – SR form. In the newest study, a suite of two-dimensional NMR techniques, molecular dynamics (MD) simulations, and density functional theory (DFT) calculations led to the complete NMR resonance assignment of all 22 symmetry-unique ligands in solution. The chemical shift of each ligand environment is a function of electronic shielding by neighboring species, which affects the local magnetic field experienced by that ligand. The tethered ligands are confined in space, amplifying the differences in each ligand's local field. Total correlation spectroscopy (TOCSY) and heteronuclear single-quantum correlation spectroscopy (HSQC) successfully assigned each proton to its resonance, while nuclear Overhauser effect spectroscopy (NOESY) and rotating frame nuclear Overhauser effect spectroscopy (ROESY) assessed through-space connectivity of ligands. MD simulations found that a ligand's dynamics were strongly influenced by its interactions with nearby ligands and the conformational free space. Overall, the results found five distinct ligand environments classified by extent of electronic shielding; the more shielded an environment, the more upfield its chemical shift. In order of most shielding to most deshielding (upfield to downfield shifts), those ligand environments were a) edge-to-face aromatic interaction, b) face-to-face aromatic interaction, c) isolated ligand, d) ligand-to-sulfur interaction, and e) ligand-to-gold interaction. Gold metal strongly deshielded the ligand (perhaps an effect of the Knight shift), whereas the perpendicular-plane aromatic rings were the only shielding environment. Splitting of HSQC peaks was observed for conformationally-restricted ligands with strong ligand-ligand interactions. In addition, TOCSY cross-peak intensity was stronger for those less mobile ligands, which supported the dynamics data from MD simulations and DFT calculations. This study alludes to the possibility of controlling ligand exchange on a particle surface at the single-molecule level, an enormously powerful tool for particle engineering.

Other studies on these atomically-precise gold nanoclusters revealed how robust NMR spectroscopy can be in deciphering the surface.[101] Multiple reports identify two ligand environments corresponding to either two binding modes,[102,103] or the different symmetry environments offered by the polyhedral vertex versus the polyhedral edge.[100] Nanoclusters such as the $Au_{102}SR_{44}$ in the above study[98] or $Au_{38}SR_{24}$ where R = CH_2CH_2PH, were found to have inherently chiral metal cores. Even though the ligands are not themselves chiral, the core chirality appears to dramatically influence the ligands' resonant frequencies. NMR was able to resolve separate ligand proton resonances on a nanocluster, arising from so-called "diastereotopic" CH_2 protons; the geminal α CH_2 protons had chemical shifts separated by an unexpectedly large 0.8 ppm.[104] The chirality of the metal core induced diastereotopicity in geminal protons, which could be separated by their distinctive NMR shifts.

3.1.3 Theory for NMR spectroscopy of shape-anisotropic particles

A powerful theory takes form from this preceding body of work. NMR spectroscopy can interpret the precise molecular character of particle surfaces: it can identify distinct reactive sites, pinpoint regiospecificity of bound ligands, elucidate spatial ligand shell morphology, and decipher degrees of molecular order and mobility. This leads us to an adaptation of the theory to particles with shape anisotropy. If a spherical particle can have reactive sites so distinct as to markedly change NMR signatures, a shape-anisotropic particle must have regions for which similar unique signatures are observed. For a gold nanorod, evidence exists that the ends are eminently reactive because of a disordered, fluxional bilayer at that high radius of curvature. In fact, any ligand at the end should have high mobility and low-density packing relative to a ligand along the ordered long axis. Therefore, ligands at the ends—of which there are fewer than ligands at the sides—should be expected to have a distinct NMR signature from the "bulk" bound signal. In particular, ligands at the ends of rods are expected to exhibit narrower linewidths because of their freer mobility. They may also resonate at a different frequency, a function of the distinct chemical environment at the ends.

Through-bond and through-space correlations are also useful measures of ligand shell character. Correlation spectroscopy (COSY) identifies nuclei of the same type that are spin-spin (J) coupled, or connected by fewer than four bonds. The pulse sequence consists of a two 90° pulses (p1 and p2) separated by a specific evolution time (t1) and followed by a measurement period (t2). On the resulting two-dimensional spectrum, the horizontal and vertical axes each displays the frequencies for the nucleus (i.e., the one-dimensional spectrum). The coordinates where the frequencies meet identify coupling. Diagonal peaks always arise from nuclei that have the same chemical shift (i.e., the same nucleus), and cross-peaks arise from different nuclei that are through-bond coupled. Total correlation spectroscopy (TOCSY, also sometimes called homonuclear Hartmann-Hahn spectroscopy, or HOHAHA) is a derivative of COSY; its cross-peaks identify nuclei that are coupled both directly and through a series of couplings. Therefore, nuclei that are part the same aliphatic chain or aromatic ring, for example, would all appear coupled in a TOCSY spectrum, as long as they are not separated by a heteroatom that interrupts the spin system. If multiple ligand environments are present and give rise to distinct resonances, TOCSY can correlate nuclei in the same environment. In other words, if four resonances arise from two spin-spin coupled ligand protons, indicating two distinct environments, TOCSY can identify which pair of resonances arises from the same proton. Nuclear Overhauser effect spectroscopy (NOESY) reveals nuclei coupled through space within 5 Å of each other, illustrating the spatial distribution of ligands on the particle surface. NOESY has been used to determine the ligand shell morphology of small mixed-monolayer spheres on the basis of strength of cross-peaks.[95,97,105,106] Janus particles exhibit weaker NOESY cross-peaks than a particle with a randomly-mixed monolayer, because the binary ligands are neighbors only at the single Janus interface; in random mixing, there is much more proximal interaction between disparate ligands.

Extending the theory a step further, we expected the diffusion constants, and to some degree the T_2 relaxation values, to be fingerprints for the reactive environment, and thus location, of the ligand nuclei. The diffusion constant of a nucleus is not determined by only the diffusion rate of the overall species—in this case the particle—but also by the viscosity and conformational mobility in the local molecular environment. This effect is seen in lipid vesicles, in which the diffusion rate of lipid molecules in a highly-packed gel bilayer are 1-2 orders of magnitude slower than those in a fluid bilayer.[107] In proteins that do not have isotropic rotational diffusion (as would a hard sphere), a specific anisotropic rotational diffusion tensor must be applied to obtain heteronuclear (^{15}N-^{1}H) relaxation times.[94] Because these relaxation rates depend on the orientations and fluctuations of the ^{15}N-^{1}H vectors, they are inherently tied to the tumbling anisotropy—and conformation—of the protein.[108,109] Such diffusion data have been used to determine long-range order and local dynamics in proteins.[110,111]

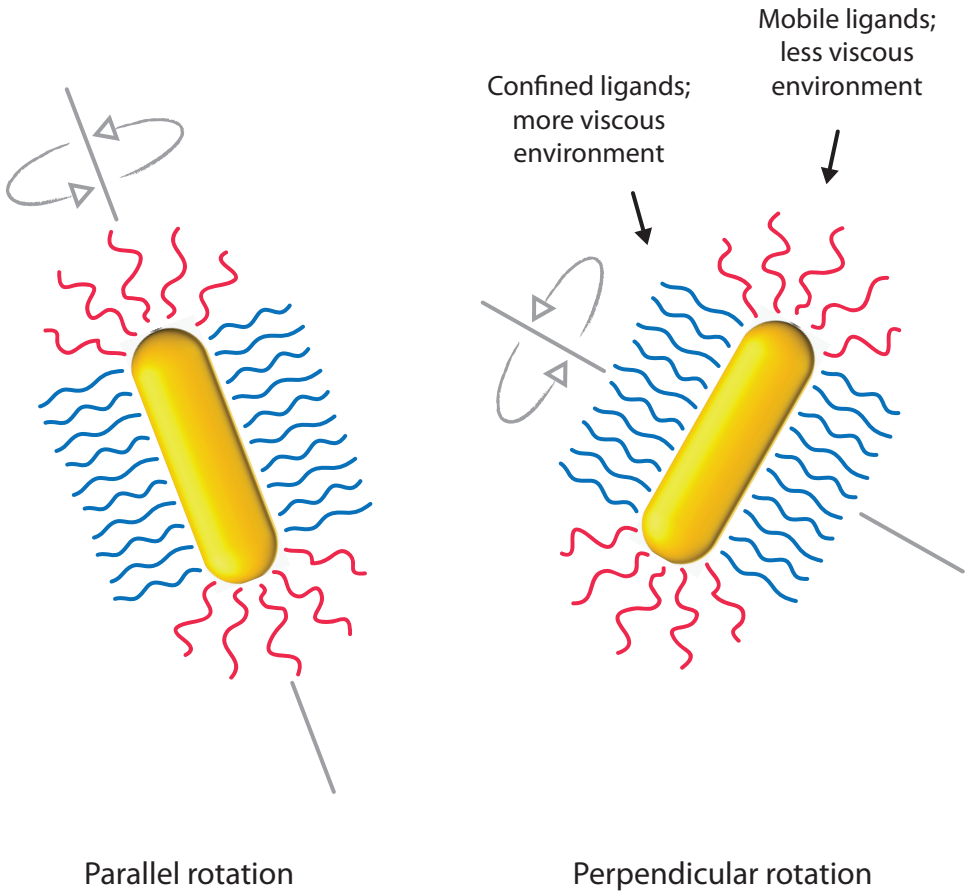

Figure 3.2 Two mechanisms come into play when considering the diffusion of ligands on non-spherical particles. Rotational tumbling occurs both parallel and perpendicular to the major axis, which can affect the observed diffusion of ligands on the longitudinal or transverse axes. Ligands on the transverse axis are also thought to be more mobile in a less viscous local environment, and therefore have a faster measured diffusion coefficient, than the ordered ligands on the long axis.

Using a nanorod as our example of shape anisotropy, consider the tumbling behavior of both the rod and the ligands. Their diffusion has both translational and rotational contributions, where translation occurs at a much longer time scale (milliseconds) than rotation (microseconds).[112] The translational diffusion coefficient of the rod describes the Brownian motion of the particle through solution. It has been shown by fluorescence correlation spectroscopy that translational diffusion of a gold nanorod in solutions of polymers or colloidal spheres is significantly affected by the direction of translation: diffusion parallel to the long axis conforms quite well to the bulk solution viscosity, whereas diffusion normal to the long axis endures high friction.[113] The rotational diffusion coefficient is difficult to measure because rotation occurs on such a fast timescale, but it is affected by the distribution of mass within the particle, which is dramatically anisotropic in an inorganic nanorod.

Three possible models, at least, have been developed to predict both types of diffusion in rods: hydrodynamic stick theory, Tirado and Garcia de la Torre's relations, and Broersma's relations. The hydrodynamic stick theory, which assumes a prolate ellipsoid shape, predicts that the ratio of the parallel diffusion coefficient $D_{\parallel}$ to the perpendicular diffusion coefficient $D_{\perp}$ for a rod always equals two, no matter the aspect ratio κ.[114] Broersma's relations are valid only for cylinders with aspect ratios above 3.5. Tirado and Garcia de la Torre's relations assume a rodlike geometry and may be the best fit for nanorods. The effect of rod length on both translational and rotational diffusion coefficients was studied on CdSe nanorods by fluorescence correlation spectroscopy.[112] The experimental diffusion coefficients agreed well with the theoretical predictions, particularly Tirado and Garcia de la Torre's relations. As expected, length (L) affects rotational diffusion much more dramatically than it does translational diffusion, with the translational diffusion coefficient scaling as L^{-1} and the rotational diffusion coefficient varying as L^{-3}. Because rotational diffusion is so sensitive to length or size, it is possible that it contributes to the measured diffusion of organic ligands on gold rods, arising from rotation normal to or along the long axis.

Two-dimensional diffusion-ordered spectroscopy (DOSY) is a powerful NMR technique that correlates resonances in a spectrum to their diffusion coefficients, with the ability to resolve individual species in a complex mixture. For diffusion of a nucleus to be tracked, it needs to be "labeled" in some way. In a DOSY experiment, the phase of the spin "labels" the nucleus. Pairs of pulsed field gradients are applied along the z-direction: the first pulse gradient dephases the spins to distinguish them from each other, and the second rephases them to collect the NMR signal. The nuclei are allowed to diffuse in the time interval between the pulses. The longer the distance diffused (i.e., the faster the diffusion), the smaller the signal intensity is. The gradient strength is modulated sequentially, with stronger field gradients causing a greater reduction in signal intensity. The rate of signal attenuation is proportional to the diffusion coefficient of that spin. The Stejskal-Tanner equation describes the relation between the intensity change and the diffusion coefficient:

$$I = I_0 e^{-D\gamma^2 g^2 \delta^2 (\Delta - \delta/3)} \tag{3.1}$$

I: observed intensity

I_0: reference intensity before attenuation

D: diffusion coefficient

γ: gyromagnetic ratio of the observed nucleus

g: gradient strength

δ: gradient duration

Δ: diffusion delay

Or, simplified to highlight the exponential character of decay:

$$I = I_0 e^{-DQ} \tag{3.2}$$

The gradient strength g is varied over the course of the DOSY experiment, and gradient duration δ and diffusion delay Δ are optimized for the system and held constant. From the diffusion coefficient D, the hydrodynamic radius of the molecule can be estimated using the Stokes-Einstein equation.

$$r = \frac{kT}{6\pi\eta D} \tag{3.3}$$

However, this equation assumes that the molecule is a hard sphere, and does not take into account non-spherical geometry or flexibility of the molecule. For small molecules, shape effects change D no more than 10% until aspect ratios are higher than three, after which geometry must be taken into account. D is also greatly affected by the viscosity of the fluid through which the molecule moves, which for small molecules in dilute solutions is just the solvent, but for molecules tethered to particles, likely contains a local viscosity contribution as well. Therefore, shape-anisotropic particles are expected to show diffusion behavior that deviates significantly from either small molecules or assumptions of the Stokes-Einstein equation.

3.2 High-yield gold rods: Obtaining necessary concentrations for NMR

A primary challenge for studying gold nanorods by NMR is the sheer concentration required in the probe (10^{16}-10^{18} nuclei, or about 10^{-5} M). The yield for gold rods prepared from the standard seeded growth procedure is low (about 15% gold conversion); a typical batch of 1 L of these rods can be concentrated to perhaps 10 mL of a 10 nM solution. This is not nearly concentrated enough for strong detection by NMR. As a result, the signal-to-noise ratio in ^{1}H NMR spectra of rods is inadequate, and the baseline too noisy, to properly assign resonances. Also contributing to the poor resolution is the large size of the rods (typically about 15 x 45 nm for aspect ratio = 3), so they tumble very slowly in solution and have fast relaxation values and broad linewidths, as described earlier.

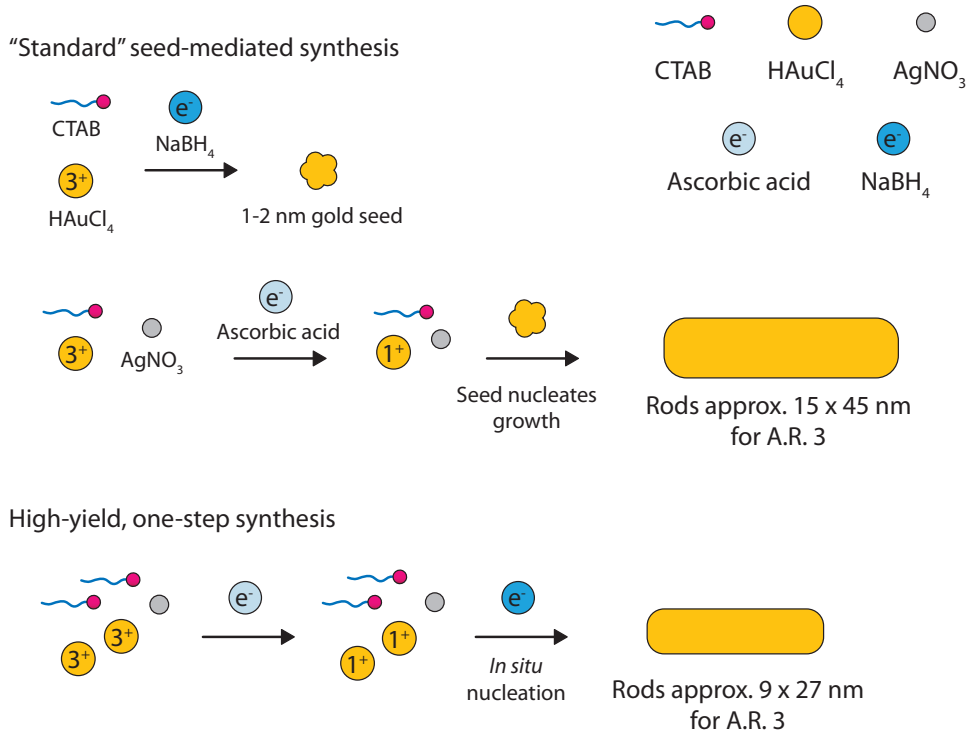

Figure 3.3 Schematic depicting the differences between the "standard" two-step, seed-mediated gold nanorod synthesis, and the new high-yield, one-step synthesis.

To overcome these two issues, the seeded growth procedure was modified to synthesize gold rods in strikingly high yield. In comparison to the standard method, a typical batch of 1 L of these new rods yields around 10 mL of a 400 nM solution. Rods produced this way also have dimensions slightly smaller than short rods (9 x 27 nm for aspect ratio = 3), and thus tumble a bit more rapidly, giving rise to narrower linewidths. (Note: the concentration of the new rods was determined by a calibration curve of extinction coefficients for standard rods, which may not be exactly fitted for these rods. However, the new rods do not differ in dimensions such that this assumption is unreasonable.)

The new "small" rods were synthesized by an *in situ* seeded growth procedure (Figure 3.3). In the original procedure, gold seeds (1-2 nm) are synthesized separately by reducing chloroauric acid ($HAuCl_4$, Au(I)) with sodium borohydride ($NaBH_4$) to Au(0). These seeds are then added to the growth solution of CTAB, $HAuCl_4$, silver nitrate ($AgNO_3$), and ascorbic acid, where they nucleate growth. In the *in situ* procedure, $NaBH_4$ is added directly to a modified growth solution. We believe that nucleating seeds form instantaneously throughout the solution. Within 5 minutes, the solution is a deeply opaque red-wine color, demonstrating how quickly the rods form in high yield.

The rods were characterized by UV-Vis spectroscopy and transmission electron microscopy (TEM). The features of the UV-Vis spectrum are indistinguishable from that of the standard short rods, with narrow, well-defined plasmon resonances for the transverse and longitudinal axes. No additional plasmon resonances are present, suggesting that the rods have a very low polydispersity. TEM images confirm the morphology and low polydispersity. These data point to the new *in situ* procedure as a robust, high-yield method to produce large quantities of concentrated rod solutions, previously a limiting factor for NMR studies. This procedure opens the door for any other studies requiring large amounts of rods, such as thermal gravimetric analysis (TGA) and numerous applications.

From the UV-Vis spectrum, the concentration of the new rods was estimated using a calibration curve based on extinction coefficients for short rods (see note earlier). The number of CTAB molecules in solution was estimated in order to determine whether CTAB could be detected by NMR.

A rod can be roughly assumed as a cylinder, whose surface area can be calculated by:

$$S = 2\pi rh + 2\pi r^2 \tag{3.4}$$

r: radius of the transverse axis

h: length of the longitudinal axis

For a rod with dimensions 9 x 27 nm, the surface area is approximately 890 nm^2. The footprint of CTAB, assuming a bilayer, is approximately 6 molecules/nm^2, leading to an estimate of 5340 CTAB molecules per rod. Given that a typical NMR sample is 1 mL in volume and assuming a sample concentration of 200 nM, there are 1.2 x 10^{14} rods present. Thus, the sample contains 6.4 x 10^{17} CTAB molecules, at a concentration of 10^{-3} M. This is well within the range of necessary nuclei to detect a strong signal.

Indeed, the ^{1}H NMR spectrum of the small rods have a much improved signal-to-noise ratio over the standard rods, with visible, distinct resonances that can be assigned to specific CTAB protons.

3.3 Particles with shape anisotropy: Bilayer versus monolayer

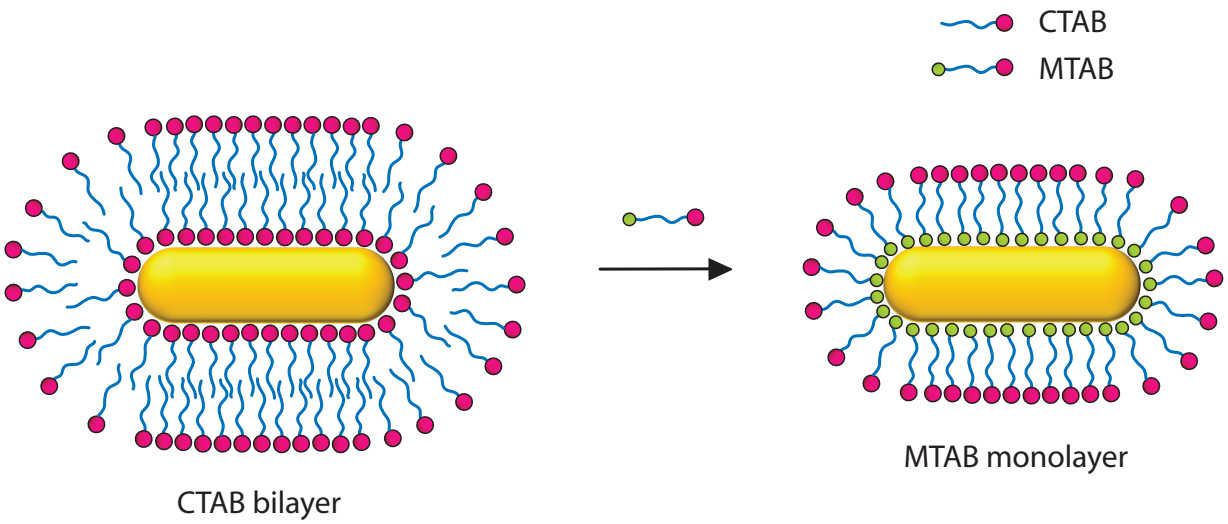

Figure 3.4 The CTAB bilayer can be replaced quantitatively by a monolayer of CTAB's thiolated analog, MTAB. NMR spectral differences between the two surface chemistries provide insight into their molecular compositions and conformations.

The difficulties in studying the CTAB bilayer are inescapable. There could be at least four distinct environments between the inner and outer leaflets and the transverse and longitudinal axes. For the purposes of this work, we are more concerned with the two axes, where the bilayer structure is a function of the shape anisotropy and provides a route to chemical anisotropy. So, to remove the variable of the two leaflets for simplicity, CTAB molecules were substituted with their thiolated analogue, (16-mercaptohexadecyl) trimethylammonium bromide (MTAB).[115] MTAB forms a monolayer on the particle's surface, the thiol binding to the gold and the ammonium headgroup at the solvent interface. MTAB molecules along the longitudinal axis should be more densely arranged than those at the transverse side. If broadening of the CTAB headgroup protons is due primarily to the chemical heterogeneity of the inner and outer leaflets, then a substantially sharper peak should be observed for the analogous protons in the MTAB monolayer. Similarly, changes in the MTAB splitting patterns should appear only if those in CTAB are not related to inner and outer leaflet differences, or if the monolayer is much more uniform than the bilayer in its degree of molecular order.

Comparison of NMR signatures of monolayer (MTAB) and bilayer (CTAB) surfaces revealed compelling differences, as discussed in this section.

3.3.1 Chemical shifts

Bilayer

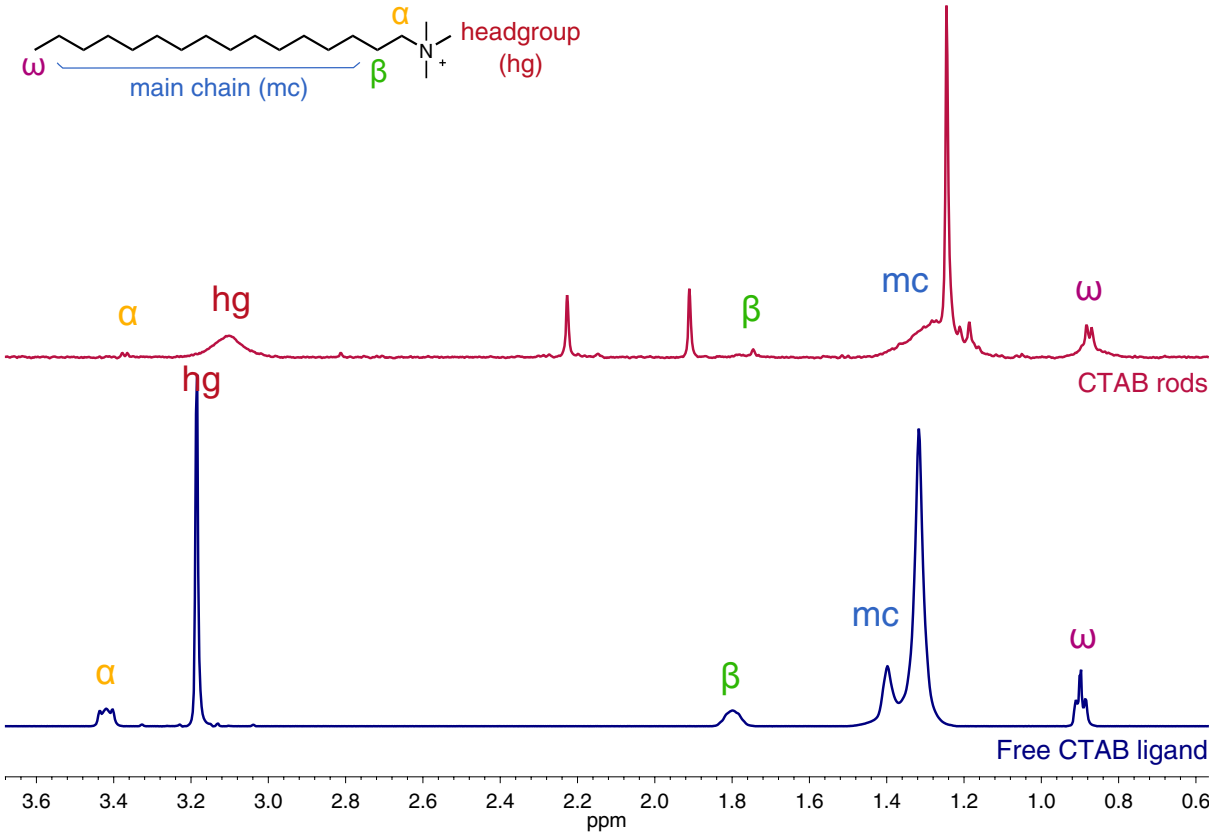

Figure 3.5 ^{1}H NMR of CTAB rods and free CTAB ligand.

As compared to the chemical shifts of free CTAB molecules, all of the CTAB proton resonances shift upfield in the spectrum of CTAB rods, indicating their attachment to the surface of rods. Upfield chemical shifts suggest ordering and immobilization of CTAB on the surface, which is consistent with the theory that CTAB forms an ordered bilayer. In previous studies, the change in chemical shift of a ligand's protons increases with the protons' proximity to the gold surface. Protons that are closer to the surface are more immobilized, and may experience a Knight shift, in which conduction electrons in metals induce an "extra" field; the more a proton's environment changes from the free molecule form, the more dramatic the expected spectral change. To study the correlation between change in chemical shift and proximity to the gold surface for CTAB, $\Delta\delta$ for each proton type was plotted with increasing distance from the ammonium headgroup. However, it was recognized that because CTAB forms a bilayer on the surface, with protons on both the inner and outer leaflet the correlation is probably not straightforward: the NH_4^+ group has two distinct

populations, one that is attached to the gold surface and one that is facing solution (proximal and outer, respectively). A slight trend was observed: as distance from the NH_4^+ group increases, the change in upfield shift decreases, with the exception of the main chain protons (which are hard to deconvolute).

Monolayer

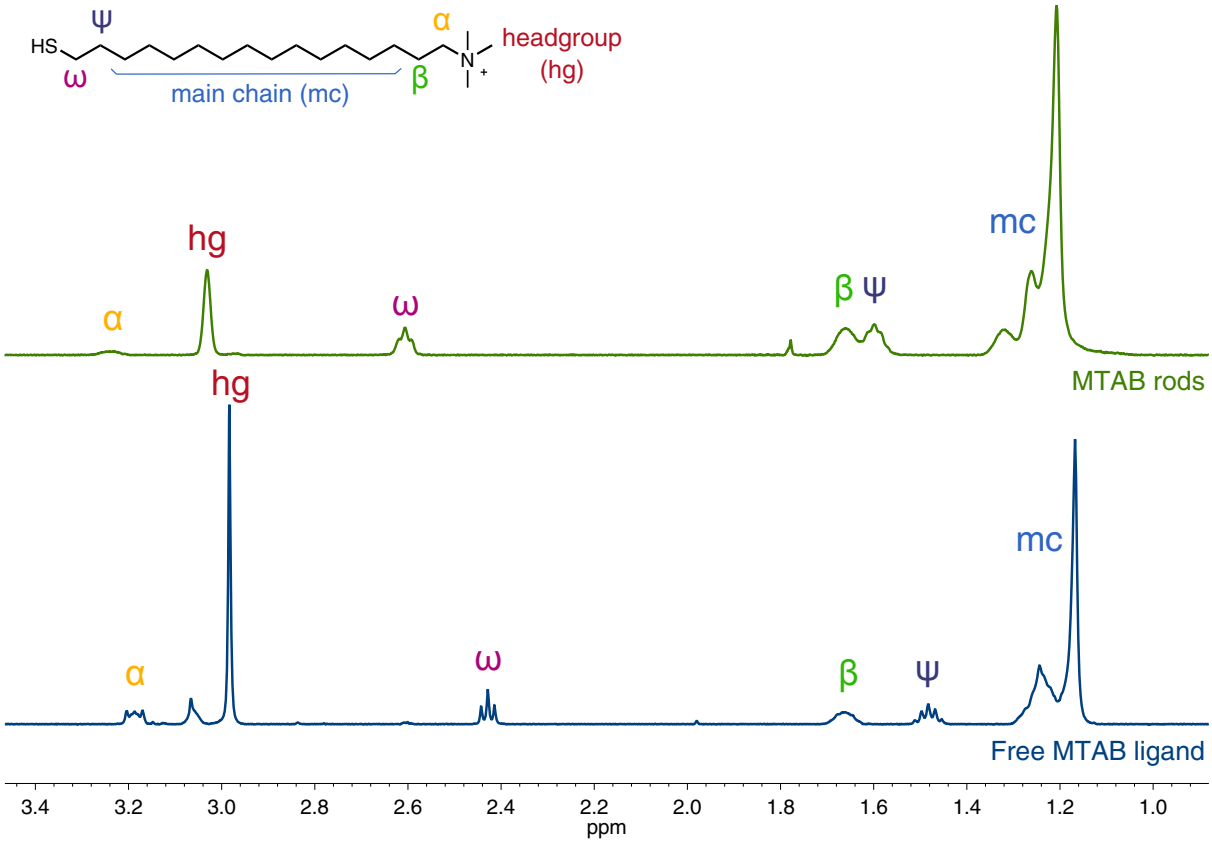

Figure 3.6 ^{1}H NMR of MTAB rods and free MTAB ligand.

From the disappearance of the CTAB ω methyl resonance at 0.74 ppm, it is clear that the CTAB has been completely displaced by MTAB, at least to the extent measurable by NMR (Figure 3.6). Interestingly, MTAB protons experience a *downfield* shift when they bind to gold, opposite to bound CTAB, which shifts *upfield*.

Discussion

The divergence in resonance shifts highlights the differences in the CTAB-gold and MTAB-gold bonds: CTAB is thought to attach electrostatically with its charged headgroup, whereas MTAB forms a covalent thiolate linkage. As revealed

in the NMR studies of atomically-precise gold nanoclusters, even atom-level differences in the gold-thiol bond, and ligand-gold or ligand-ligand interactions, can dramatically change the chemical shift.[98] In another theory, it has been hypothesized that CTAB's upfield shift is actually attributable to formation of a CTAB-silver bromide complex at the headgroup, a sort of miniature Knight shift.[51,116]

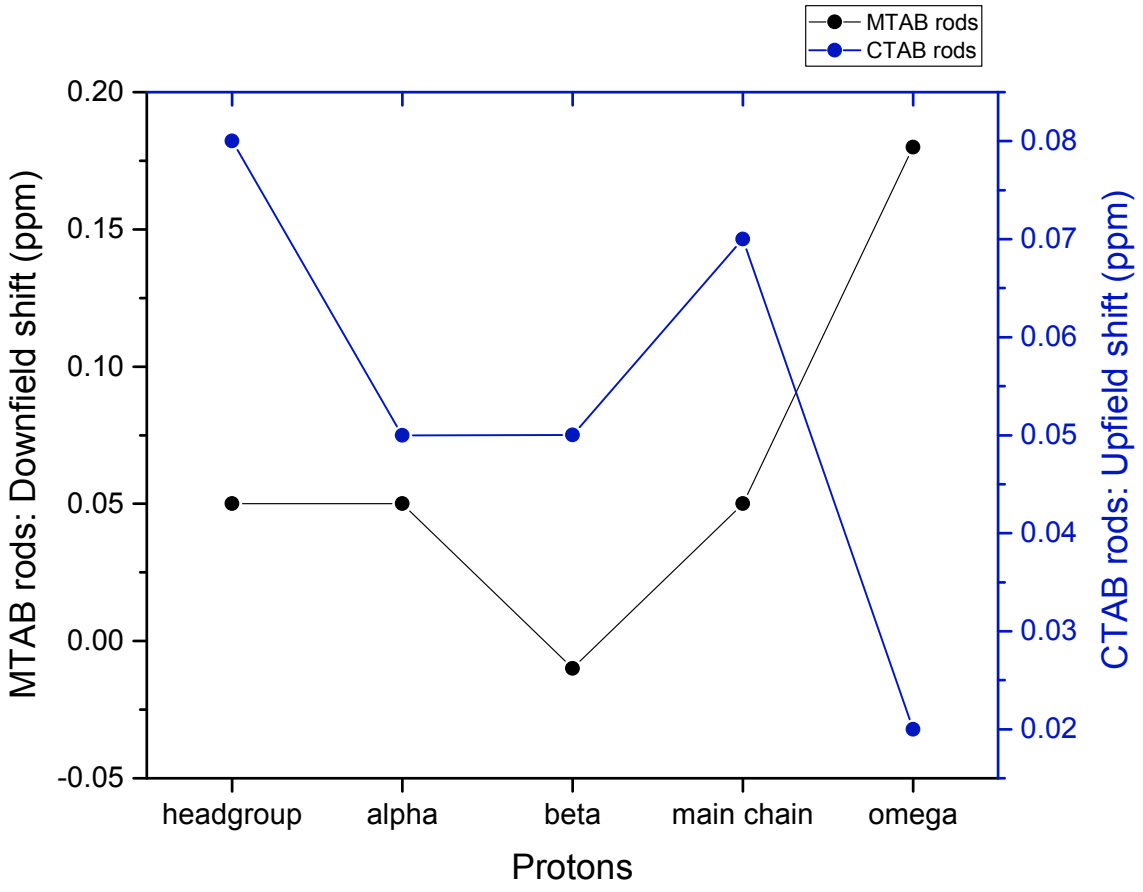

Figure 3.7 The absolute changes in chemical shift of MTAB or CTAB protons follow different trends with increasing distance from the headgroup.

The absolute frequency shift upon binding for each proton, by increasing distance from the headgroup, was graphed for MTAB and CTAB (Figure 3.7). MTAB shifts represent downfield shifts, whereas CTAB shifts indicate upfield shifts. For MTAB, the ψ (not shown in graph) and ω protons (those closest to the thiol linkage) shift the most downfield, by 0.09 and 0.18 ppm, respectively. The headgroup, α, and main chain protons experience a smaller downfield shift, by 0.05 ppm. The β proton, surprisingly, shifts upfield by 0.01 ppm. In CTAB, the headgroup protons shift the most upfield, by 0.08 ppm, followed by the main chain protons (0.07 ppm) and then α and β protons (0.05 ppm). The ω protons shift the least, by only 0.02 ppm. The difference in trends between the two capping agents can be explained by the protons' distance from the gold surface. Overall, it appears that the trend for frequency shift of MTAB protons correlates to

distance from the thiol, and thus the gold: the closer to the gold, the greater the shift. Likewise, CTAB protons' shift increases with proximity to the ammonium headgroup. However, this trend can be rationalized in two ways: 1) the inner leaflet of CTAB does indeed have observable NMR resonances, so we are observing protons close to the gold surface shift more; 2) the CTAB resonances arise from either both leaflets or the outer leaflet, and the formation of a CTAB-AgBr complex at the headgroup causes the dramatic shift of the headgroup, which tapers off with the number of bonds. Either way, it appears that the chemical environment of the CTAB headgroup changes the most upon binding; the ω proton moves from a micellar interior to a fairly similar bilayer interior, where it continues to be surrounded by other ω and aliphatic protons.

3.3.2 Splitting patterns

Bilayer

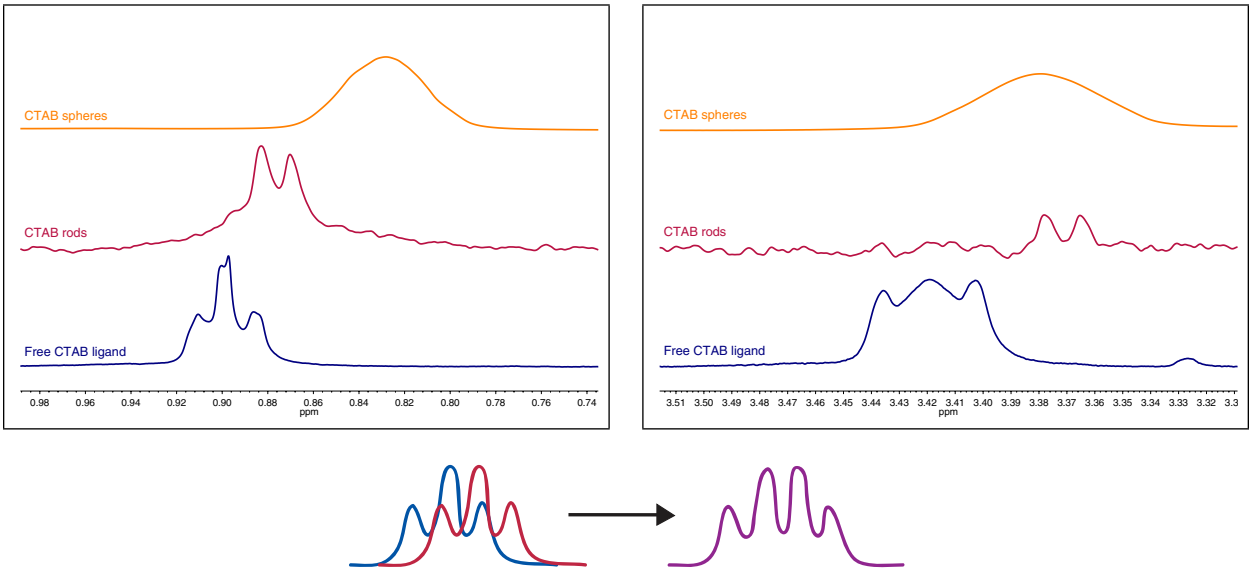

Figure 3.8 The splitting patterns for CTAB's ω protons (top, left) and α protons (top, right) appear to change from triplets, in the free ligand, to overlapping triplets, in the bound ligand. A schematic of overlapping triplets appears at bottom.

The splitting patterns of the α and ω protons (the only types of protons with distinctive splitting patterns) are very interesting and shed further insight into the bilayer structure (Figure 3.8). In both cases, the protons are triplets in the free CTAB spectrum but appear to be doublets or quadruplets in the rod spectrum. The chemical structure of CTAB has presumably not changed, so it is impossible for those protons to split into doublets or quadruplets. There is a more likely explanation: there are overlapping triplets, separated just enough from each other as to appear to have only two (or

four) peaks. Bimodal peaks have been observed in polydisperse nanoparticle samples, corresponding to two different sizes of particles, and thus, ligand environments.[93] Perhaps the overlapping triplets are a marker of two populations of CTAB: the inner or outer leaflets, or the longitudinal or transverse axes. Given that ω protons are implicated here but should not differ much between the inner and outer leaflets, it is more reasonable that bimodal resonances correspond to CTAB environments on the two axes: one tightly, and one loosely, packed.

Monolayer

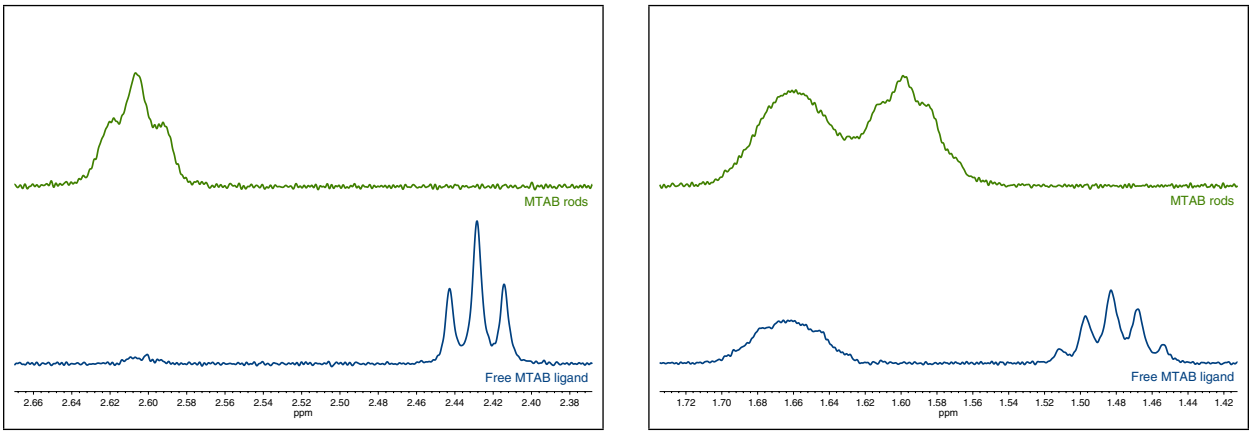

Figure 3.9 The splitting patterns for MTAB's ω protons (left) and β and ψ protons (right) appear the same in the free and bound ligands.

To test the validity of this hypothesis, splitting patterns of MTAB protons were examined. As expected, splitting did not change from the free to bound state in any MTAB protons (Figure 3.9). The ω protons, a triplet in the free ligand form, was still a triplet in bound form—a less-resolved, but unmistakable, triplet. The consistency in splitting was also observed for the multiplet ψ protons.

Discussion

These observations directly support our theory that CTAB rods have at least two separate ligand environments. A schematic of the ω protons on CTAB and MTAB rods is pictured in Figure 3.10. On a CTAB rod, ω protons can occupy a variety of chemically distinct environments: does the bimodality of the peaks correspond to the two bilayer leaflets, or to the two anisotropic axes? The case is less strong for bimodality arising from the two leaflets. Although the level of bilayer interdigitation is not expressly known, it is presumed from the thickness of the bilayer (analyzed by transmission electron microscopy and dynamic light scattering) that there is very little interdigitation, at least along the long axis. The ω protons in both the inner and outer leaflet, then, are in about the same environment. The α proton peak also

apppears to be bimodal, with overlapping triplets that must be similar in broadening and intensity for a doublet-like shape to emerge; however, α protons in the inner leaflet are extremely close to the gold surface and are expected to broaden significantly more than α protons in the outer leaflet. For these reasons, it is more likely that the anisotropic axes represent the two distinct ligand environments, with the ω bimodal peak arising from the densely-packed ω protons along the long axis and the diffuse ω protons at the transverse axis. In the MTAB monolayer, the ω protons are all three bonds away from the gold surface, a uniform chemical environment for all, so bimodality is not observed.

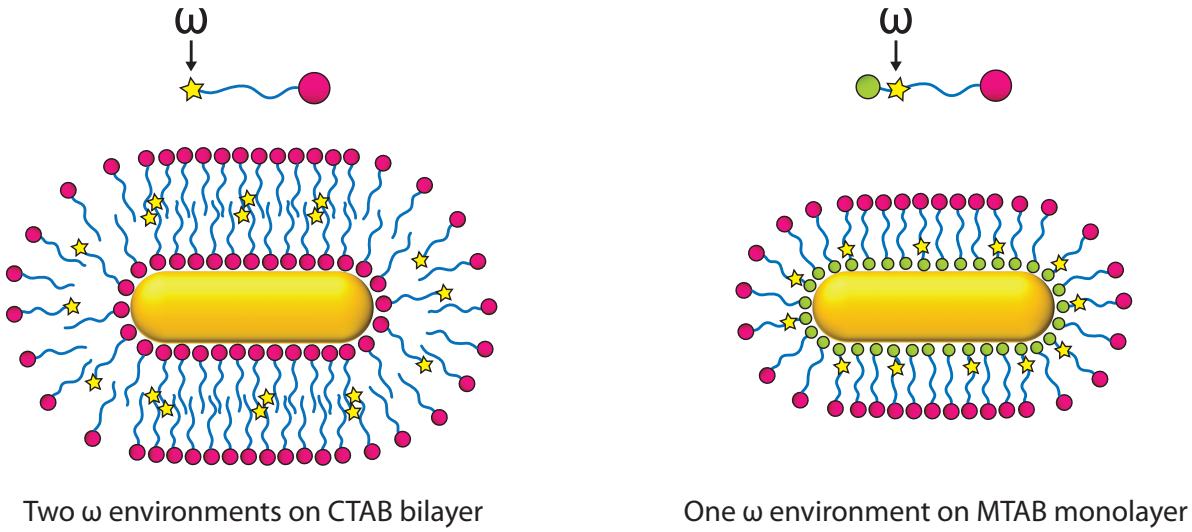

Figure 3.10 The CTAB bilayer appears to have two ω proton chemical environments, whereas the MTAB bilayer appears to have only one. We believe that the two CTAB ω proton environments arise from the tightly-packed hydrophobic tails along the long axes, and the loosely-associated tails at the transverse axes. MTAB's ω protons are all presumed to be very close to the gold surface.

If ligands are more mobile at the transverse ends, MTAB rods should also feature two distinct environments: the side-by-side ordered monolayer of molecules along the long axis and the molecules at the curved ends. The MTAB headgroup proton peak does not obviously appear bimodal, although the singlet is broadened; the chemical environment may not differ enough at the two axes to resolve into two frequencies. However, the main chain peak shape in the rods notably diverges from that of the free ligand, with three apexes instead of two; this may suggest the presence of two chemical environments.

3.3.3 Line broadening

Line broadening of resonances can indicate a) proximity of the protons to the gold surface, b) a more ordered, less mobile conformation, or c) a heterogeneous population of protons (averaging of resonances). Linewidths were compared

between free CTAB molecules and CTAB rods (Figure 3.11).

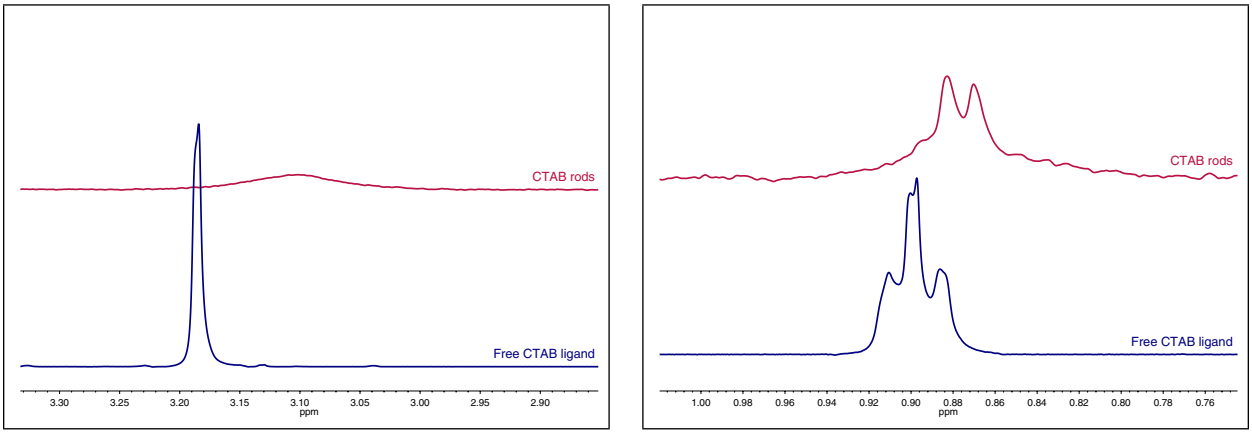

Figure 3.11 CTAB's headgroup protons (left) experience significant line broadening after attachment to gold, whereas its ω protons (right) broaden much less.

It is important to note that for the spectrum of free CTAB molecules, at the concentration measured, CTAB is actually in a micellar structure, with headgroup protons facing solution and ω protons inside. The headgroup protons feature significant line broadening. Because the proximal and outer headgroup protons are in very different environments, the broadening may be due to these distinct two populations. Additionally, the proximal headgroups—which should be quite broad—may contribute to the broadening, or they may be so broad as to be smeared into the baseline. Alternatively, a different way to consider the CTAB heterogeneity is between the longitudinal and transverse axis molecules. The outer headgroup protons, being the most mobile of any protons in the system, are probably most sensitive to differences in the bilayer conformation. Outer headgroups along the longitudinal axis are more closely packed, whereas those at the transverse axis are likely more mobile because of the increased radius of curvature there. It is reasonable to think that those different chemical environments can broaden the linewidth significantly; in the free CTAB (micellar) structure, there is essentially only one population of headgroups. The headgroup broadening is especially dramatic when compared to the ω protons, which show very little broadening. This finding is consistent with the ω protons neighboring each other in a bilayer, a fairly homogenous environment. Although the ω protons are immobilized in a bilayer, they are not necessarily more confined than they would be in the free CTAB micelles; the linewidths are comparable. Solid-state NMR studies have shown that for CTAB in an intercalated bilayer, the tails remain relatively mobile.[117]

3.3.4 Integrations

Integrations of the resonances are difficult to interpret for particle spectra, because some linewidths may be broadened into the baseline. This was true for both MTAB and CTAB rods: integration values of bound ligands did not match calculated values, whereas integrations were quantitative for free ligands.

Regardless, a variable temperature study was performed on CTAB rods and the spectra integrated to determine whether temperature could induce mobility changes. In particular, we wondered whether cooling the sample would "freeze" the CTAB in their respective populations. The temperature of the NMR samples was varied from 10-40°C (all other studies were done at 25°C); unfortunately, the D_2O solvent prevented lower temperatures. The lineshapes and relative chemical shifts (referenced to a signal peak) do not change much within this temperature range, but a large effect on the proton integrations was observed (Figure 3.12).

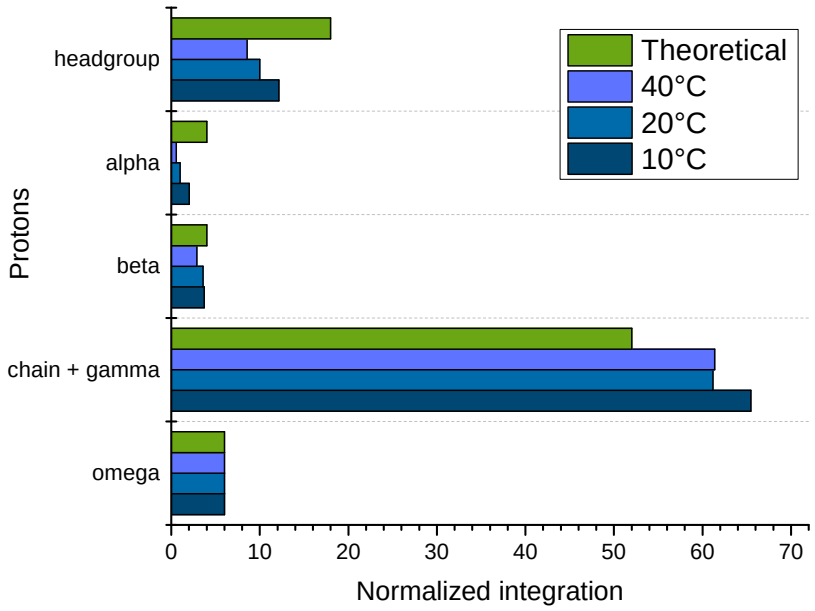

Figure 3.12 Integrations of CTAB rod protons in temperatures ranging from 10 to 40°C.

The integrations were normalized to the ω protons in two CTAB molecules—6 protons—in order to model the structure of the CTAB bilayer. In general, the integrations decrease with higher temperature. This puzzling result can probably be attributed to the fact that molecular tumbling speeds up at a higher temperature, so T_1 relaxation is longer. If the T_1 value chosen for the experiment was too short, the integrations at the higher temperature will be less accurate and farther from the theoretical value.

There was also a trend that the integrations for the headgroup and α protons are much smaller than the theoretical value at all studied temperatures; in contrast, the main chain and γ protons are close to, or even larger than, the theoretical. One potential explanation is that the head group and α protons are in two very heterogeneous environments in the CTAB bilayer: at the gold surface and at the outer interface. The protons close to the gold surface are likely to be significantly broadened and disappear into the baseline, reducing the integration. Another factor to consider is that the outer protons have a longer T_1 than their inner equivalents, so their integrations may not be as accurate if the chosen T_1 is too short. This may skew the headgroup and α integrations.

3.4 Markers of shape anisotropy

The ^{1}H NMR spectrum of CTAB rods features three unexpected sharp peaks at approximately 1.1, 1.8 and 2.1 ppm, as well as an occasional small sharp peak in the aromatic region. The obvious contenders—synthetic byproducts, typical impurities, and excess free CTAB ligand—were all ruled out. The peaks did not change intensity with increasing rounds of centrifugation, up to three times (after which the rods are unstable), nor did any of them appear to any degree in the spectrum of supernatant from the first round of centrifugation; only CTAB peaks were present in the supernatant (Figure 3.13).

The fact that the peaks are not removed by purification suggests that they are not starting materials or byproducts of the reaction, but rather that they belong to a species that is heavy enough to pellet during centrifugation or are associated with the rods. The sharp peak at 1.1 ppm does not have the same chemical shift as that of the main chain of free CTAB, which is closer to 1.2 ppm, suggesting that it does not arise from free CTAB in solution, and obviously the downfield shifts cannot be explained by free CTAB (Figure 3.13). The peaks were conspicuously absent from the NMR spectrum of CTAB spheres, in which only the CTAB resonances appear (Figure 3.14). Because the synthesis of rods and spheres use the same starting materials, except for $AgNO_3$, which is not used for spheres, the distinction in their spectra supports the idea that the peaks are not synthetic byproducts. The primary distinguishing features of rods over spheres are the $AgNO_3$ starting material and shape anisotropy. Is it possible that the sharp peaks are markers of shape anisotropy and arise from variations in reactive sites along the geometry of a rod, much like the reports of NMR signals for distinct binding sites in spheres (*vide supra*)?

The linewidths of the mysterious peaks are narrower than the bound CTAB peaks, a telling sign that they may be bound to a region with looser packing and higher ligand mobility. They might also be somewhat detached from the gold surface, as in a species or counterion that is loosely associated with the particle, with a bond strong enough to

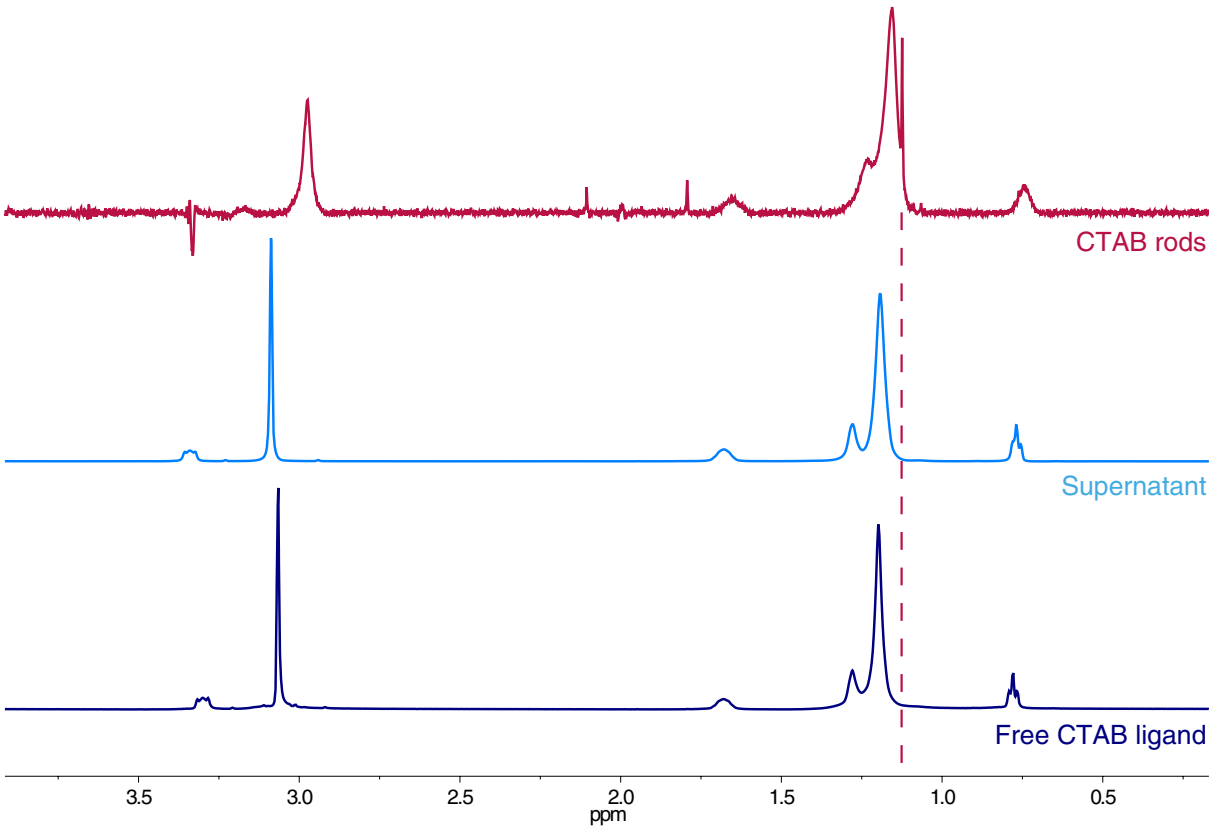

Figure 3.13 ^{1}H NMR of CTAB rods, supernatant collected from centrifuged CTAB rods, and free CTAB ligand. The sharp peaks observed in CTAB rods cannot be assigned to synthetic byproducts or excess ligand, because they do not disappear with increasing purification and are not observed in the supernatant.

prevent it from being centrifuged away, but weak enough to appear closer in likeness to a free ligand.

The unidentified peak at 1.1 ppm has a much larger integral value than the other two unidentified peaks, suggesting that the species resonating at that frequency contains many equivalent protons, or that the concentration of the species at that frequency is higher than the concentration of the species resonating at 1.8 or 2.1 ppm. In other words, the protons at 1.1 ppm could belong to a long aliphatic chain, or to an abundant methyl group. One possibility is that these protons belong to CTAB attached in a quasi-monolayer on the ends of rods: the bilayer is thought to be less organized, even fluxional, at the ends. If the aliphatic chains are unfavorably close to the water interface there, they may resonate at a different chemical shift. The slightly faster diffusion rate could be attributed to the local mobility of ligands at the ends.

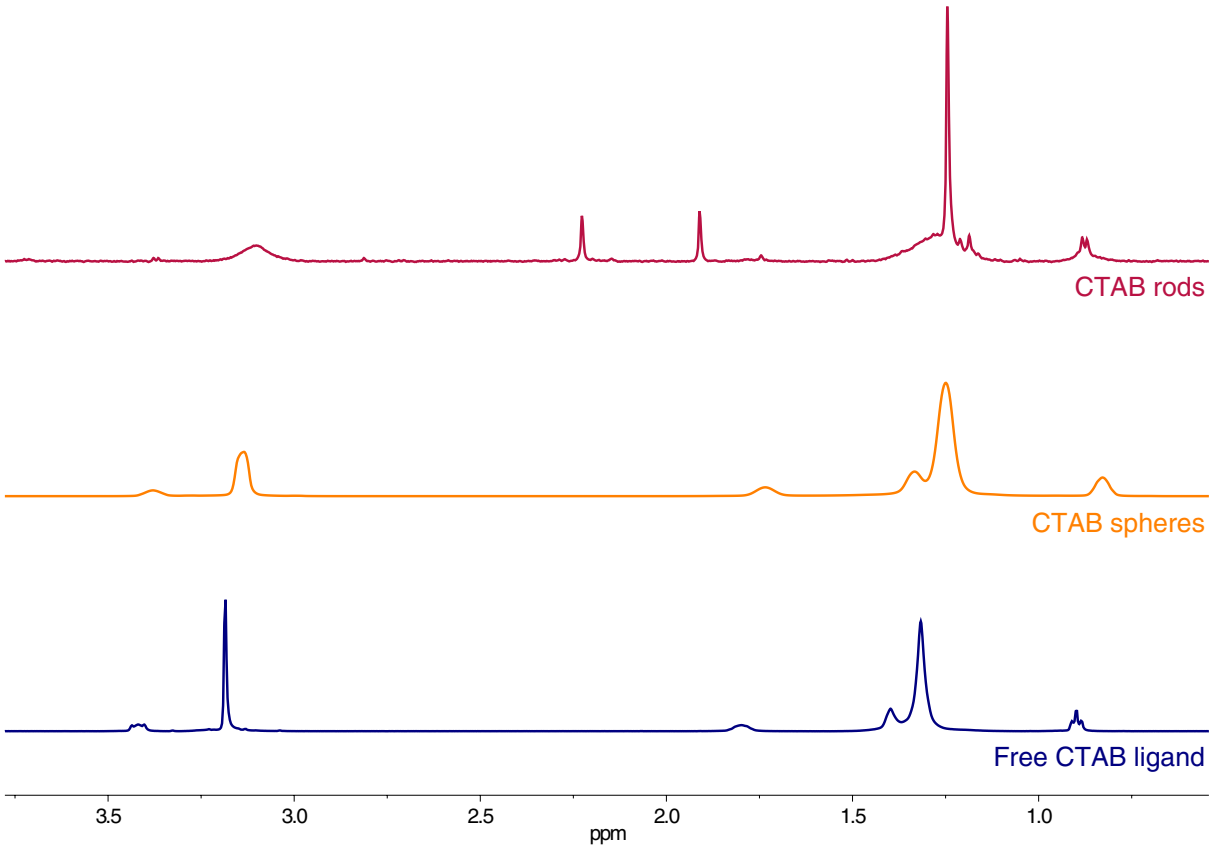

Figure 3.14 ^{1}H NMR of CTAB rods, CTAB spheres, and free CTAB ligand. The sharp peaks are observed only in rods, not in spheres. Could they be an indicator of anisotropy and differences in chemical environments?

3.4.1 Two-dimensional NMR studies

Correlation spectroscopy (COSY) and total correlation spectroscopy (TOCSY)

Both COSY and TOCSY experiments were performed on CTAB rods to identify through-bond correlations between protons on neighboring carbon atoms. Correlations between the aliphatic CTAB protons were expected. If the unidentified sharp peaks are part of the same spin system, TOCSY should identify them; because the peaks are singlets, it is unlikely that they are on neighboring carbon atoms and correlate by COSY.

In the COSY spectrum, the only clear cross-peaks are between the unidentified peaks at 2.2 and 6.8 ppm, which indicates that those protons are on neighboring carbon atoms; the other visible cross-peaks around 5 ppm are artifacts from the suppressed water signal. The TOCSY spectrum supports the correlation between the unidentified peaks. The spectrum also shows a spin-coupled system between the ω and main chain protons in the region between 0.8 and 1.2

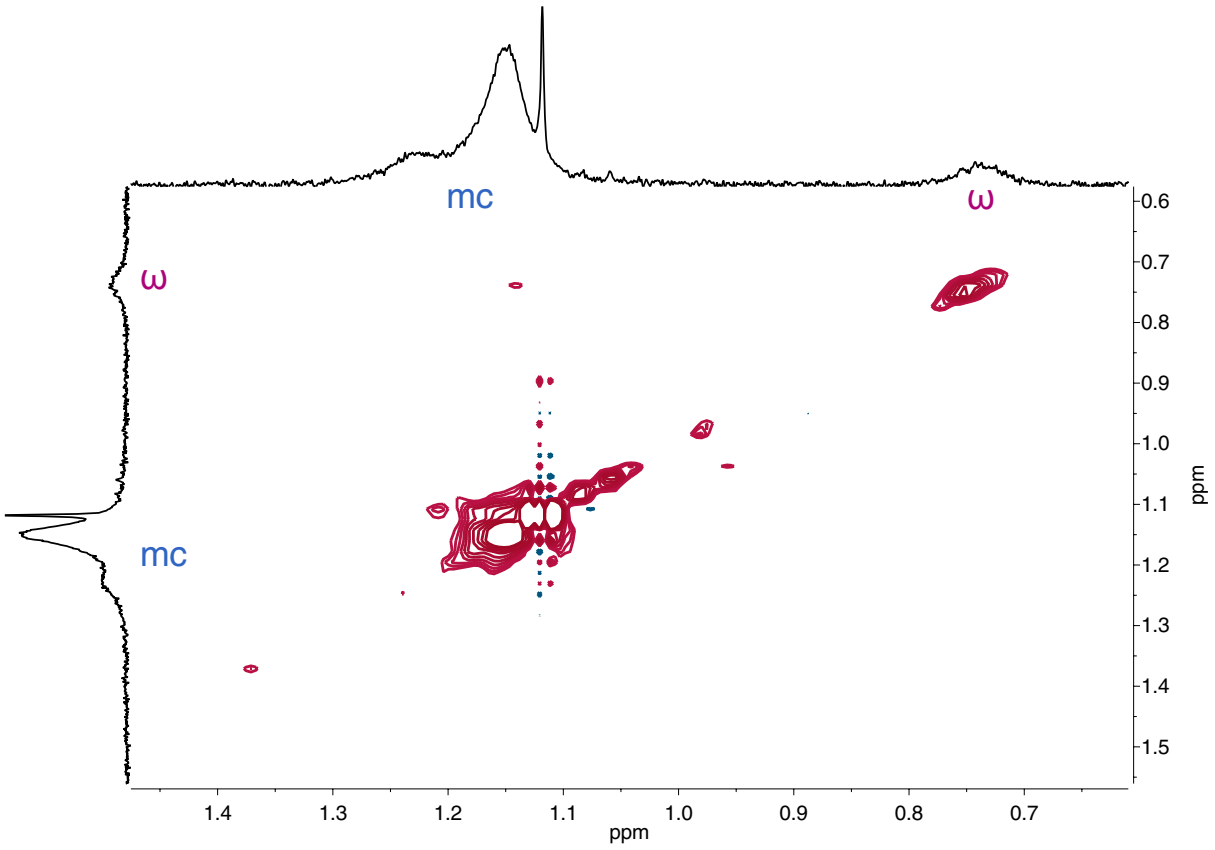

Figure 3.15 ^{1}H-^{1}H TOCSY NMR of CTAB rods. Very weak correlations between the main chain and ω protons are observed.

ppm, as expected, although the correlations are quite weak (Figure 3.15). The α and β proton signals are likely too weak to appear in the coupled system. There are no visible cross-peaks between the CTAB peaks and the unidentified peaks, further suggesting that they are not part of the same species or, at least, spin-coupled network.

It is very possible that the CTAB bilayer is too fluxional or convoluted to produce clear correlations. Indeed, the TOCSY spectrum of MTAB rods is well-resolved, with cross-peaks observed for all protons except the headgroup protons, which are isolated from the main spin system (Figure 3.16). The clear spectrum indicates that two-dimensional NMR techniques can accurately render ligands on even large particles with shape anisotropy. The difference in resolution between MTAB rods and CTAB rods suggests, not surprisingly, that ligands in a monolayer are more easily elucidated than those in a bilayer. It also supports the recent finding that more restricted, static ligands give more intense correlation signals: the motion of MTAB, bound covalently in a monolayer, is probably more restricted than that of CTAB, which is in constant dynamic exchange with its free form in solution.[98] MTAB rods are significantly more stable to multiple rounds of centrifugation and less toxic to cells, because the thiol molecules do not easily desorb.[118]

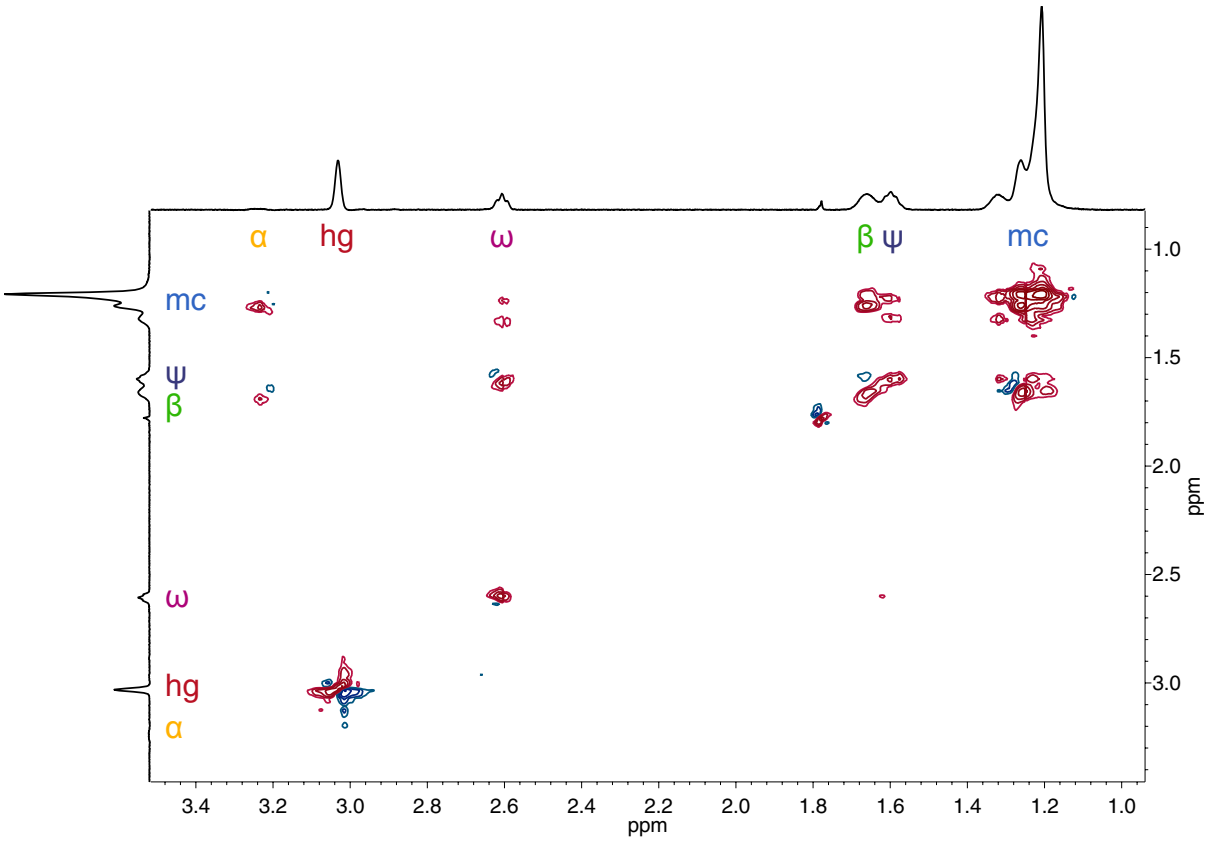

Figure 3.16 ^{1}H-^{1}H TOCSY NMR of MTAB rods. Strong correlations are observed for all the protons in the aliphatic spin system, and not for the headgroup, as expected.

Nuclear Overhauser effect spectroscopy (NOESY)

NOESY identifies though-space coupling of nuclei within 0.5 nm of each other, so we hoped to develop a deeper understanding of the spatial morphology of the CTAB bilayer, through characteristics such as degree of interdigitation and molecular spacing.

The NOESY spectrum was phased such that the cross-peaks are opposite in sign to the diagonal, which is standard for small molecules; however, because CTAB molecules are attached to large, bulky nanoparticles, it is possible that the cross-peaks and diagonal should be phased to the same sign. The spectrum is littered with cross-peak signals that are difficult to discern from artifacts, but there is a distinct cross-peak pattern in the CTAB ω and main chain region. This may suggest that these protons are within 0.5 nm of each other, perhaps through interdigitation, although the cross-peaks could also be through-bond artifacts. Overall, it appears it is too difficult to resolve the NOESY spectra of CTAB rods.

3.4.2 Diffusion-ordered spectroscopy (DOSY)

Bilayer

Diffusion-ordered spectroscopy (DOSY) correlates the diffusion coefficients of species with their chemical shifts, so it is a convenient technique for separating mixtures of species. We performed ^{1}H DOSY NMR on CTAB rods in order to determine whether the unidentified sharp peaks and the CTAB are attached to the same particles. Taking it a step further, we were interested in whether the diffusion constants of the CTAB at the fluxional ends and the packed sides were distinct enough to observe by DOSY. Because the diffusion rate of a nucleus is a function of the viscosity of its local environment, it is reasonable to think that the more loosely-bound CTAB would have a slightly faster diffusion rate. The rotational tumbling differences between ligands parallel to the long axis (on the ends) and those parallel to the short axis (on the sides) may also result in distinguishable differences between the diffusion coefficients. Therefore, DOSY may allow us to differentiate between chemical shifts arising from ligands at specific regions of the rod.

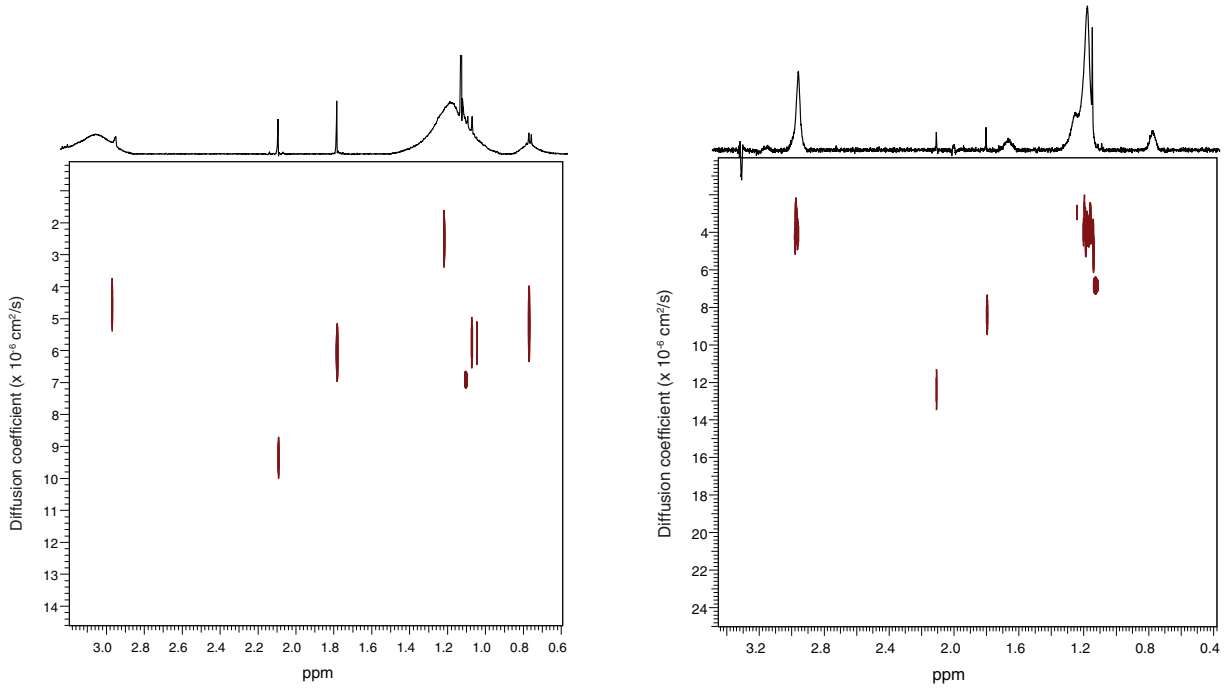

Figure 3.17 ^{1}H DOSY NMR of two samples of CTAB rods, A (left) and B (right). CTAB protons diffuse at different rates. The sharp peaks have distinct diffusion coefficients, indicating that they are not the same species or at unique binding sites.

As shown in the diffusion transforms of two different rod batches, A and B, the nuclei vary widely in their diffusion coefficients (Figure 3.17). For rods A, the slowest-diffusing species (2.5 x 10^{-6} cm^2/s) appears to be the bulk main chain signal. The headgroup diffuses at a rate similar to the ω protons (4.6 x 10^{-6} cm^2/s and 5.2 x 10^{-6} cm^2/s, respectively).

A couple of closely-resolved sharp peaks buried in the broad main chain peak diffuse slightly more quickly (5.8 x 10^{-6} cm^2/s) and are close in diffusion rate to the sharp peak at 1.8 ppm (6.1 x 10^{-6} cm^2/s). The sharp peak at 1.1 ppm diffuses noticeably more quickly (6.9 x 10^{-6} cm^2/s). Finally, the sharp peak at 2.1 ppm diffuses at a significantly faster rate than all the other peaks (9.4 x 10^{-6} cm^2/s). The trends in diffusion coefficients for rods B are similar, although only the high-integral CTAB peaks (main chain and headgroup protons) and all three sharp upfield peaks could be resolved. The main chain and headgroup protons, respectively, had the same diffusion coefficient (4 x 10^{-6} cm^2/s). The unidentified peak at 1.1 ppm diffused slightly more quickly, at a rate of 7 x 10^{-6} cm^2/s. The unidentified peak at 1.8 ppm had a diffusion coefficient of 8 x 10^{-6} cm^2/s, and the unidentified peak at 2.1 ppm had the fastest diffusion rate, at 12 x 10^{-6} cm^2/s (or 1 x 10^{-5} cm^2/s) (Table 3.1).

Table 3.1 Diffusion coefficients of the protons of CTAB rods, as measured by DOSY NMR.

	Rods A		Rods B	
Proton type	δ (ppm)	D (x 10^{-6} $cm^2 \cdot s^{-1}$)	δ (ppm)	D (x 10^{-6} $cm^2 \cdot s^{-1}$)
Omega	0.74	5.2	0.74	not observed
Unidentified	1.05	5.8	not observed	-
Unidentified	1.08	5.8	not observed	-
Unidentified	1.11	6.9	1.12	6.8
Main chain	1.17	2.5	1.16, 1.23	3.0 to 5.2
Beta	1.61	not resolved	1.65	not resolved
Unidentified	1.78	6.1	1.79	8.3
Unidentified	2.09	9.4	2.11	12.5
Headgroup	2.96	4.6	2.97	3.6
Alpha	3.23	not resolved	3.17	not resolved

These diffusion data are interesting on several levels. They validate the theory that DOSY can resolve diffusion coefficients of ligands bound to particles, and that the diffusion rates of different nuclei on the same ligand may diverge based on the local viscosity of the nucleus's environment. Of the three observable CTAB peaks, the bulk main chain diffuses the most slowly, perhaps because it is well-ordered. However, the entire main chain region, from approximately 1.0 - 1.5 ppm, is actually a cluster of distinct diffusion rates; two small sharp peaks (just upfield of the giant sharp peak at 1.1 ppm) diffuse more than twice as quickly as the bulk main chain, and the giant peak at 1.1 ppm diffuses almost three times as quickly. Could these fast diffusing nuclei be assigned to main chain protons on the end axes, where the CTAB bilayer is fluxional and mobile? The headgroup protons and ω protons diffuse more quickly than the bulk main chain, indicative of their relative mobility. The solvent-facing headgroups, more likely probed by NMR than gold-bound headgroups, are expected to be fairly mobile. The ω protons, especially at the fluxional ends, may also be flexible; as mentioned before, solid-state NMR has shown that CTAB tails in a bilayer are fairly mobile.[117] Intriguing, however, is that the diffusion rates of the sharp peaks at 1.8 and 2.1 ppm unequivocally differ. They are not part of the same

species, as would be expected for a free-floating small molecule that gives rise to both peaks. If they are in fact the same molecule, they must be in very different chemical environments to produce such distinct frequencies and diffusion constants. Further, the diffusion rate of the peak at 1.8 ppm is surprisingly close to that of the sharp main chain region peaks, as well as the headgroup and ω peaks; if it were truly a free molecular impurity, it would diffuse much more quickly than ligands attached to the particle.

Monolayer

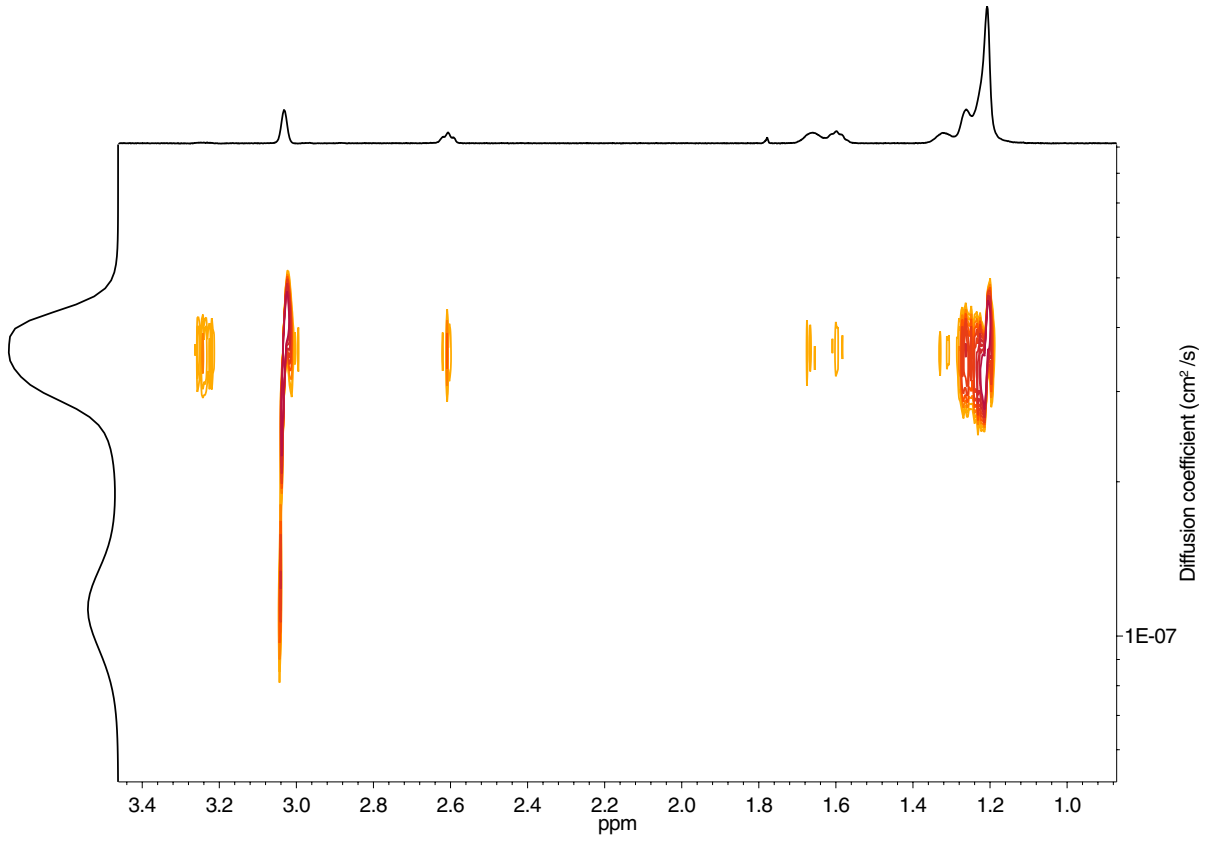

Figure 3.18 ^{1}H DOSY NMR of MTAB rods. All protons diffuse at the same rate, but the headgroup protons are split into a second population that diffuses at one-third of the rate of the other protons.

An entirely different set of trends was observed in the DOSY spectrum of MTAB rods (Figure 3.18). All 1-D proton peaks were able to be resolved in the DOSY transform, and all protons diffused at the same rate (3.5×10^{-7} cm²/s)—with the exception of the headgroup protons, which had two populations with distinct diffusion coefficients (one at 3.5×10^{-7} cm²/s, like the other protons, and one at 1.2×10^{-7} cm²/s). This second population diffuses nearly three times as slowly as the bulk population. The headgroup protons are at the water interface and are likely to be the most mobile protons,

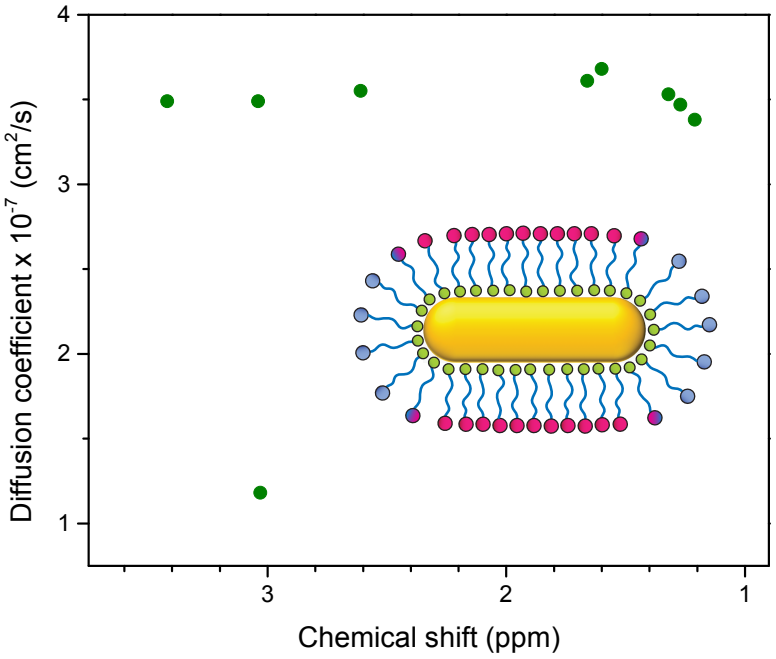

Figure 3.19 Diffusion coefficients of the protons of MTAB rods, as measured by DOSY NMR. The headgroup protons diffuse at two different rates, which can potentially be explained by distinct ligand environments at the rods' two axes, colored blue and pink in the schematic.

especially at the rods' ends, where they presumably "fan out" into solution. Therefore, they are most likely to experience disparate chemical environments at the rods' sides and ends (Figure 3.19). This intriguing data suggests that DOSY can indeed identify ligands at specific regions of a shape-anisotropic particle on the basis of their diffusion coefficients.

3.4.3 T_2 relaxation rates

The T_2 relaxation values of each CTAB nucleus were determined to provide further insight into their local environments (Table 3.2). The relaxation rate is determined by molecular motions that cause fluctuations in the local magnetic field experienced by the nucleus, and thus how quickly the spins lose phase coherence. The slower the molecular tumbling and more crowded the electronic environment is, the spin experiences more intense (and more anisotropic) field fluctuations, leading to rapid relaxation. T_2 values for ligands bound to particles have been found to get shorter with closer distance to the particle surface. T_2 values for the rod spectrum were calculated by the relationship:

$$T_2 = \frac{1}{\pi LWHH} \tag{3.5}$$

$LWHH$: linewidth at half-height of the resonance peak

Table 3.2 Calculated T_2 values of the protons of CTAB rods.

Proton type	δ (ppm)	T_2 (ms)	Relative tumbling rate
Omega	0.74	26	moderate
Unidentified	1.12	79	fast
Main chain	1.19	4.0	very slow
Unidentified	1.79	95	very fast
Unidentified	2.11	95	very fast
Headgroup	2.97	7.7	slow

3.4.4 Anisotropic reactivity

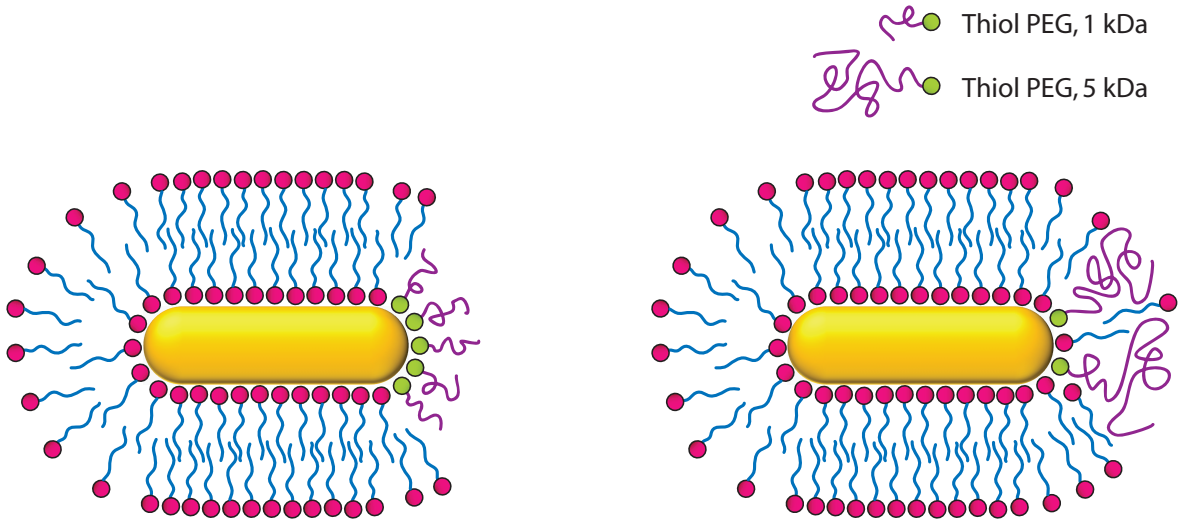

Figure 3.20 Smaller thiol PEG (1 kDa) is theorized to more completely displace the CTAB bilayer at the rod ends, whereas a bulkier 5 kDa thiol PEG may not remove all the CTAB.

The peaks with fast diffusion and relaxation rates may arise from ligands at the rods' ends, which are reactive hotspots. If this is the case, these ligands should be easily displaced by new ligands, resulting in a change in or complete disappearance in the original sharp peaks. Thiolated poly(ethylene glycol) (PEG) has been shown to first select for the ends of gold rods, permitting further anisotropic functionalization.[40]

Low equivalents of a thiolated PEG with a molecular weight of either 1 kDa or 5 kDa were added to CTAB rods, allowed to react for 24 hours, and centrifuged. The changes in the NMR spectra were in line with our reactive hotspot theory. Whereas the peak at 2.1 ppm did not appear to change, the integration of the peak at 1.8 ppm decreased after

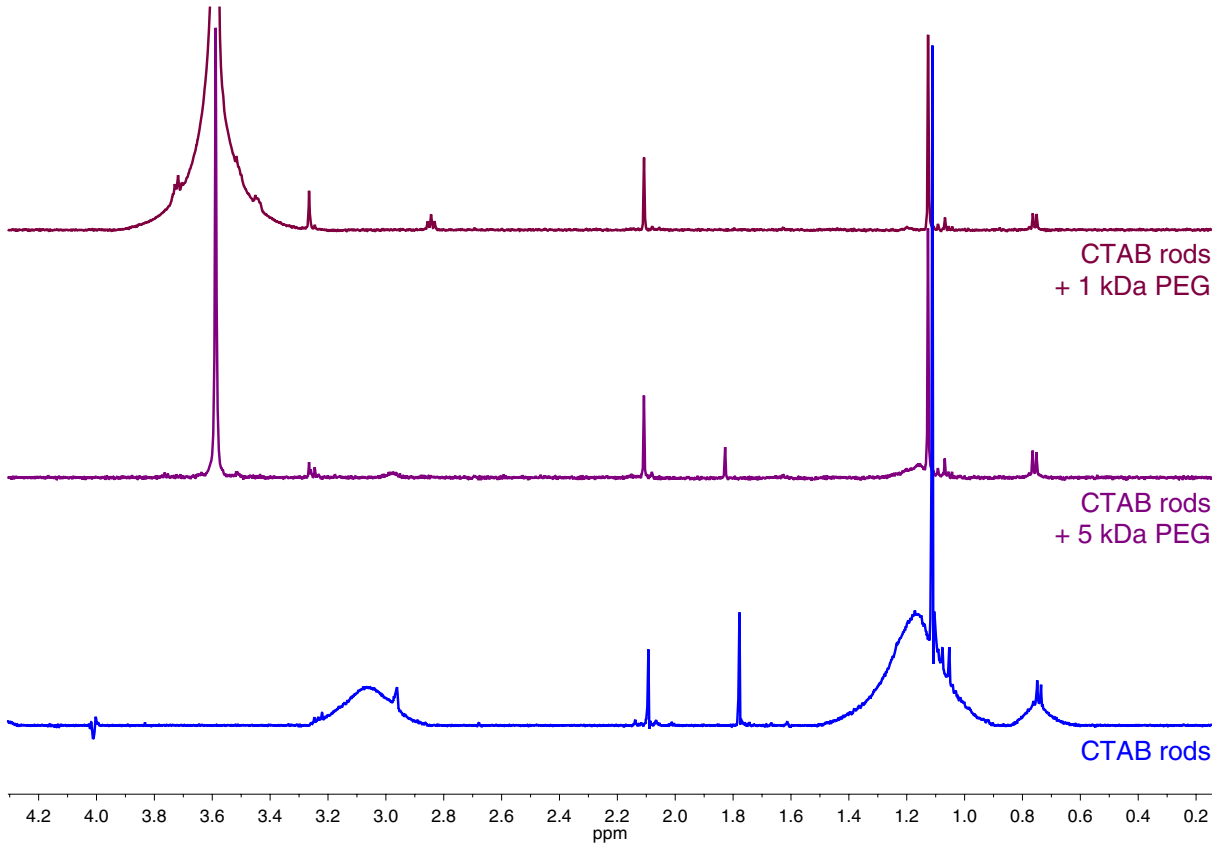

Figure 3.21 ^{1}H NMR of CTAB rods, and CTAB rods reacted with either 1 kDa or 5 kDa thiol PEG. The upfield sharp peak decreases in intensity after introduction of 5 kDa PEG, whereas it disappears completely with 1 kDa PEG. The downfield sharp peak does not markedly change in intensity.

addition of 5 kDa PEG (the relative integrals between peaks at 2.1 and 1.8 ppm dropped from 1:1.5 to 1:0.3), and disappeared entirely with 1 kDa PEG (Figure 3.21).

Reaction monitoring of the ligand exchange with 1 kDa PEG over the first 10 hours showed that the high-field resonance shifted downfield over time, from 1.86 to 1.89 ppm (Figure 3.22). The peak at 2.1 ppm had no such shift in frequency. Clearly, addition of PEG causes a change in the chemical environment of the shifting peak. This environmental change could arise from PEG binding spatially close to the species in question, or gradual release of the species from the gold surface. The disappearance of the peak after purification supports both of these mechanisms. If PEG prefers to bind to the ends of the rods, and the peak at 1.8 ppm gradually shifts in frequency before disappearing entirely, it follows that the peak at 1.8 is displaced by the PEG—and that it was probably originally located at the rods' ends. In addition, it is evident that the peaks at 1.8 and 2.1 ppm are not from a single species. Perhaps both peaks can be assigned to the same molecule at two different binding sites, one at the reactive ends that is easily displaced (1.8 ppm)

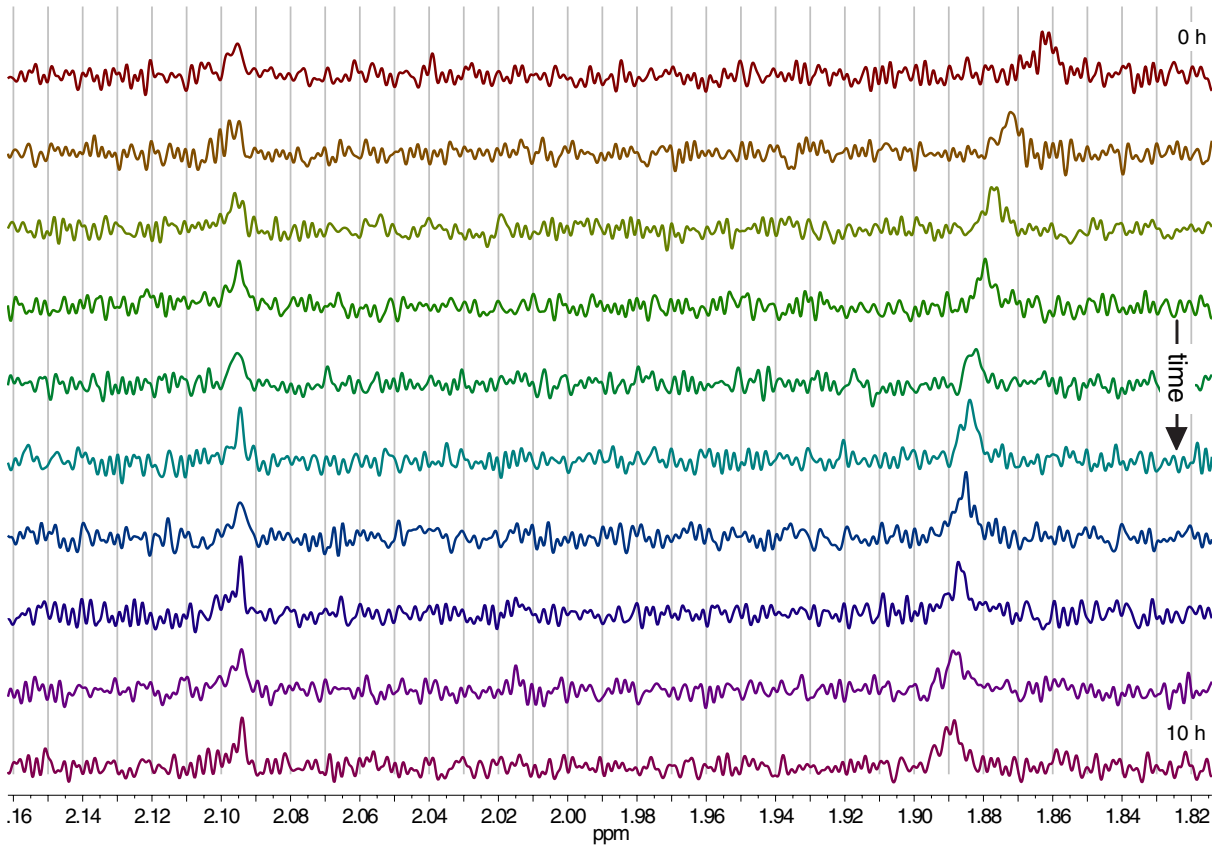

Figure 3.22 ^{1}H NMR reaction monitoring of 1 kDa thiol PEG and CTAB rods over 10 hours. The sharp peak at 1.86 ppm shifts downfield as the reaction progresses, suggesting a gradual change in its local chemical environment.

and one elsewhere on the rod where it is more impervious to replacement (2.1 ppm). The lower molecular weight PEG was more effective at displacement than its larger analog, which can be explained by how difficult it is for large, bulky PEG (which has only a single thiol group) to pierce the CTAB bilayer and access the gold surface. The small molecular weight PEG can easily permeate the bilayer and kick off ligands.

A similar set of experiments was performed to confirm the effect of PEG molecular weight on displacement efficiency. 5 kDa and 10 kDa thiolated PEG, and 10 kDa disulfide PEG (which was analyzed by Ellman's assay to have approximately 1% thiol, presumably 5 kDa) were added to CTAB rods, with the expectation that the larger PEG species would not only preferentially bind to the ends, but would also have more difficulty in replacing CTAB on the tightly-packed long axis. NMR spectra of the PEG-functionalized rods were analyzed for residual CTAB resonances, which would indicate inefficient displacement. Indeed, only the spectrum of rods functionalized with the 10 kDa thiol PEG unambiguously indicated leftover CTAB, with broad and prominent peaks around 1.1 ppm (main chain) and 3.0 (headgroup). As expected, the 5 kDa thiol PEG and the disulfide PEG (which may attach as the 1% of 5 kDa thiol present)

seemed to displace most, if not all, of the CTAB.

3.4.5 Aging

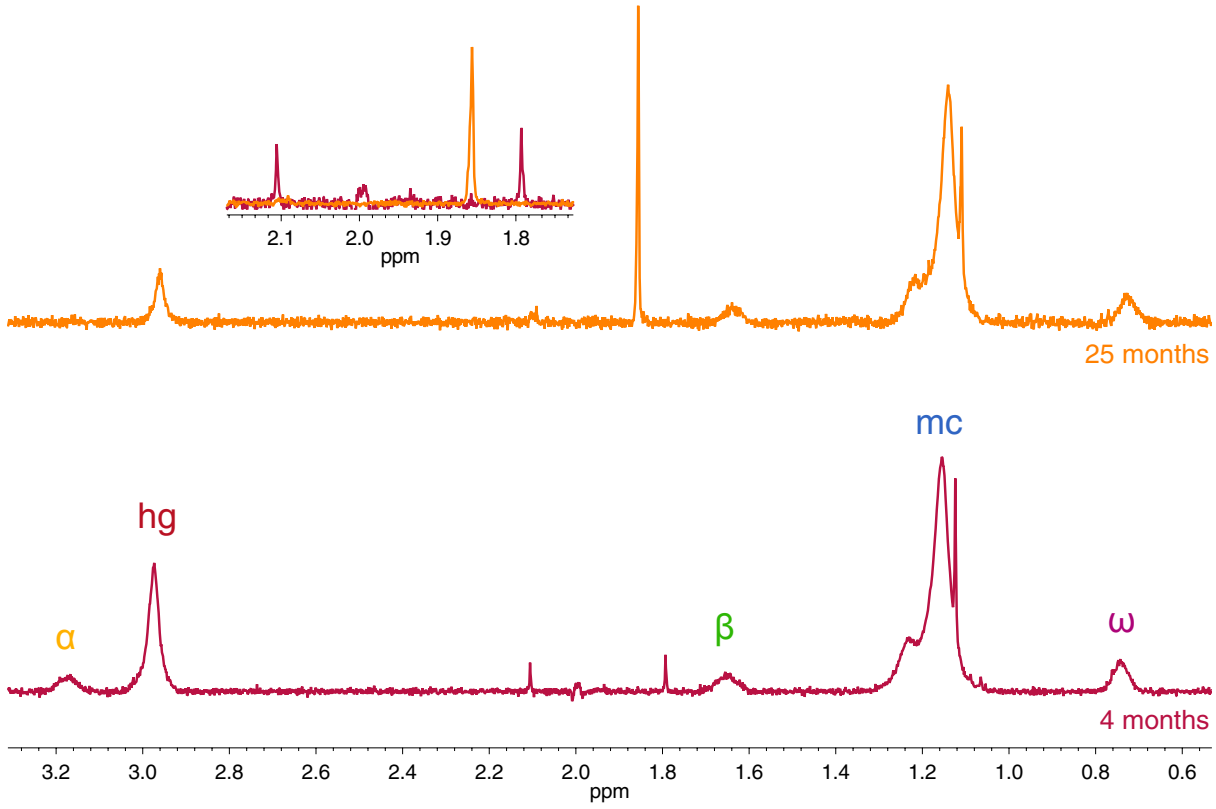

Figure 3.23 ^{1}H NMR of the same sample of CTAB rods 4 months and 25 months after synthesis. Obvious spectral changes occur with aging: the two sharp peaks become one at a new middle frequency, and integrations of headgroup and α protons decrease significantly in intensity.

The process of aging appears to change the character of the surface of CTAB rods. The proton NMR spectrum of CTAB rods was taken at 4 months after synthesis, and then again 25 months after synthesis. (The same sample was used, and the rods were not removed from the tube between experiments.) After 25 months, the integration ratios between the CTAB resonances are significantly different from the 4-month spectrum (Table 3.3). Integrations were measured relative to the main chain peak (normalized at 1). The ω protons remained at the same relative integration value (0.08). The β proton integration was 2/3 of its original (0.06 to 0.04), and the α proton resonance was not observed at all (0.05 to 0.0). The headgroup protons had an integration at only 1/3 the value of the original (0.28 to 0.10).

Table 3.3 Integrations for CTAB protons at 4 months and 25 months after synthesis. All integrations were normalized to the main chain peak, which was set at 1.00.

Proton type	δ (ppm)	Integration (4 mo.)	Integration (25 mo.)	% Integration of original
ω	0.74	0.08	0.08	100
Main chain	1.19	1.00	1.00	100
β	1.65	0.06	0.04	67
Headgroup	2.97	0.28	0.10	36
α	3.17	0.05	0.00	0

No longer present were the two sharp peaks at 1.79 and 2.11 ppm; they were replaced by one single resonance at a new frequency of 1.86 ppm. Two primary possibilities exist for the identity of this single peak. In one possibility, the two peaks have coalesced, suggesting that they are the same chemical species; in this case the two peaks would arise from two distinct chemical environments, or from exchange that is very slow on the NMR timescale. Coalescence of the two peaks into one would indicate the merging of the two environments, or now-rapid chemical exchange. The other possibility is that one of the peaks has disappeared, and the other has shifted in frequency.

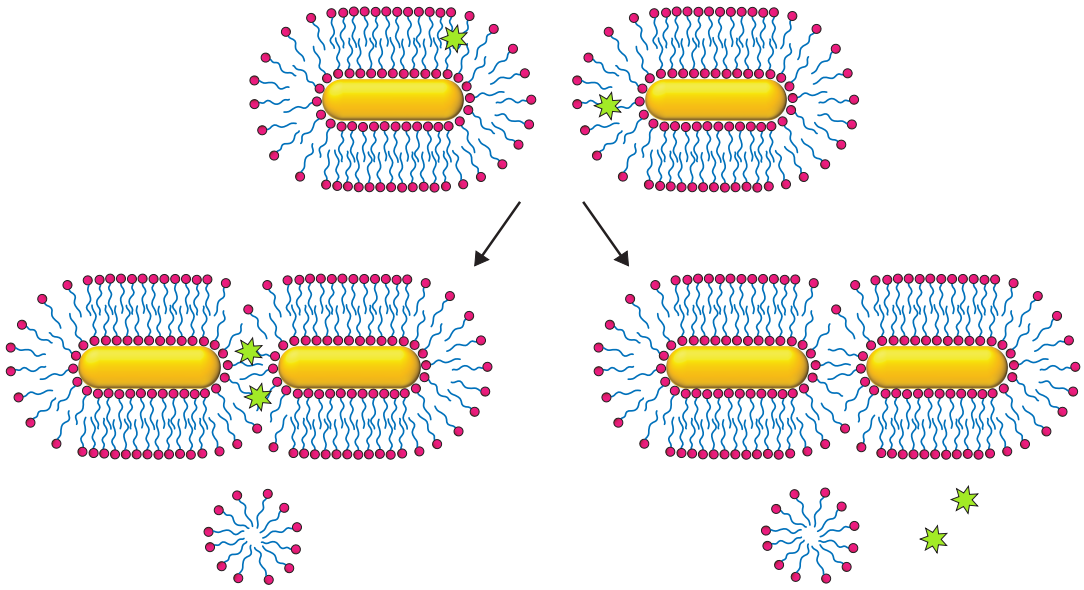

Figure 3.24 The ends of CTAB rods are thought to be "sticky," so a possible mechanism of aging is end-to-end agglomeration. This effect may merge the chemical environments that give rise to the two sharp peaks, explaining the new single peak at a frequency between the original peaks—whether that single peak is still associated with the rod (left outcome) or in solution (right outcome).

How can these spectral changes be rationalized? The most obvious outcome of aging is aggregation or reversible flocculation, in which particles begin to settle together. Because of the presumed fluxionality of the CTAB bilayer at the ends of the rods, it has been proposed that the ends are "sticky," lacking the charge density and electrostatic repulsion

of a dense headgroup shell.[36] TEM images of rods suggest that they prefer to agglomerate in end-to-end or end-to-side formations, and high-power centrifugation drives the rods to fuse end-to-end.[36] Therefore, in certain circumstances, it appears that the fluxional end bilayers on two different rods can merge into a single bilayer adjoining the the two rods. During this agglomeration, perhaps the original two distinct chemical environments merge into one environment (Figure 3.24). During the anisotropic PEG exchange experiment, we observed the gradual downfield shift of the peak at 1.8 ppm before purification led to its complete disappearance, whereas the peak at 2.1 ppm did not change in intensity or frequency. The new single peak appears between the two original peaks, but is close in chemical shift to where the 1.8 ppm peak moved during PEG exchange. This supports one of two ideas: 1) that increasing the electronic density of a ligand environment (as in the case of agglomeration or PEG displacement) changes its resonant frequency; or 2) that the two species have been displaced are now in solution. The larger relative integral of the new single peak, as compared to the sum of both original peaks, suggests that the second theory holds more merit.

3.4.6 Hofmann elimination theory

If the peaks at 1.8 and 2.1 ppm are indeed the same molecule at two very different binding sites, what is the identity of that molecule? Protons with chemical shifts in the range of approximately 0.8 – 3.0 ppm, or some subset within, that are of interest include R_2N-CH, $NC-CH$, R_2NH, and $R_2C=CR-CH$ (a few other protons have frequencies in this range, but their functional groups offer no obvious relevancy to our system). $Br-CH$ has a frequency between 2.8 – 3.8 ppm. Because the three sharp peaks (1.1, 1.8, 2.2 ppm) are singlets, there does not appear to be any spin-spin (J) coupling between them if they are part of the same species; this is consistent with the COSY and TOCSY findings.

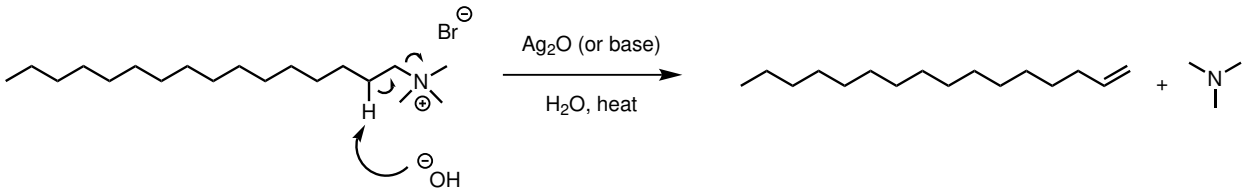

Figure 3.25 In a Hofmann elimination reaction, a quaternary ammonium is transformed into a tertiary amine and an alkene in the presence of base.

For different protons of the same species to not experience spin-spin coupling, they must be separated by more than three bonds. This essentially rules out any alkyl chain, or neighboring methyl ($-CH_3$), methylene ($-CH_2$), or methine ($-CH$) groups, in which case quadruplet, triplet, or doublet splitting patterns would be observed. We then consider possible species in the solution, including starting reagents and byproducts. Seeds are first made from $HAuCl_4$, CTAB, and $NaBH_4$ and are added without purification into the growth solution, which contains $HAuCl_4$, CTAB, $AgNO_3$, and ascorbic acid. The seed solution may contain byproducts or complexes from the gold reduction. Of these starting

reagents, there are no obvious byproducts that would excite at the frequencies of interest.

The protons that excite in this range of frequencies, as mentioned above, tend to be part of a species with either nitrogen or an alkene group present. Thus, we turned our attention to CTAB: what reactions are possible to perform on quaternary ammonium groups? Quaternary ammoniums are rather unreactive, so there is only one realistic candidate: the Hofmann elimination.

The quaternary ammonium group (NR_4^+) makes a terrific leaving group. Therefore, in the presence of a base, an E2 elimination reaction can occur, kicking off the now-neutral NR_3 species and forming an alkene. The major product is special, however, in that the double bond formed is not at the most-substituted position (the Zaitsev product), but at the least-substituted position (called, of course, the Hofmann product). This is because the NR_4^+ leaving group is so bulky as to cause steric hindrance in the transition state leading to the Zaitsev product, whereas the transition state leading to the Hofmann product has a considerably lower energy.

So, if Hofmann elimination were to occur on a CTAB molecule, the products would be trimethylamine and 1-hexadecene. In water, trimethylamine weakly ionizes to produce trimethylammonium ions. The predicted ^{1}H NMR chemical shifts in $CDCl_3$ (not D_2O) are 2.2 ppm for trimethylamine ($-CH_3$) and 2.9 and 8.6 ppm for trimethylammonium ($-CH_3$ and $-NH$, respectively). In the rod sample in D_2O, perhaps the two sharp peaks around 1.9 and 2.2 arise from trimethylamine and trimethylammonium, respectively. Because the rod NMR samples contain a mixture of H_2O and D_2O, the $-NH$ proton may partially exchange with deuterium, leading to a mix of $-NH$ and $-ND$ species. The presence of an $-NH$ species that can undergo hydrogen bonding or chemical exchange and appear at a variety of chemical shifts matches very well with our observance of a weak downfield peak anywhere in the range of 6.8 to almost 9 ppm; the frequency changes by sample, each of which has a different concentration and water percentage. In addition, the COSY and TOCSY data highlight a correlation between the protons at 2.2 and 6.8 ppm. Because the methyl and exchangeable protons of trimethylammonium are spin-spin coupled, this correlation coincides with the presence of this species. The spectrum of 1-hexadecene should have a collection of resonances in the 4.5 – 6.0 ppm range for the vinylic protons, and further upfield for allylic and methyl protons. These may show up weakly at low concentrations. However, 1-hexadecene should give rise to a fairly strong signal for the alkyl chain, presumably around 1.2 – 1.3 ppm (similar to for CTAB). Thus, it is possible that the sharp peak around 1.1 ppm arises from hexadecene.

Assignment of the enigmatic peaks to elimination products is compelling, but are the conditions during gold nanorod synthesis conducive for Hofmann elimination? In the typical reported reaction, a quaternary ammonium iodide salt is treated with silver oxide, water, and heat. The silver oxide forms AgOH with water, which ionizes into Ag^+ and ^-OH. The hydroxide ion exchanges with the iodide, and silver iodide precipitates out. Finally, the hydroxide

abstracts the β-proton to the ammonium, forming the alkene and pushing off the tertiary amine. These conditions can be modified. The iodide salt is simply a carry-over from a common proceeding step, exhaustive alkylation of an amine by methyl iodide, and the ammonium can just as easily have another counterion (in CTAB's case, bromide). Silver oxide is used as a base so that Ag^+ can complex out with the iodide, but in practice almost any base can be used: the critical step is formation of hydroxide to drive the elimination reaction. In the case of gold nanorod synthesis, $AgNO_3$ ionizes to Ag^+ and NO_3^-, and the silver ion can presumably complex with the bromide. The reaction takes place in water, so in the presence of a base, ^-OH should be readily available. Inconveniently, though, the Hofmann elimination usually requires high heat (temperatures up to 400°C). However, there is one report of Hofmann elimination occurring at room temperature, in very concentrated aqueous solutions of surfactants—including a CTAB analog, cetyltrimethylammonium methacrylate.[119] The study hypothesizes that when these surfactants are so concentrated as to be liquid crystalline, the abundant -OH ions are sufficiently close to the ammonium groups to drive Hofmann elimination without heat. On a gold nanorod surface, the ordered CTAB molecules also have a high local concentration. With the presence of the right base, Hofmann elimination is not out of the question.

3.5 Particles with shape and functional anisotropy

3.5.1 Mixed ligand shell

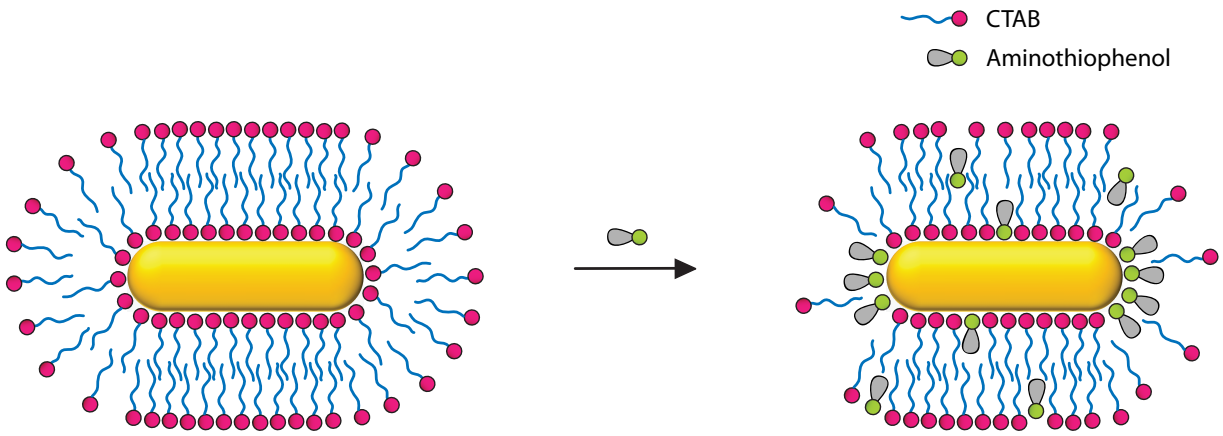

Figure 3.26 Introduction of aminothiophenol to CTAB rods is expected to result in a mixed ligand shell with complex morphology and multiple chemical environments, a fascinating system to study by NMR spectroscopy.

The above studies on particles with shape anisotropy revealed that NMR spectroscopy is a powerful tool for interpreting ligand arrangement, morphology, dynamics, and chemical environment. The promising results led us to study

the next tier of complexity: particles with shape *and* functional anisotropy. We synthesized gold rods with binary ligand shells (CTAB and a second ligand) and used our NMR techniques to better understand the spatial connectivity and dynamics of mixed ligand surfaces.

To design a functionally-anisotropic rod that would be amenable to NMR analysis, we had to choose a ligand that 1) has stronger affinity for the gold surface than CTAB, 2) displays distinct proton resonances that do not overlap with CTAB's, and 3) binds to only specific regions of the rod, rather than displacing CTAB completely. One ligand that fits all three criteria is 4-aminothiophenol (ATP). The only protons are aromatic or part of the primary amine or thiol; it has no aliphatic protons that would be convoluted with the strong main chain peak of CTAB. Observation of aromatic and aliphatic peaks in the ^{1}H NMR spectrum would indicate both ATP and CTAB are present, and the large frequency gap between those peaks aids resolution of two-dimensional correlations (e.g., NOESY).

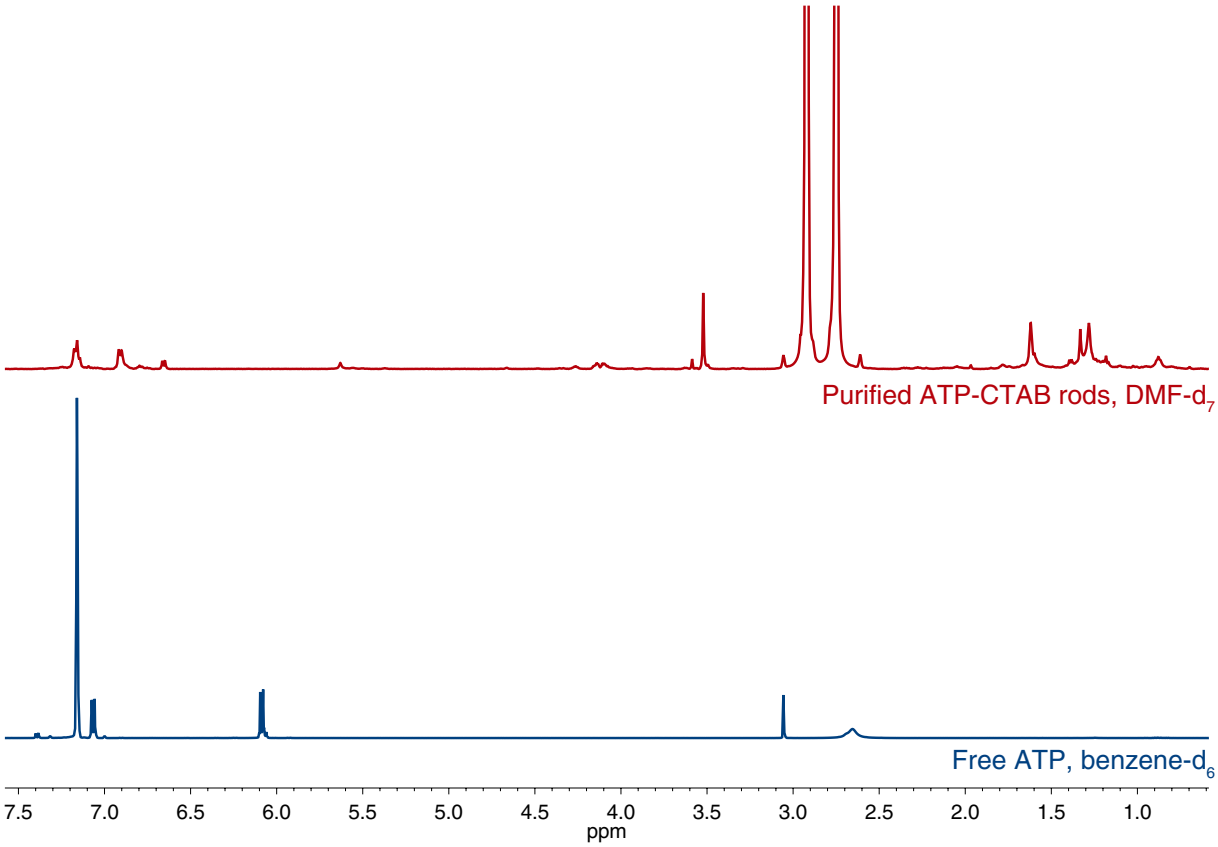

Figure 3.27 ^{1}H NMR of ATP-CTAB rods and free ATP ligand.

What makes ATP especially interesting, however, are the variegated paths in behavior it can exhibit upon interaction with a gold rod (Figure 3.26). Its thiol group forms a robust bond with gold, of course, but because it is only a single bond away from the bulky aryl ring, the thiol may have a higher barrier to accessing the gold interface. Therefore, it is

not likely to displace all the CTAB molecules, and it may prefer the exposed ends more than even the typical thiol. It is also well-accepted that small hydrophobic or aromatic species partition in the aliphatic core of the CTAB bilayer.[54,120] If ATP participates in some or all of these mechanisms, the mixed ligand shell will be quite heterogeneous and complex, and NMR spectroscopy is especially primed to decipher its character.

ATP in THF-d was added slowly dropwise to a very concentrated solution of CTAB rods in D_2O while the solution was rapidly stirred. After 1 hour of stirring, a proton NMR spectrum was taken of the reaction mixture (not shown). The rods were then purified by two rounds of centrifugation, and the pure rods were analyzed by NMR (Figure 3.27).

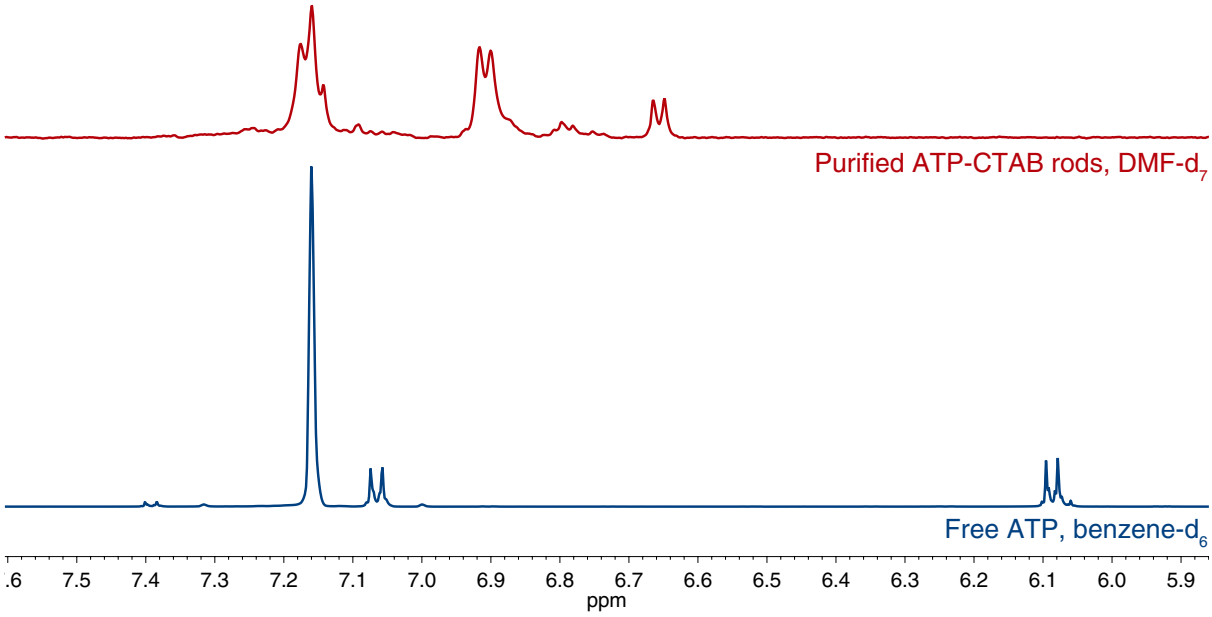

Figure 3.28 ^{1}H NMR of the aromatic region of ATP-CTAB rods and free ATP ligand. The aromatic region of CTAB-ATP rods reveals three peaks; free ATP has only two aromatic peaks. The additional peak in the CTAB-ATP rod spectrum may represent a second chemical environment or binding site.

The purified rods had distinct and intense resonances in both the aliphatic and aromatic regions, confirming that both CTAB and ATP were present on the surface in a mixed ligand shell. A closer examination of the aromatic region revealed interesting spectral features. Free ATP gives rise to two aromatic proton resonances, corresponding to the pairs of equivalent protons at the *ortho* and *meta* positions. In the unpurified reaction mixture, five aromatic resonances are

observed, probably corresponding to bound and free forms of ATP. The purified rods have three aromatic resonances—one more than is seen in the free ligand. Could the multiple peaks represent ATP in different chemical environments?

To help answer this question, 2-D NMR studies are necessary. TOCSY was performed on a different sample of CTAB-ATP rods, with the expectation that aromatic protons in the same ligand environment would be distinguishable by cross-peaks, and that correlations would not be found between ATP molecules in different chemical environments. The three aromatic resonances in this sample had slightly different chemical shifts than the above sample, but all gave rise to diagonal peaks, suggesting that none were artifacts or residual impurities. Cross-peaks were observed for only two of the resonances (Figure 3.29); the third does not appear to be spin-coupled—as would be expected if it were chemically distinct. Although this result is preliminary, it founds the exciting theory that ligand environments can be deciphered by TOCSY.

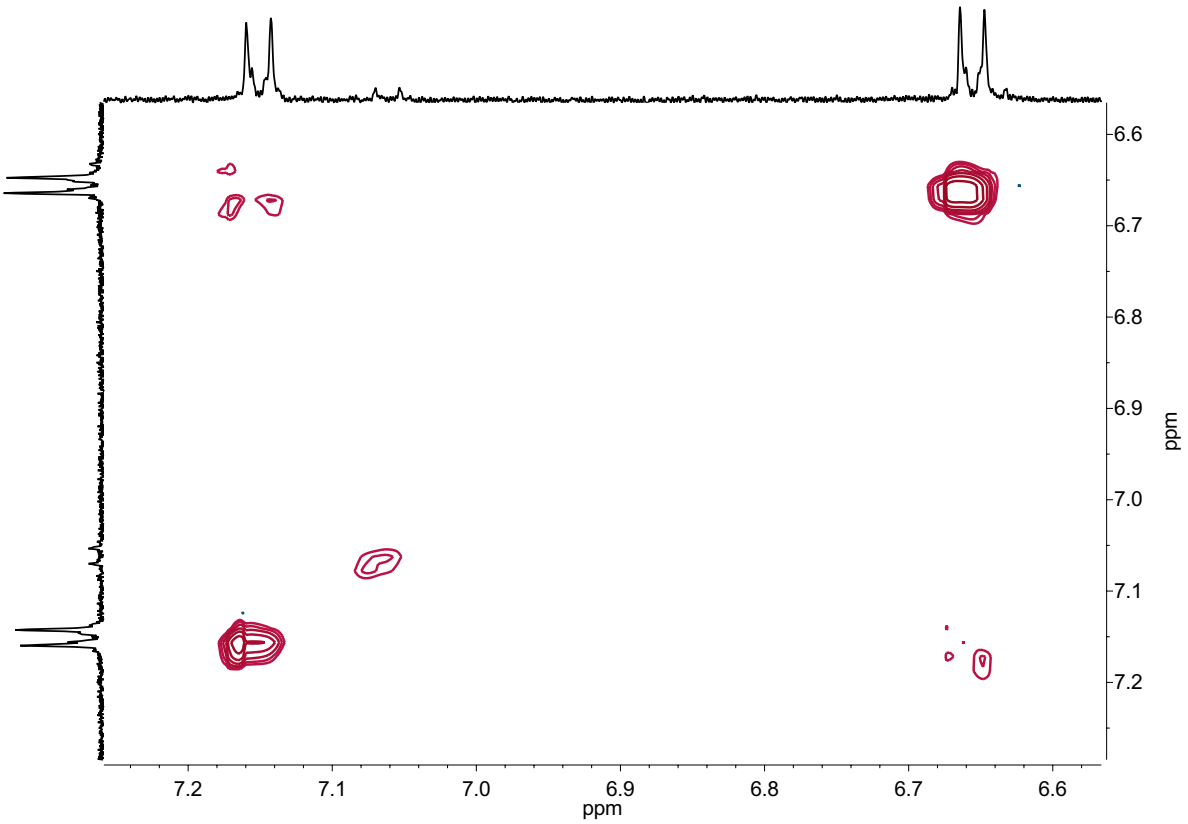

Figure 3.29 ^{1}H-^{1}H TOCSY NMR of ATP-CTAB rods. Three aromatic resonances give rise to diagonal peaks, but only two of the resonances are spin-coupled. The resonance that is not coupled is thought to be part of a separate chemical environment.

In future studies, NOESY may also reveal spatial arrangements of ATP: if it sequesters in the hydrophobic core of the CTAB bilayer, attaches to the gold surface indiscriminately, or targets only the gold ends.

3.5.2 Optimization of functional anisotropy

We sought a way to maximize the difference in dynamic mobility between CTAB on the ends and sides. Previous work replaced CTAB with a similar surfactant containing an olefin handle at the end of the alkyl chain, 11-(acryloyloxy)-undecyltrimethylammonium bromide.[121,122] When the surfactant forms a bilayer on the particle surface, the alkene groups are in close proximity to each other at the core of the bilayer. Upon addition of a cationic initiator, they polymerize, "zipping" the bilayer together and preventing molecular desorption. We will take advantage of the presumed looser surfactant molecules on the ends, hypothesizing that polymerization will occur less efficiently between those molecules, and that purification and subsequent thiol exchange will replace the monomeric surfactant at these ends. Meanwhile, the polymerized surfactant along the long axis should be resistant to thiol displacement.

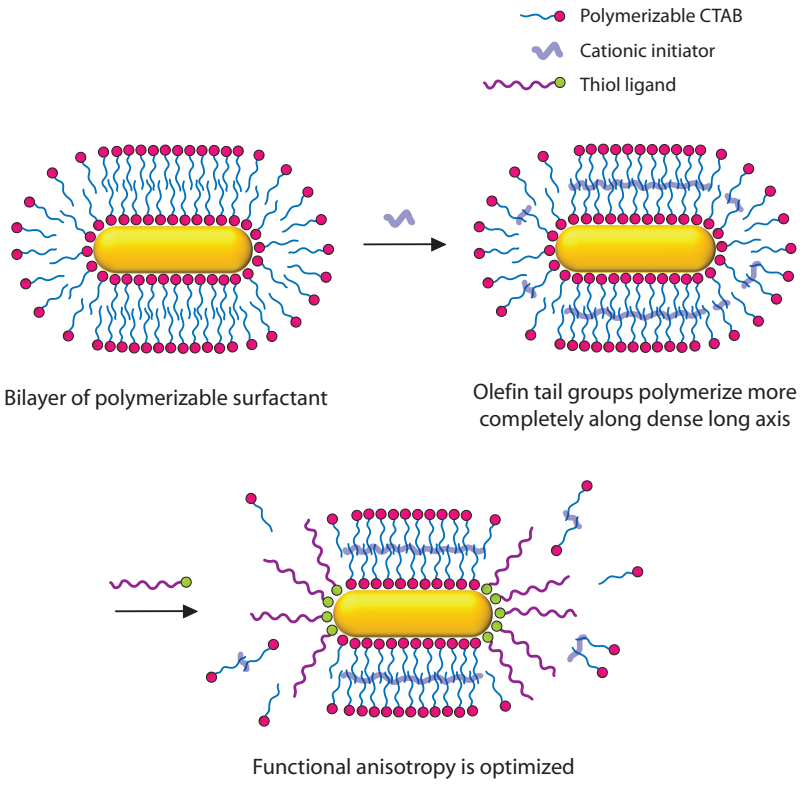

Figure 3.30 Polymerizing the surfactant bilayer at the long axes and leaving the ends open to exchange may be a promising, efficient route to functional anisotropy.

3.6 Experimental

3.6.1 General

All materials were used as received, unless otherwise indicated. Nanoparticle reactions were performed in new polyethylene centrifuge tubes, new glass vials, or glassware cleaned with aqua regia. Reported reaction temperatures refer to the temperature of the heating medium. Ultrapure deionized water was collected from a Barnstead NANOPURE water filtration system. Dynamic light scattering (DLS) and ζ-potential data were taken on a Brookhaven ZetaPALs analyzer. UV-vis spectra were obtained on a Varian Cary Scan 500 spectrometer. Transmission electron microscopy (TEM) samples were prepared on Lacey Formvar/Carbon, 200 mesh, 97 μm grids (Ted Pella), and TEM images were taken on a JEOL 2100 instrument and processed with Gatan DigitalMicrograph and ImageJ.

3.6.2 Synthesis of particles

High-yield CTAB gold nanorods

In an Erlenmeyer flask was combined aqueous solutions of CTAB (900 mL of 0.2 M), $HAuCl_4$ (10 mL of 0.1 M), and $AgNO_3$ (20 mL of 0.01 M). Ascorbic acid (50 mL of 0.04 M) was added, and the red-orange mixture was swirled until it became colorless. The mixture was treated with a fresh, ice-cold solution of $NaBH_4$ (100 μL of 0.01 M) and was swirled vigorously. After 1-2 min, the solution began to turn a deep wine-purple. The rods were allowed to form for 16 h. For purification, the rod solution was centrifuged once at 12,000 rcf for 60 min, and the pellet was redispersed in D_2O and centrifuged a second time under the same conditions.

MTAB gold nanorods

Concentrated, as-synthesized CTAB gold nanorods (0.5 mL) were added dropwise to an aqueous solution of MTAB (2 mL of 0.5 mg/mL). The mixture was vortexed vigorously for 1 min, then placed under gentle agitation for 24 h. The solution was centrifuged twice at 11,000 rcf for 30 min.

3.6.3 NMR experiments

Most of the nuclear magnetic resonance (NMR) spectra were acquired using a Varian Unity Inova narrow-bore 500 MHz spectrometer, although studies were also performed on a Varian Unity 400 MHz, Varian Unity Inova 400 MHz, Varian Unity 500 MHz, Varian VXR 500 MHz, Varian Unity Inova 600 MHz, or Agilent VNMRS 750 MHz spectrometer. Spectra were processed with MNova or VnmrJ. Chemical shifts are reported in parts per million (ppm) and were referenced to the residual proton solvent peak. Splitting patterns are designated as s (singlet), d (doublet), t (triplet), q (quadruplet), dd (doublet of doublets), m (multiplet), and br (broad). For aqueous nanoparticle samples containing residual water, the large water peak was suppressed using presaturation, with a presaturation delay of 2 s and a 4-step purge. Unless mentioned otherwise, acquisition time was set at 1 s.

Diffusion-ordered spectroscopy (DOSY)

Arrayed spectra were acquired using the gradient compensated STE with δPFGSE solvent suppression pulse sequence (DgcsteSL dpfgse), with the gradient strength (gzlvl1) varied between 50 and 32500. Depending on the sample, the number of scans (nt) = 128 or 256, number of increments (ni) = 15 or 32, diffusion delay (del) set between 50 and 250 ms, and gradient duration (gt1) = 2 s. DOSY experiments were processed using either VnmrJ or MNova by peak integrations.

Correlation spectroscopy (COSY) and total correlation spectroscopy (TOCSY)

For COSY, parameters were as follows: number of scans per t1 (nt) = 8, number of t1 increments (ni) = 256, relaxation delay = 1 s, and complex points = 2048. For TOCSY, parameters were set as follows: number of scans per t1 (nt) = 4 or 8, number of t1 increments (ni) = 256, relaxation delay = 1 s, mixing time = 80 ms, and complex points = 2048.

Nuclear Overhauser effect spectroscopy (NOESY)

Data was acquired with the number of scans (nt) = 128, number of increments = 200, presaturation delay = 1 s, and mixing time = 250 ms. The spectrum was manually phased until the sign of the cross-peaks were opposite that of the diagonal.

Chapter 4

Supramolecular Anisotropic Building Blocks

4.1 Introduction

Supramolecular chemistry describes the study of noncovalent bonds, such as hydrogen-bonding, ionic, π-π, and van der Waals interactions. Because supramolecular associations are often reversible and occupy a wide range of bond strengths, they offer many advantages to materials chemists over covalent bonds. The incredible diversity of supramolecular motifs allows their integration into almost any molecular scaffold.

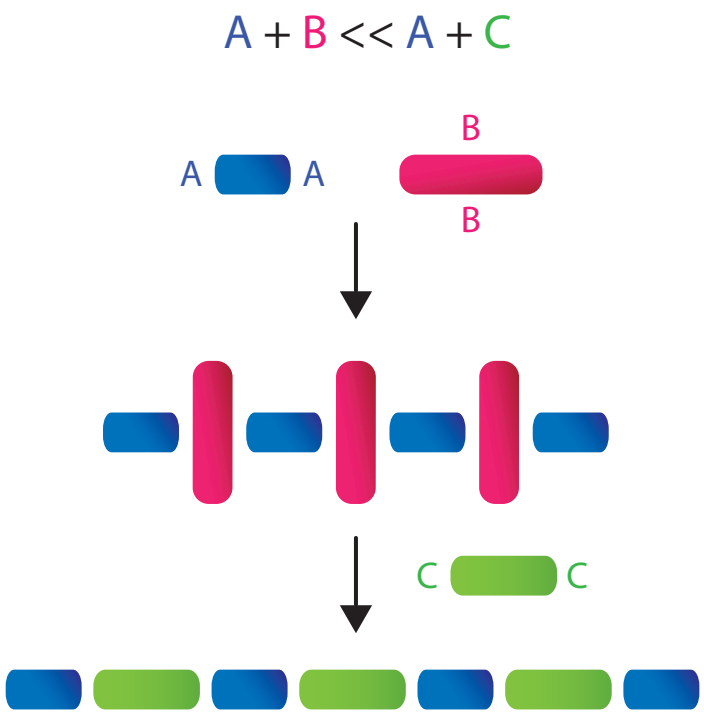

Figure 4.1 The association constants of reversible supramolecular building blocks can be exploited to design dynamic assemblies.

Through tethered supramolecular units on their surface, gold nanorods may be equipped with specific and orthogonal molecular recognition abilities. These "supramolecular nanorods" can self-assemble in solution to form ordered arrays; the potential for anisotropic functionalization of either axis promises a new degree of complexity. Perhaps most interestingly, the reversibility of noncovalent bonds broadens the scope beyond static architectures to favor dynamic, reorganizing assemblies. By introduction of a competing supramolecular unit whose complex has a higher association constant, the assemblies may self-sort *in situ* to accommodate the more strongly-binding complex. In this manner, association constants between motifs can be exploited to obtain exquisite control over self-assembly on the nanoscale. The supramolecular bond can also be envisioned as a Velcro-like bond that can be fastened and unfastened through certain stimuli (competition, solvent, pH, or heat), prompting the creation of a dynamic nanoparticle surface that adapts to its surroundings by adopting or shedding a noncovalent coat.

4.1.1 Quadruple hydrogen-bonding motifs

As a supramolecular motif, hydrogen-bonding in particular provides an incomparable amount of control: H-bonds between complementary molecules are specific, strong, and high-fidelity. Nature, of course, organizes many higher-order structures through H-bonding pairs, such as the nucleobases that are stitched together and coiled to make DNA. Artificial hydrogen-bonding modules, often inspired by bio-organic frameworks, can be designed to form complexes with desired association constants. Because H-bonds are directional and vary in strength (1-40 kcal/mol), their binding can be regulated by fine-tuning molecular structure. Much of the power of H-bonds for self-assembly lies in their specificity, supporting orthogonal interactions between multiple complementary molecules.

Table 4.1 K_{assoc} and K_{dimer} values for DAN, DeUG, and UPy complexes.

Complex	Association constant (M^{-1})
UPy·DAN	$K_{assoc} = 10^6$
UG·DAN	$K_{assoc} = 10^7$
DeUG·DAN	$K_{assoc} = 10^8$
UPy·UPy	$K_{dimer} = 10^7$
UG·UG	$K_{dimer} = 200$
DeUG·DeUG	$K_{dimer} = 880$
DAN·DAN	$K_{dimer} < 10$

Of all the efforts to design robust H-bonding modules for self-assembly, one notable strategy uses linear arrays of H-bonds. Motifs featuring four contiguous H-bonds balance association fidelity, bond strength, and synthetic ease, and are the subject of this work.[123] As proposed by Jorgensen, the order of H-bonding donors (D) and acceptors (A) in a parallel array hugely influences the binding strength, an effect of secondary electrostatic interactions.[124] Interactions

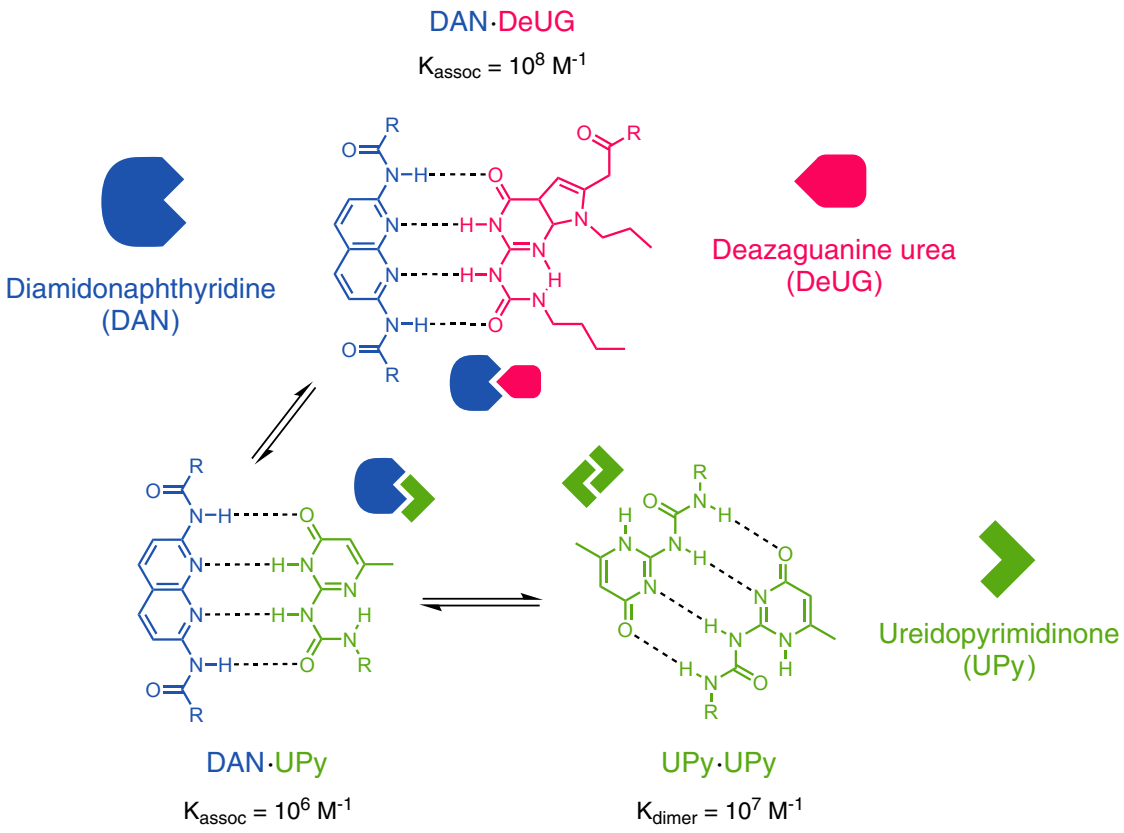

Figure 4.2 Equilibria between DAN, DeUG, and UPy quadruple hydrogen-bonding modules, noting their association and dimerization constants.

between diagonal hydrogen atoms are repulsive, whereas those between diagonal donors and acceptors are attractive. By this logic, the maximum number of consecutive donors or acceptors in a species should contribute the strongest binding; indeed, an AAAA-DDDD array was shown to exhibit exceedingly strong binding (K_{assoc} > 3 x 10^{12} M^{-1} in chloroform).[125] Versatile quadruple H-bonding motifs based on the heterocyclic scaffold of DNA and RNA nucleobases have been widely studied. Of these, 2-ureido-4-pyrimidinone (UPy) is particularly adaptable because it exists in three tautomers that each displays unique bonding behavior. The 4[1H]-pyrimidinone tautomer contains a DDAA array and readily dimerizes in chloroform (K_{dimer} = 10^7 M^{-1}), whereas the 6[1H]-pyrimidinone monomer further tautomerizes into the dimerizing DADA pyrimidin-4-ol.[126] The DDAA dimer has two attractive and one repulsive interactions, and is both predicted and observed to have a higher K_{dimer} than the DADA dimer, in which all three interactions are repulsive. The tautomer, and thus the order of the array, is determined by two possible conformations of an intramolecular hydrogen bond, the arrangement of which is influenced by solvent and electronics. Thus, UPy's binding selectivity and strength can be tuned by modification of substituents on the molecule. In addition, UPy reconfigures its conformation to form heterocomplexes with other quadruple-bonding modules; it adopts an ADDA array to form strong bonds

with DAAD diamidonaphthyridine (DAN) motifs ($K_{assoc} = 10^6\ M^{-1}$). Another base pair mimic similar in framework to UPy, ureidoguanosine (UG), and its more stable and selective analog, ureido-7-deazaguanine (DeUG), also bind with DAN derivatives ($K_{assoc} = 10^7\ M^{-1}$ for UG·DAN and $K_{assoc} = 10^8\ M^{-1}$ for DeUG·DAN) but advantageously feature very low dimerization constants ($K_{dimer} = 200\ M^{-1}$ for UG and $K_{dimer} = 880\ M^{-1}$ for DeUG).[127] In nonpolar solvents, DeUG is preorganized in an ADDA conformation, priming it to have a high affinity for DAN. DAN itself also dimerizes weakly ($K_{dimer} < 10\ M^{-1}$). Given some combination of UPy, DeUG, and DAN, several permutations of homo- and heterocomplexes can form. Exploiting strengths of the association constants ensures control over the specific molecular recognition events that govern self-assembly of rods (Table 4.1, Figure 4.2).

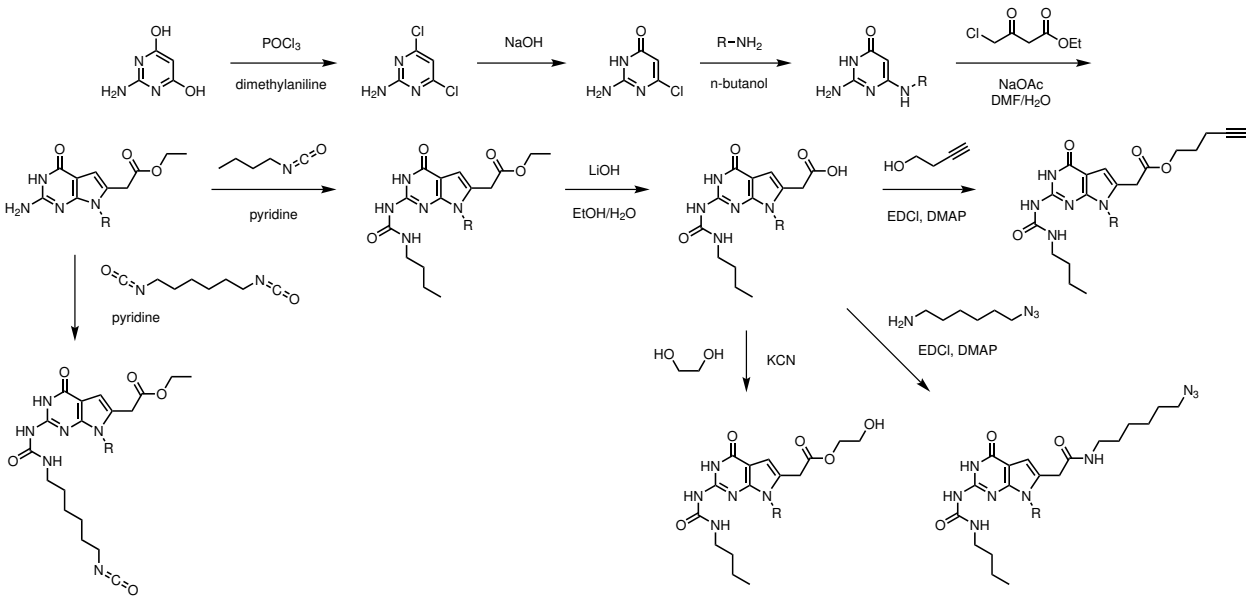

Figure 4.3 DeUG features two synthetic handles that can be transformed into a variety of practical functional groups.

UPy, DeUG, and DAN all feature synthetic handles for functionalization with groups useful for gold surface chemistry. As mentioned above, nucleobase derivatives UPy and DeUG share a similar structure, from which analogous tethers can be attached at the C6 urea position (Figure 4.3). Forming the urea from an alkyldiisocyanate yields UPy or DeUG with an isocyanate-terminated chain, convenient for further transformations because isocyanates react readily with amines, thiols, and alcohols. In fact, amine-isocyanate and thiol-isocyanate reactions are gaining popularity as "click" reactions, because they can proceed in nearly quantitative yield within minutes under mild reaction conditions (neat or benign solvent, ambient temperature). Alternatively, DeUG features a synthetic handle at the C8 position that can accommodate such groups as a carboxylic acid, alcohol, azide, and alkyne (Figure 4.3).

DAN has been previously unsymmetrically functionalized to include amine, carboxylic acid, isocyanate, and bromine

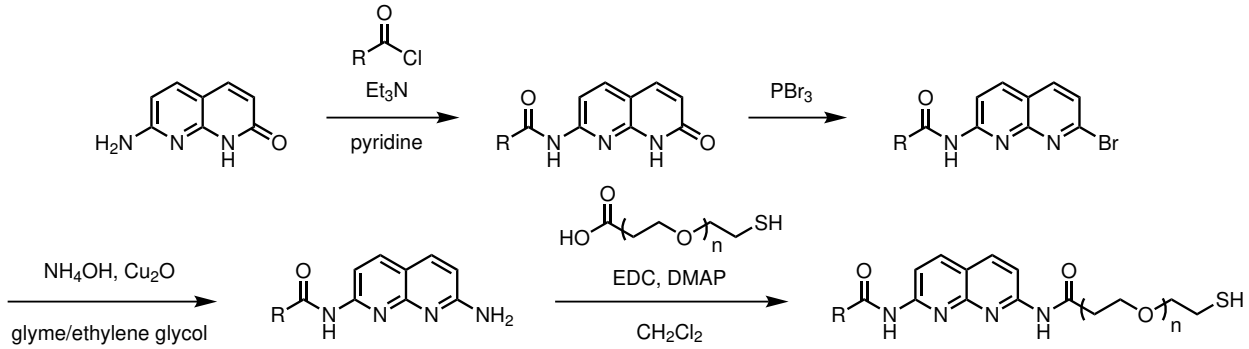

Figure 4.4 DAN can be unsymmetrically functionalized with a thiol species for binding to gold.

species, as well as a thiol group (Figure 4.4). As one example, a brominated DAN unit can be integrated as a side-chain into commercially-available polystyrene, via C-H activation and palladium-catalyzed cross-coupling. With this synthesis, DAN may be integrated into thiol-terminated polystyrene, yielding a thiolated DAN polymer. The versatility of UPy, DeUG, and DAN derivatives makes them tremendously useful for attachment to gold nanorods. Amine-functionalized rods, for example, should react readily with the isocyanate or carboxylic acid derivatives, and azide rods may be "clicked" to the alkyne analogs. Thiolated derivatives may bind selectively to the reactive rod ends, yielding particles with functional anisotropy and "valence"-like reactivity that can be be assembled with exquisite control over orientation (Figure 4.1).

4.1.2 Cavitands and cucurbituril chemistry

Gold nanochemistry does present a major challenge for hydrogen-bonding: H-bonding proceeds most efficiently in noncompetitive, nonpolar solvents, such as chloroform, and is severely disrupted in water. Unfortunately, it is difficult to transfer gold nanorods to a completely anhydrous environment, especially one that is nonpolar. To make the aqueous nature of this chemistry work for rather than against us, we explored host-guest motifs that perform in water. Cavitands, synthetic receptors with hydrophobic interiors capable of sequestering molecules, emerged as superior candidates. Of the variety of cavitands known, including calixarenes, cyclodextrins, and pillararenes, cucurbiturils were chosen because they are capable of forming unusual ternary complexes.

Although macrocycles derived from glycoluril and formaldehyde have been around in unknown form since the early twentieth century, it was not until after molecular recognition entered mainstream chemistry in the late 1970s that cucurbiturils began to cultivate a story of their own. In 1981, after elucidating their structure, Mock and colleagues coined the term for these pumpkin-shaped molecules after the *cucurbitaceae* plant family, sparking interest in the cucurbiturils' high affinity and selectivity. Cucurbituril chemistry is a younger field than most of the other cavitands; only

in the past decade or so has the library of cucurbituril homologues been expanded,[128,129] and so has followed their chemistry and application.[130]

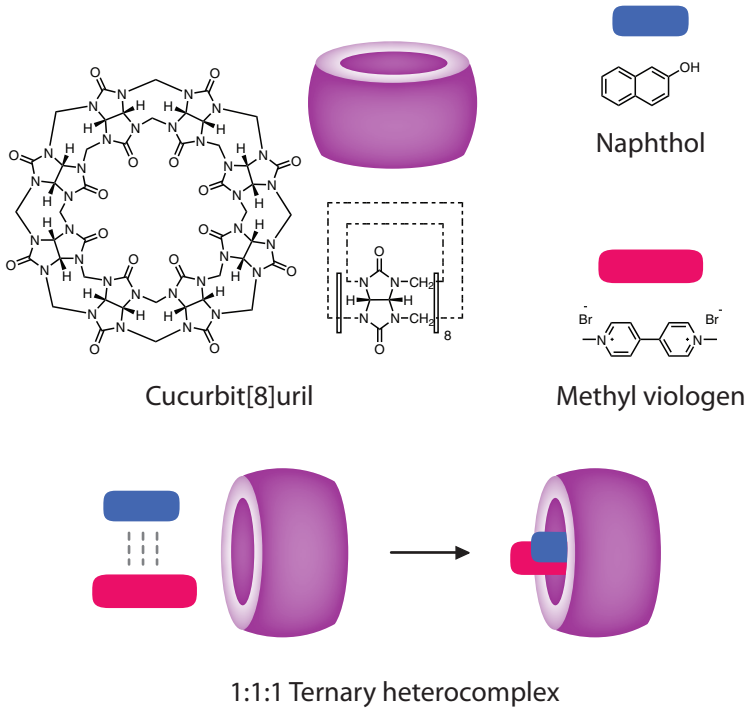

Figure 4.5 Cucurbit[8]uril, methyl viologen, and naphthol derivatives form an extremely strong heteroternary complex, based on synergistic charge-transfer and hydrophobic associations.

The cucurbituril family now comprises cyclic oligomers with between five and ten repeat units (CB[n]), defined by a hydrophobic cavity accessed by two openings sheathed in ureido carbonyl groups.[131] All cucurbiturils have a depth of 9.1 Å and a width and volume dependent on the oligomer size, ranging from a capacity of 82 Å^3 for CB[5] to 479 Å^3 for CB[8] (CB[10] has not yet been isolated as a free form). The cavity has a high affinity for positively-charged guests through ion-dipole interactions, but each homologue is a unique host. CB[8] has a more sophisticated molecular recognition profile than its smaller cousins,[132] as it is capable of binding two aromatic rings at once and thus can form 1:2 termolecular complexes. The two arenes bind cooperatively, so binding of the first arene increases the cavity's affinity for the second. Even more interestingly, CB[8] can form 1:1:1 heteroternary complexes if the two different guests have an intrinsic association (Figure 4.5). This is the case for electron-poor viologens and electron-rich hydroxynaphthalenes, which associate via charge-transfer interactions.[133,134] CB[8] forms a 1:1 host-guest complex with methyl viologen (MV^{2+}) ($K_{assoc} = 10^5$-10^6 M^{-1}) but not a 1:2 complex, presumably because of electrostatic repulsion between the two viologens. CB[8] does not bind electron-rich naphthalenes on their own. However, introduction of methyl viologen and naphthalene to the cucurbituril drives formation of the 1:1:1 complex, which is enormously strong (K_{assoc} up to 10^{12} M^{-1}.[135,136] Heteroternary complexes are rare in host-guest chemistry, but they provide a high-fidelity

approach to controlling assembly of multiple components.

Few reports exist of precise assembly of heterogeneous nanoscale species—that is, associating at least two varieties of nanoparticles in a defined order. As discussed in a previous chapter, this type of control can be achieved only with anisotropic particles; two isotropic spheres with complementary functionality would form large, indiscriminate aggregates. Gold rods can be assigned "valence" through regiospecific interactions at either axis, but so far only end-to-end attachment of equivalent rods has been demonstrated. It would be highly desirable to form alternating assemblies of varied populations of rods or end-to-side structures, nearing the level of monomeric control afforded by organic copolymers (Figure 4.1). Not only is this sort of heterogenous assembly interesting on a fundamental level, plasmonic "copolymers" would be expected to display emergent optical and electronic properties through coupling effects.

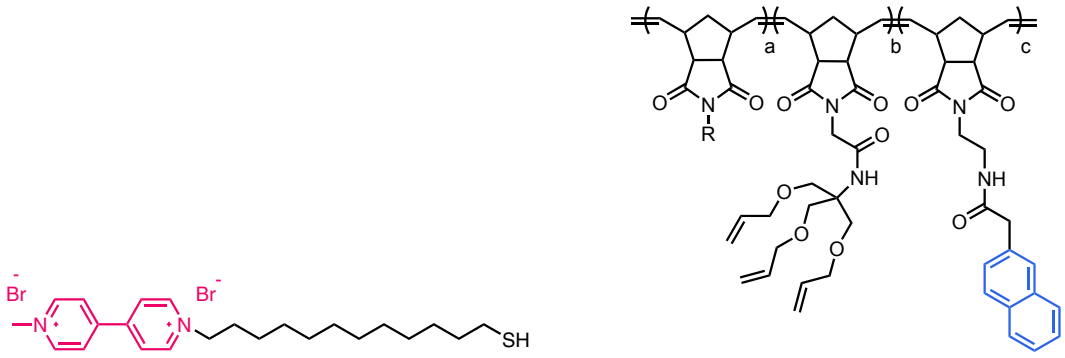

Figure 4.6 Structures of functional components used in CB[8] complex studies: Methyl viologen thiol (left) and the linear polymer precursor of naphthalene-ONP (right).

The robust and specific CB[8], MV^{2+}, and naphthalene ternary complex was chosen as the motif for heterogeneous assembly. Because MV^{2+} is highly positive and its derivatives polar, we reasoned that it would be the best candidate of the three to attach to the positively-charged gold rods. The methyl viologen framework can be unsymmetrically functionalized with a thiol group separated by a long, flexible carbon linker, which is necessary to extend the MV^{2+} component away from the gold surface and make it available for supramolecular interaction (Figure 4.6).[137,138] The thiolated MV^{2+} is soluble in water, convenient for gold functionalization. Based on literature reports of thiols binding selectively to rod ends, we aimed to conjugate the MV^{2+} specifically at the two transverse poles.[139] As another possible bonding chemistry, the carbonyl-rimmed cucurbiturils have been shown to bind to gold monolayers, spheres,[140] and rods[139] through perpendicular, chelate-like interactions between the carbonyl groups and gold.

A collaboration within our group provided water-soluble organic nanoparticles (ONPs) conjugated with naphthalene species (naph-ONPs) (Figure 4.6). These organic particles were prepared from linear polymers in a multi-step, versatile synthesis: functional norbornene dicarboximide monomers were joined by ring-opening metathesis poly-

merization (ROMP), followed by amidation of side chains with triallyl tris(hydroxymethyl)aminomethane, which is capable of undergoing ring-closing metathesis to crosslink the polymer into a nanoparticle.[141] The two naph-ONPs used in this study were approximately 15 nm in diameter, with an estimated 12 or 25 naphthalenes per particle. We hypothesized that gold rods end-functionalized with MV^{2+} and the naph-ONPs would assemble in the presence of CB[8]. Because the rods have a width diameter of approximately 10-15 nm, it seemed likely that assemblies would form with naph-ONPs as tetravalent cores.

4.2 Quadruple hydrogen-bonding modules

4.2.1 Functionalization of particles

The CTAB rods featured a narrow longitudinal plasmon band at 690 nm and appeared quite monodisperse. By TEM, they were determined to have an aspect ratio of about 3 and dimensions of about 45 x 15 nm. CTAB rods were modified with amine moieties for further reaction with UPy-isocyanate or DeUG-isocyanate, via either ligand exchange with 4-aminothiophenol or polyelectrolyte-wrapping with poly(acrylic acid) (PAA) and then poly(allylamine hydrochloride) (PAH). Aminothiophenol rods posed several issues. Although they could be redispersed in DMF, they showed considerable aggregation by UV-vis (Figure 4.7). H-bonding units functionalized on these rods would be only 1-2 nm from the surface, and to compound the problem, any incompletely-exchanged CTAB would encase the molecules, precluding hydrogen-bonding to other rods. On the other hand, PAH rods were very stable in DMF, because polyelectrolytes provide a protective cushion between the rods and the solvent. Each polymer layer provides an approximately 1.5 nm coating thickness on top of the CTAB bilayer (about 4 nm thick). Small molecules should then be approximately 7-8 nm from the gold surface and free to H-bond at the solvent interface. On these bases, PAH rods were chosen for further functionalization with UPy and DeUG. Successful PAA and PAH wrapping was confirmed by ζ-potential data, which oscillated from positive for CTAB rods (+19 ± 1 mV), to negative for PAA rods (-20 ± 1 mV), back to positive for PAH rods (+28 ± 1 mV).

The on-particle urea formation between UPy-isocyanate or DeUG-isocyanate and PAH rods was performed in DMF, using 1,8-diazabicycloundec-7-ene (DBU) as a non-nucleophilic base and solubilizing agent. Within 30 minutes of reaction, UPy-functionalized rods began to flocculate and formed a powdery precipitate, indicating a change in rod solubility, and DeUG-functionalized rods settled slightly but remained in solution. These observations are consistent with the solubility of the organic molecules: UPy-isocyanate is only sparingly soluble in DMF whereas DeUG-isocyanate is soluble. The precipitate could be redispersed in either DMF or chloroform with sonication and demon-

strated remarkable stability to multiple rounds of centrifugation and solvation. Several purification approaches were attempted to remove residual water, DMF, and small molecules. Lyophilization of PAH rods before reaction with isocyanate yielded a powder that could not be dispersed in DMF, so was not a viable method. To yield stable rods, UPy- or DeUG-functionalized rods in DMF could be vacuum dried, or centrifuged twice in chloroform.

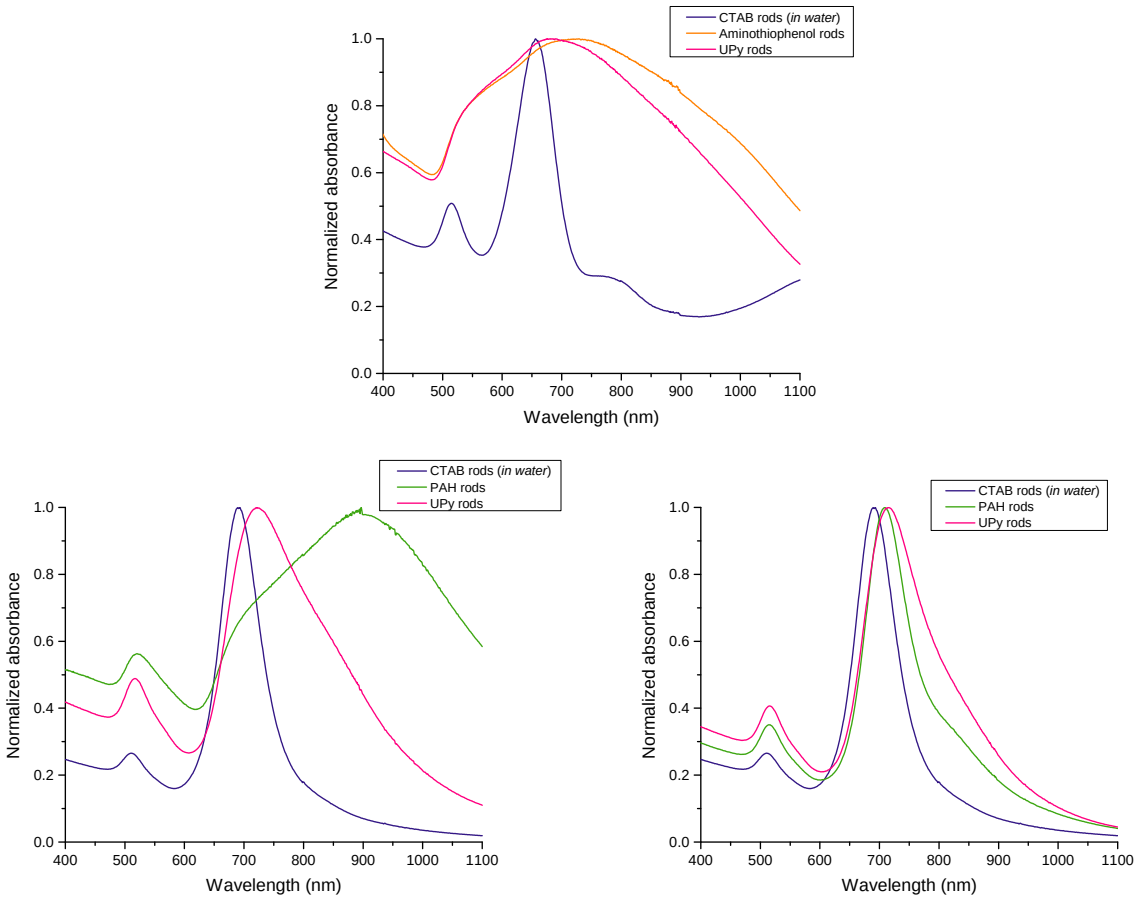

Figure 4.7 UPy rods were successfully synthesized through a PAH rod intermediate, as shown by the narrow plasmon bands in chloroform (bottom, left) and DMF (bottom, right). Functionalization through an aminothiophenol rod intermediate aggregated in chloroform (top).

In UV-vis spectra taken in DMF, both PAH rods and UPy rods displayed sharp plasmon bands, which confirms both rods' stability in DMF (Figure 4.7). However, in chloroform, the difference in stability between the two rods is striking: PAH rods have a significantly broadened plasmon band and appear to aggregate in chloroform, as expected, whereas the UPy rods' plasmon band is well-defined (Figure 4.7). Because the stability of rods in a given solvent is a function of their surface chemistry, the narrow plasmon band of UPy rods in chloroform results suggest that UPy is indeed attached to the rod surface, allowing them to be dispersed in the nonpolar solvent. Dynamic light scattering (DLS) measurements help confirm successful functionalization: UPy rods featured a larger effective diameter than PAH

rods in both DMF and chloroform, consistent with an increase in surface coating thickness. Because UPy has a very high dimerization constant ($K_{dimer} = 10^7\ M^{-1}$ in chloroform at 25°C), UPy-functionalized rods should form H-bonded aggregrates in nonpolar solvents. Even though both rods have large effective diameters in chloroform, it is important to note that aggregates of PAH rods likely reflect instability, whereas those of UPy rods may be induced by H-bonding (Figure 4.8).

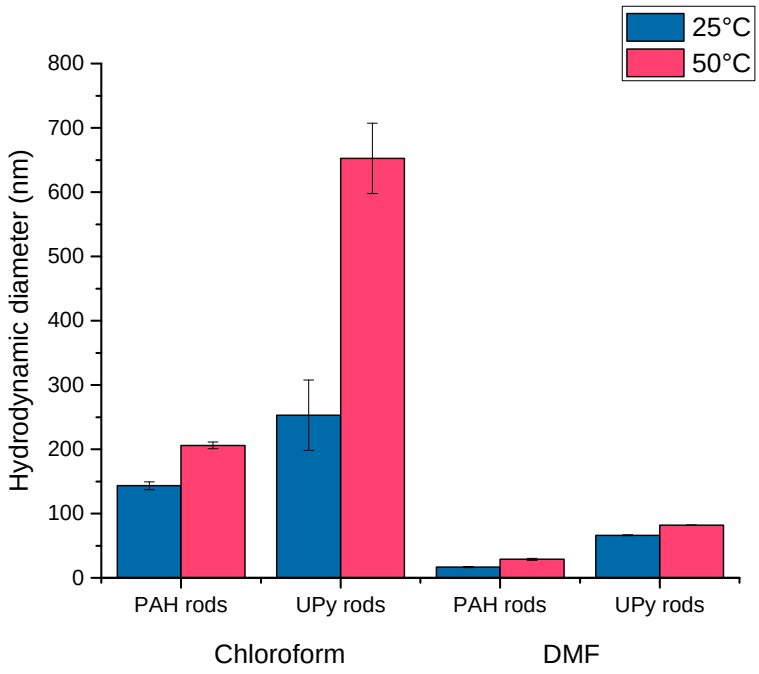

Figure 4.8 The hydrodynamic diameter of UPy rods is greater than precursor PAH rods in both chloroform and DMF. In DMF, the small increase in diameter suggests successful functionalization, whereas in chloroform the large size increase indicates self-assembly of UPy rods through dimerization.

To elucidate the nature of the aggregates, TEM samples were prepared for both sets of rods in either DMF or chloroform. Monitoring self-assembly of particles via TEM is not a precise indicator of what occurs in solution, because evaporation of the solvent on the grid can induce aggregation, but TEM images can at least diagnose the tendencies of particles to assemble, aggregate, or disperse in both solution and the solid-state. Evaporation effects can be reduced by submerging the grid in a droplet of the solution for 10 minutes, and then wicking away excess solvent. DMF samples were prepared using this method; chloroform samples evaporated too quickly, so they were prepared by drop-casting. Chloroform samples were both aggregated on the grid, possibly from rapid evaporation, and thus were inconclusive. The DMF samples offered more promising results: PAH rods were scattered across the grid as discrete rods, whereas UPy rods formed small clusters (Figure 4.9). Because the UV-vis spectra of both rods in DMF showed narrow plasmon

bands, it is unlikely that UPy rods form these clusters in DMF solution. The clusters on the grid may reflect the rods' solid-state behavior, and in the absence of competing solvent it appears that the UPy rods hydrogen-bond to each other as the organic modules dimerize.

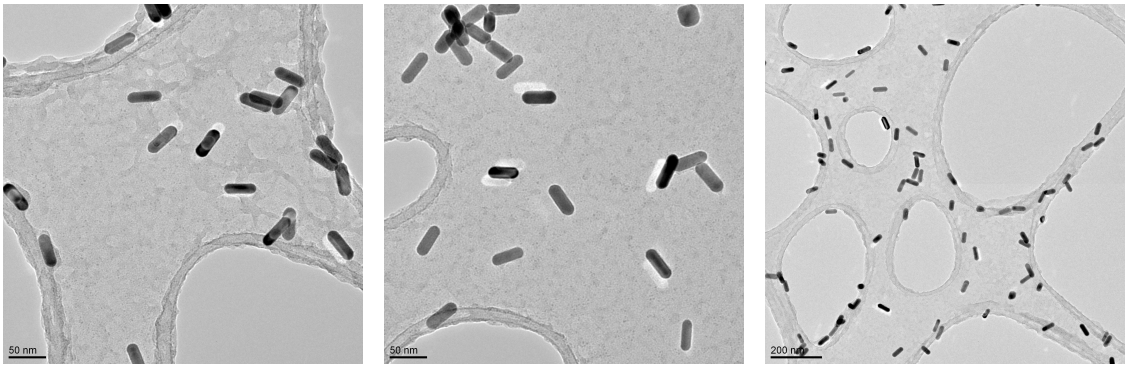

(a) PAH rods.

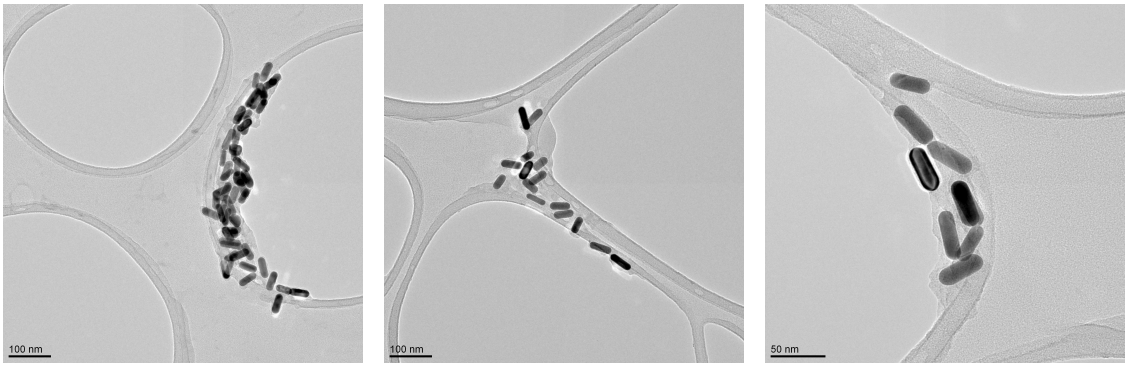

(b) UPy rods.

Figure 4.9 TEM images of PAH and UPy rods drop-casted from suspensions in DMF. UPy rods form small, H-bonded clusters as they dry, whereas PAH rods disperse evenly.

4.2.2 Self-assembly studies

The distinctive hydrogen-bonding properties of UPy and DeUG rods allow for a number of interesting competition studies. In contrast to UPy, DeUG only very weakly dimerizes with itself, so DeUG rods should not form H-bonded networks in chloroform. Both modules associate strongly and selectively with DAN. Therefore, the addition of excess DAN to chloroform solutions of each set of rods should give rise to juxtaposing effects: DAN should break apart UPy rod aggregates, but fuse together DeUG rods.

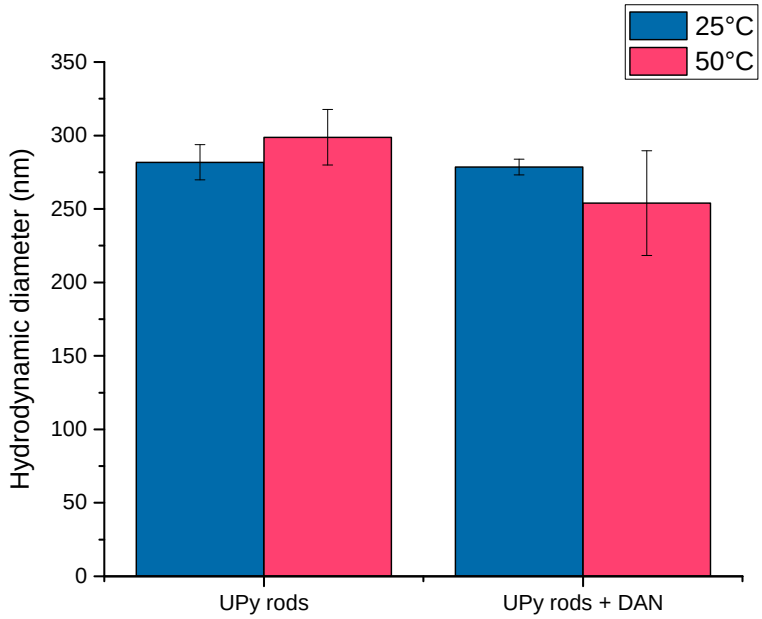

Figure 4.10 DLS data from DAN competition studies. UPy rod assemblies do not disassemble with introduction of competing DAN units.

UPy rods were mixed with a large excess of small molecule DAN in chloroform. DLS measurements were taken before and after DAN addition at both 20°C and 50°C. Kdimer of UPy is estimated to be an order of magnitude larger than K_{assoc} of UPy·DAN, so the effect of heat on hydrogen bonding may favorably shift the equilibrium or encourage conformational adjustments to help the molecules come into contact. No significant size difference was observed at either temperature between UPy rods alone or with DAN. This apparent lack of H-bonding interaction may stem from competing agents sequestered on or around the rod surface, including water and DMF.

The synthesis of anhydrous, purified H-bonding rods is necessary to observe strong H-bonding. Several ideas are in place to achieve anhydrous rods, but all attempts so far did not work. PAH rods were first neutralized by titrating with sodium hydroxide, then lyophilized into a powder and redispersed in DMF. The isocyanate and DBU were added to the rods and allowed to react, and the functionalized rods were subjected to two centrifugation cycles to remove unreacted starting material. The rods could be washed at this step, although a compatible solvent was not found. Finally, the purified pellet or precipitate was vacuum dried to remove residual DMF or water, and redispersed in chloroform. Unfortunately, the rods became unstable at various stages of this process. Future competition studies on anhydrous rods will systematically explore DAN·(UPy rod), DAN·(DeUG rod), and (UPy small molecule)·(UPy rod) interactions at various temperatures and in nonpolar and H-bonding solvents. In addition, X-ray photoelectron spectroscopy (XPS),

inductively coupled plasma mass spectrometry (ICP-MS), or thermogravimetric analysis (TGA) will help elucidate the number of molecules functionalized on the surface to calculate a molar ratio of DAN to UPy or DeUG.

4.3 Cucurbituril complexes

4.3.1 Functionalization of particles

Methyl viologen thiol (MV^{2+} – thiol) was conjugated to gold nanorods by adding approximately 10^6 mole equivalents of the thiol, in an aqueous solution, to a solution of rods. The mixture was allowed to react for 20 hours with gentle agitation, and centrifuged once. The functionalized rods appeared stable, with no broadening of the plasmon bands.

4.3.2 Self-assembly studies

Table 4.2 Molar equivalents of ternary complex components, with low equivalents of CB[8].

Molar ratio (Rod:ONP:CB)	MV^{2+} rods (µl, 1.7 nM)	Naph-ONP 1 (µl, 17 nM)	Naph-ONP 2 (µl, 17 nM)	CB[8] (µl, 17 nM)
1:1:1	250	25	-	25
1:1:1	250	-	25	25
4:1:4	250	6.25	-	25
4:1:4	250	-	6.25	25
1:0:1 (no ONP)	250	-	-	25
1:1:0 (no CB)	250	25	-	-

Table 4.3 Molar equivalents of ternary complex components, with high equivalents of CB[8].

Molar ratio (Rod:ONP:CB)	MV^{2+} rods (µl, 1.7 nM)	Naph-ONP 1 (µl, 17 nM)	Naph-ONP 2 (µl, 17 nM)	CB[8] (µl, 170 nM)
1:1:100	250	25	-	250
1:1:100	250	-	25	250
4:1:400	250	6.25	-	250
4:1:400	250	-	6.25	250
1:0:100 (no ONP)	250	-	-	250
1:1:0 (no CB)	250	250	-	-

To assemble the CB[8], MV^{2+} gold nanorods, and naph-ONPs, mixtures were prepared in varying molar ratios, with either one molar equivalent of CB (Table 4.2) or excess CB (Table 4.3). For each mixture, a dilute aqueous solution of CB[8] (which is only weakly soluble in water) was added to the MV^{2+} rods and gently vortexed for 5 min to create

MV^{2+}:CB[8] complexes at the ends of rods ($K_{assoc} = 10^5 - 10^6\ M^{-1}$), activating the ends for strong attachment to the naph-ONPs ($K_{assoc} = 10^{12}\ M^{-1}$). The solutions were treated with with aqueous solution of naph-ONPs and gently vortexed for another 5 minutes, and then gently agitated for 24 hours. Two varieties of naph-ONPs were used: naph-ONP 1 was estimated to have 12 copies of the naphthalene conjugated to the particle; naph-ONP 2 was estimated to have 25 copies conjugated. After the day of agitation, each sample was drop-cast onto a grid and imaged by TEM.

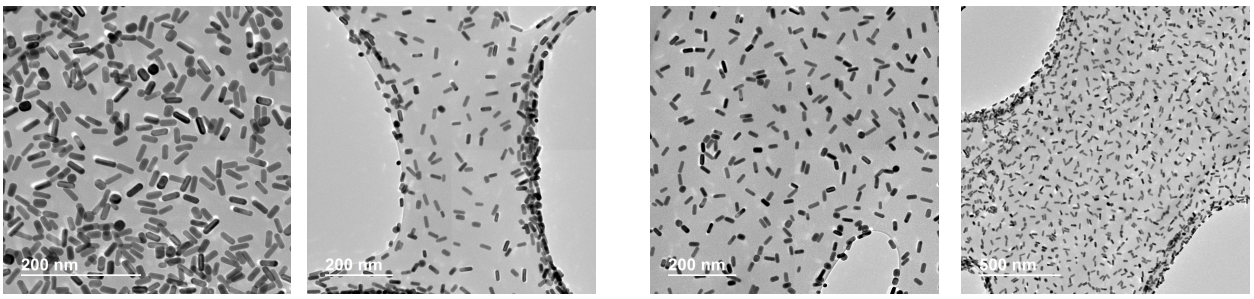

(a) Naph-ONP 1. **(b)** Naph-ONP 2.

Figure 4.11 TEM images of 1:1:1 molar ratio complexes.

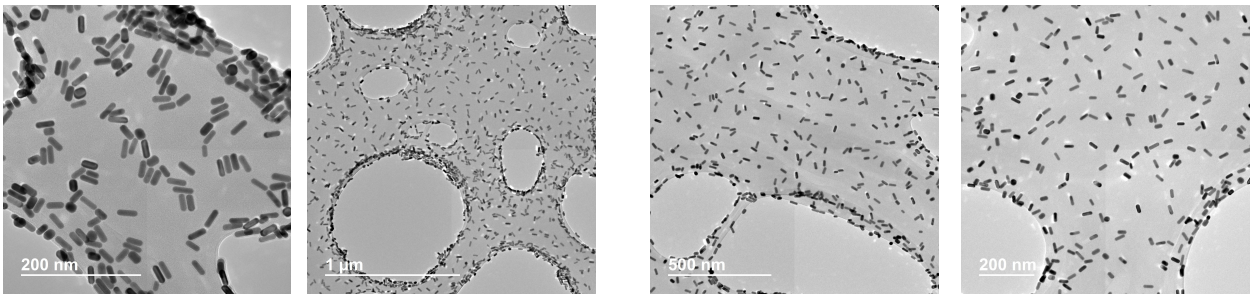

(a) Naph-ONP 1. **(b)** Naph-ONP 2.

Figure 4.12 TEM images of 1:1:100 molar ratio complexes.

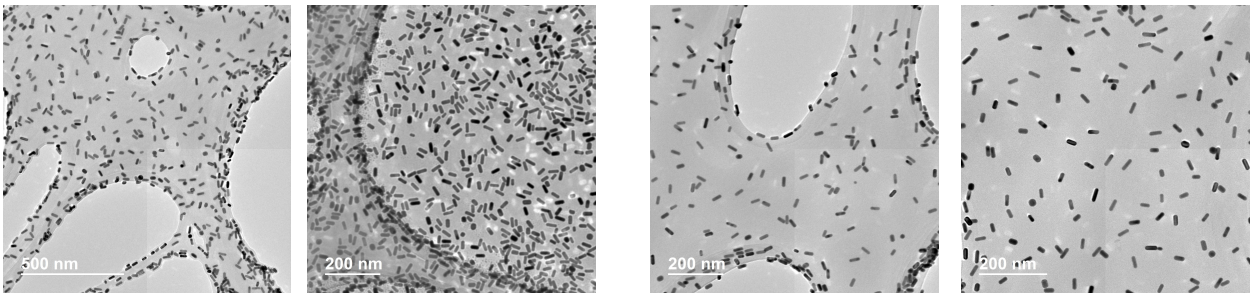

(a) Naph-ONP 1. **(b)** Naph-ONP 2.

Figure 4.13 TEM images of 4:1:400 molar ratio complexes.

To determine molar ratios, we assumed that each rod had several MV^{2+}-thiol species per end. Based on the diameters of the ONPs (15 nm) and the rods (10-15 nm), naph-ONPs were visualized with quadrants, each quadrant

displaying approximately 3 naphthalene groups (naph-ONP 1) or 6 naphthalenes (naph-ONP 2). By varying the component stoichiometry, a variety of architectures could form, from discrete shapes with tetrahedral-like symmetry to three-dimensional superlattices.

TEM images of assemblies in molar ratios of rod:ONP:CB 1:1:1 (Figure 4.11), 1:1:100 (Figure 4.12), and 4:1:400 (Figure 4.13) are shown, using either naph-ONP 1 or naph-ONP 2. No discrete assemblies are obvious, although the rods do appear more spatially dispersed on the grid than typical CTAB rods are; perhaps they are separated by ONPs (which are not high-contrast so do not typically appear in TEM images). It is equally possible that assemblies are not forming, and there are a few reasons for why this might be. The naphthalene groups are separated from the polymer backbone by only a short spacer (a few bonds in length), and their hydrophobic character probably encourages them to sequester inside the body of the ONP in aqueous solution. Furthermore, naphthalene may not be electron-rich enough to form the charge-transfer complexes with MV^{2+}; most literature reports use naphthol derivatives or naphthalenes with other electron-donating substituents. The ONPs may also be too flexible, without a defined shape—unlike inorganic nanoparticles—to promote assembly of discrete morphologies. Future studies will use ONPs functionalized with long-linker naphthol groups.

4.4 Experimental

4.4.1 General

All materials were used as received, unless otherwise indicated. Nanoparticle reactions were performed in new polyethylene centrifuge tubes, new glass vials, or glassware cleaned with aqua regia. Reported reaction temperatures refer to the temperature of the heating medium. Ultrapure deionized water was collected from a Barnstead NANOPURE water filtration system. Dynamic light scattering (DLS) and ζ-potential data were taken on a Brookhaven ZetaPALs analyzer. DLS viscosity and refractive index were set as water parameters for aqueous samples, water parameters for DMF samples, and chloroform parameters for chloroform samples (for chloroform: at 20°C, viscosity = 0.593 cP and nD = 1.490; at 50°C, viscosity = 0.425 cP and nD = 1.477). UV-vis spectra were obtained on a Varian Cary Scan 500 spectrometer. Transmission electron microscopy (TEM) samples were prepared on Lacey Formvar/Carbon, 200 mesh, 97 μm grids (Ted Pella), and TEM images were taken on a JEOL 2100 instrument and processed with Gatan DigitalMicrograph and ImageJ.

Nuclear magnetic resonance (NMR) spectra were acquired using a Varian Unity 400 MHz, Varian Unity Inova 400

MHz, Varian Unity 500 MHz, Varian VXR 500 MHz, or Varian Unity Inova narrow-bore 500 MHz spectrometer. Spectra were processed with MNova or VnmrJ. Chemical shifts are reported in parts per million (ppm) and were referenced to the residual proton solvent peak. Splitting patterns are designated as s (singlet), d (doublet), t (triplet), q (quadruplet), dd (doublet of doublets), m (multiplet), and br (broad).

4.4.2 Synthesis of hydrogen-bonding modules

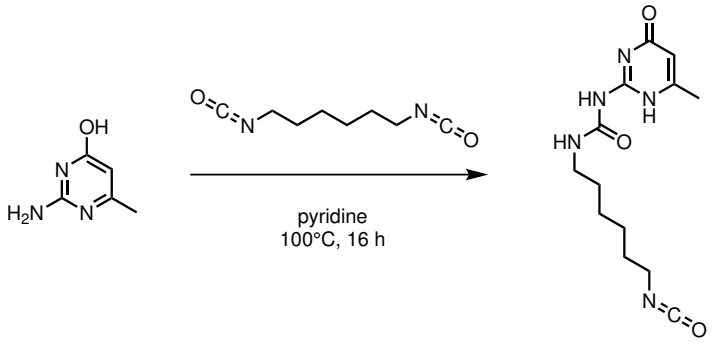

2(6-isocyanatohexylaminocarbonylamino)-6-methyl-4[1H]pyrimidinone (UPy-isocyanate)[142]

A solution of 2-amino-4-hydroxy-6-methylpyrimidine (5.0 g, 40 mmol), hexamethylene diisocyanate (45 mL, 280 mmol), and distilled, anhydrous pyridine (3.3 mL, 40 mmol) was stirred at 100°C under nitrogen for 16 h. The mixture was cooled to RT, and pentane (60 mL) was added. The white precipitate was vacuum filtered and washed with acetone, and then dried *in vacuo* to afford UPy-isocyanate as a fluffy white powder (11.5 g, 98%). ^{1}H NMR (500 MHz; $CDCl_3$): δ 13.11 (s, 1H), 11.86 (s, 1H), 10.19 (s, 1H), 5.82 (s, 1H), 3.29 (m, 4H), 2.23 (s, 3H), 1.68-1.57 (m, 4H), 1.48-1.32 (m, 4H) ppm (Figure 4.14).

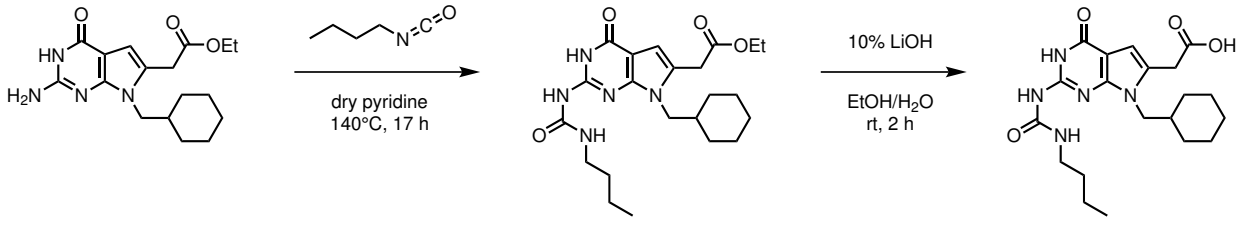

N9-cyclohexyl-ureido-7-deazaguanine ethyl ester (cyclohexyl-DeUG ethyl ester)

Butylisocyanate (70 μL, 0.6 mmol) was added slowly to a solution of (2-amino-7-cyclohexylmethyl-4-oxo-4,7-dihydro-3H-pyrrolopyrimidin-6-yl)-acetic acid ethyl ester (57 mg, 0.2 mmol) in distilled, anhydrous pyridine (2 mL). The

slightly yellow mixture was stirred at 140°C under nitrogen for 17 h. The red-brown solution was cooled to RT and concentrated *in vacuo*. The deep red oil was dissolved in chloroform (5 mL) and washed with water (7 x 5 mL), and the organic layer was dried over sodium sulfate, filtered, and concentrated. The red residue was triturated with 1:1 (v:v) petroleum ether:acetone (3 mL) to afford cyclohexyl-DeUG ethyl ester as a fine off-white powder (14 mg, 19%). ^{1}H NMR (500 MHz; $CDCl_3$): δ 11.13 (br s, 1H), 6.77 (s, 1H), 4.19 (q, 2H), 3.86 (d, 2H), 3.72 (s, 2H), 3.45 (dt, 2H), 1.72 (m, 6H), 1.56-1.46 (m, 4H), 1.28 (t, 3H), 1.17 (m, 3H), 0.98-0.96 (m, 5H) ppm (Figure 4.15).

N9-cyclohexyl-ureido-7-deazaguanine carboxylic acid (cyclohexyl-DeUG acid)

To a solution of cyclohexyl-DeUG ethyl ester (10 mg) in 95% ethanol (0.5 mL) was added 10% (w/v) aqueous LiOH (0.5 mL) to make a 1:1 (v:v) ethanol:LiOH mixture. The mixture was stirred at RT for 2 h and washed with chloroform (3 x 1 mL). The aqueous portion was acidified with 5 M HCl to pH 2 to precipitate the product as a white powder.

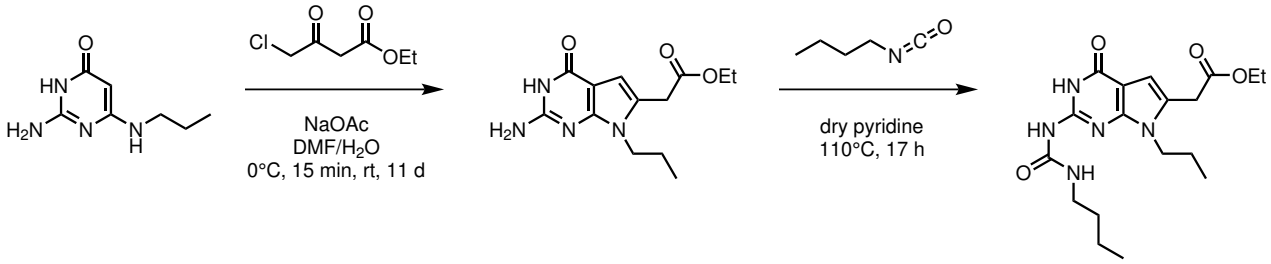

N9-propyl-deazaguanine ethyl ester (propyl-deazaguanine ethyl ester)

To a stirred suspension of 2-amino-6-(propylamino)pyrimidinone (1.0 g, 5.9 mmol) in DMF (48 mL) was added sodium acetate (0.49 g, 5.9 mmol) in water (12 mL). The solution was cooled in an ice-water bath, and ethyl-4-chloroacetoacetate (1.7 mL, 12 mmol) was slowly added dropwise. The pale yellow solution was allowed to warm to room temperature. After 1 h the solution became deep red and darkened over the course of 24 h. After 11 days of stirring at RT, the solution had become orange-red with a pale yellow precipitate. The suspension was poured into water (150 mL) and vacuum filtered, and the orange filtrate was concentrated *in vacuo* to yield a red residue. The residue was diluted with $CHCl_3$ (50 mL) and washed with brine (2 x 25 mL) and water (2 x 25 mL). The aqueous portions were backextracted with $CHCl_3$ (2 x 25 mL). The organic layer was washed with brine again (2 x 25 mL), dried over sodium sulfate, filtered, and concentrated to yield a thick red-orange oil. The residue was triturated with 9:1 (v:v) petroleum ether:ethyl acetate (3 x 100 mL) to yield an orange-red powder (1.25 g, 76%). ^{1}H NMR (500 MHz; DMSO-d_6): δ 10.23 (s, 1H), 6.18 (s, 1H), 6.10 (s, 1H), 4.09 (q, 2H), 3.80 (t, 2H), 3.72 (s, 2H), 1.61 (sextet, 2H), 1.19 (t, 3H), 0.82 (t, 3H) ppm (Figure 4.16).

N9-propyl-ureido-7-deazaguanine ethyl ester (propyl-DeUG ethyl ester)

Butylisocyanate (0.7 mL, 6 mmol) was added slowly via syringe to a solution of propyl-deazaguanine ethyl ester (0.5 g, 2 mmol) in distilled, anhydrous pyridine (13 mL). The mixture was stirred at 110°C under nitrogen for 17 h. The red-brown solution was cooled to RT and concentrated *in vacuo*. The red-black tar-like residue was dissolved in chloroform (10 mL) and washed with water (4 x 10 mL). The organic layer was dried over sodium sulfate, filtered, and concentrated. The thick red-black oil was triturated with 1:1 (v:v) petroleum ether:acetone (2 x 25 mL) to yield a red-orange powder. ^{1}H NMR (500 MHz; $CDCl_3$): δ 6.79 (s, 1H), 4.19 (q, 2H), 3.97 (t, 2H), 3.72 (s, 2H), 3.44 (q, 2H), 1.77 (q, 2H), 1.62 (dt, 2H), 1.47 (dq, 2H), 1.28 (t, 3H), 0.97 (dt, 6H) ppm)Figure 4.17).

4.4.3 Synthesis of cucurbituril complex modules

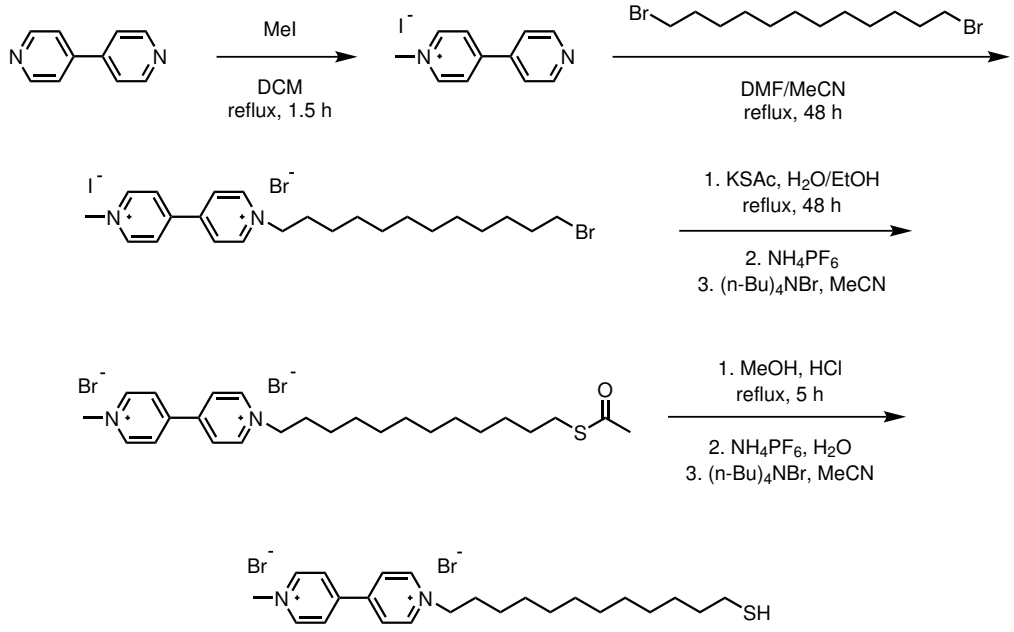

1-methyl-4,4′-bipyridinium iodide

4,4'-bipyridine (2.0 g, 12.8 mmol) was dissolved in dichloromethane (30 mL). Methyl iodide (1.0 mL, 16.1 mmol) in dichloromethane (10 mL) was added dropwise under stirring, and the deep yellow mixture was boiled at reflux for 1.5 h. The mixture was vacuum filtered to yield the crude product as a bright yellow solid, which was then recrystallized in methanol (20 mL). The yellow crystals were dried by vacuum filtration and washed with ether to afford the product (1.15 g, 30%). ^{1}H NMR (400 MHz; D_2O): δ 8.87 (d, 2H), 8.75 (d, 2H), 8.36 (d, 2H), 7.88 (d, 2H), 4.41 (s, 3H) ppm

(Figure 4.18).

12-bromo-1-(methyl-4,4′-bipyridinium)-dodecane

1-methyl-4,4'-bipyridinium iodide (1.1 g, 3.69 mmol) and 1,12-dibromododecane (2.4 g, 7.27 mmol) were dissolved in a mixture of DMF (6 mL) and acetonitrile (30 mL), and the orange solution was boiled at reflux for 48 h. The orange solid was isolated by vacuum filtration to yield the product (2.11 g, 91%). ^{1}H NMR (400 MHz; DMSO-d_6): δ 9.39 (d, 2H), 9.29 (d, 2H), 8.78 (d, 2H), 8.76 (d, 2H), 4.68 (t, 2H), 4.44 (s, 3H), 3.52 (t, 2H), 1.97 (t, 2H), 1.78 (t, 2H), 1.31-1.25 (m, 16 H) ppm (Figure 4.19).

1-methyl-4,4′-bipyridinium-dodecanethioacetate

12-bromo-1-(methyl-4,4'-bipyridinium)-dodecane (2.0 g, 3.2 mmol) was dissolved in a mixture of water (200 mL) and ethanol (80 mL). The flask was flushed with Ar, and potassium thioacetic acid (0.91 g, 8 mmol) was added. The yellow-orange solution was boiled at reflux under Ar for 48 h, after which the solution had become violet. Ammonium hexafluorophosphate (2.09 g, 12.8 mmol) was added, and the resulting off-white/yellow precipitate was isolated by vacuum filtration. The powder was redissolved in acetonitrile (50 mL) and treated with tetrabutylammonium bromide (4.13 g, 12.8 mmol) to produce a bright yellow precipitate. The solid was vacuum filtered to yield the product (1.70 g, 92%). ^{1}H NMR (500 MHz; DMSO-d_6): δ 9.38 (d, 2H), 9.28 (d, 2H), 8.78 (d, 2H), 8.75 (d, 2H), 4.67 (t, 2H), 4.44 (s, 3H), 2.81 (t, 2H), 2.31 (s, 3H), 1.97 (m, 2H), 1.48 (m, 2H), 1.31-1.24 (m, 16 H) ppm (Figure 4.20).

1-methyl-4,4′-bipyridinium-dodecanethiol bisbromide (MV2+-thiol)

To 1-methyl-4,4'-bipyridinium-dodecanethioacetate (1.6 g, 2.8 mmol) dissolved in methanol (22.5 mL) was added a 1.25 M solution of HCl in methanol (22.5 mL). The mixture was boiled at reflux for 5 h. A pale yellow oil was isolated by rotary evaporation and resuspended in water (50 mL). Treatment with ammonium hexafluorophosphate (1.83 g, 11.2 mmol) produced a white precipitate, which was collected by vacuum filtration and redissolved in acetonitrile (50 mL). Tetrabutylammonium bromide was then added, and the resulting bright yellow precipitate was isolated by vacuum filtration to yield the product (0.94 g, 63%). ^{1}H NMR (500 MHz; D_2O): δ 9.12 (d, 2H), 9.06 (d, 2H), 8.55 (d, 2H), 8.53 (d, 2H), 4.73 (t, 2H), 4.51 (s, 3H), 2.54 (t, 2H), 2.09 (t, 2H), 1.58 (m, 2H), 1.39-1.27 (m, 16H) ppm (Figure 4.21).

4.4.4 Synthesis of particles

CTAB rods

Gold nanorods of controlled aspect ratio were synthesized in high yield via a surfactant-stabilized, seed-mediated growth method. To make 1-2 nm spherical seeds, fresh, cold sodium borohydride ($NaBH_4$) (0.6 mL, 0.01 M) was added to a solution of chloroauric acid ($HAuCl_4$) (250 μL, 0.01 M) in cetyltrimethylammonium bromide (CTAB) (9.75 mL, 0.1 M). The seed solution was stirred rapidly for 10 minutes, and then allowed to "age" for at least 1 hour to quench excess $NaBH_4$. To synthesize rods of varying aspect ratio, a certain volume (0.01 to 0.1 mL) of 0.01 M silver nitrate ($AgNO_3$), chloroauric acid (0.5 mL, 0.01 M), and ascorbic acid (55 μL, 0.1 M) were added to CTAB (9.5 mL). After the solution was inverted several times until it became colorless, seed (12 μL) was added and the mixture inverted again. The rods were allowed to form overnight (14-16 hours), centrifuged twice at 11,000 rcf for 15 m to remove excess CTAB, and redispersed in water. The aspect ratio was controlled by the amount of silver nitrate added. To make a large batch of rods, a typical procedure was as follows: In a 1 L Erlenmeyer flask was added 760 mL 0.1 M CTAB, 0.48 mL 0.1 M $AgNO_3$, 40.0 mL $HAuCl_4$, 4.4 mL 0.1 ascorbic acid, and 960 μL gold seed. The mixture was swirled vigorously and allowed to sit 22 h, after which it was centrifuged twice at 11,000 rcf for 20 minutes.

4 nm PAH AuNPs

PAH AuNPs were synthesized by polyelectrolyte wrapping of 4 nm citrate AuNPs. In a typical flow reactor synthesis, 20.0 mL of $HAuCl_4$ (0.01 M) and 6.0 mL of sodium citrate (0.1 M) were combined in an 2 L Erlenmeyer flask containing 1600 mL of nanopure deionized water. In a second 2 L Erlenmeyer flask, 1614.0 mL of nanopure deionized water was chilled in an ice-water bath. 12.0 mL of chilled aqueous $NaBH_4$ (0.1 M) was added to the cold flask, which was swirled briefly. A flow line was placed into each 2 L flask and the flow reactor pump was started at a setting of 40 mL/min. Once the two solutions combined in the flow reactor line, the solution turned a light red-brown and the synthesized particles were collected in a 4 L polyethylene bottle with gentle stirring. The resulting citrate AuNP solution was then stirred for at least 3 h. The 4 nm citrate AuNPs were then wrapped with 15,000 g/mol M_w PAH to prepare 4 nm PAH AuNPs. To the approximately 3.2 L of as-synthesized particles, 32.0 mL of NaCl (100 mM) and 100.0 mL of a PAH solution (10 mg/mL in 1 mM NaCl) was added with vigorous stirring. The nanoparticles were then allowed to stir overnight in the wrapping solution. The PAH AuNPs were subsequently concentrated in a diafiltration membrane, then purified by centrifugation (13,000 rcf for 55 min) or diafiltration (15,000 MWCO membrane).

4 nm $MPNH_2$ AuNPs

400 mL of nanopure deionized water, 0.9 mL of $HAuCl_4$ (0.1 M), 5.7 mL of HCl (0.1 M), and 0.5 mL of 3-aminopropanethiol (0.1 M) were stirred at vortex for 10 min. Then, 4.0 mL of fresh sodium borohydride solution (0.1 M) was added to the mixture. The solution rapidly turned red-brown and was stirred for 3 h. The $MPNH_2$ AuNPs were then purified by diafiltration, as described above.

4.4.5 Functionalization of particles

Polyelectrolyte-wrapped rods (PAA or PAH)

CTAB rods were dispersed in water (1 mL), and NaCl solution (100 μL, 0.01 M) and 10 mg/mL (in 0.001 M NaCl) poly(acrylic acid) (PAA) solution (200 μL) were added at once. The solution was vortexed for 1 min and allowed to sit undisturbed for 2.5 h. Rods were purified by centrifugation at 7,000 rcf for 6 min and redispersed in water. The process was repeated for poly(allylamine hydrochloride) (PAH). After PAH rods were centrifuged, the pellet was redispersed in water or organic solvent.

4-aminothiophenol rods, two-step ligand exchange

To a stirring solution of mPEG rods in THF (1 mL) was added dropwise 4-aminothiophenol in THF (1 mL, 5 mg/mL). The solution was stirred for 24 h, at which point the solution had changed color from red-brown to gold-green with some visible precipitation. The mixture was centrifuged at 5,000 rcf for 20 min.

4-aminothiophenol rods, direct addition

To a stirring solution of concentrated CTAB rods in water (1 mL, 12 nM) was added dropwise 4-aminothiophenol in THF (1 mL, 5 mg/mL). The solution was stirred for 24 h, at which point the solution was still deeply-colored with a metallic sheen and visible precipitation of some rods to the sides of the vial. The mixture was centrifuged at 5,000 rcf for 20 min.

4-aminothiophenol rods, anhydrous

To a CTAB-saturated growth solution of CTAB rods (30 mL), prior to centrifugation or purification, was added slowly dropwise a concentrated solution of 4-aminothiophenol (0.25 g) in THF (3 mL) while vigorously stirring. The solution changed color from red-brown to blue-grey, and rods slowly precipitated over 45 h as the solution was stirred. The black precipitate was centrifuged at 3000 rcf for 10 m, the yellow-lime supernatant decanted, and the precipitate centrifuged twice in THF at 3000 rcf for 5 min. The precipitate was redispersed in THF via sonication.

UPy rods, PAH intermediate

To twice-centrifuged PAH rods in DMF (0.5 mL) was added a solution of UPy-isocyanate (2.5 mg) and DBU (5 μL) in DMF (0.5 mL). The mixture was sonicated for 10 min, then allowed to sit for 48 h. The rods precipitated out of solution within 30 min. They were purified by centrifugation twice at 5000 rcf for 15 min in DMF and were dried *in vacuo* at 70°C. The dried rods were redispersed in chloroform via sonication and were centrifuged twice at 5000 rcf for 15 min in chloroform.

UPy rods, 4-aminothiophenol intermediate

To aminothiophenol rods (direct addition) in DMF (0.5 mL) was added a solution of UPy-isocyanate (2.5 mg) and DBU (1 μL) in DMF (0.5 mL). The mixture was sonicated for 5 min, then allowed to sit for 60 h. The rods precipitated out of solution, were purified by centrifugation at 5000 rcf for 15 min, and could be redispersed in DMF or chloroform with sonication.

DeUG rods

To twice-centrifuged PAH rods in DMF (0.5 mL) was added a solution of DeUG-isocyanate (2.5 mg) and DBU (5 μL) in DMF (0.5 mL). The mixture was sonicated for 10 min, then allowed to sit for 48 h. The rods settled to a lower layer, but did not precipitate. They were purified by centrifugation twice at 5000 rcf for 15 min in DMF and were dried *in vacuo* at 70°C. The dried rods were redispersed in chloroform via sonication and were centrifuged twice at 5000 rcf for 15 min in chloroform.

MV^{2+} rods

To 10 mL of a 1 x 10^{-4} M solution of MV^{2+}-thiol in water (1 x 10^{-6} mol) was added 5 mL of 1.87 nM AuNRs (9.4 x 10^{-12} mol). The mixture was gently agitated for 20 h. The rods were centrifuged once at 12000 rcf for 20 min.

4.4.6 Assembly studies

Hydrogen-bonding competition studies

Solutions of hydrogen-bonding rods were studied by dynamic light scattering (DLS). UPy or DeUG rods were dispersed in chloroform via sonication. To the rod solution (1 mL, 1 nM) was added a chloroform solution (0.5 mL) of bishexyl-DAN (1 mg). The mixture was shaken for 1 min before each DLS measurement. Samples were allowed to reach equilibrium to either 20°C or 50°C in the DLS instrument, and measurements were taken at that temperature.

Cucurbituril, methyl viologen rods, naphthalene organic nanoparticles

Mixtures of CB[8], MV^{2+}-functionalized gold nanorods, and naph-ONPs were prepared in varying molar ratios. For each mixture, CB[8] was added to the rods and gently vortexed for 5 min. The solution was treated with naph-ONPs and gently vortexed for another 5 min, and then gently agitated for 24 hours.

4.4.7 Supplementary information

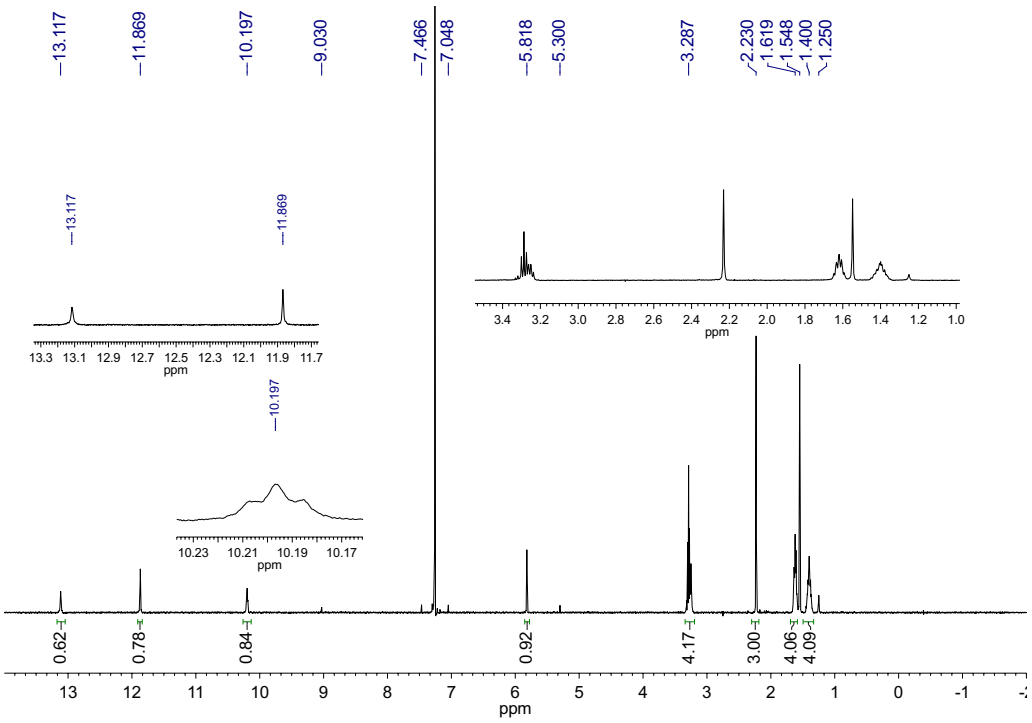

Figure 4.14 ^{1}H NMR: UPy-isocyanate.

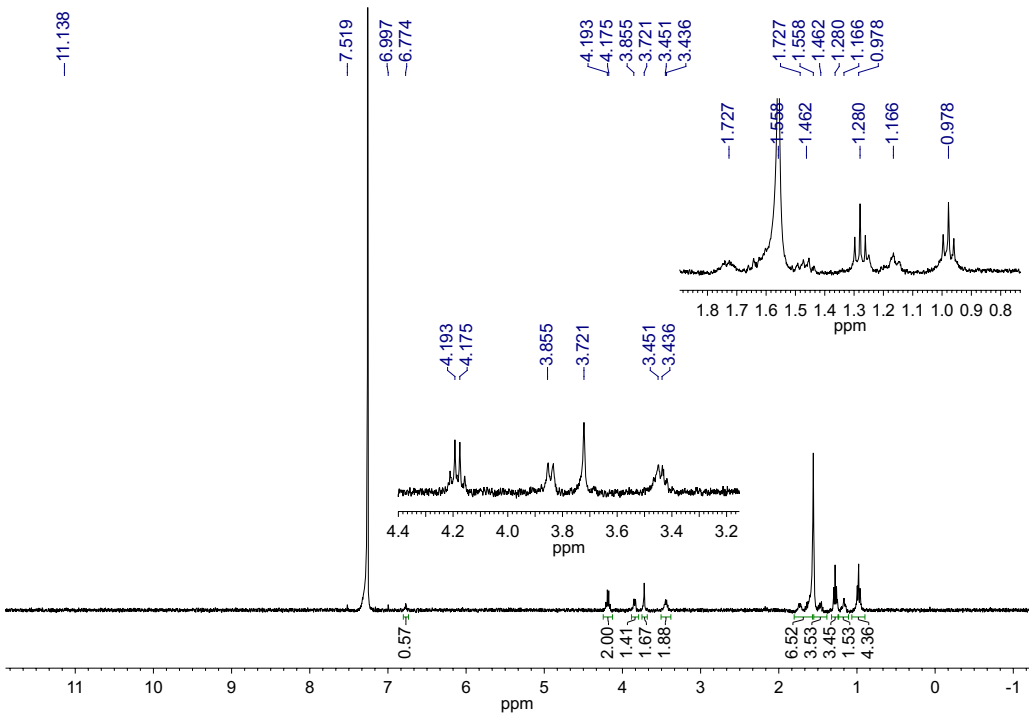

Figure 4.15 [1]H NMR: N9-cyclohexyl-ureido-7-deazaguanineethylester.

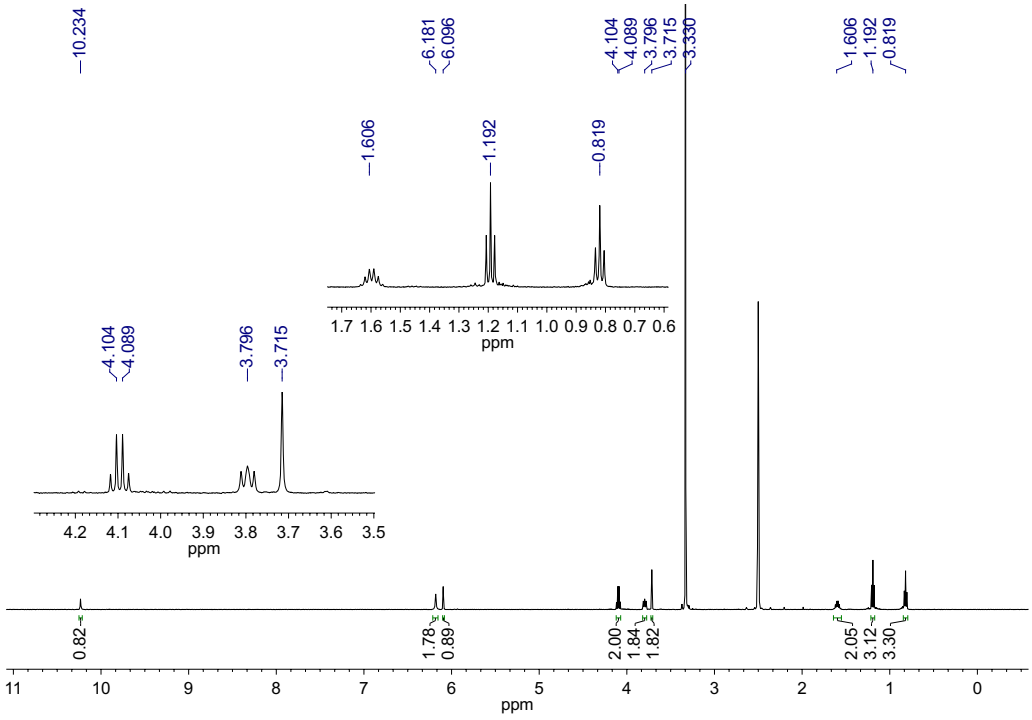

Figure 4.16 [1]H NMR: N9-propyl-deazaguanineethylester.

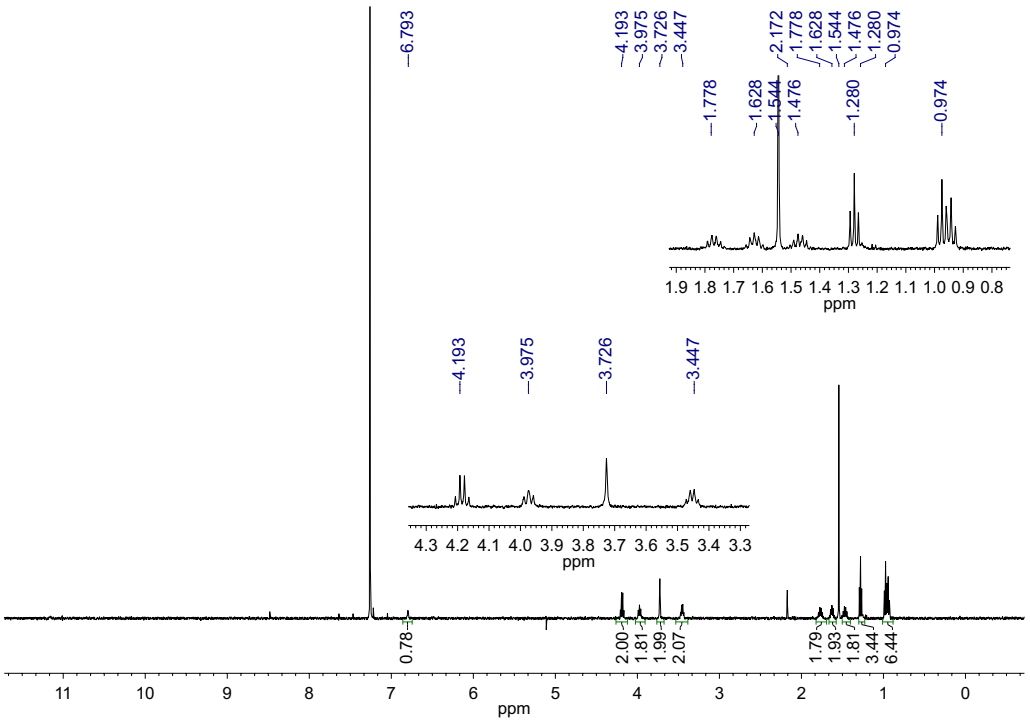

Figure 4.17 [1]H NMR: N9-propyl-ureido-7-deazaguanineethylester.

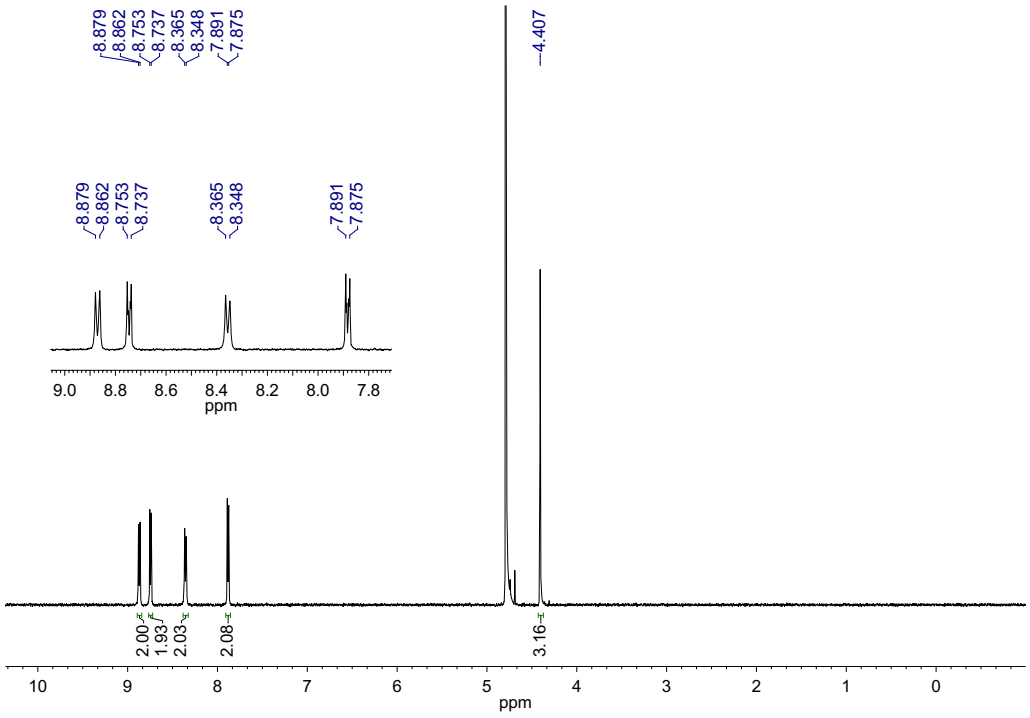

Figure 4.18 [1]H NMR: 1-methyl-4,4′-bipyridinium iodide.

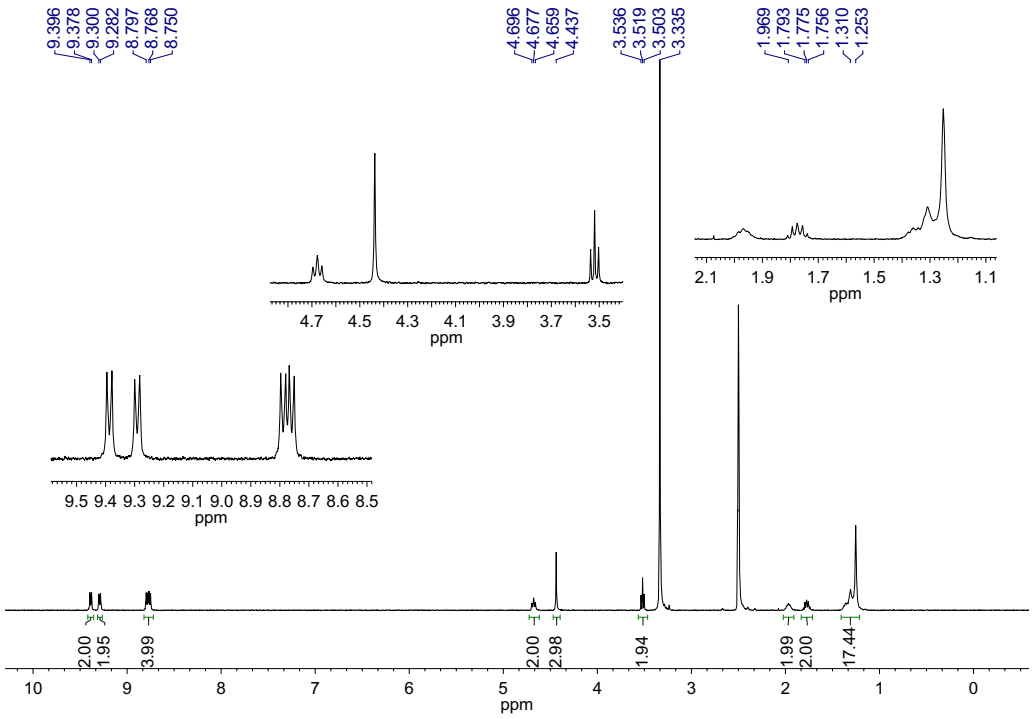

Figure 4.19 [1]H NMR: 12-bromo-1-(methyl-4,4′-bipyridinium)-dodecane.

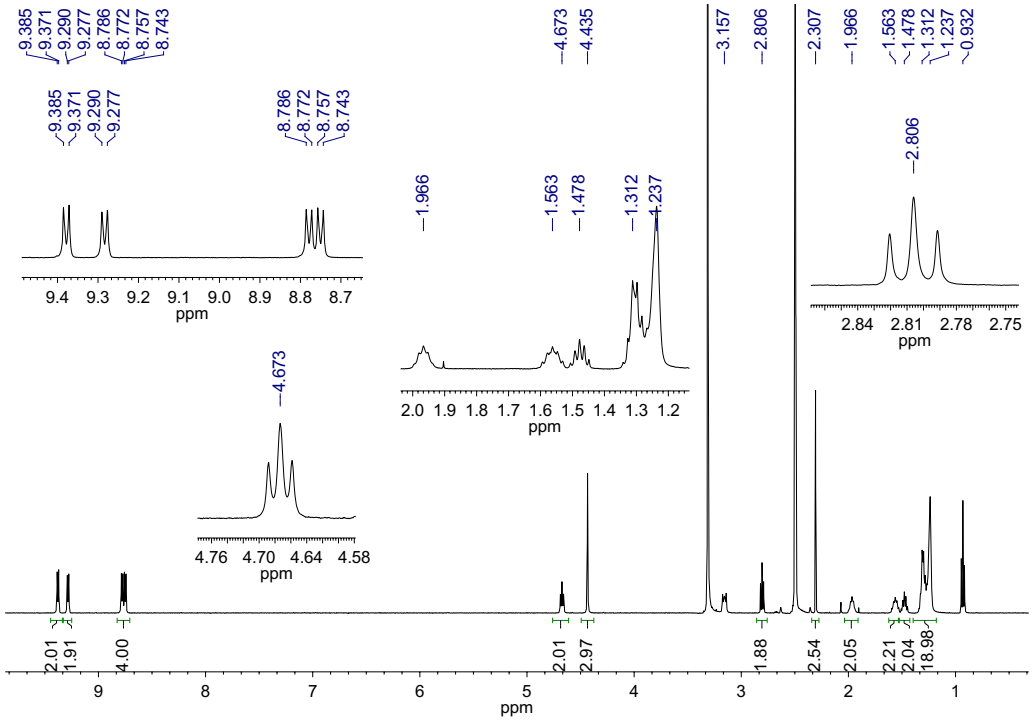

Figure 4.20 [1]H NMR: 1-methyl-4,4′-bipyridinium-dodecanethioacetate.

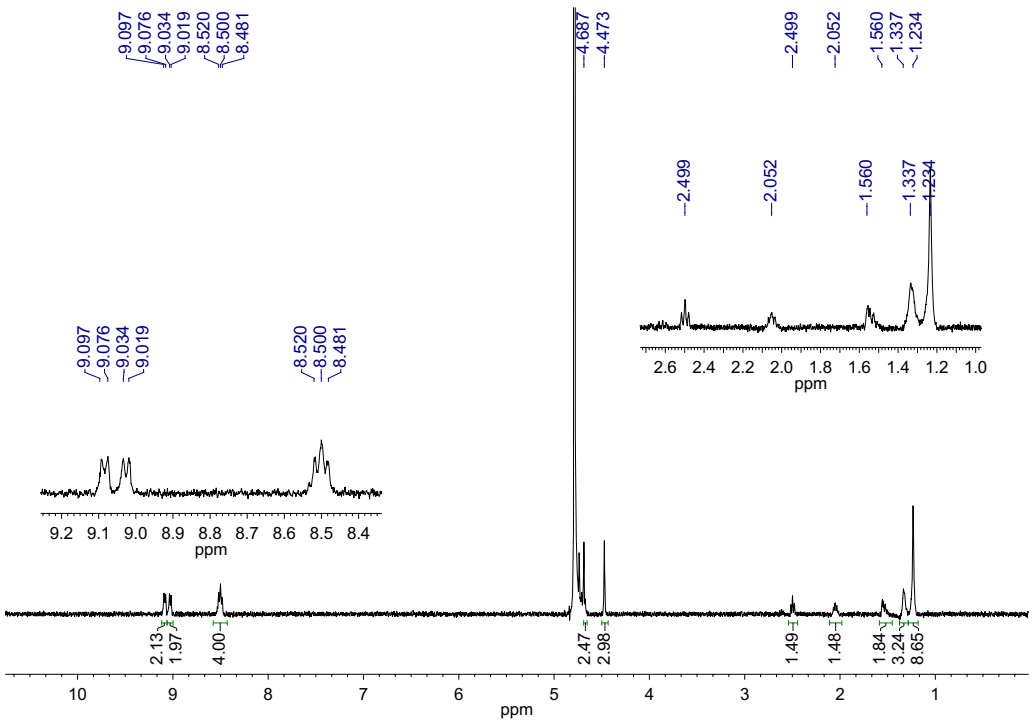

Figure 4.21 ^{1}H NMR: 1-methyl-4,4′-bipyridinium-dodecanethiol bisbromide.

Chapter 5

NMR Studies of Complex Nanoparticle-Biology Interactions

5.1 Introduction

Engineered nanoparticles hold promise for varied technologies, but the consequences of their ubiquity are just beginning to be understood. Particles on the 1 – 100 nm length scale have fundamentally interesting properties that are exploited in consumer, environmental, and biomedical applications. In biomedicine, nanoparticles are being directly used for pharmaceutics, therapeutics, imaging, diagnostics, and drug delivery, because their tiny dimensions are suited for blood circulation and cell uptake (Figure 5.1). Particles are also used in bulk quantities to clean environmental contaminants from water and air, or to power batteries in electric vehicles. But the short- and long-term events in the lifetime of a particle, especially after it completes its intended function, are still largely unknown.[143,144] A nanoparticle comes into contact with and interacts with systems from the ecosystem and organismal levels down to the cellular and molecular regime (Figure 5.2). What effects does a particle exert on its surroundings—biological and environmental—and what are the molecular mechanisms driving those interactions? The answers to these questions will lead the design of future generations of particles that leave their environments without a trace.

Nanoparticles are known to acquire a corona of matter, including proteins and other biomolecules, when they are submerged in biological fluids.[146,147] This biomolecular blanket dramatically changes the surface chemistry of the particle and dictates its fate in that environment.[148,149] The extent of corona formation depends on initial charge, size, functionalization, and other particle qualities, but specific causes and details of the mechanism are not clear. Recently, as interest in lipid interactions has grown, it has been proposed that lipids also have the tendency to form coronas.[150] At the interface of a particle and a cell, the particle may cloak itself in lipids pulled from the cell membrane, either disturbing the cell's integrity or promoting cellular uptake.

To understand the causal molecular mechanisms, it is necessary to probe the interface between nanoparticles and biological systems. Unfortunately, it remains a huge challenge to extract molecular-level information about events at that interface, especially in a living system, because no perfect experimental technique exists to do so. Supported

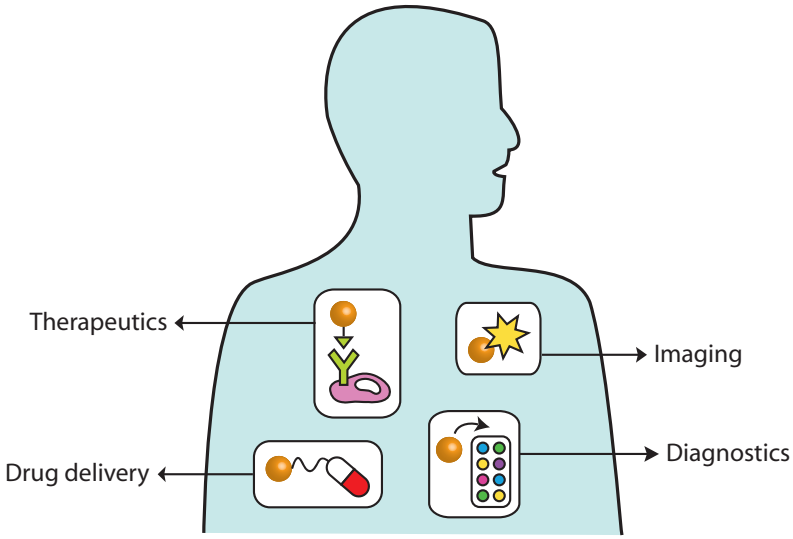

Figure 5.1 Nanotechnology has the potential to improve human health through use in therapeutics, imaging, drug delivery, and diagnostics.[145]

lipid bilayers and suspended lipid vesicles can act as effective, if somewhat rudimentary, models for phospholipid cell membranes. Binding interactions of particles on these constructed bilayers may be studied by a selection of techniques, including nonlinear optical spectroscopies such as second harmonic generation (SHG) and sum frequency generation (SFG), quartz crystal microbalance with dissipation monitoring (QCM-D), X-ray photoelectron spectroscopy (XPS), atomic force microscopy (AFM), and fluorescence microscopy.[151]

Nuclear magnetic resonance (NMR) spectroscopy can extract functional group-specific detail at a degree inaccessible by most techniques. This work presents NMR data that is critical to understanding the phenomena that govern the nano-bio interface. Because NMR requires fairly large amounts of sample, the NMR data hones in on what features are worth a further look with more sensitive techniques, in realistic concentrations.

Phospholipids were chosen for their biological relevance and physical properties. The phase transition temperature of a lipid bilayer, T_c, is the temperature at which the bilayer changes from a gel (solid) to fluid (liquid) phase. T_c is influenced primarily by the strength of intermolecular interactions between neighboring lipid molecules, which are in turn determined by the length and degree of saturation in the aliphatic chain. Longer chains subject more van der Waals forces on their neighbors, and saturated chains pack tightly together with very little free space. On the other hand, unsaturated chains introduce rigid kinks at the double bonds that disrupt ordered packing and reduce the strength of intermolecular forces. Therefore, lipids with long saturated chains tend to have very high T_c values and are more likely to be in the gel phase at ambient temperature, whereas lipids with short or unsaturated chains have lower T_c values. The lipid molecules in fluid bilayers freely diffuse laterally, which repair gaps when damage occurs to the bilayer. Lipids in

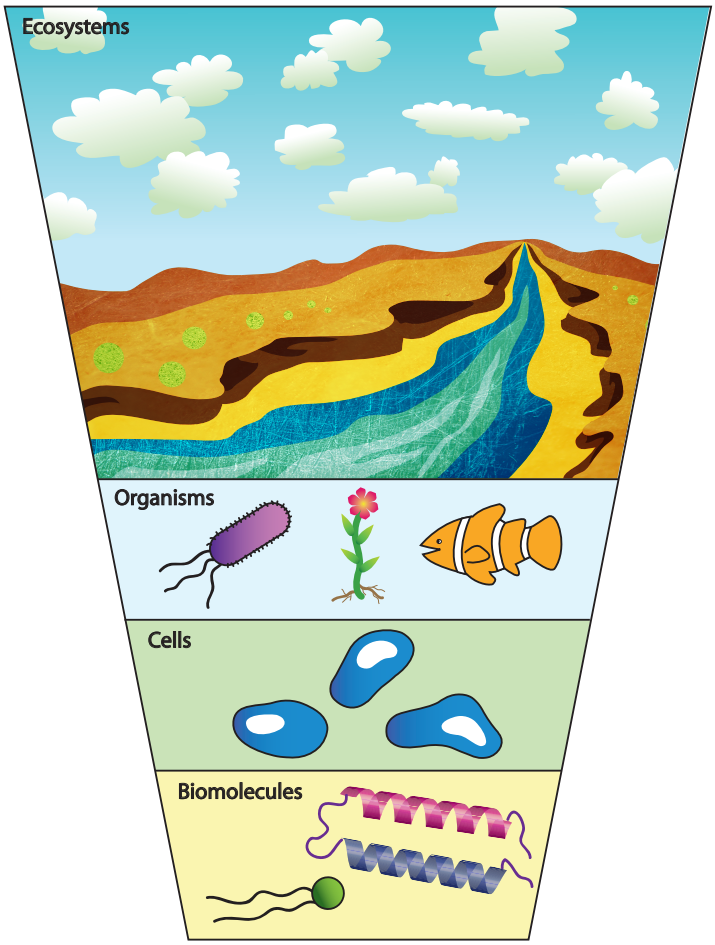

Figure 5.2 Nanoparticles interact with biological systems at several levels, from the ecosystem and organisms to cells and molecules.[145]

a gel bilayer are locked into position and cannot easily fill in holes, so they are more likely to suffer irreparable damage.

The zwitterionic lipid 1,2-dimyristoyl-sn-glycero-3-phosphocholine (DMPC) (Figure 5.4a) and negatively-charged lipid 1,2-dimyristoyl-sn-glycero-3-phospho-(1-rac-glycerol) (DMPG) (Figure 5.4b) were selected as high-T_c lipids that form a gel bilayer at 20°C (T_c = 24°C and 23°C, respectively). The zwitterionic lipid 1,2-dioleoyl-sn-glycero-3-phosphocholine (DOPC) (Figure 5.4c) and positively-charged lipid 1,2-dioleoyl-3-trimethylammonium-propane (DOTAP) (Figure 5.4d) were chosen as low-T_c, liquid bilayer-forming lipids (T_c = -17°C). PC-type lipids are pervasive in biological systems as one of the major constituents of cell membranes, whereas PG makes up usually 1-2% of membranes in animals and up to 20% in bacterial membranes.

Surface charge appears to be one variable that heavily influences a particle's behavior in a biological system.[152,153]

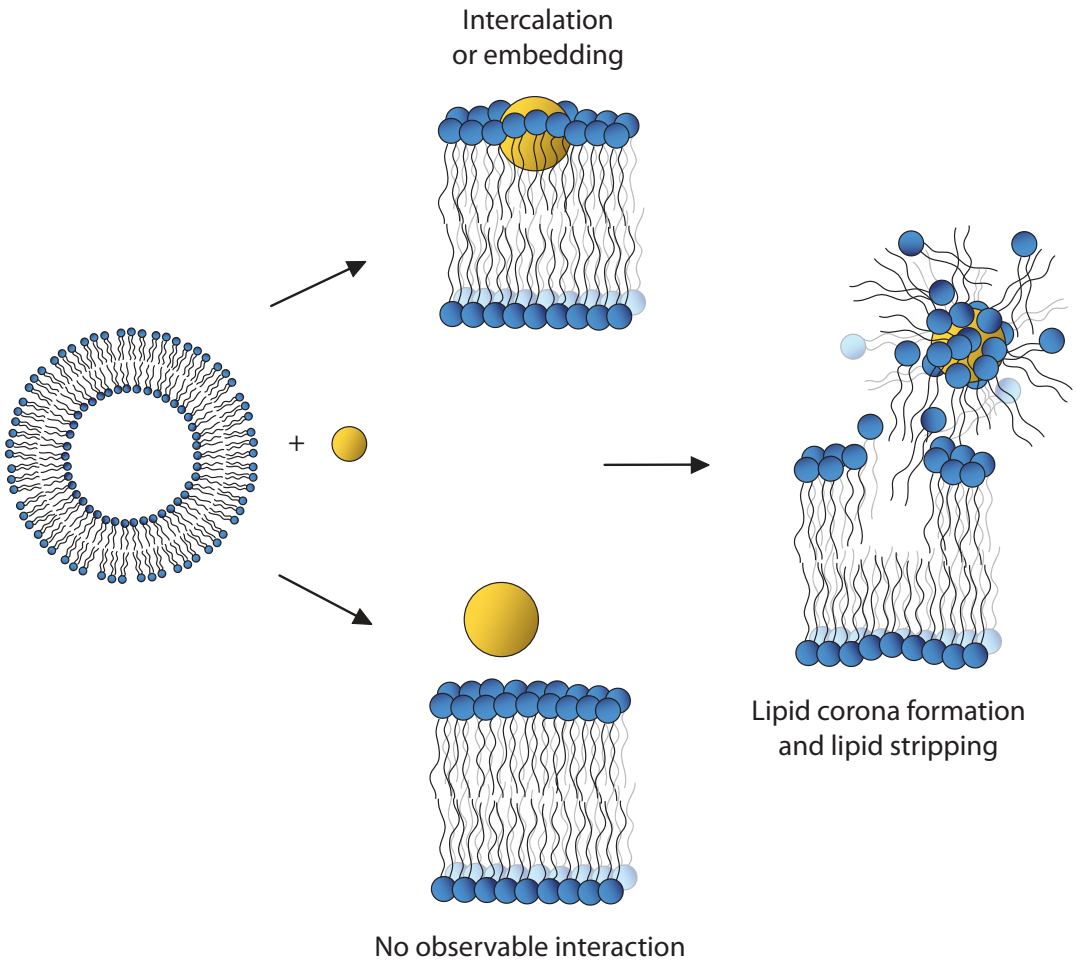

Figure 5.3 Nanoparticles and lipid vesicles may interact in a variety of pathways.

A swath of evidence[154,155] has found that cationic particles[156] more adversely impact cell membranes than anionic or neutral particles do.[157,158] 4 nm gold nanoparticles were functionalized with a variety of ligands: the cationic polyelectrolyte poly(allylamine hydrochloride) (PAH), anionic mercaptopropionic acid (MPA), and cationic mercaptopropylamine ($MPNH_2$).

5.2 Lipid corona formation: DMPC:DMPG and PAH gold particles

Lipid vesicles composed of a 9:1 mixture of DMPC and DMPG were prepared in Tris buffer in D_2O (10 mM Tris, 100 mM NaCl, pD 7 – 8). The high salt concentration was chosen both to simulate biological conditions, and to screen charges on both the vesicles and particles to limit the influence of electrostatics in their interactions. Vesicles (12 nM) were allowed to interact with PAH AuNPs (10 nM) for 2 hours, at which point the NMR spectra were acquired.

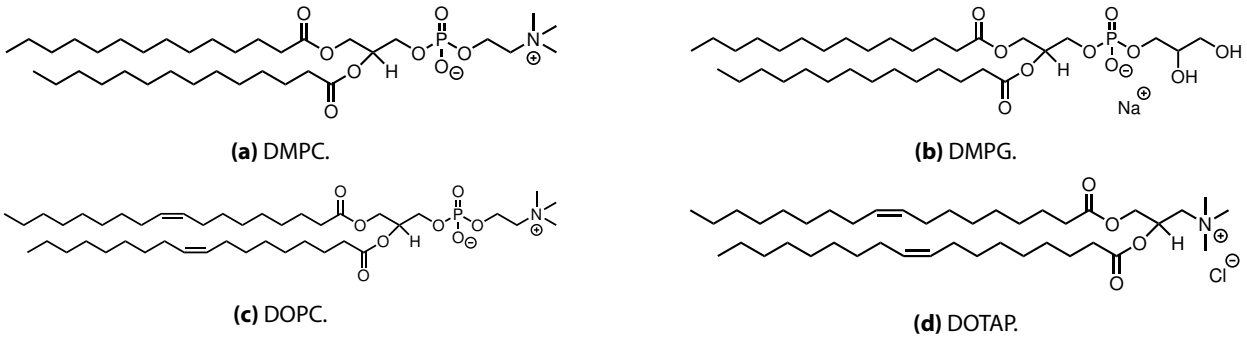

(a) DMPC. **(b)** DMPG. **(c)** DOPC. **(d)** DOTAP.

Figure 5.4 Structures of lipids used in this study.

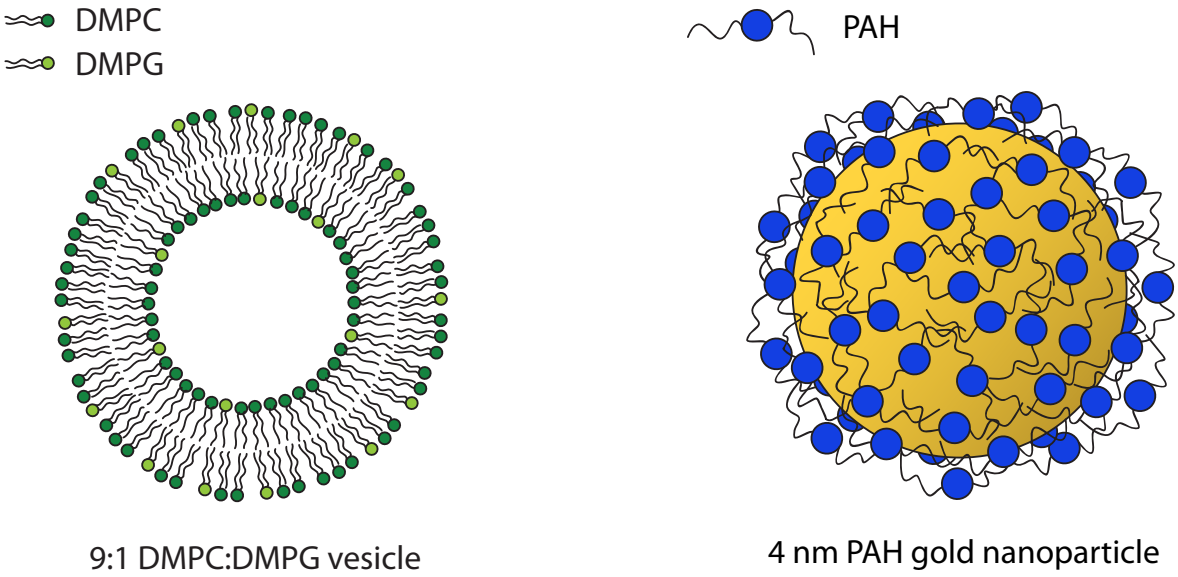

Figure 5.5 The components of the DMPC:DMPG lipid vesicle and 4 nm PAH AuNP system. Not to scale.

In the lipid vesicle spectrum, only the ammonium headgroup protons ($-N-CH_3$, 3.16 ppm) produce a visible, strong signal; the hydrocarbon proton resonances are broadened beyond detection because the lipids exist in the lipid ordered phase at the experimental temperature (20°C, below the transition temperatures of DMPC and DMPG). The sharp peak around 3.6 ppm is identified as Tris buffer. Upon exposing the vesicles to PAH AuNPs, the headgroup proton resonance disappears (Figure 5.6, Table 5.1). This observation can best be explained by attachment of the headgroup to another species, immobilizing the protons and broadening the resonance into the baseline.

The PAH proton resonances shed insight into the chemical environment at the surface of the gold nanoparticle (Figure 5.7, Table 5.1). Free PAH polymer gives rise to three distinct resonances corresponding to its chain group methylene group ($-R_2-CH_2$, 1.43 ppm), chain group methine group ($-R_3-CH$, bimodal: 1.87 and 1.96 ppm), and side group methylene group ($-N-CH_2$, 2.95 ppm). When PAH is wrapped around the gold particles, all PAH proton

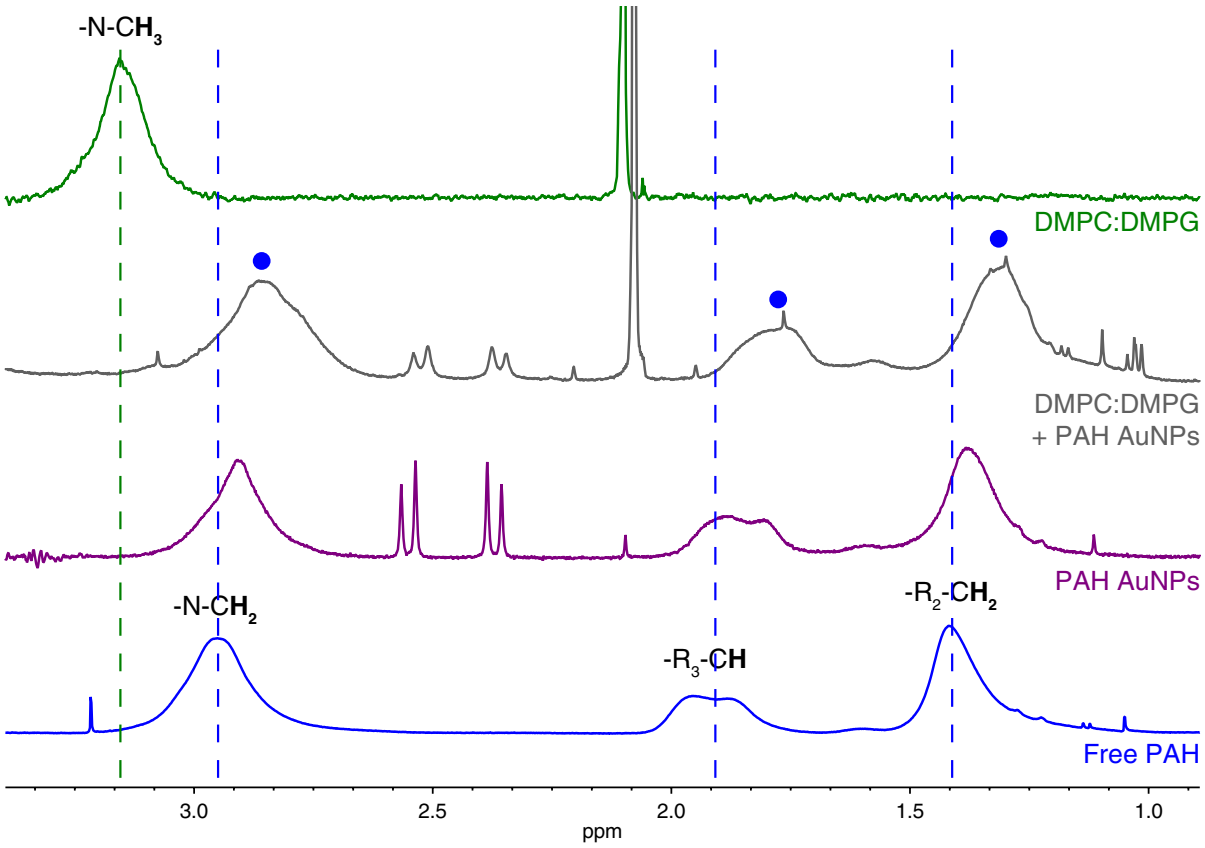

Figure 5.6 ^{1}H NMR of DMPC:DMPG vesicles and 4 nm PAH AuNPs. The lipid headgroup disappears, suggesting a strong molecular interaction occurs between the two species.

resonances shift upfield as compared to the free polymer, consistent with observed trends for bound ligands. The PAH AuNP protons shift even further upfield after interaction with the lipid vesicles, which suggests that the PAH layer is now sandwiched between the gold surface and an additional species. The sharp doublet of doublets at 2.4 ppm arise from citrate molecules, which are likely bound as counterions on the outside of the PAH AuNPs. Their signal becomes noticeably dampened after the particles interact with the vesicles. Taken together, NMR signals from the vesicles before and after interaction with the particles support the proposed idea—supported by collaborators' parallel studies—that lipids form a corona on the surface of the PAH AuNPs.

The accumulation of lipids on the surface of PAH AuNPs should correspond to a decrease in the particles' diffusion coefficient. DOSY NMR experiments were performed on the mixture of interacted DMPC:DMPG vesicles and PAH AuNPs to determine the diffusion coefficients of the species in the mixture. Three diffusion coefficients are apparent in the spectrum, suggesting that there are three types of species or complexes. The slowest diffusion coefficient (4.5 x 10^{-7} cm^2/s) correlates with the PAH and citrate resonances, confirming that they are part of the same complex. Because

Table 5.1 Chemical shifts of the DMPC:DMPG vesicle and 4 nm PAH AuNP system.

	Lipid protons δ (ppm)	PAH protons δ (ppm)		
	$-N-CH_3$	$-N-CH_2$	$-R_3-CH$	$-R_2-CH_2$
DMPC:DMPG	3.16	-	-	-
Free PAH	-	2.95	bimodal: 1.96, 1.87	1.42
PAH AuNPs	-	2.91	bimodal: 1.89, 1.81	1.38
DMPC:DMPG + PAH AuNPs	not observed	2.86	unimodal: 1.78	1.31

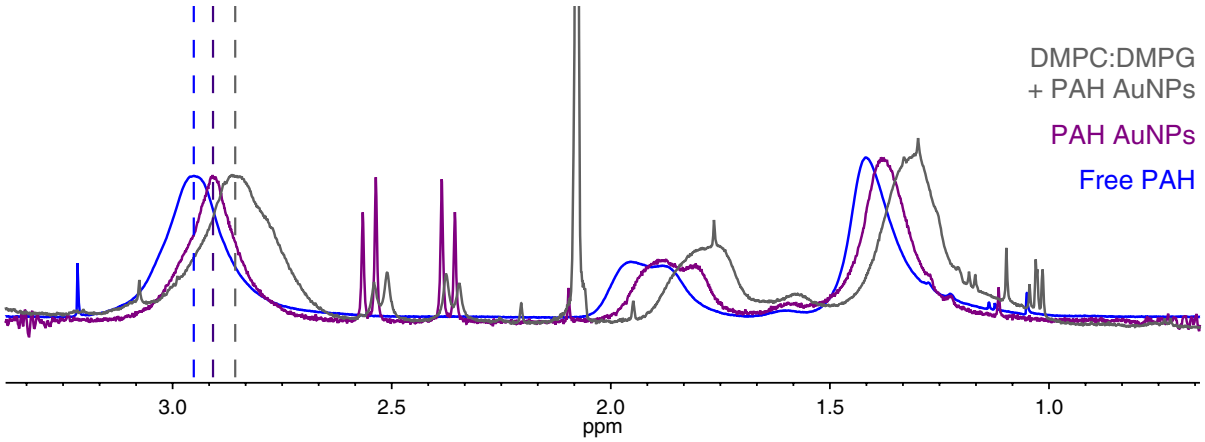

Figure 5.7 ^{1}H NMR of DMPC:DMPG vesicles and 4 nm PAH AuNPs, focusing on resonances arising from PAH. The PAH resonances shift upfield after gold particle wrapping and even further after lipid vesicle interaction, suggesting increasing levels of shielding.

of the narrow linewidth of the peaks, it is more likely that the citrate resonances arise from citrate bound ionically to the outside of the PAH AuNPs, than from citrate sandwiched between the gold and PAH, which would be broadened. The fastest diffusing species are the Tris buffer and small organic impurities in solution (5.2 x 10^{-6} cm^2/s). The third diffusion coefficient (1.6 x 10^{-6} cm^2/s) arises from a collection of peaks with chemical shifts between 2.8 – 3.0 ppm. In the 1-D spectrum, those peaks are buried in the large resonance of the PAH side group methylene protons, but DOSY deconvolutes that signal and identifies that a third species is present. The proximity of the peaks to the lipid headgroup chemical shift suggests that they may arise from a lipid-containing species. This species could be fragments of a disintegrated lipid vesicle, or lipids attached loosely to the outside of the PAH AuNPs. As protein coronas are thought to have both "hard" and "soft" shells, it is reasonable to think that lipid coronas have strongly- and loosely-bound components as well. For example, in one possible model of a lipid corona, the lipids form a bilayer around the particle, much as they would independently in water, with some lipid headgroups bound to the particle surface and some facing solution. These outer lipids would be quite loosely bound and may have a diffusion coefficient distinguishable from the particle itself. Indeed, the diffusion coefficient of a lipid analogue is approximately 10^{-8} cm^2/s in a fluid lipid membrane, but only 10^{-9} to 10^{-11} cm^2/s in gel lipid membranes.[159] Clearly, the local mobility of a lipid dramatically affects its measured diffusion coefficient. Their chemical shift would also diverge from those of lipids in a vesicle, a

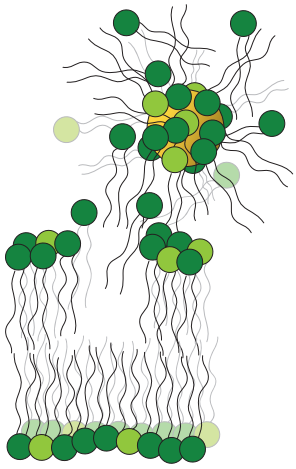

Figure 5.8 It is proposed that a lipid corona forms when 4 nm PAH AuNPs interact with DMPC:DMPG lipid bilayers.

signature of the different electronic environment.

Table 5.2 Molecular sizes of species in the DMPC:DMPG and PAH AuNP mixture, as calculated by the Stokes-Einstein equation.

Speculated species	D ($cm^2 \cdot s^{-1}$)	Calculated molecular size (nm)
Particle	4.5 x 10^{-7}	5.5
Loosely-associated lipids	1.6 x 10^{-6}	1.6
Small organics	5.2 x 10^{-6}	0.5

$$r = \frac{k_B T}{6\pi\eta D} \tag{5.1}$$

k_B: Boltzmann constant, 1.4 x 10^{-23} $kg \cdot m^2 \cdot s^{-2} \cdot K^{-1}$

T: temperature, 298 K

η: viscosity for water at 298 K, 8.9 x 10^{-4} $kg \cdot m^{-1} \cdot s^{-1}$

D: diffusion coefficient, in $m^2 \cdot s^{-1}$

The Stokes-Einstein equation was used to estimate the sizes of the three species. Although the equation is not expected to give highly-precise radii, the values obtained can provide a rough idea of the relative sizes. The diffusion rates, in decreasing speed, were estimated to have diameters of approximately 0.5, 1.6, and 5.5 nm, respectively (Table 5.2). These values correspond relatively well to the hypothesized species. A particle with a 4 nm gold core, a wrapping

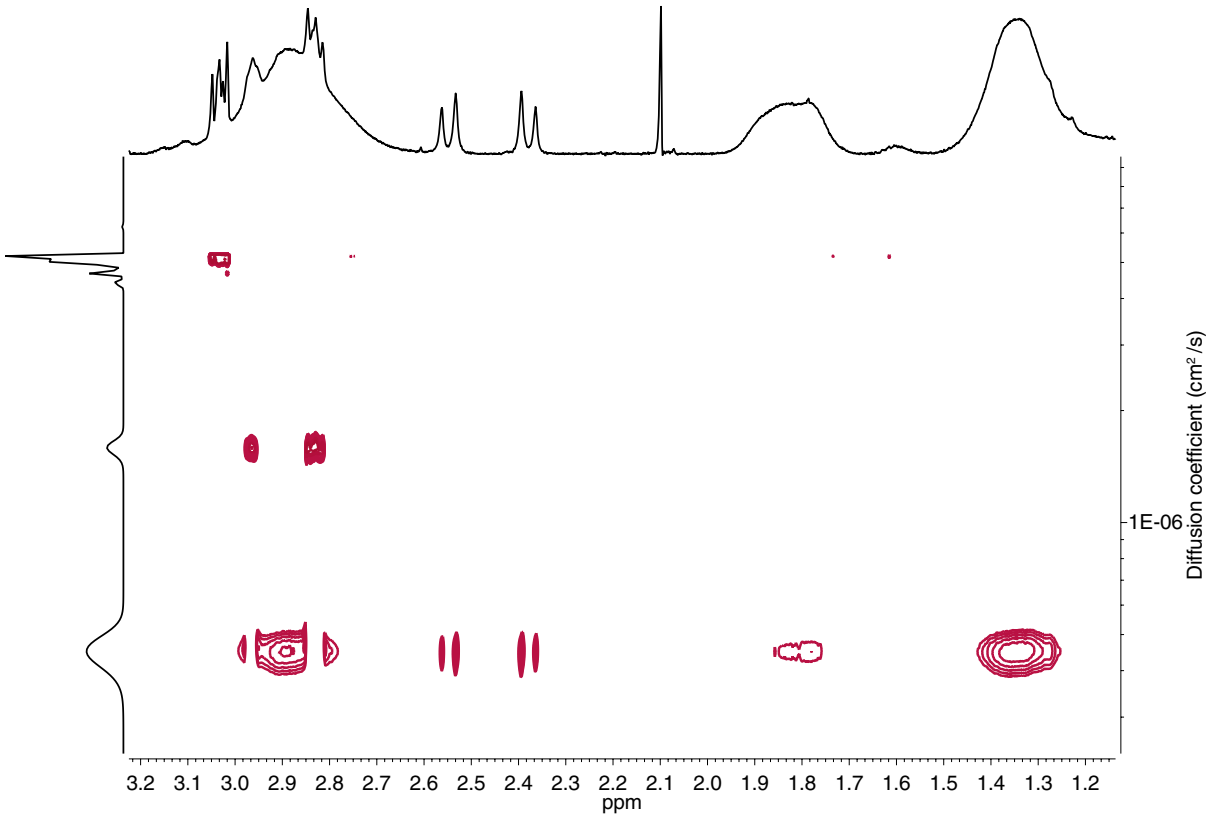

Figure 5.9 ^{1}H DOSY NMR of DMPC:DMPG vesicles and 4 nm PAH AuNPs. A diffusion population corresponding to a hypothesized lipid "soft corona" is observed (middle diffusion population).

of PAH, and a lipid corona might be around 6 nm, and small organic molecules are typically < 1 nm. It is reasonable to suggest that the 1.6 nm species, then, is a lipid (or a few lipids bound together). Loosely-associated lipids in a "soft" corona would move rather freely in solution. In other words, measured locally, those lipids have a diffusion coefficient close to that of a free lipid. The DOSY results provide further evidence that a lipid corona forms on the surface of PAH AuNPs.

5.3 No interaction: DOPC:DOTAP and gold particles

NMR experiments were then carried out on 9:1 DOPC:DOTAP lipid vesicles and 4 nm PAH AuNPs or MPA AuNPs. Lipid vesicle chemical shifts were assigned as shown in Figure 6. The lipid vesicles feature three prominent broad peaks for the headgroup ($-N-CH_3$, 3.15 ppm) and aliphatic ($-CH_2$, 1.20 ppm, and $-R-CH_3$, 0.80 ppm) protons. Allylic ($-C=C-CH_2$) protons are also visible at 1.90 ppm. The MPA AuNPs exhibit narrow NMR peaks that are typical for

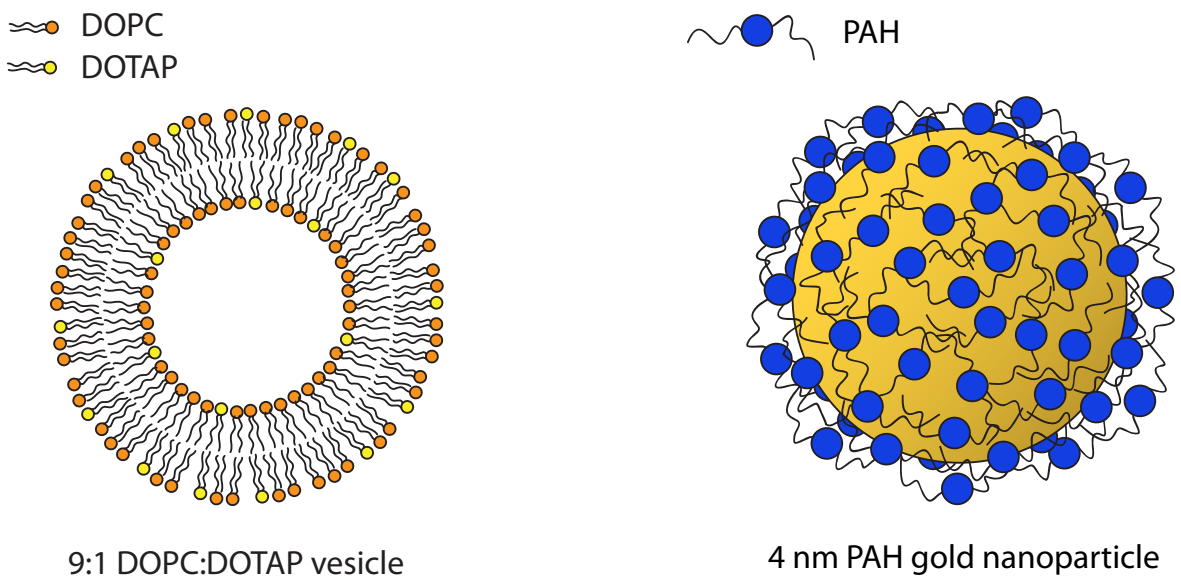

Figure 5.10 The components of the DOPC:DOTAP and 4 nm PAH AuNP system. Not to scale.

small molecules freely tumbling in solution, such as MPA detached from the NPs. MPA is a short enough ligand, and all its protons are located sufficiently close to the NP core, that any resonances from attached MPA are almost certainly broadened beyond detection, and we would not expect to see them in the spectrum. Given that we expect some free ligand to be in solution, it is likely that the narrow resonance peaks in the MPA AuNP spectrum arise from this small amount of detached MPA (the low signal-to-noise ratio points to how small this amount is). It is clear that MPA is attached to the gold because the particles would not be stable or well-dispersed without that passivating layer. Finally, the PAH AuNPs show citrate signatures near 2.5 ppm and broadened NMR features consistent with the presence of bound PAH ligand.

Table 5.3 Chemical shifts of the DOPC:DOTAP and 4 nm PAH AuNP system.

	Lipid protons δ (ppm)			PAH protons δ (ppm)		
	-N-CH3	-R2-CH2	-R-CH3	-N-CH2	-R3-CH	-R2-CH2
DOPC:DOTAP	3.15	1.20	0.80	-	-	-
Free PAH	-	-	-	2.95	1.96, 1.87	1.42
PAH AuNPs	-	-	-	2.91	1.89, 1.81	1.38
DOPC:DOTAP + free PAH	3.15	1.20	0.80	2.92	1.92, 1.83	1.41
DOPC:DOTAP + PAH AuNPs	3.15	1.20	0.80	2.93	1.92, 1.85	1.41
DOPC:DOTAP + MPA AuNPs	3.15	1.20	0.80	-	-	-

To study the interactions between the vesicles and particles, a free ligand control was first performed. The 9:1 DOPC:DOTAP vesicles (12 mM) were allowed to interact with free PAH (10 nM) for 2 hours in Tris buffer in D_2O

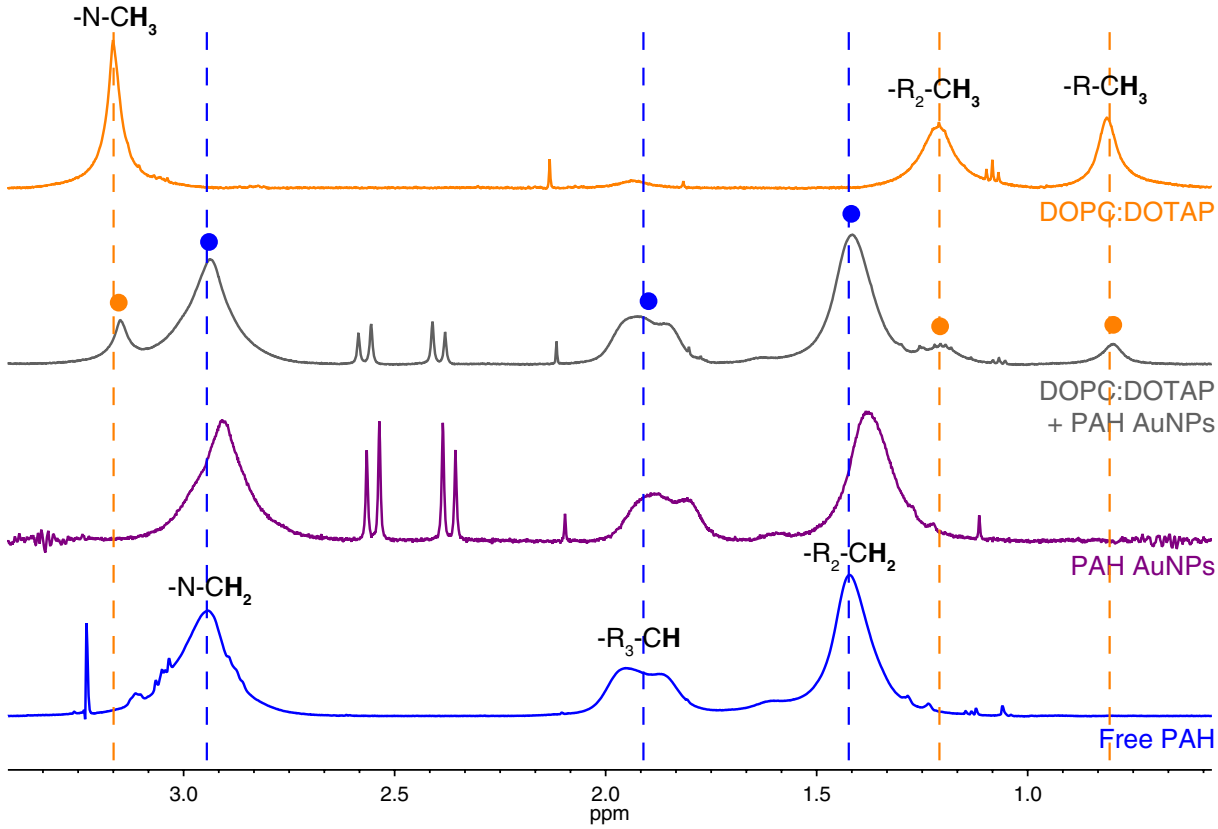

Figure 5.11 ^{1}H NMR of DOPC:DOTAP vesicles and 4 nm PAH AuNPs. The lipid resonances do not change, suggesting that no major interaction occurs, at least as observable by NMR.

(10 mM Tris, 100 mM NaCl, pD 7 – 8), at which point NMR spectra were acquired. If the particle or polymer were to attach to the outer surface of the liposome, one would expect the lipid signals—particularly those of the headgroup protons—to broaden or shift. Alternatively, if the liposome were to fragment, mobilization of the aliphatic chains should give rise to sharper peaks. Yet, the chemical shifts and line widths of the lipid peaks remain the same, suggesting that the liposome does not undergo substantial changes in morphology or surface chemistry upon interaction with the free PAH ligand.

The 9:1 DOPC:DOTAP vesicles (12 mM) were then allowed to interact with PAH AuNPs (10 nM) and MPA AuNPs (10 nM) particles for 2 hours in Tris buffer in D_2O (10 mM Tris, 100 mM NaCl, pD 7 – 8), at which point the NMR spectra were acquired. The NMR response of the DOPC:DOTAP vesicles (as shown by the headgroup and aliphatic resonances) barely changes upon interaction with the MPA AuNPs (Figure 5.11, Table 5.3)).

In contrast, when the PAH AuNPs interact with DOPC:DOTAP vesicles, the NMR signals from the PAH chain group methylene group (1.38 ppm), chain group methine group (1.85 ppm), and side group methylene group (2.91

ppm) shift downfield by 0.02–0.03 ppm and appear between those of free PAH and the PAH AuNPs (Figure 5.12, Table 5.3). This response is consistent with the notion that the surface-bound PAH loosens its attachment to the particle upon contact with the lipid vesicles, more resembling free PAH, at least in terms of what is measured in NMR. Meanwhile, we find that the lipid vesicle itself is not structurally affected.

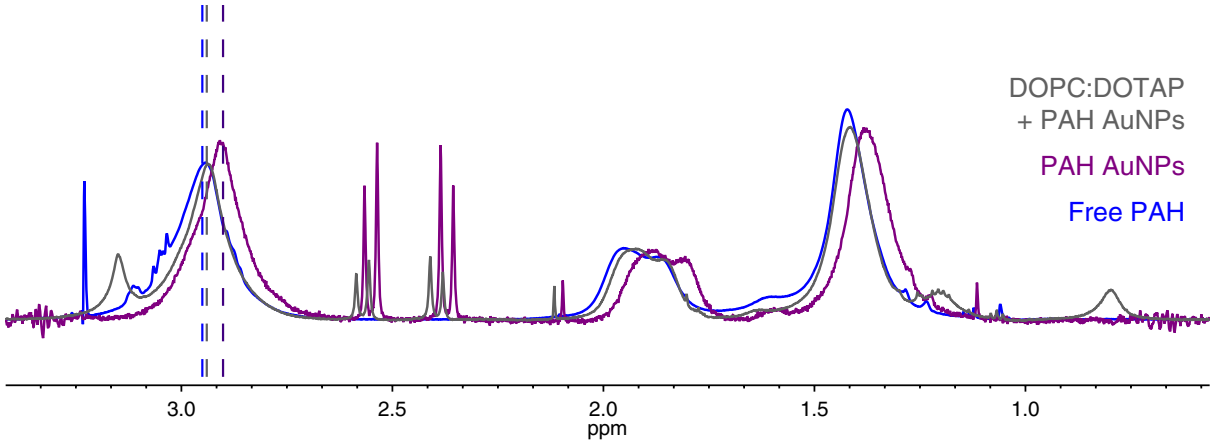

Figure 5.12 ^{1}H NMR DOPC:DOTAP vesicles and 4 nm PAH AuNPs, focusing on the resonances arising from PAH. The PAH resonances shift back upfield after the particles' interaction with the lipids, suggesting the PAH is closer to its free form.

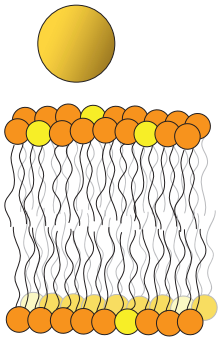

Figure 5.13 It is proposed that there is no major interaction between DOPC:DOTAP lipids and 4 nm PAH AuNPs, at least as is observable by NMR.

5.4 Other vesicles

Lipid vesicles of only zwitterionic DOPC or DMPC were interacted with either 4 nm PAH AuNPs, 15 nm PAH AuNPs, or 4 nm $MPNH_2$ AuNPs (5 mg lipid or approximately 12 mM, 10 nM particle for each experiment). All particle types had NH_3^+ groups on the surface for comparison. ^{1}H NMR spectra of each interaction, however, were not particularly interesting: the resonances for each lipid vesicle did not undergo any obvious change after interaction, suggesting that no major interaction happened in any of the cases, at least which would be observable by NMR. This is somewhat

surprising, since the 4 nm PAH AuNP was the "villain" of previous studies, showing disruption ability when the other particles did not; if terminal amine groups are indeed the primary cause of vesicle disruption, one might expect all three amine-terminated particles—or at the least, the 4 nm PAH AuNPs—to have some effect on the zwitterionic vesicles. However, from these studies, it appears that the purely-zwitterionic DMPC vesicles are more stable to 4 nm PAH AuNPs than their negatively-charged DMPG-doped equivalents. Is it a matter of charge? It is also likely that the ratio of lipids to particles matters, especially in cases where the interaction or disruption may be subtle. 9:1 DMPC:DMPG lipid vesicles were interacted with 4 nm PAH AuNPs in a high lipid-to-NP ratio (5 mg lipid, 10 nM particle, as in previous experiments) or a low lipid-to-NP ratio (2 mg lipid, 50 nM particle). In prior studies, the DMPC:DMPG headgroup resonance disappeared after interaction with 4 nm PAH AuNPs. In the high lipid-to-NP experiment, the lipid headgroup resonance was still observable, although the alkyl chain resonances were not; the headgroup resonance had a lower integration than the control (lipid vesicle alone). On the other hand, in the low lipid-to-NP interaction spectrum, only the PAH resonances were visible, suggesting that the lipid reonances were "quenched" by the interaction. It appears that the ratio does matter, as should be expected. To ensure that the lack of interaction observed above between DMPC + 4 nm PAH AuNPs was not a matter of relative concentration, a ratio study was performed in a similar manner; DMPC and 4 nm PAH AuNPs were interacted in either high or low lipid-to-NP ratio. In both the high and low lipid-to-NP ratios, all PAH and lipid resonances are still observable (although the relative integrations of each changes, of course). This is a very different result than was found for DMPC:DMPG vesicles. These results suggest than among the matrix of interactions studied here, only 9:1 DMPC:DMPG vesicles and 4 nm PAH AuNPs show an observable interaction by NMR.

5.5 Effects of cholesterol in vesicles

In a fluid lipid bilayer, the lipid molecules diffuse laterally, switching positions with neighboring lipids within the same leaflet (they do not flip between inner and outer leaflets easily due to the energetic cost of disturbing the hydrophobic core). The molecules in a gel lipid bilayer, on the other hand, are essentially fastened in place. When an event disrupts the bilayer, such as a nanoparticle penetrating or pulling off lipids, a fluid bilayer will quickly repair the damage, whereas a gel bilayer cannot reorganize its lipids to fill in the gaps. The gel bilayer is left prone to irreparable deterioration.

With a tiny hydrophilic head (a hydroxyl group) and a hydrophobic body of rigid fused rings and short aliphatic tail, the structure of cholesterol allows it to intercalate between lipid molecules in a bilayer. Indeed, it is well-known that adding cholesterol to a fluid bilayer increases its mechanical rigidity and limits lateral diffusion (and ability to repair damage). Interestingly, cholesterol influences the properties of fluid and gel lipid bilayers differently (Figure

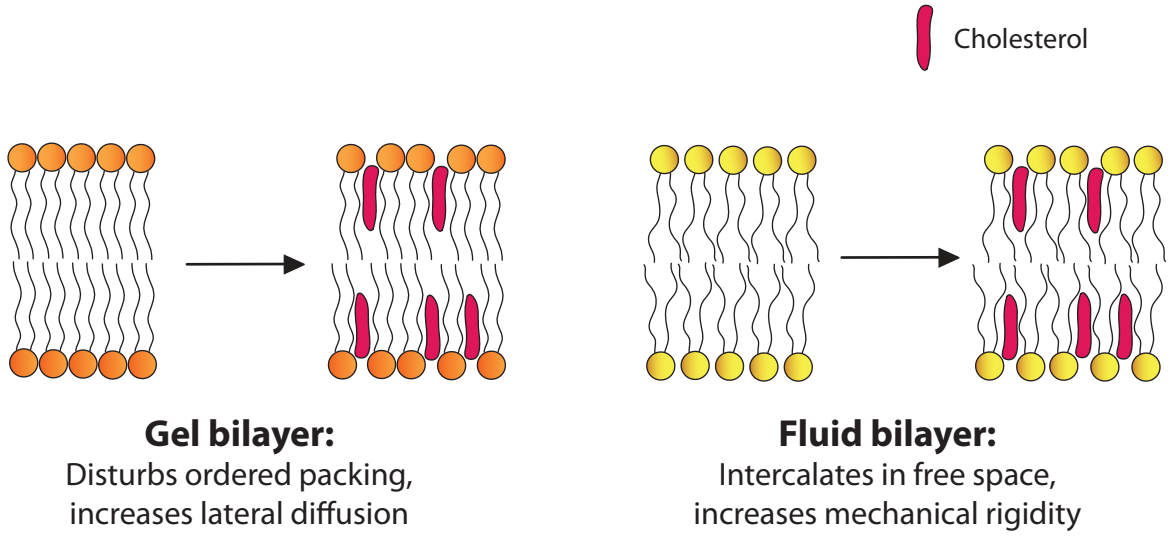

Figure 5.14 Cholesterol interacts with gel and fluid bilayers in contrasting mechanisms.

5.14. Whereas in a fluid bilayer the cholesterol reduces the flexibility of lipid tails by packing into open space, in a gel bilayer it disturbs the organization of the well-packed saturated tails. This disruption actually increases the lateral diffusion coefficient of the lipid molecules.[160,161]

Thus, it was proposed that cholesterol would exert two very different effects on the interaction of fluid or gel bilayers with nanoparticles. Two systems were chosen: a) the gel bilayer (at RT = 25°C), 9:1 DMPC:DMPG vesicles, whose disruption by 4 nm PAH AuNPs is observable by NMR, and b) the fluid bilayer, DOPC vesicles, which do not appear to interact with 4 nm PAH AuNPs by NMR. Doping the 9:1 DMPC:DMPG vesicles with cholesterol might render it able to repair itself, protecting it from the damaging effects of the particles. Meanwhile, adding cholesterol to DOPC would lock its constituent lipid molecules into place, perhaps making it vulnerable to the particles. If the effect in either system was significant, the change might be observable by NMR (the headgroup resonance appearing or any resonances disappearing, respectively).

Vesicles composed of varying molar ratios of DOPC and cholesterol (DOPC:cholesterol = 100:0, 90:10, 80:20, and 70:30) were prepared by rehydrating and extruding a homogenous mixture in Tris buffer in D_2O (10 mM Tris, 100 mM NaCl, pD 7 – 8) (Figure 5.15). Each vesicle type (5 mg) was interacted with 4 nm PAH AuNPs (10 nM) for 2 hours, then analyzed by NMR. However, none of the resonances of the lipid-cholesterol formulations changed after interaction with the particles. This suggests that, at least at the ratios and concentrations measured, and to the extent observable by NMR, decreasing membrane fluidity by doping in cholesterol does not make DOPC more sensitive to 4 nm PAH AuNPs. However, it should be noted that as a bulk measurement, NMR is not likely to diagnose whether

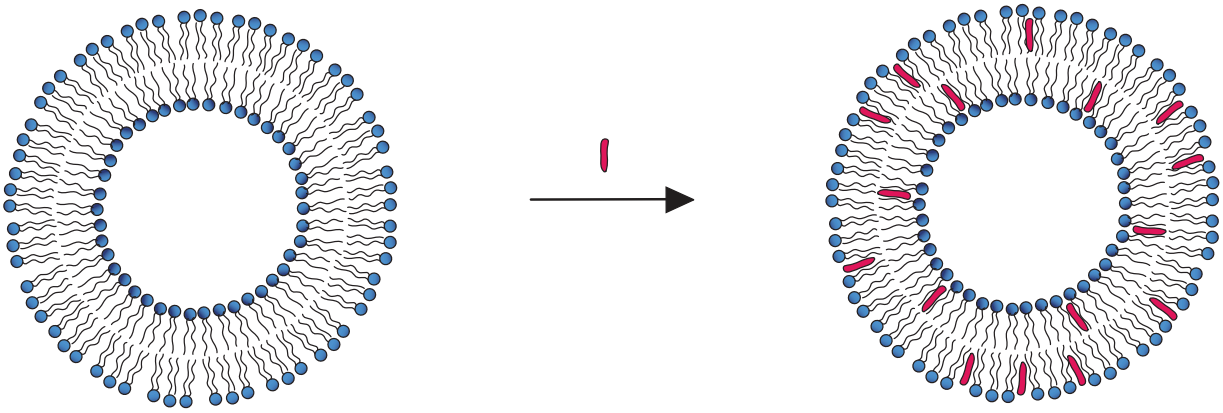

Figure 5.15 Cholesterol was added to lipid vesicles to observe its effect on the bilayers' interactions with nanoparticles.

localized regions of the vesicle have changed (e.g., small holes). Also, any interaction that does not involve changes in the chemical environment of the lipid protons is unlikely to show up on an NMR spectra. This study highlights the need for multiple methods of analysis in lipid vesicle-nanoparticle interactions.

5.6 Experimental

5.6.1 General

All materials were used as received, unless otherwise indicated. Nanoparticle reactions were performed in new polyethylene centrifuge tubes, new glass vials, or glassware cleaned with aqua regia. Reported reaction temperatures refer to the temperature of the heating medium. All water used was ultrapure deionized water collected from a Barnstead NANOPURE water filtration system. PallALL Minimate tangential flow filtration capsules for AuNP purification were obtained from VWR. Lipids were purchased from Avanti Polar Lipids as organic solutions and stored at 4°C, and individual ampules were used within one month after opening. Lipid extrusion supplies (extruder, syringes, membranes, filter supports) were also purchased from Avanti Polar Lipids.

Dynamic light scattering (DLS) and ζ-potential data were taken on a Brookhaven ZetaPALs analyzer. UV-vis spectra were obtained on a Varian Cary Scan 500 spectrometer. Transmission electron microscopy (TEM) samples were prepared on Lacey Formvar/Carbon, 200 mesh, 97 μm grids (Ted Pella), and TEM images were taken on a JEOL 2100 instrument and processed with Gatan DigitalMicrograph and ImageJ. Nuclear magnetic resonance (NMR) spectra were acquired using a Varian Unity Inova narrow-bore 500 MHz spectrometer. Spectra were processed with MNova or Vn-

mrJ. Chemical shifts are reported in parts per million (ppm) and were referenced to the residual proton solvent peak. Splitting patterns are designated as s (singlet), d (doublet), t (triplet), q (quadruplet), dd (doublet of doublets), m (multiplet), and br (broad). In samples with high water concentration, the water peak was suppressed using presaturation.

5.6.2 Synthesis of particles

4 nm PAH AuNPs

PAH AuNPs were synthesized by polyelectrolyte wrapping of 4 nm citrate AuNPs. In a typical flow reactor synthesis, 20.0 mL of $HAuCl_4$ (0.01 M) and 6.0 mL of sodium citrate (0.1 M) were combined in an 2 L Erlenmeyer flask containing 1600 mL of nanopure water. In a second 2 L Erlenmeyer flask, 1614.0 mL of water was chilled in an ice-water bath. 12.0 mL of chilled aqueous $NaBH_4$ (0.1 M) was added to the cold flask, which was swirled briefly. A flow line was placed into each 2 L flask and the flow reactor pump was started at a setting of 40 mL/min. Once the two solutions combined in the flow reactor line, the solution turned a light red-brown and the synthesized particles were collected in a 4 L polyethylene bottle with gentle stirring. The resulting citrate AuNP solution was then stirred for at least 3 h. The 4 nm citrate AuNPs were then wrapped with 15 kDa PAH to prepare 4 nm PAH AuNPs. To the approximately 3.2 L of as-synthesized particles, 32.0 mL of NaCl (100 mM) and 100.0 mL of a PAH solution (10 mg/mL in 1 mM NaCl) was added with vigorous stirring. The nanoparticles were then allowed to stir overnight in the wrapping solution. The PAH AuNPs were subsequently concentrated in a diafiltration membrane (50 kDa MWCO), then purified by centrifugation twice (13,000 rcf for 55 min).

15 nm PAH AuNPs

In an Erlenmeyer flask, 1 L of $HAuCl_4$ (0.8 mM) was heated and stirred to a rolling boil, at which point 16 mL of sodium citrate (5% (w/v)) was added at once. The solution immediately turned colorless, then black, and then deep red. The deep red solution was stirred and boiled for 30 min to yield 15 nm citrate AuNPs. The particles were allowed to cool slowly to room temperature. The particles were centrifuged at 8000 rcf for 40 min, and the pellets were redispersed in 1 L of 1 mM NaCl and stirred overnight with 50 mL of PAH solution (10 mg/mL of 15 kDa PAH in 1 mM NaCl). The PAH AuNPs were centrifuged once at 6000 rcf for 25 min.

4 nm MPA AuNPs

A 500 mL aqueous solution of $HAuCl_4$ (1.5 mM) and MPA (3.0 mM) was prepared in an Erlenmeyer flask. The pH of the growth solution was adjusted to approximately 8.5 by the addition of dilute aqueous sodium hydroxide, and stirred at vortex for 10 min. 10.0 mL of fresh sodium borohydride solution (0.1 M) was then added to the reaction mixture. The combined solutions rapidly changed color to a deep orange-brown, and the reaction mixture was stirred for a further 3 hours. The MPA AuNPs were then concentrated and purified by diafiltration (40 volume equivalents of nanopure water in a 50 kDa MWCO membrane).

4 nm $MPNH_2$ AuNPs

400 mL of water, 0.9 mL of $HAuCl_4$ (0.1 M), 5.7 mL of HCl (0.1 M), and 0.5 mL of 3-aminopropanethiol (0.1 M) were stirred at vortex in an Erlenmeyer flask for 10 min. Then, 4.0 mL of fresh sodium borohydride solution (0.1 M) was added to the mixture. The solution rapidly turned red-brown and was stirred for 3 h. The $MPNH_2$ AuNPs were then purified by diafiltration (40 volume equivalents of nanopure water in a 50 kDa MWCO membrane).

5.6.3 Particle characterization

The diameters of the 4 nm PAH AuNP cores were determined in solution by UV-vis to be approximately 3.5 nm, and TEM size analysis indicated that the PAH AuNPs possessed a core diameter of 4.5 ± 1.4 nm (n = 1085). ζ-potentials of the PAH AuNPs determined at pH 7.4 (10 mM Tris buffer) and at 1 and 100 mM NaCl were +38 ± 3 and +32 ± 2 mV, respectively, and their number-averaged hydrodynamic diameter at 1 mM NaCl was found to be 6 ± 2 nm and ranged between 20 and 80 nm at 100 mM NaCl. For the MPA AuNPs, core diameter was 4.2 ± 1.2 nm (n = 613). ζ potentials of the negatively charged MPA AuNPs determined at pH 7.4 (10 mM Tris) and 1 and 100 mM NaCl were −29 ± 1 and −27 ± 2 mV, respectively, and their number-averaged hydrodynamic diameter at 0.001 M NaCl was found to be 9 ± 2 nm. At 100 mM NaCl, the number-averaged hydrodynamic diameter of the MPA AuNPs increased from between 100 to 400 nm to between 420 and 450 nm over the course of 2 h. UV-vis spectra indicate that for 10 nM MPA or PAH AuNPs maintained at 100 mM NaCl and pH 7.4 (10 mM Tris), the electronic properties of the particles do not change much over the course of 150 min, whereas measurements of the hydrodynamic diameters indicate that the MPA AuNPs aggregate.

5.6.4 Lipid vesicle preparation

DMPC, DMPG, DOPC, and DOTAP were purchased solvated in organic solutions. Cholesterol was purchased as a solid and dissolved in chloroform before use. Lipid mixtures in organic solvent were combined and vortexed for 30 s in a glass vial to afford a homogenous mixture. The solvent was evaporated by blowing N_2 over the sample, and the film was dried in a vacuum desiccator for at least 6 h. The lipid cake was hydrated in Tris buffer (10 mM Tris, 100 mM NaCl, pD 7 – 8 or pH 7.4) in D_2O for NMR experiments or H_2O for other experiments. The mixture was vortexed for 30 seconds to totally solvate the lipids. The lipid solution was extruded through a 0.05 μm membrane filter 11 times until the cloudy white solution became translucent white. Lipid vesicles were kept at 4°C and used up to 5 days after extrusion.

5.6.5 NMR experiments

Sample preparation

In a typical experiment, lipid vesicles (12 mM) and nanoparticles (10 nM) or free PAH polymer (10 nM) were combined in the Tris buffer in D_2O to a total volume of 1 mL, agitated gently with a Pasteur pipette in an NMR sample tube for 10 s and then allowed to interact at room temperature for 2 h before NMR spectra acquisition.

NMR spectra acquisition

NMR samples were prepared from concentrated aqueous nanoparticle solutions in D_2O. ^1H NMR spectra were acquired using a Varian Unity Inova 500 MHz narrow bore, Varian VXR 500 MHz, Varian Unity Inova 600 MHz, or Agilent VNS 750 MHz narrow bore spectrometer. Chemical shifts are reported in parts per million (ppm) and were referenced to the residual proton solvent peak. For aqueous nanoparticle samples prepared in D_2O containing residual water, the large water peak was suppressed using presaturation. Unless stated otherwise, the presaturation delay for aqueous samples was 2 s and the acquisition time was 1 s, with a 2- or 4-step purge. All NMR spectra were processed using Mnova or VnmrJ.

Chapter 6

References

1 Wilhelm, T. The smallest chemical reaction system with bistability. *BMC Systems Biology* **2009**, *3:90*.

2 Stuart, M. A. C.; Huck, W. T. S.; Genzer, J.; Müller, M.; Ober, C.; Stamm, M.; Sukhorukov, G. B.; Szleifer, I.; Tsukruk, V. V.; Urban, M.; Winnik, F.; Zauscher, S.; Luzinov, I.; Minko, S. Emerging applications of stimuli-responsive polymer materials. *Nature Materials* **2010**, *9*, 101–113.

3 Ludlow, R. F.; Otto, S. Systems chemistry. *Chemical Society Reviews* **2008**, *37*, 101–8.

4 Brodsley, L.; Frank, C.; Steeds, J. W. Prince Rupert's drops. *Notes and Records of the Royal Society of London* **1986**, *41*, 1–26.

5 Ichimura, K. Nonlinear organic reactions to proliferate acidic and basic molecules and their applications. *The Chemical Record* **2002**, *2*, 46–55.

6 Diesendruck, C. E.; Steinberg, B. D.; Sugai, N.; Silberstein, M. N.; Sottos, N. R.; White, S. R.; Braun, P. V.; Moore, J. S. Proton-coupled mechanochemical transduction: a mechanogenerated acid. *Journal of the American Chemical Society* **2012**, *134*, 12446–9.

7 Lenhardt, J. M.; Black, A. L.; Craig, S. L. *gem*-Dichlorocyclopropanes as abundant and efficient mechanophores in polybutadiene copolymers under mechanical stress. *Journal of the American Chemical Society* **2009**, *131*, 10818–9.

8 Wu, D.; Lenhardt, J. M.; Black, A. L.; Akhremitchev, B. B.; Craig, S. L. Molecular stress relief through a force-induced irreversible extension in polymer contour length. *Journal of the American Chemical Society* **2010**, *132*, 15936–15938.

9 Arimitsu, K.; Kudo, K.; Ohmori, H.; Ichimura, K. Factors affecting photosensitivity enhancement of chemically amplified photoresists by an acid amplifier. *Journal of Materials Chemistry* **2001**, *11*, 295–301.

10 Ito, H.; Ichimura, K. 4-(tert-Butoxycarbonyloxy) benzyl p-toluenesulfonates as acid amplifiers applicable to chemically amplified photoresists. *Macromolecular Chemistry and Physics* **2000**, *138*, 132–138.

11 Arimitsu, K.; Kudo, K.; Ichimura, K. Autocatalytic fragmentation of acetoacetate derivatives as acid amplifiers to proliferate acid molecules. *Journal of the American Chemical Society* **1998**, *7863*, 37–45.

12 Kudo, K.; Arimitsu, K.; Ohmori, H.; Ito, H.; Ichimura, K. 3-Phenyl-3,3-ethylenedioxy-1-propyl sulfonates as acid amplifiers to enhance the photosensitivity of positive-working photoresists. *Chemistry of Materials* **1999**, *11*, 2119–2125.

13 Arimitsu, K.; Ichimura, K. Phototriggered acid proliferation to enhance photosensitivity of chemically amplified photoresists. *Macromolecular Chemistry and Physics* **2001**, *202*, 453–460.

14 Park, S.-W.; Arimitsu, K.; Ichimura, K. Polymers with acid-amplifying side chains as positive-type photoresists. *Journal of Photopolymer Science and Technology* **2004**, *17*, 427–432.

15 K. Arimitsu, K. I. Trioxane derivative as an acid amplifier exhibiting a non-linear organic reaction. *Chemistry Letters* **1998**, 823–824.

16 Kruger, S. A.; Higgins, C.; Cardineau, B.; Younkin, T. R.; Brainard, R. L. Catalytic and autocatalytic mechanisms of acid amplifiers for use in EUV photoresists. *Chemistry of Materials* **2010**, *22*, 5609–5616.

17 Brainard, R. L.; Kruger, S. A.; Higgins, C. Kinetics, chemical modeling and lithography of novel acid amplifiers for use in EUV photoresists. *Journal of Photopolymer Science and Technology* **2009**, *22*, 43–50.

18 Sarmini, K.; Kenndler, E. Ionization constants of weak acids and bases in organic solvents. *Journal of Biochemical and Biophysical Methods* **1999**, *38*, 123–137.

19 Anslyn, E. V.; Dougherty, D. A. *Modern Physical Organic Chemistry*; 2006; Vol. 69; p 1146.

20 Pehk, T.; Kiirend, E.; Lippmaa, E.; Ragnarsson, U. General approach to measurements of pKa differences by ^{13}C NMR spectroscopy. *Journal of the Chemical Society, Perkin Transactions 2* **1996**, *2*, 2351.

21 Cistola, D. P.; Small, D. M.; Hamilton, J. A. Ionization behavior of aqueous short-chain carboxylic acids: a carbon-13 NMR study. *Journal of Lipid Research* **1982**, *23*, 795–799.

22 Priola, A.; Passerini, N.; Bruzzone, M.; Cesca, S.; Mistrali, F. Cationic cyclization of cis-1,4-polybutadiene. *Die Angewandte Makromolekulare Chemie* **1980**, *88*, 1–19.

23 Golub, M. A.; Heller, J. Cyclohydrochlorination of 3,4-polyisoprene. *Journal of Polymer Science Part B: Polymer Letters* **1964**, *2*, 523–527.

24 Chan, C.; Lin, C. Use of trifluoromethanesulfonic acid as catalyst for the cyclization of polyisoprene. *Journal of Applied Polymer Science* **2006**, *101*, 3666–3669.

25 Riyajan, S.; Liaw, D.-J.; Tanaka, Y.; Sakdapipanich, J. T. Cationic cyclization of purified natural rubber in latex form with a trimethylsilyl triflate as a novel catalyst. *Journal of Applied Polymer Science* **2007**, *105*, 664–672.

26 Walther, A.; Göldel, A.; Müller, A. H. E. Controlled crosslinking of polybutadiene containing block terpolymer bulk structures: a facile way towards complex and functional nanostructures. *Polymer* **2008**, *49*, 3217–3227.

27 McCreedy, K.; Keskkula, H. Effect of thermal crosslinking on decomposition of polybutadiene. *Polymer* **1979**, *20*, 1155–1159.

28 Burrows, N. D.; Vartanian, A. M.; Abadeer, N. S.; Grzincic, E. M.; Jacob, L. M.; Lin, W.; Li, J.; Dennison, J. M.; Hinman, J. G.; Murphy, C. J. Anisotropic nanoparticles and anisotropic surface chemistry. *Journal of Physical Chemistry Letters* **2016**, *7*, 632–641.

29 Sacanna, S.; Pine, D. J.; Yi, G.-R. Engineering shape: the novel geometries of colloidal self-assembly. *Soft Matter* **2013**, *9*, 8096–8106.

30 Devries, G. A.; Brunnbauer, M.; Hu, Y.; Jackson, A. M.; Long, B.; Neltner, B. T.; Uzun, O.; Wunsch, B. H.; Stellacci, F. Divalent metal nanoparticles. *Science* **2007**, *315*, 358–61.

31 Zhang, G.; Wang, D. Decoration of microspheres with gold nanodots-giving colloidal spheres valences. *Angewandte Chemie International Edition* **2005**, *44*, 7767–7770.

32 Pawar, A. Fabrication, assembly, and application of patchy particles. *Macromolecular Rapid Communications* **2010**, *31*, 150–168.

33 Mokari, T.; Rothenberg, E.; Popov, I.; Costi, R. Selective growth of metal tips onto semiconductor quantum rods and tetrapods. *Science* **2004**, *304*, 1787–1790.

34 Kudera, S.; Carbone, L.; Casula, M. F.; Cingolani, R.; Falqui, A.; Snoeck, E.; Parak, W. J.; Manna, L. Selective growth of PbSe on one or both tips of colloidal semiconductor nanorods. *Nano Letters* **2005**, *5*, 445–449.

35 Jana, N. R.; Gearheart, L.; Obare, S. O.; Murphy, C. J. Anisotropic chemical reactivity of gold spheroids and nanorods. *Langmuir* **2002**, *18*, 922–927.

36 Orendorff, C. J.; Alam, T. M.; Sasaki, D. Y.; Bunker, B. C.; Voigt, J. A. Phospholipid-gold nanorod composites. *ACS Nano* **2009**, *3*, 971–83.

37 Caswell, K. K.; Wilson, J. N.; Bunz, U. H. F.; Murphy, C. J. Preferential end-to-end assembly of gold nanorods by biotin- streptavidin connectors. *Journal of the American Chemical Society* **2003**, *125*, 13914–13915.

38 Zhen, S.; Huang, C.; Wang, J.; Li, Y. End-to-end assembly of gold nanorods on the basis of aptamer-protein recognition. *Journal of Physical Chemistry C* **2009**, *113*, 21543–21547.

39 Xu, L.; Kuang, H.; Xu, C.; Ma, W.; Wang, L.; Kotov, N. A. Regiospecific plasmonic assemblies for *in situ* Raman spectroscopy in live cells. *Journal of the American Chemical Society* **2012**, *134*, 1699–709.

40 Wang, F.; Cheng, S.; Bao, Z.; Wang, J. Anisotropic overgrowth of metal heterostructures induced by a site-selective silica coating. *Angewandte Chemie International Edition* **2013**, *52*, 10344–10348.

41 Nie, Z.; Fava, D.; Kumacheva, E.; Zou, S.; Walker, G. C.; Rubinstein, M. Self-assembly of metal-polymer analogues of amphiphilic triblock copolymers. *Nature Materials* **2007**, *6*, 609–14.

42 Liu, K.; Nie, Z.; Zhao, N.; Li, W.; Rubinstein, M.; Kumacheva, E. Step-growth polymerization of inorganic nanoparticles. *Science* **2010**, *329*, 197–200.

43 Lukach, A.; Liu, K.; Therien-Aubin, H.; Kumacheva, E. Controlling the degree of polymerization, bond lengths, and bond angles of plasmonic polymers. *Journal of the American Chemical Society* **2012**, *134*, 18853–9.

44 Klinkova, A.; Thérien-Aubin, H.; Choueiri, R. M.; Rubinstein, M.; Kumacheva, E. Colloidal analogs of molecular chain stoppers. *Proceedings of the National Academy of Sciences of the United States of America* **2013**, *110*, 18775–9.

45 El-Sayed, M. A. Some interesting properties of metals confined in time and nanometer space of different shapes. *Accounts of Chemical Research* **2001**, *34*, 257–64.

46 Murphy, C. J.; Sau, T. K. Anisotropic metal nanoparticles: Synthesis, assembly, and optical applications. *Journal of Physical Chemistry B* **2005**, *109*, 13857–70.

47 Govorov, A. O.; Richardson, H. H. Generating heat with metal nanoparticles. *Nano Today* **2007**, *2*, 30–38.

48 Huang, J.; Jackson, K. S.; Murphy, C. J. Polyelectrolyte wrapping layers control rates of photothermal molecular release from gold nanorods. *Nano Letters* **2012**, *12*, 2982–7.

49 Sau, T. K.; Murphy, C. J. Seeded high yield synthesis of short Au nanorods in aqueous solution. *Langmuir* **2004**, *20*, 6414–20.

50 Nikoobakht, B.; El-Sayed, M. A. Evidence for bilayer assembly of cationic surfactants on the surface of gold nanorods. *Langmuir* **2001**, *17*, 6368–6374.

51 Liu, X. H.; Luo, X. H.; Lu, S. X.; Zhang, J. C.; Cao, W. L. A novel cetyltrimethyl ammonium silver bromide complex and silver bromide nanoparticles obtained by the surfactant counterion. *Journal of Colloid and Interface Science* **2007**, *307*, 94–100.

52 Badia, A.; Singh, S.; Demers, L. Self-assembled monolayers on gold nanoparticles. *Chemistry - A European Journal* **1996**, *2*, 359–363.

53 Murphy, C. J.; Thompson, L. B.; Alkilany, A. M.; Sisco, P. N.; Boulos, S. P.; Sivapalan, S. T.; Yang, J. A.; Chernak, D. J.; Huang, J. The many faces of gold nanorods. *Journal of Physical Chemistry Letters* **2010**, *1*, 2867–2875.

54 Alkilany, A. M.; Frey, R. L.; Ferry, J. L.; Murphy, C. J. Gold nanorods as nanoadmicelles: 1-naphthol partitioning into a nanorod-bound surfactant bilayer. *Langmuir* **2008**, *24*, 10235–10239.

55 Wijaya, A.; Hamad-Schifferli, K. Ligand customization and DNA functionalization of gold nanorods via round-trip phase transfer ligand exchange. *Langmuir* **2008**, *24*, 9966–9.

56 Alkilany, A. M.; Yaseen, A. I. B.; Park, J.; Eller, J. R.; Murphy, C. J. Facile phase transfer of gold nanoparticles from aqueous solution to organic solvents with thiolated poly(ethylene glycol). *RSC Advances* **2014**, *4*, 52676–52679.

57 Thierry, B.; Ng, J.; Krieg, T.; Griesser, H. J. A robust procedure for the functionalization of gold nanorods and noble metal nanoparticles. *Chemical Communications* **2009**, *1*, 1724–6.

58 Zhao, Y.; Pérez-Segarra, W.; Shi, Q.; Wei, A. Dithiocarbamate assembly on gold. *Journal of the American Chemical Society* **2005**, *127*, 7328–9.

59 Gole, A.; Murphy, C. J. Polyelectrolyte-coated gold nanorods: synthesis, characterization and immobilization. *Chemistry of materials* **2005**, *17*, 1325–1330.

60 Alkilany, A. M.; Thompson, L. B.; Murphy, C. J. Polyelectrolyte coating provides a facile route to suspend gold nanorods in polar organic solvents and hydrophobic polymers. *ACS Applied Materials & Interfaces* **2010**, *2*, 3417–21.

61 Alkilany, A. M.; Thompson, L. B.; Boulos, S. P.; Sisco, P. N.; Murphy, C. J. Gold nanorods: their potential for photothermal therapeutics and drug delivery, tempered by the complexity of their biological interactions. *Advanced Drug Delivery Reviews* **2012**, *64*, 190–199.

62 Alkilany, A. M.; Lohse, S. E.; Murphy, C. J. The gold standard: gold nanoparticle libraries to understand the nano-bio interface. *Accounts of Chemical Research* **2013**, *46*, 650–661.

63 Kolb, H. C.; Finn, M. G.; Sharpless, K. B. Click chemistry: diverse chemical function from a few good reactions. *Angewandte Chemie - International Edition* **2001**, *40*, 2004–2021.

64 Moses, J. E.; Moorhouse, A. D. The growing applications of click chemistry. *Chemical Society Reviews* **2007**, *36*, 1249–62.

65 Zhang, T.; Zheng, Z.; Ding, X.; Peng, Y. Smart surface of gold nanoparticles fabricated by combination of RAFT and click chemistry. *Macromolecular Rapid Communications* **2008**, *29*, 1716–1720.

66 Gole, A.; Murphy, C. J. Azide-derivatized gold nanorods: functional materials for "click" chemistry. *Langmuir* **2008**, *24*, 266–72.

67 Haag, R.; Sunder, A.; Stumbé, J.-F. An approach to glycerol dendrimers and pseudo-dendritic polyglycerols. *Journal of the American Chemical Society* **2000**, *122*, 2954–2955.

68 Kainthan, R. K.; Muliawan, E. B.; Hatzikiriakos, S. G.; Brooks, D. E. Synthesis, characterization, and viscoelastic properties of high molecular weight hyperbranched polyglycerols. *Macromolecules* **2006**, *39*, 7708–7717.

69 Burakowska, E.; Quinn, J. R.; Zimmerman, S. C.; Haag, R. Cross-linked hyperbranched polyglycerols as hosts for selective binding of guest molecules. *Journal of the American Chemical Society* **2009**, *131*, 10574–80.

70 Burakowska, E.; Haag, R. Dendritic polyglycerol core-double-shell architectures: synthesis and transport properties. *Macromolecules* **2009**, *42*, 5545–5550.

71 Troutman, T. S.; Leung, S. J.; Romanowski, M. Light-induced content release from plasmon-resonant liposomes. *Advanced Materials* **2009**, *21*, 2334–2338.

72 Siegers, C.; Biesalski, M.; Haag, R. Self-assembled monolayers of dendritic polyglycerol derivatives on gold that resist the adsorption of proteins. *Chemistry - A European Journal* **2004**, *10*, 2831–2838.

73 Kainthan, R. K.; Janzen, J.; Levin, E.; Devine, D. V.; Brooks, D. E. Biocompatibility testing of branched and linear polyglycidol. *Biomacromolecules* **2006**, *7*, 703–9.

74 Zhou, L.; Gao, C.; Xu, W.; Wang, X.; Xu, Y. Enhanced biocompatibility and biostability of CdTe quantum dots by facile surface-initiated dendritic polymerization. *Biomacromolecules* **2009**, *10*, 1865–74.

75 Zill, A.; Rutz, A. L.; Kohman, R. E.; Alkilany, A. M.; Murphy, C. J.; Kong, H.; Zimmerman, S. C. Clickable polyglycerol hyperbranched polymers and their application to gold nanoparticles and acid-labile nanocarriers. *Chemical Communications* **2011**, *47*, 1279–1281.

76 Yeh, P.-Y. J.; Kainthan, R. K.; Zou, Y.; Chiao, M.; Kizhakkedathu, J. N. Self-assembled monothiol-terminated hyperbranched polyglycerols on a gold surface: a comparative study on the structure, morphology, and protein adsorption characteristics with linear poly(ethylene glycol)s. *Langmuir* **2008**, *24*, 4907–4916.

77 Obare, S. O.; Jana, N. R.; Murphy, C. J. Preparation of polystyrene- and silica-coated gold nanorods and their use as templates for the synthesis of hollow nanotubes. *Nano Letters* **2001**, *1*, 601–603.

78 Discher, D. E.; Eisenberg, A. Polymer vesicles. *Science* **2002**, *297*, 967–73.

79 Discher, D. E.; Ahmed, F. Polymersomes. *Annual Review of Biomedical Engineering* **2006**, *8*, 323–41.

80 Ernenwein, D.; Vartanian, A. M.; Zimmerman, S. C. Self-assembling amphiphilic hyperbranched polyglycerol-polystyrene copolymers for encapsulation. *Macromolecular Chemistry and Physics* **2015**, *216*, 1729–1736.

81 Mueller, W.; Koynov, K.; Fischer, K.; Hartmann, S.; Pierrat, S.; Basché, T.; Maskos, M. Hydrophobic shell loading of PB-*b*-PEO vesicles. *Macromolecules* **2009**, *42*, 357–361.

82 Ghoroghchian, P. P.; Lin, J. J.; Brannan, A. K.; Frail, P. R.; Bates, F. S.; Therien, M. J.; Hammer, D. A. Quantitative membrane loading of polymer vesicles. *Soft Matter* **2006**, *2*, 973.

83 Binder, W. H.; Sachsenhofer, R.; Farnik, D.; Blaas, D. Guiding the location of nanoparticles into vesicular structures: a morphological study. *Physical Chemistry Chemical Physics : PCCP* **2007**, *9*, 6435–6441.

84 Mai, Y.; Eisenberg, A. Controlled incorporation of particles into the central portion of vesicle walls. *Journal of the American Chemical Society* **2010**, *132*, 10078–84.

85 Hickey, R. J.; Haynes, A. S.; Kikkawa, J. M.; Park, S.-J. Controlling the self-assembly structure of magnetic nanoparticles and amphiphilic block-copolymers: from micelles to vesicles. *Journal of the American Chemical Society* **2011**, *133*, 1517–25.

86 Shen, Y.; Kuang, M.; Shen, Z. Gold nanoparticles coated with a thermosensitive hyperbranched polyelectrolyte: towards smart temperature and pH nanosensors. *Angewandte Chemie International Edition* **2008**,

87 Jackson, A. M.; Myerson, J. W.; Stellacci, F. Spontaneous assembly of subnanometre-ordered domains in the ligand shell of monolayer-protected nanoparticles. *Nature Materials* **2004**, *3*, 330–6.

88 Cesbron, Y.; Shaw, C. P.; Birchall, J. P.; Free, P.; Levy, R. Stripy nanoparticles revisited. *Small* **2012**, *8*, 3714–3719.

89 Stirling, J.; Lekkas, I.; Sweetman, A.; Djuranovic, P.; Guo, Q.; Pauw, B.; Granwehr, J.; Levy, R.; Moriarty, P. Critical assessment of the evidence for striped nanoparticles. *PLoS ONE* **2014**, *9*, e108482.

90 Furó, I. NMR spectroscopy of micelles and related systems. *Journal of Molecular Liquids* **2005**, *117*, 117–137.

91 Knight, W. D. Nuclear magnetic resonance shift in metals. *Physical Review* **1949**, *76*, 1259–1260.

92 Marbella, L. E.; Millstone, J. E. NMR techniques for noble metal nanoparticles. *Chemistry of Materials* **2015**, *27*, 2721–2739.

93 Kohlmann, O.; Steinmetz, W. NMR diffusion, relaxation, and spectroscopic studies of water soluble, monolayer-protected gold nanoclusters. *Journal of Physical Chemistry B* **2001**, *105*, 8801–8809.

94 Case, D. A. Molecular dynamics and NMR spin relaxation in proteins. *Accounts of Chemical Research* **2002**, *35*, 325–331.

95 Tavasoli, E.; Guo, Y.; Kunal, P.; Grajeda, J.; Gerber, A.; Vela, J. Surface doping quantum dots with chemically active native ligands: controlling valence without ligand exchange. *Chemistry of Materials* **2012**, *24*, 4231–4241.

96 Zhang, B.; Yan, B. Analytical strategies for characterizing the surface chemistry of nanoparticles. *Analytical and Bioanalytical Chemistry* **2010**, *396*, 973–82.

97 Liu, X.; Yu, M.; Kim, H.; Mameli, M.; Stellacci, F. Determination of monolayer-protected gold nanoparticle ligand-shell morphology using NMR. *Nature Communications* **2012**, *3*, 1182.

98 Salorinne, K.; Malola, S.; Wong, O. A.; Rithner, C. D.; Chen, X.; Ackerson, C. J.; Häkkinen, H. Conformation and dynamics of the ligand shell of a water-soluble Au_{102} nanoparticle. *Nature Communications* **2016**, *7*, 10401.

99 Jadzinsky, P. D.; Calero, G.; Ackerson, C. J.; Bushnell, D. A.; Kornberg, R. D. Structure of a thiol monolayer-protected gold nanoparticle at 1.1 A resolution. *Science* **2007**, *318*, 430–433.

100 Wong, O. A.; Heinecke, C. L.; Simone, A. R.; Whetten, R. L.; Ackerson, C. J. Ligand symmetry-equivalence on thiolate protected gold nanoclusters determined by NMR spectroscopy. *Nanoscale* **2012**, *4*, 4099.

101 Parker, J. F.; Choi, J. P.; Wang, W.; Murray, R. W. Electron self-exchange dynamics of the nanoparticle couple $[Au_{25}(SC_2Ph)_{18}]^{0/1-}$ by nuclear magnetic resonance line-broadening. *Journal of Physical Chemistry C* **2008**, *112*, 13976–13981.

102 Venzo, A.; Antonello, S.; Gascón, J. A.; Guryanov, I.; Leapman, R. D.; Perera, N. V.; Sousa, A.; Zamuner, M.; Zanella, A.; Maran, F. Effect of the charge state (z = -1, 0, +1) on the nuclear magnetic resonance of monodisperse $Au_{25}[S(CH_2)_2Ph]_{18}^{z}$ clusters. *Analytical Chemistry* **2011**, *83*, 6355–6362.

103 Wu, Z.; Jin, R. Stability of the two Au-S binding modes in $Au_{25}(SG)_{18}$ nanoclusters probed by NMR and optical spectroscopy. *ACS Nano* **2009**, *3*, 2036–2042.

104 Qian, H.; Zhu, M.; Gayathri, C.; Gil, R. R.; Jin, R. Chirality in gold nanoclusters probed by NMR spectroscopy. *ACS Nano* **2011**, *5*, 8935–8942.

105 Kim, H.; Carney, R. P.; Reguera, J.; Ong, Q. K.; Liu, X.; Stellacci, F. Synthesis and characterization of Janus gold nanoparticles. *Advanced Materials* **2012**, *24*, 3857–3863.

106 Pradhan, S.; Brown, L. E.; Konopelski, J. P.; Chen, S. Janus nanoparticles: reaction dynamics and NOESY characterization. *Journal of Nanoparticle Research* **2009**, *11*, 1895–1903.

107 Lindblom, G.; Orad, G.; Ranlindblom, G. NMR studies of translational diffusion in lyotropic liquid crystals and lipid membranes. *Progress in Nuclear Magnetic Resonance Spectroscopy* **1994**, *26*, 483–515.

108 Brüschweiler, R.; Liao, X.; Wright, P. E. Long-range motional restrictions in a multidomain zinc-finger protein from anisotropic tumbling. *Science* **1995**, *268*, 886–889.

109 Tjandra, N.; Feller, S. E.; Pastor, R. W.; Bax, A. Rotational diffusion anisotropy of human ubiquitin from ^{15}N NMR relaxation. *Journal of the American Chemical Society* **1995**, *117*, 12562–12566.

110 Tjandra, N.; Garrett, D. S.; Gronenborn, A. M.; Bax, A.; Clore, G. M. Defining long range order in NMR structure determination from the dependence of heteronuclear relaxation times on rotational diffusion anisotropy. *Nature Structural Biology* **1997**, *4*, 443–449.

111 Ortega, A.; Garcia De La Torre, J. Efficient, accurate calculation of rotational diffusion and NMR relaxation of globular proteins from atomic-level structures and approximate hydrodynamic calculations. *Journal of the American Chemical Society* **2005**, *127*, 12764–12765.

112 Tsay, J. M.; Doose, S.; Weiss, S. Rotational and translational diffusion of peptide-coated CdSe/CdS/ZnS nanorods studied by fluorescence correlation spectroscopy. *Journal of the American Chemical Society* **2006**, *128*, 1639–1647.

113 Alam, S.; Mukhopadhyay, A. Translational anisotropy and rotational diffusion of gold nanorods in colloidal sphere solutions. *Langmuir* **2015**, *31*, 8780–8785.

114 Vasanthi, R.; Bhattacharyya, S.; Bagchi, B. Anisotropic diffusion of spheroids in liquids: slow orientational relaxation of the oblates. *Journal of Chemical Physics* **2002**, *116*, 1092–1096.

115 Smith, A. M.; Marbella, L. E.; Johnston, K. A.; Hartmann, M. J.; Crawford, S. E.; Kozycz, L. M.; Seferos, D. S.; Millstone, J. E. Quantitative analysis of thiolated ligand exchange on gold nanoparticles monitored by ^{1}H NMR spectroscopy. *Analytical Chemistry* **2015**, *87*, 2771–2778.

116 Hubert, F.; Testard, F.; Spalla, O. Cetyltrimethylammonium bromide silver bromide complex as the capping agent of gold nanorods. *Langmuir* **2008**, *24*, 9219–22.

117 Suresh, R.; Vasudevan, S.; Ramanathan, K. Dynamics of methylene chains in an intercalated surfactant bilayer by solid-state NMR spectroscopy. *Chemical Physics Letters* **2003**, *371*, 118–124.

118 Vigderman, L.; Manna, P.; Zubarev, E. R. Quantitative replacement of cetyl trimethylammonium bromide by cationic thiol ligands on the surface of gold nanorods and their extremely large uptake by cancer cells. *Angewandte Chemie International Edition* **2012**, *51*, 636–41.

119 Soltero, J. F. A.; Manrı, R. Unusual Hofmann elimination under mild conditions in polymerizable cationic surfactant systems. *Langmuir* **2002**, *18*, 3767–3772.

120 Ye, X.; Jin, L.; Caglayan, H.; Chen, J.; Xing, G.; Zheng, C.; Doan-Nguyen, V.; Kang, Y.; Engheta, N.; Kagan, C. R.; Murray, C. B. Improved size-tunable synthesis of monodisperse gold nanorods through the use of aromatic additives. *ACS Nano* **2012**, *6*, 2804–17.

121 Alkilany, A. M.; Murphy, C. J. Gold nanoparticles with a polymerizable surfactant bilayer: synthesis, polymerization, and stability evaluation. *Langmuir* **2009**, *25*, 13874–13879.

122 Alkilany, A. M.; Nagaria, P. K.; Wyatt, M. D.; Murphy, C. J. Cation exchange on the surface of gold nanorods with a polymerizable surfactant: polymerization, stability, and toxicity evaluation. *Langmuir* **2010**, *26*, 9328–9333.

123 Sijbesma, R. P.; Meijer, E. W. Quadruple hydrogen bonded systems. *Chemical Communications* **2003**, 5–16.

124 Jorgensen, W. L.; Pranata, J. Importance of secondary interactions in triply hydrogen bonded complexes: guanine-cytosine vs uracil-2,6-diaminopyridine. *Journal of the American Chemical Society* **1990**, *112*, 2008–2010.

125 Blight, B. A.; Hunter, C. A.; Leigh, D. A.; McNab, H.; Thomson, P. I. T. An AAAA–DDDD quadruple hydrogen-bond array. *Nature Chemistry* **2011**, *3*, 244–48.

126 Beijer, F. H.; Sijbesma, R. P.; Kooijman, H.; Spek, A. L.; Meijer, E. W. Strong dimerization of ureidopyrimidones via quadruple hydrogen bonding. *Journal of the American Chemical Society* **1998**, *120*, 6761–6769.

127 Anderson, C. A.; Jones, A. R.; Briggs, E. M.; Novitsky, E. J.; Kuykendall, D. W.; Sottos, N. R.; Zimmerman, S. C. High-affinity DNA base analogs as supramolecular, nanoscale promoters of macroscopic adhesion. *Journal of the American Chemical Society* **2013**, *135*, 7288–7295.

128 Kim, J.; Jung, I.-s.; Kim, S.-y.; Lee, E.; Kang, J.-k.; Sakamoto, S.; Yamaguchi, K.; Kim, K. New cucurbituril homologues: syntheses, isolation, characterization, and X-ray crystal structures of cucurbit[n]uril (n = 5, 7, and 8). *Journal of the American Chemical Society* **2000**, *122*, 540–541.

129 Lee, J. W.; Samal, S.; Selvapalam, N.; Kim, H.-J.; Kim, K. Cucurbituril homologues and derivatives: new opportunities in supramolecular chemistry. *Accounts of Chemical Research* **2003**, *36*, 621–630.

130 Masson, E.; Ling, X.; Joseph, R.; Kyeremeh-Mensah, L.; Lu, X. *RSC Advances*; 2012; Vol. 2; p 1213.

131 Lagona, J.; Mukhopadhyay, P.; Chakrabarti, S.; Isaacs, L. The cucurbit[n]uril family. *Angewandte Chemie International Edition* **2005**, *44*, 4844–4870.

132 Kim, H.-J.; Jeon, W. S.; Ko, Y. H.; Kim, K. Inclusion of methylviologen in cucurbit[7]uril. *Proceedings of the National Academy of Sciences of the United States of America* **2002**, *99*, 5007–11.

133 Rauwald, U.; Scherman, O. A. Supramolecular block copolymers with cucurbit[8]uril in water. *Angewandte Chemie International Edition* **2008**, *47*, 3950–3953.

134 Ko, Y. H.; Kim, E.; Hwang, I.; Kim, K. Supramolecular assemblies built with host-stabilized charge-transfer interactions. *Chemical Communications* **2007**, 1305–1315.

135 Kim, H.-J.; Heo, J.; Jeon, W. S.; Lee, E.; Kim, J.; Sakamoto, S.; Yamaguchi, K.; Kim, O.; Kim, K. Selective inclusion of a hetero-guest pair in a molecular host: formation of stable charge-transfer complexes in cucurbit[8]uril. *Angewandte Chemie International Edition* **2001**, *40*, 1526–1529.

136 Zheng, Y.; Yu, Z.; Parker, R. M.; Wu, Y.; Abell, C.; Scherman, O. A. Interfacial assembly of dendritic microcapsules with host–guest chemistry. *Nature Communications* **2014**, *5:5772*.

137 Jones, S. T.; Zayed, J. M.; Scherman, O. A. Supramolecular alignment of gold nanorods via cucurbit[8]uril ternary complex formation. *Nanoscale* **2013**, *5*, 5299–5302.

138 Coulston, R. J.; Jones, S. T.; Lee, T.-C.; Appel, E. A.; Scherman, O. A. Supramolecular gold nanoparticle-polymer composites formed in water with cucurbit[8]uril. *Chemical communications* **2011**, *47*, 164–166.

139 Jones, S. T.; Taylor, R. W.; Esteban, R.; Abo-Hamed, E. K.; Bomans, P. H. H.; Sommerdijk, N. A. J. M.; Aizpurua, J.; Baumberg, J. J.; Scherman, O. A. Gold nanorods with sub-nanometer separation using cucurbit[n]uril for SERS applications. *Small* **2014**, *10*, 4298–4303.

140 An, Q.; Li, G.; Tao, C.; Li, Y.; Wu, Y.; Zhang, W. A general and efficient method to form self-assembled cucurbit[n]uril monolayers on gold surfaces. *Chemical communications* **2008**, 1989–1991.

141 Bai, Y.; Xing, H.; Vincil, G. A.; Lee, J.; Henderson, E. J.; Lu, Y.; Lemcoff, N. G.; Zimmerman, S. C. Practical synthesis of water-soluble organic nanoparticles with a single reactive group and a functional carrier scaffold. *Chemical Science* **2014**, *5*, 2862.

142 Keizer, H. M.; van Kessel, R.; Sijbesma, R. P.; Meijer, E. W. Scale-up of the synthesis of ureidopyrimidinone functionalized telechelic poly(ethylenebutylene). *Polymer* **2003**, *44*, 5505–5511.

143 Leroueil, P. R.; Hong, S.; Mecke, A.; Baker, J. R.; Orr, B. G.; Banaszak Holl, M. M. Nanoparticle interaction with biological membranes: does nanotechnology present a janus face? *Accounts of Chemical Research* **2007**, *40*, 335–342.

144 Ivask, A.; Suarez, E.; Patel, T.; Boren, D.; Ji, Z.; Holden, P.; Telesca, D.; Damoiseaux, R.; Bradley, K. A.; Godwin, H. Genome-wide bacterial toxicity screening uncovers the mechanisms of toxicity of a cationic polystyrene nanomaterial. *Environmental Science and Technology* **2012**, *46*, 2398–2405.

145 Murphy, C. J.; Vartanian, A. M.; Geiger, F. M.; Hamers, R. J.; Pedersen, J. A.; Cui, Q.; Haynes, C. L.; Carlson, E. E.; Hernandez, R.; Klaper, R. D.; Orr, G.; Rosenzweig, Z. Biological responses to engineered nanomaterials: needs for the next decade. *ACS Central Science* **2015**, *1*, 117–123.

146 Calzolai, L.; Franchini, F.; Gilliland, D.; Rossi, F. Protein-nanoparticle interaction: identification of the ubiquitin-gold nanoparticle interaction site. *Nano Letters* **2010**, *10*, 3101–5.

147 Lundqvist, M.; Stigler, J.; Elia, G.; Lynch, I.; Cedervall, T.; Dawson, K. A. Nanoparticle size and surface properties determine the protein corona with possible implications for biological impacts. *Proceedings of the National Academy of Sciences of the United States of America* **2008**, *105*, 14265–14270.

148 Tenzer, S.; Docter, D.; Kuharev, J.; Musyanovych, A.; Fetz, V.; Hecht, R.; Schlenk, F.; Fischer, D.; Kiouptsi, K.; Reinhardt, C.; Landfester, K.; Schild, H.; Maskos, M.; Knauer, S. K.; Stauber, R. H. Rapid formation of plasma protein corona critically affects nanoparticle pathophysiology. *Nature Nanotechnology* **2013**, *8*, 772–81.

149 Cedervall, T.; Lynch, I.; Lindman, S.; Berggård, T.; Thulin, E.; Nilsson, H.; Dawson, K. A.; Linse, S. Understanding the nanoparticle-protein corona using methods to quantify exchange rates and affinities of proteins for nanoparticles. *Proceedings of the National Academy of Sciences of the United States of America* **2007**, *104*, 2050–2055.

150 Yang, J. A.; Lohse, S. E.; Murphy, C. J. Tuning cellular response to nanoparticles via surface chemistry and aggregation. *Small* **2014**, *10*, 1642–51.

151 Troiano, J. M. et al. Direct probes of 4 nm diameter gold nanoparticles interacting with supported lipid bilayers. *Journal of Physical Chemistry C* **2015**, *119*, 534–546.

152 Hong, S.; Leroueil, P. R.; Janus, E. K.; Peters, J. L.; Kober, M. M.; Islam, M. T.; Orr, B. G.; Baker, J. R.; Banaszak Holl, M. M. Interaction of polycationic polymers with supported lipid bilayers and cells: nanoscale hole formation and enhanced membrane permeability. *Bioconjugate Chemistry* **2006**, *17*, 728–734.

153 Heikkilä, E.; Martinez-Seara, H.; Gurtovenko, A. A.; Javanainen, M.; Häkkinen, H.; Vattulainen, I.; Akola, J. Cationic Au nanoparticle binding with plasma membrane-like lipid bilayers: potential mechanism for spontaneous permeation to cells revealed by atomistic simulations. *Journal of Physical Chemistry C* **2014**, *118*, 11131–11141.

154 Fröhlich, E. The role of surface charge in cellular uptake and cytotoxicity of medical nanoparticles. *International Journal of Nanomedicine* **2012**, *7*, 5577–5591.

155 Chen, J.; Hessler, J. A.; Putchakayala, K.; Panama, B. K.; Khan, D. P.; Hong, S.; Mullen, D. G.; DiMaggio, S. C.; Som, A.; Tew, G. N.; Lopatin, A. N.; Baker, J. R.; Banaszak Holl, M. M.; Orr, B. G. Cationic nanoparticles induce nanoscale disruption in living cell plasma membranes. *Journal of Physical Chemistry B* **2009**, *113*, 11179–11185.

156 Leroueil, P. R.; Berry, S. A.; Duthie, K.; Han, G.; Rotello, V. M.; McNerny, D. Q.; Baker, J. R.; Orr, B. G.; Banaszak Holl, M. M. Wide varieties of cationic nanoparticles induce defects in supported lipid bilayers. *Nano Letters* **2008**, *8*, 420–424.

157 Mecke, A.; Uppuluri, S.; Sassanella, T. M.; Lee, D. K.; Ramamoorthy, A.; Baker, J. R.; Orr, B. G.; Banaszak Holl, M. M. Direct observation of lipid bilayer disruption by poly(amidoamine) dendrimers. *Chemistry and Physics of Lipids* **2004**, *132*, 3–14.

158 Mecke, A.; Lee, D. K.; Ramamoorthy, A.; Orr, B. G.; Banaszak Holl, M. M. Synthetic and natural polycationic polymer nanoparticles interact selectively with fluid-phase domains of DMPC lipid bilayers. *Langmuir* **2005**, *21*, 8588–8590.

159 Gennis, R. B. *Biomembranes: Molecular Structure and Function*; 1989; pp 1–417.

160 Rubenstein, J. L.; Smith, B. A.; McConnell, H. M. Lateral diffusion in binary mixtures of cholesterol and phosphatidylcholines. *Proceedings of the National Academy of Sciences of the United States of America* **1979**, *76*, 15–18.

161 Bhattacharya, S.; Haldar, S. Interactions between cholesterol and lipids in bilayer membranes. Role of lipid headgroup and hydrocarbon chain-backbone linkage. *Biochimica et Biophysica Acta - Biomembranes* **2000**, *1467*, 39–53.